Oxidation of SiC/BN/SiC Ceramic Matrix Composites and their Constituents

---

A Dissertation

Presented to

the faculty of the School of Engineering and Applied Science

University of Virginia

---

in partial fulfillment

of the requirements for the degree

Doctor of Philosophy

by

Megan Elizabeth Wilson

May

2018

APPROVAL SHEET

The dissertation

is submitted in partial fulfillment of the requirements

for the degree of

Doctor of Philosophy

AUTHOR

The dissertation has been read and approved by the examining committee:

Elizabeth Opila

Advisor

Gary Shiflet

Patrick Hopkins

Robert Kelly

James Howe

Haydn Wadley

Accepted for the School of Engineering and Applied Science:

Craig H. Benson, Dean, School of Engineering and Applied Science

May

2018

Acknowledgments

I would thank the Air Force Research Laboratory for funding this research and program managers Dr. Eric Jones and Dr. Paul Jero for their support. I would also like to thank Rolls-Royce Corporation and Rolls-Royce High Temperature Composites for supplying the composite materials studied in this work. A large thank you also goes to my advisor Beth Opila for her unending support, guidance, patience, and sharing of knowledge. Thank you to my committee members for their advice and comments, and to my fellow research group members for teaching me to work in the lab, reading my work, watching my presentations, and learning alongside me. Thank you also to the undergraduate researchers who assisted in oxidation experiments and sample preparation. Thanks to Dr. Timothy Keenan at Alfred University for use of the hot stage microscope. Thank you to James Hawbaker at Southern Research for conducting the stressed permeability CMC oxidation experiments and for writing the experimental procedure included as an appendix. The FIB sample preparation was done by Mr. Scott Apt at the Air Force Research Laboratory and Mr. Roberto Garcia at North Carolina State University. All TEM data acquisition was done by Dr. Helge Heinrich—thank you for spending your time and using your skills for this project. Last, but not least, I would like to thank my family, friends, and peers in MSE for their love, support, and confidence throughout this journey.

Table of Contents

List of Figures

List of Tables

Abstract

Silicon Carbide (SiC) based Ceramic Matrix Composites (CMCs) entered service in aircraft turbine engines as replacements for some Ni-base superalloy components in 2016. The CMCs consist of SiC fibers, a BN interphase coating, and a SiC-based matrix and have several benefits over traditional superalloys, including higher operating temperature and lower density, which both contribute to increased engine efficiency. The CMC constituents (fibers, interphase, and matrix), however, have the potential to be exposed to hot combustion gases (including H_2O and O_2), if the environmental barrier coating delaminates or cracks, or there is a crack which penetrates into the CMC itself. To be able to predict the lifetime of CMCs, their oxidation behavior in the presence of the hot combustion gases must be understood.

The oxidation behavior of CMCs is studied in this work through oxidation of individual CMC constituents (fibers and stand-alone matrix) as well as CMCs in both dry and wet O_2 environments using ThermoGravimetric Analysis (TGA). The temperatures studied were 800-1300°C, a relevant temperature range for turbine engine applications. Microscopy of oxidized materials helped to inform the key oxidation mechanisms at play.

Stand-alone SiC fibers were studied first. The oxidation behavior of Hi-Nicalon SiC fibers in dry O_2 was similar to that of bulk SiC oxidized in the same conditions. In wet O_2, however, oxidation at the higher temperatures (1200-1300°C) resulted in crystalline oxides that cracked *in situ* from hoop stresses.

The stand-alone matrix material consisted of SiC particulates in a continuous Si phase, with regions that contained boron. This material was oxidized in both dry and wet O_2 using TGA. The TGA results showed slightly increased parabolic oxidation rates at 1200 and 1300°C for the matrix material, as compared with bulk SiC, due to the presence of boron. The oxidation

kinetics at 800°C were also affected by boron, as neither linear nor parabolic oxidation behavior was observed through TGA. The oxidation behavior of the matrix material was considered as a baseline for CMC oxidation behavior.

The CMCs that were oxidized had a chemical vapor deposited SiC seal coat on all but one surface of the coupons. All CMC constituents were exposed to the oxidizing environments (O_2 or H_2O) on the exposed CMC face and reacted simultaneously to form SiO_2 and B_2O_3 reaction products. Observations with TGA, scanning electron microscopy, and transmission electron microscopy indicated that the BN interphase in the CMCs sealed rapidly with the formation of borosilicate glass droplets in all oxidizing conditions. In the interior of the composite, where the partial pressure of the oxidant is reduced, SiC preferentially oxidized at the SiC/BN interfaces, as expected from thermodynamic considerations. Overall, oxidation of CMCs was minimal, reaching only ~20 μm below the surface in the most extreme conditions tested (wet O_2 at 1300°C for 100h).

Thermally grown borosilicate glass droplets sealed the BN interphase on the exposed CMC surface. The exact composition of the borosilicate phase, however, could not be determined with typical spectroscopic techniques. A study of stand-alone borosilicate glasses of known compositions was conducted to probe the composition and properties of the thermally grown borosilicate glass. Borosilicate glasses ranging from 74-100 wt% B_2O_3 (balance SiO_2) were synthesized in a box furnace and heated using a hot stage microscope to understand the temperature and viscosity of each composition on forming a spherical droplet shape. The resulting relationships between composition, temperature, and viscosity were used to determine the range in composition of the thermally grown borosilicate glasses on CMCs was likely between 43-63 wt% B_2O_3.

All of the results—from the stand-alone glasses, oxidation of individual CMC constituents, and oxidation of CMCs—were integrated together to develop a description of CMC oxidation mechanisms. The identified mechanisms are valid for all temperatures and environments studied here, and describe the borosilicate glass sealing of the exposed BN interphase, along with the preferential oxidation of SiC phases (fibers and matrix) below the exposed CMC surface. In addition to the mechanistic description, a comparison to current CMC oxidation models was conducted. Mechanisms and parameters in the existing models were assessed and values of these parameters consistent with observations of the present study were recommended for improved SiC/BN/SiC life prediction models.

1. Introduction

1.1. Motivation

Improved efficiency of aircraft turbine engines has been a topic of much research over the past 50 years. The use of nickel-base superalloys and thermal barrier coatings has allowed for increased engine efficiencies via increased inlet temperatures in the turbine engine.[1; 2; 3; 4] However, the operating temperature of aircraft turbine engines was approaching the melting temperature of the nickel-base superalloys.[3] Further increases in turbine inlet temperature require the development of new materials for the hot zones of the turbine engines. Ceramic Matrix Composites (CMCs) have been under development for decades to enable these increased temperatures. CMCs were first inserted in commercial aircraft turbine engines in 2016 (in the GE LEAP engine as a superalloy replacement for the shroud) due to their lower density (about one-third that of nickel-base superalloys) and higher temperature capabilities (up to 1400°C) with a reduction in cooling air.[2] However, lifetime prediction models for CMCs based on thermochemical or thermomechanical behavior of the composites are limited due to insufficient data available. This dissertation aims to provide CMC oxidation data over a wide range of parameters (including time, temperature, environment, and load) for the first time and to develop relevant descriptions of CMC oxidation mechanisms.

1.2. Background and Use of Ceramic Matrix Composites

The CMCs studied in this work consist of SiC fibers, a BN interphase layer, and a SiC-based matrix, written: SiC/BN/SiC for fiber/interphase/matrix. The requisite mechanical properties are achieved due to the structure and processing of the CMCs. The fibers are the load-bearing constituent and provide the required strength.[4] The BN interphase between the fibers

and matrix is needed to deflect matrix cracks around the fibers and to allow for fiber pull-out instead of fiber fracture, thereby increasing composite toughness.

1.2.1. CMC Processing

There are several different routes for CMC processing. The route used for the CMCs studied in this work begins with the SiC fiber tows (bundles of 500 fibers) that are woven in a 2-D ply and the plies are stacked or woven into a 3-D pattern. The woven-fiber structure exists to make the mechanical properties of the CMCs closer to isotropic. After the fiber preforms are formed in the desired component shape, the BN interphase is deposited on the fibers, typically using a Chemically Vapor Infiltration (CVI) technique, which allows for a uniform interphase thickness. The SiC-based matrix of CMCs can be processed in a variety of ways. The SiC matrix for the composites in this study was fabricated by a multi-step process. First, a stoichiometric SiC layer is deposited using CVI, leaving a porous composite. A SiC slurry is then infiltrated to deposit SiC particulates, followed by a Melt Infiltrated (MI) Si to create a dense matrix. “Dense” throughout this dissertation is meant to describe a matrix with minimal porosity relative to those fabricated by polymer infiltration and pyrolysis (PIP), an alternative matrix processing method that is less desirable for aero-turbine engines because internal oxidation can occur in the CMC, even in the absence of an applied stress.[5]

1.2.2. Applications, Advantages, and Drawbacks for CMC Usage

CMC components in aircraft turbine engines could have Environmental Barrier Coatings (EBCs) to protect against hot combustion gases.[6] However, some components will remain uncoated and cracks or spallation of the EBCs could lead to exposed CMCs in the engine. The exact environments the CMC components would be exposed to in an aircraft turbine engine are unknown, so several assumptions are made here. Based on the input from Rolls-Royce for testing

to 1300°C, it is assumed that the maximum temperature of exposure would be 1300°C for the CMCs. If a 15,000h engine life is assumed with flights in the range of 1-10h (as bounding cases), the engine would experience a minimum of 1500 thermal cycles with a pressure of up to 50 atm.[7] Although thermal cycling and high gas pressures and velocities are experienced in turbine engines, these conditions are not addressed in the current work. The thermochemical behavior in the high temperature conditions with appropriate combustion gas products are studied in this work.

Exposure of a bare CMC to hot oxidizing gases (O_2 and H_2O) at high temperatures ($T \geq$ 800°C) in a turbine engine could result in CMC component degradation. CMC constituents (fibers, interphase, and matrix) would be exposed to the oxidizing environment if the applied coatings delaminated, reacted, or spalled off, or if a crack penetrates the CMC itself.

Formation of oxides are not desirable, especially at the fiber/BN interface due to the associated reduction in mechanical properties. The retention of the BN interphase and the SiC fibers is critical to the lifetime of the CMCs. If the BN interphase is not protected against oxidation, the toughness of the composite will be reduced. Oxidation of the SiC fibers would reduce the strength of the composite, leading to failure of the CMC by brittle fracture. Therefore, oxidation of the SiC and BN phases is of primary concern for this work.

1.3. Bulk Si and SiC Oxidation

To best describe the oxidation processes relevant to this work, three terms are defined here and used throughout the dissertation: mechanism, rate, and kinetics. ***Mechanism*** is defined as the dominant (or slowest) molecular-level process occurring during oxidation. Examples such as a diffusion-controlled mechanism or a reaction-rate-controlled mechanism will be described in following sections. ***Rate*** refers to the rate at which the relevant mechanism proceeds. And

kinetics is defined as the numerical expressions that describe the relevant oxidation mechanisms. Examples such as parabolic oxidation kinetics (describing the diffusion-controlled mechanism) and linear oxidation kinetics (describing the reaction-rate-controlled mechanism) will be described in following sections.

1.3.1. Si Oxidation

Bulk SiC oxidation has been studied extensively, as will be discussed in the following section. The understanding of bulk SiC oxidation follows from an understanding of Si oxidation, as best described in the classic study conducted by Deal and Grove.[8] For both Si and SiC oxidation, a SiO_2 oxide scale forms (reactions 1 to 4):

$$Si + O_2(g) = SiO_2 \quad [1]$$

$$Si + 2H_2O(g) = SiO_2 + 2H_2(g) \quad [2]$$

$$SiC + \frac{3}{2}O_2(g) = SiO_2 + CO(g) \quad [3]$$

$$SiC + 3H_2O(g) = SiO_2 + CO(g) + 3H_2(g) \quad [4]$$

Deal and Grove found that Si oxidation can be described by a linear-parabolic kinetics given by the following equation:

$$x^2 + Ax = Bt + x_i^2 + Ax_i \quad [5a]$$

Equation 5a can also be written as:

$$x^2 + Ax = B(t + \tau) \quad [5b]$$

where x is the oxide thickness, B is the parabolic oxidation rate constant (also written as k_p), B/A is the linear oxidation rate constant (also written as k_l), t is time, and τ is time-shift constant which corrects for the presence of the native oxide layer, x_i. For long-term oxidation experiments, x_i and τ are neglected. Parabolic oxidation kinetics are observed when diffusion of the oxidant through the oxide scale limits scale growth. Linear oxidation kinetics are observed when the surface reaction limits oxide formation. The linear-parabolic law given by Deal and

Grove can be approximated by linear kinetics at short times ($t << A^2/4B$) with the following equation:

$$x = k_l t \quad [6]$$

This approximation also holds true at low temperatures when $t << A^2/4B$ for reasonable experiment durations. Alternately, the linear-parabolic kinetics can be approximated by parabolic kinetics at long times or high temperatures (when $t >> A^2/4B$) by the following equation:

$$x^2 = k_p t \quad [7]$$

The parabolic oxidation rate constant (k_p) can be defined in terms of the properties of SiO_2 using the following:

$$k_p = B = \frac{2D_{eff}C^*}{N} \quad [8]$$

where D_{eff} is the effective diffusivity of the oxidant through the oxide layer, C^* is the solubility of the oxidant in the oxide, and N is the number of oxidant molecules incorporated into a unit volume of oxide. D_{eff} is attributed to molecular permeation of O_2 or H_2O through the SiO_2 layer.

1.3.2. SiC Oxidation

SiC oxidation mechanisms follow the oxidation behavior of Si described by Deal and Grove. This statement is explicitly true in the parabolic oxidation regime where diffusion of the oxidant through SiO_2 is the rate-limiting mechanism for either Si or SiC. For SiC, however, the linear kinetics will depend on the Reactions 3 and 4 instead of Reactions 1 and 2.

A recent review of bulk SiC oxidation studies was conducted by Presser and Nickel,[9] giving a summary of the literature on oxidation of SiC oxidized in dry O_2 or dry air environments. Presser and Nickel reported that SiC followed Deal and Grove-type oxidation mechanisms, as expected. Below 1350°C permeation of molecular oxygen dominated. Above 1350°C, the importance of oxygen ingress via network diffusion increased,[9] but molecular O_2

permeation still dominated up to 1500°C.[10] Presser & Nickel also stated that the parabolic oxidation rate constants were dependent on temperature, according to the enthalpy of permeation for the oxidant through the SiO_2 scale, as expected from Deal and Grove.[8; 9]

1.3.3. Wet Oxidation of Si and SiC

The Si and SiC phases in CMCs will react with H_2O (Reactions 2 and 4), in addition to O_2, in high-temperature combustion environments. For this reason, a wet oxidizing environment is also of interest. Deal and Grove oxidized bulk Si in 84 vol% H_2O (by bubbling O_2 through 95°C liquid H_2O) and found that the Si parabolic oxidation rates were at least one order of magnitude greater in the wet O_2 compared to dry O_2.[8] They attributed this to faster permeation of H_2O (g) through SiO_2 than O_2 through SiO_2. Although the diffusion of molecular H_2O through silica is ~100 times slower than O_2, the solubility of H_2O in silica is ~1000 times greater than O_2, allowing for the faster permeation.[8] This faster permeation of H_2O (g) through SiO_2 also applies to silica formed on SiC, and increased SiC oxidation rates have also been observed in wet O_2.[9]

There is some controversy in the literature about the magnitude of increased SiC parabolic oxidation rates in H_2O. Similar to the results reported by Deal and Grove, it was reported in several studies that oxidation of SiC by H_2O (g) also increased the oxidation rate.[9; 11; 12] However, the results in these studies were affected by impurity-enhanced oxidation—impurities coming either from the furnace setup or sintering aids in the material. H_2O in a gas stream can enhance the transport of impurities (from the furnace tube, sample holder, sample, etc.) to the surface of SiC, which further increases the oxidation rate.[13; 14] However, in high-purity fused quartz furnace tubes (99.995% pure), 10 vol% H_2O (g) in O_2 resulted in SiC parabolic oxidation rates only twice that of dry O_2 at the same temperatures.[13] Therefore, in a clean environment, there is a minimum H_2O (g) content in the gas stream required for enhanced

oxidation. The required H_2O content for each oxidation temperature was determined experimentally; for 1200 and 1400°C, 2.5 and 4.8 vol% H_2O are required, respectively.[15] Parabolic oxidation rates for both Si and SiC increase with the partial pressure of the oxidant for permeation through SiO_2, according to Equation 9:

$$k_p \propto P_{O_2}^n \; or \; P_{H_2O}^n \quad [9]$$

where *n* is equal to 1 for Si and SiC.[16; 17]

Si or SiC oxidation in a wet environment is complicated, however, by the SiO_2 volatilization reaction given in Reaction 10:

$$SiO_2 + 2H_2O(g) = Si(OH)_4(g) \quad [10]$$

This volatilization reaction is a surface reaction and follows linear kinetics.[18] This reaction occurs simultaneously with the SiO_2 formation reaction, which follows parabolic kinetics, as stated above. These two mechanisms compete and result in paralinear kinetic behavior. A model for paralinear behavior was developed by Tedmon for Cr oxidation and volatilization,[19] and extended to SiC by Opila, et al.[20]:

$$\frac{dx}{dt} = \frac{k_p}{2x} - k_{l,v} \quad [11]$$

Where $k_{l,v}$ is the linear volatilization rate. After long oxidation times, or with a thick oxide, the two competing mechanisms reach a steady state where the oxide formed per time is equal to the oxide volatilized per time.[18] The oxidation temperature will affect both the linear and parabolic rates, and therefore the steady state oxide thickness. Although there is a constant oxide thickness when steady state is achieved, there is also a linear SiC recession rate, proportional to the linear volatility rate.[18; 21]

1.3.4. Amorphous and Crystalline Forms of SiO_2

Amorphous SiO_2 is typically formed during SiC oxidation, but several crystalline phases have also been observed. Kingery, et al. report three possible crystalline forms of SiO_2 at pressures of interest: quartz, tridymite, and cristobalite.[22] Cristobalite is the highest-temperature phase, with a melting temperature of 1723°C.[23] Cristobalite transitions to tridymite at 1470°C, which transitions to quartz at 867°C (as shown in Figure 1).[22]

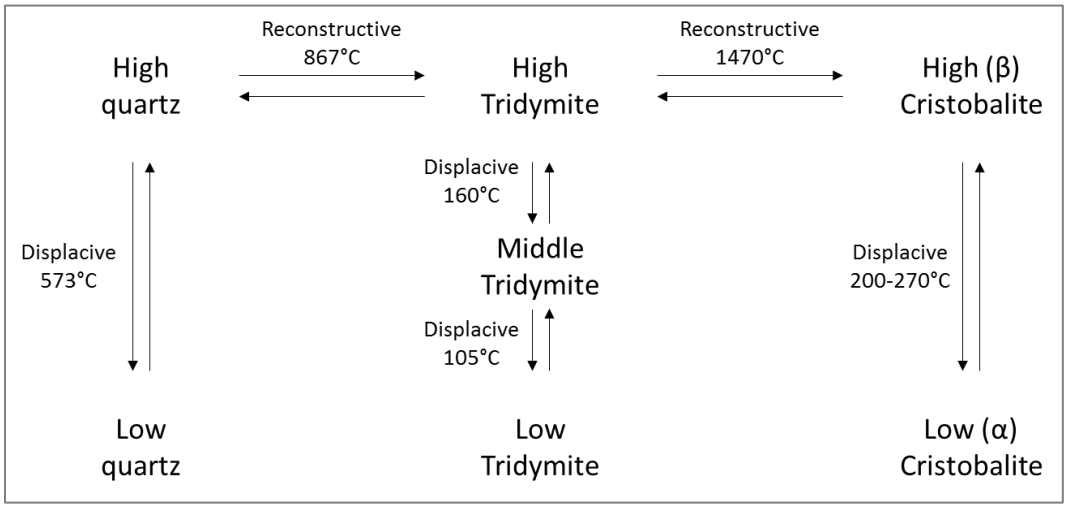

Figure 1. Polymorphic forms of silica, adapted from Kingery, et al.[22]

Cristobalite is the most commonly observed crystalline phase during SiC oxidation.[24] Cristobalite experiences a transformation from β (high temperature polymorph) to α (low temperature polymorph) around 270°C, causing cracking of the crystalline scale on cooling due to a 4.9 vol% decrease.[25] Oxidant diffusivity in β-cristobalite should be similar to diffusivity through amorphous SiO_2 due to their similar structures (Figure 2), but is difficult to measure due to the cracks that occur in the transition to α-cristobalite when cooling through 270°C to room temperature.[13]

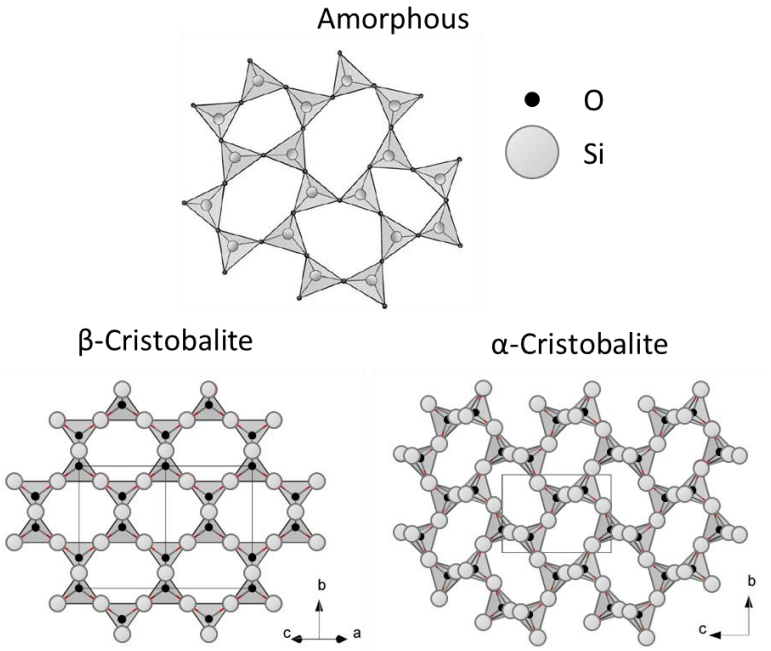

Figure 2. Amorphous SiO_2 structure (top)[9] *and cristobalite structures (bottom).*

Tridymite also has several polymorphs and has the most open crystalline structure with > 50% void space in a unit cell.[24] Tridymite has been observed on SiC oxidized in wet O_2 with an Al_2O_3 tube (with high impurity content).[13] Crystalline quartz has not been observed in SiC oxidation.[24]

The temperature at which cristobalite forms is determined by the purity of the oxidizing environment and the rate of the phase transitions.[24] As mentioned above, the presence of impurities from Al_2O_3 furnace components, or from sintering aids in SiC, not only increase the oxidation rate, but also increase the nucleation rate of cristobalite and tridymite.[14; 26] Cristobalite is observed below its equilibrium temperature (1470°C) because the phase transitions in SiO_2 are sluggish.[24] The glass transition temperature for amorphous silica is 1100-1150°C, causing amorphous silica to be the most commonly observed SiO_2 polymorph after SiC oxidation at temperatures < 1200°C and cristobalite to be observed at temperatures > 1200°C.

1.4. SiC Fiber Oxidation

It is critical to understand the oxidation mechanisms of load-bearing SiC fibers to determine the thermochemical life of the CMCs. If fiber recession, surface flaw formation, or hoop stresses occur due to oxidation, the strength of the CMC will decrease. SiC fiber oxidation could differ from bulk SiC oxidation due to geometry, chemistry, and stoichiometry. Several types of SiC fibers exist for CMC applications,[27] the most widely used being the three types in the Nicalon fiber family (Nippon-Carbon, Japan). The composition of the Nicalon family of fibers and other SiC fibers are listed in Table 1.

Table 1. SiC fiber compositions from Flores, et al.[27]

Fiber Type	Mol% Si	Mol% C	Mol% O	Other (Mol %)
Nicalon (Nippon-Carbon)	36.9	49.3	13.9	n/a
Tyranno S (UBE Industries)	32.7	45.9	20.7	0.8 (Ti)
Hi-Nicalon (Nippon-Carbon)	41.5	57.9	0.6	n/a
Hi-Nicalon (S) (Nippon-Carbon)	48.6	51.1	0.2	n/a
Sylramic iBN (COI Ceramics)	46.4	47.0	1.0	0.9 (Ti), 4.1 (B), (0.6) N

Hi-Nicalon fibers, which have excess free-C, but minimal excess O, were used in this work. Oxidation studies on all types of SiC fibers have been conducted and were recently reviewed[28] (included as Appendix A). Parabolic oxidation rate constants and activation energies were reported in most studies and found to vary by fiber composition. This variation could be due to the excess C and O in the fibers and the amount of SiC available for oxidation. [28] Hi-Nicalon fiber oxidation behavior closely resembled CVD SiC oxidation behavior. No studies have reported linear oxidation kinetics for Hi-Nicalon fibers. Only two studies have reported linear oxidation kinetics for Hi-Nicalon S.[29; 30] Linear oxidation kinetic studies of SiC fibers are not well documented, leaving a gap in the literature that will be addressed by this work.

Additionally, all of the fibers in studies that exist to date were oxidized in dry O_2, dry air, or small amounts of H_2O (g) (1-2 vol%). No studies have examined fiber oxidation with

significant water vapor contents. This is another gap in knowledge that will be addressed by this work.

1.5. BN Interphase Oxidation

As discussed earlier, CMCs require an interphase material between the fibers and the matrix to deflect cracks around the fibers and allow for fiber pullout, providing toughness. The first interphase material introduced in CMCs was pyrocarbon (PyC), used because of its layered, graphitic structure and good mechanical properties.[31] PyC, however, oxidizes to CO (g), removing it from the CMC. This makes it a poor candidate for an interphase material in oxidizing environments.

The current preferred interphase material used in CMCs is α-BN because it has a hexagonal, layered structure[32] with a high oxidation resistance relative to other BN structures. The BN interphases in current CMCs, however, are only partially crystalline. Reported BN oxidation rates vary widely, but it is agreed that BN oxidation rates depend on the crystallinity, porosity, impurities, and microstructure of the BN.[32] Oxidation of BN has been shown to occur more readily than SiC oxidation at low temperatures ($T \leq 800°C$).[33] The BN oxidation reactions of concern for this work include:

$$2BN + \frac{3}{2}O_2(g) = B_2O_3(l) + N_2(g) \quad [12]$$

$$2BN + 3H_2O(g) = B_2O_3(l) + N_2(g) + 3H_2(g) \quad [13]$$

In wet O_2, the oxidation product B_2O_3 (l) can react with water vapor to form volatile gaseous hydroxide species (Reactions 14-16). Liquid boria can also volatilize to B_2O_3 (g) in either oxidizing environment (Reaction 17).

$$B_2O_3(l) + H_2O(g) = \frac{2}{3}(HBO_2)_3(g) \quad [14]$$

$$B_2O_3(l) + H_2O(g) = 2HBO_2(g) \quad [15]$$

$$B_2O_3(l) + 3H_2O(g) = 2H_3BO_3(g) \quad [16]$$

$$B_2O_3(l) = B_2O_3(g) \quad [17]$$

An understanding of BN interphase oxidation is critical to understand the overall CMC oxidation behavior, but is unknown for the CMCs oxidized in this work. This gap in knowledge will be addressed in *Chapter 5. Ceramic Matrix Composite Oxidation* and *Chapter 7. Implications for Life Prediction of CMCs*.

1.6. Borosilicate Glass

When BN and SiC are simultaneously exposed to an oxidizing environment, their respective oxides can form a borosilicate glass (Reaction 18).

$$xB_2O_3(l) + ySiO_2(s) = xB_2O_3 \cdot ySiO_2(l,s) \quad [18]$$

Borosilicate glasses have variable compositions,[34] with low melting temperatures near 440°C (Figure 3). At CMC operating temperatures near 1200°C, the liquid phase is of interest.

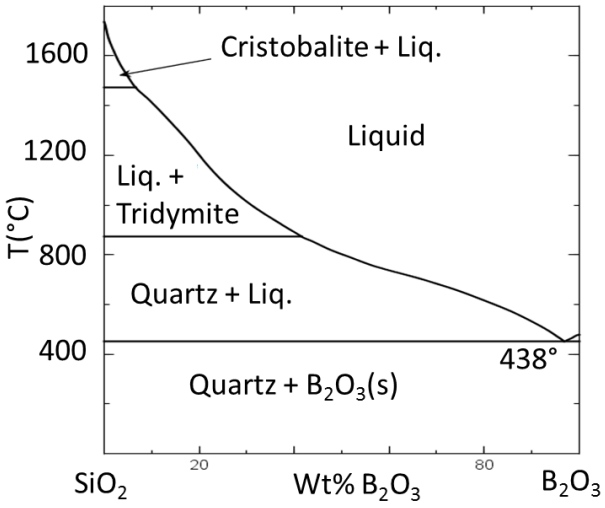

Figure 3. SiO_2 - B_2O_3 phase diagram.[35]

Many properties can change with the borosilicate composition. Of interest to this work are the permeability and viscosity of the borosilicates. Oxygen permeability through molten B_2O_3 was determined by Brown and Doremus[36] to be several orders of magnitude faster than O_2 permeation through amorphous SiO_2 by Norton.[37] This is due to the modification of the silica

network by boron atoms,[38] allowing for faster permeation of O_2 through the more open network structure. Although an increase in permeation is expected with the inclusion of boria, a correlation between borosilicate composition and oxidant permeability has not been determined.

The glass viscosity also changes with composition (Figure 4), which will relate to the ability of the glass to flow over the CMC surface, as discussed in *Chapter 6. Viscosity and Melting Behavior of Borosilicate Glasses*.

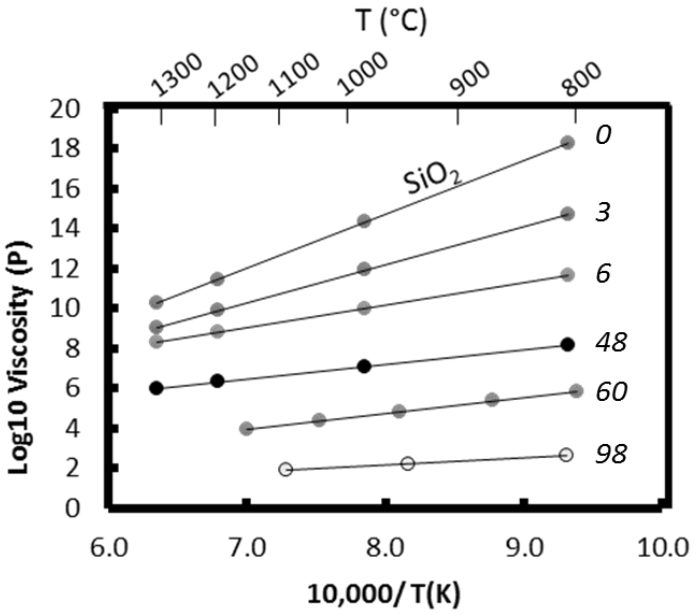

Figure 4. Effect of B_2O_3 content on borosilicate glass viscosities; data from Yan, et al.[39] *and Bruckner, et al.* [40] *Values next to lines refer to wt% B_2O_3.*

Bruckner, et al., measured the viscosities of the glasses with a rotating viscometer.[40; 41] The viscosity of each glass (of known composition) was measured at 2 to 12 different temperatures, depending on the composition.[40] Yan, et al., calculated the viscosities based on a relationship of sintering, glass density, and glass composition.[39] The viscosity of a borosilicate glass can decrease by many orders of magnitude as the B_2O_3 content increases.[39; 40]

If the composition of a borosilicate glass is unknown, its viscosity can still be determined by characteristic melting behaviors, following the technique first established by Scholze.[42]

Scholze used a Hot-Stage Microscope (HSM) to melt different types of glasses with known compositions and viscosities and found that a definitive viscosity corresponded to characteristic glass shapes, regardless of composition. Glass samples compacted into cylindrical shapes were heated in the HSM and silhouette images were recorded during heating. A ramp rate of 5°C/min was used. An example from Scholze's work is shown in Figure 5, showing the room temperature glass, softening point, half sphere point, and flow point.[42]

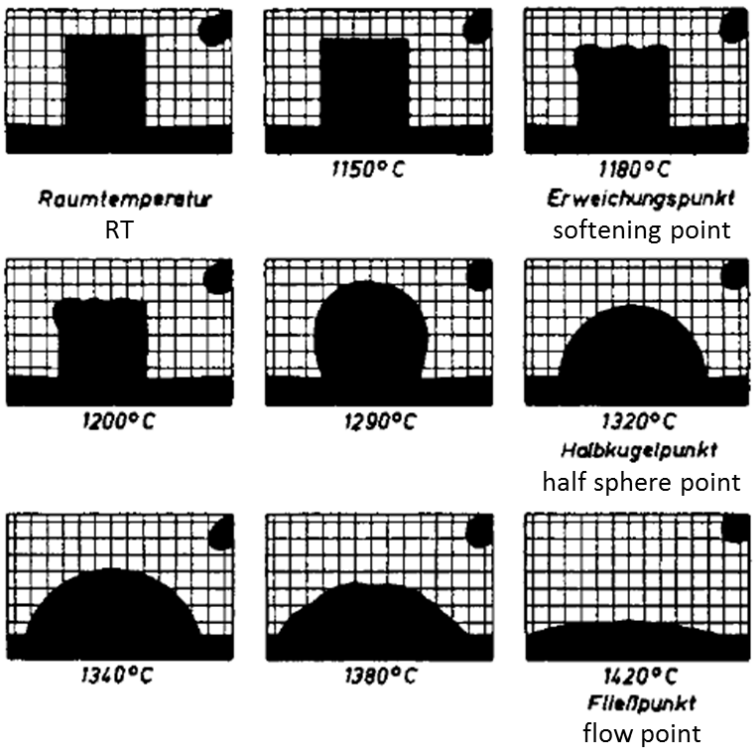

Figure 5. Silhouette images of an ash melting as temperature was increased from Room Temperature (RT) to its melting point in a hot stage microscope by Scholze.[42]

Knowing the temperature-viscosity curves for these glasses, Scholze was able to determine the viscosity that corresponded with each characteristic point for each glass and determined that these characteristic points corresponded to the same viscosities for all glasses.[42]

Similar work was repeated by Pascual, et al.,[43] and confirmed the characteristic points for glasses. Later, Pascual, et al.,[44] determined a characteristic viscosity for the sphere shape of

glasses. Today, computer software can be used in conjunction with HSM to identify the characteristic points of glasses following ASTM 1857.[45] The software can then be used to determine temperature-viscosity curves for any given glass, which can be a useful tool when rigorous viscosity testing equipment such as rotational viscometers or large glass batches are unavailable.

1.6.1. Thermally Grown Borosilicate Glasses

Understanding the compositions and viscosities of thermally grown borosilicates is of interest for CMC oxidation for several reasons. First, if a borosilicate forms on the surface of a CMC during oxidation, oxidant diffusion will be affected. The diffusivity of O_2 in borosilicate glasses is higher than through SiO_2, due to modification of the SiO_2 network structure by B_2O_3,[38] causing an increase in CMC oxidation rates.[33] Schlichting reported O_2 permeation rates up to 4 orders of magnitude higher in a borosilicate with 30% B_2O_3, as compared to pure SiO_2.[38] In the CMC system, however, the viscosity of the borosilicate could change with time due to boria volatility (Reactions 14 to 17). In the most extreme case, the viscosity would increase as B_2O_3 volatilizes, until only solid SiO_2 remains.[46] When this occurs, the oxidation mechanism would then be controlled by oxidant diffusion through solid SiO_2. Simultaneously, however, viscous flow of SiO_2 allows for stress relaxation in the oxide above 950°C.[47; 48; 49]

Thermally grown borosilicates could also be of interest along BN/SiC interfaces in the interior of CMCs, rather than on an exposed surface, where the glass could seal gaps along an interface or internal crack, limiting further oxidation. In the interior of a CMC (along a crack or gap along an interface), the Po_2 is reduced. A reduction in Po_2 affects the relative oxidation behavior of the BN and SiC phases. When the Po_2 is decreased, the more thermodynamically stable oxide (SiO_2) will form, as shown by the Ellingham diagram in Figure 6.[50]

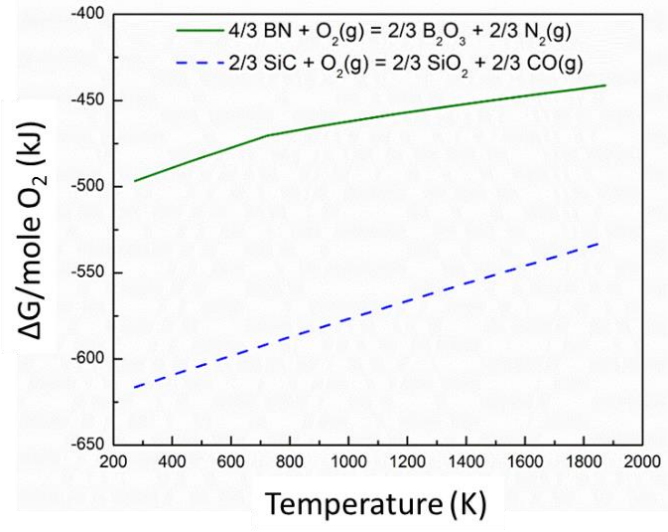

Figure 6. Ellingham diagram for BN and SiC oxidation in dry O_2 from Opila, et al.[50]

CMC oxidation models must consider both the formation of a borosilicate on the surface (high oxidant pressure) and in the interior of the composites (low oxidant pressure) as it will affect the overall oxidation behavior of the composite. The composition and phase distribution of thermally grown borosilicate glasses on CMCs have not been studied previously. This critical gap in the literature will be addressed by this work.

1.7. SiC-Based Matrix Oxidation

Matrix processing methods such as CVI and Slurry-SMI result in deviations in structure and composition of the matrix material as compared to CVD SiC. Boron-containing regions in the matrix could cause small changes in the melting temperature (~50°C) due to the B-Si eutectic temperature (Figure 7).

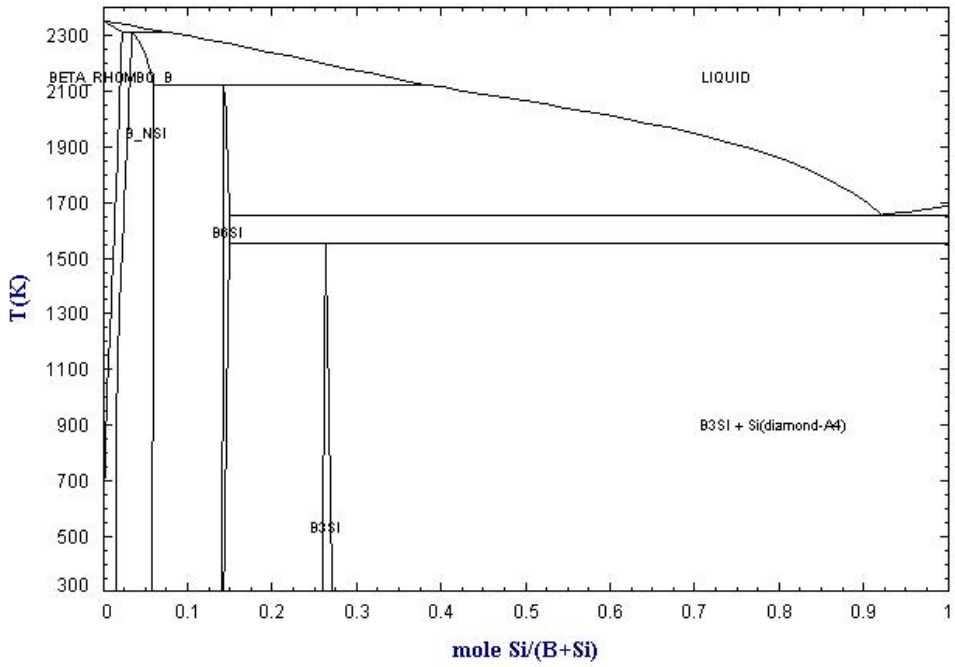

Figure 7. B-Si phase diagram from FactSage[35].

These deviations could cause changes in the oxidation behavior. However, to our knowledge, no oxidation studies of the stand-alone matrix material have been conducted. This knowledge gap will be addressed for Slurry-SMI matrix materials for the first time in this work.

1.8. SiC/BN/SiC CMC Oxidation

Moderate oxidation of SiC fibers or the BN interphase in a CMC exposed to the environment can create a protective oxide layer against further oxidation, but severe oxidation damage would lead to embrittlement of the interphase and fiber recession, which would be detrimental to the lifetime of the CMC. The oxidation behavior of SiC/C/SiC CMCs has been studied over the past few decades, but knowledge of SiC/BN/SiC CMC oxidation is limited. Figure 8 is a diagram to show the existing literature available where SiC/BN/SiC CMCs or variations of SiC-based CMCs with B-containing constituents were oxidized. The diagram also shows the oxidation studies of BN deposited on SiC (but not in a composite).

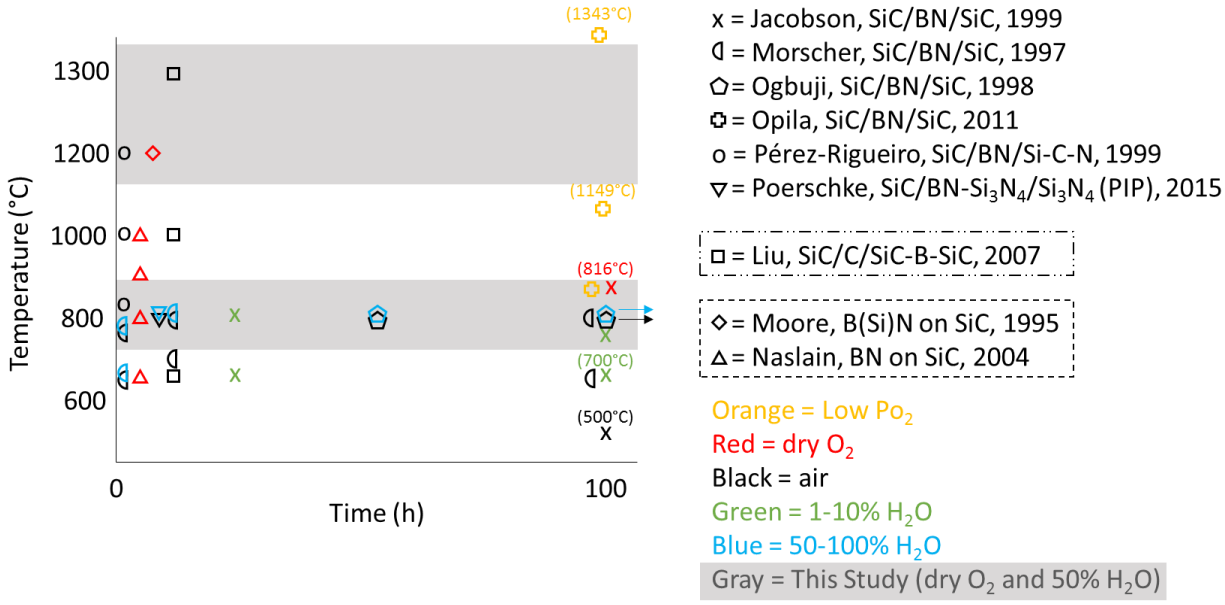

Figure 8. Diagram of all known SiC/BN/SiC oxidation studies (symbols) and this work (gray shaded areas) as a function of time and temperature.

(≤ 816°C) due to the premise that the CMCs are more prone to oxidation damage at this temperature where SiO_2 formation rates are low.[5; 33; 51; 52] Jacobson, et al. and Morscher, et al. observed volatility of the interphase (or the oxidized interphase) at 800°C and below.[33; 52] A model for this will be described in the following section.

Ogbuji observed a condensed oxide in place of the interphase after oxidation testing, with "pin-hole" pores adjacent to the fiber intersection points.[51] However, in the work by Ogbuji, each oxidized CMC was loaded to failure before characterization; no post-oxidation characterization was conducted. The CMCs oxidized by Poerschke, et al. had a dual-layer BN-Si_3N_4 interphase and a porous Si_3N_4 matrix produced by the more oxygen permeable Polymer Infiltration and Pyrolysis (PIP).[5] Despite these differences from a dense SiC/BN/SiC CMC, Poerschke, et al. observed oxidation of the SiC fiber at the SiC/BN interface, with the matrix and interphase layers remaining mostly intact.

Two other BN-interphase CMC oxidation studies were conducted to include higher temperatures, but were either conducted for short times (1h)[53] or with a low partial pressure of oxygen relevant for hypersonic flight.[54]

Liu, et al. conducted oxidation tests on SiC/C/SiC-B-SiC CMCs where the matrix consisted of SiC and B layers.[55] Although this material system is different from a SiC/BN/SiC CMC, the borosilicate formation at 700 and 1000°C could be relevant to this dissertation. Liu, et al. also observed B_2O_3 volatility at 1300°C. However, no kinetic information is provided.

The works of Moore, et al. and Naslain, et al. were included in Figure 8 because of their simultaneous oxidation of SiC and BN-coated SiC phases.[56; 57] Moore, et al. observed a uniform glassy oxidation product while Naslain, et al. reported formation of B_2O_3. However, it is expected that the BN oxidation behavior will be different in a CMC due to its constraint between two SiC phases.

There have been many stress-rupture experiments conducted for CMCs with BN interphases over the past few decades,[58; 59; 60; 61; 62; 63] to determine the mechanical properties of fibers and CMCs in oxidizing environments. Stress rupture experiments test material to failure, preventing characterization of the progression of oxidation damage, thus oxidation kinetics data cannot be obtained.

From the oxidation studies listed above, it was found that a B-containing interphase provides improved oxidation resistance compared to a carbon interphase[31; 53; 55; 57; 64] and that the oxidation resistance of a BN interphase in the CMC depends on its composition, microstructure, and thickness of the layer.[33; 57] However, only two of the studies shown in Figure 8 report kinetic data for BN interphase recession in 10% H_2O (g) or air (Figure 9).

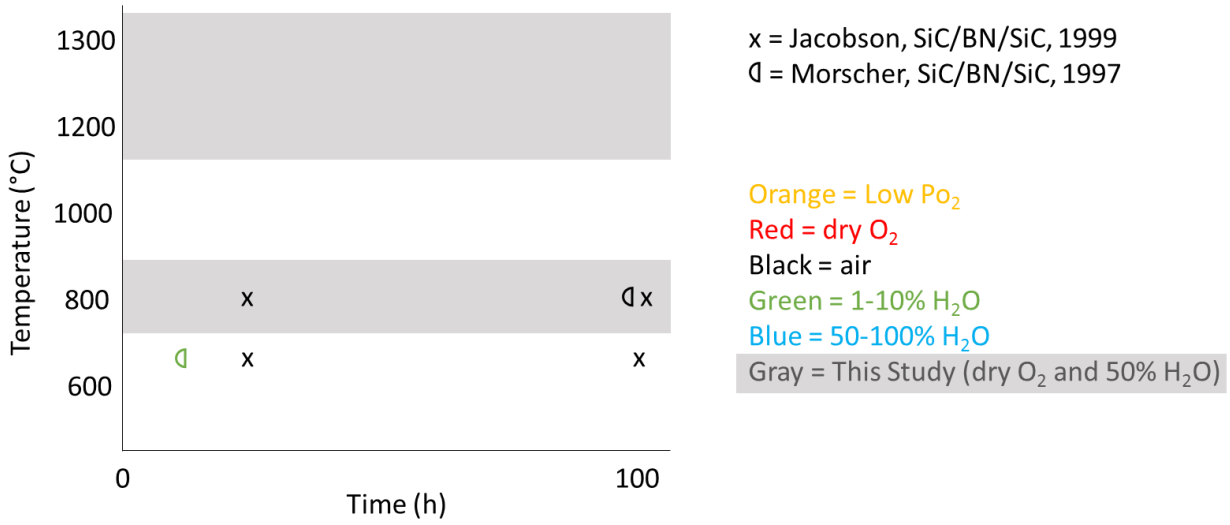

Figure 9. Diagram of all known SiC/BN/SiC oxidation kinetic data (symbols) and this work (gray shaded areas) as a function of time and temperature.

From Figure 9 and the review of CMC oxidation literature above it is evident that oxidation kinetic data for dense SiC/BN/SiC CMCs over a wide range of technologically relevant conditions (high water-vapor content and application temperatures near 1200°C) are lacking. This gap will be addressed by the oxidation of dense SiC/BN/SiC CMCs in this work over a range of time, temperature, and environmental conditions (gray shaded areas in Figure 8).

1.8.1. CMC Oxidation Mechanisms

Two key oxidation processes occur simultaneously during CMC oxidation: surface oxidation and interior oxidation. The differences between these two processes and the transport path of the oxidant are not fully understood, due to complex CMC oxidation behavior.

Several authors have previously modeled CMC oxidation behavior. First, an oxidation model for a SiC/C/SiC CMC was proposed by Filipuzzi, et al.[65] This model provides the basis for later models with a BN interphase and is therefore included here. In this model, the carbon interphase oxidized to CO (g) or CO_2 (g) and was removed from the composite, leaving an

annular void between the SiC fiber and matrix (Figure 10). The void closed over time due to SiO_2 formation from oxidation of adjacent SiC phases.

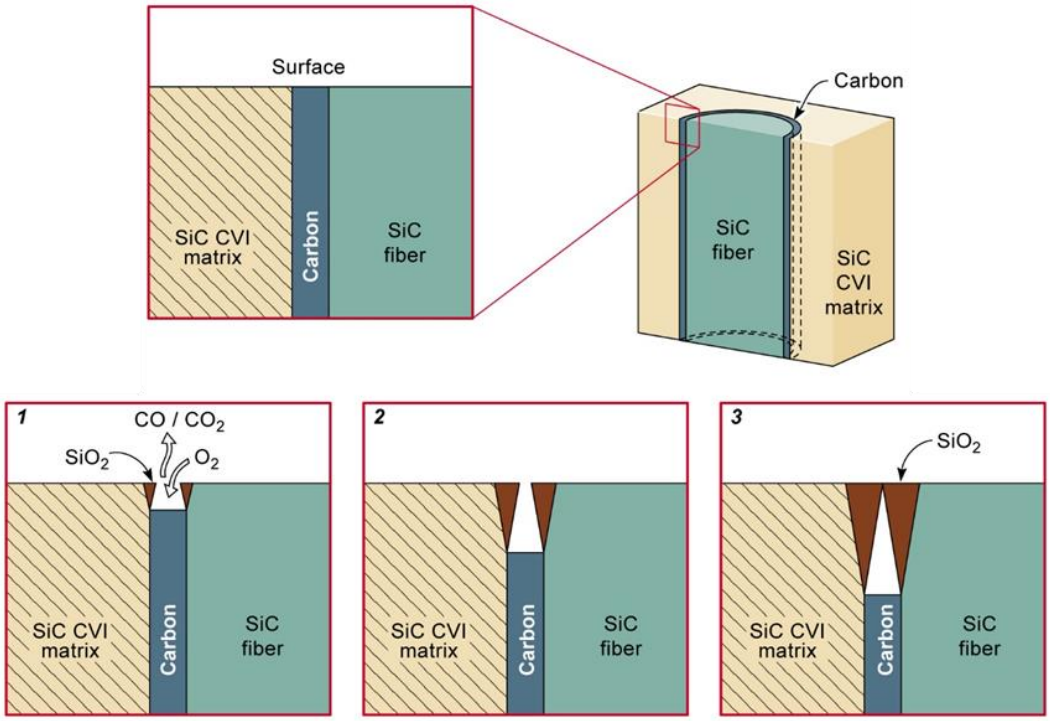

Figure 10. Model of a SiC/C/SiC CMC undergoing oxidation, removing the C interphase from the CMC; Filipuzzi, et al. [65]

The state-of-the art interphase material, BN, oxidizes to a form the condensed-phase oxide B_2O_3 (*l*), unlike carbon which forms a gas. The presence of BN therefore changes the overall CMC oxidation behavior.

Three different models were developed that proposed mechanisms for SiC/BN/SiC oxidation behavior. Xu, et al., proposed that the BN interphase and SiC fibers oxidize to form a borosilicate glass that volatilizes in the presence of H_2O (g) (Figure 11).[49] Similar to the model by Filipuzzi, et al., this model described the creation of annular voids due to the oxidation and volatilization of the interphase at 700-1000°C, followed by the growth of SiO_2 from the oxidation of the surrounding SiC phases. This model is not based on experimental evidence, but from predictions from individual constituent oxidation studies in the literature.

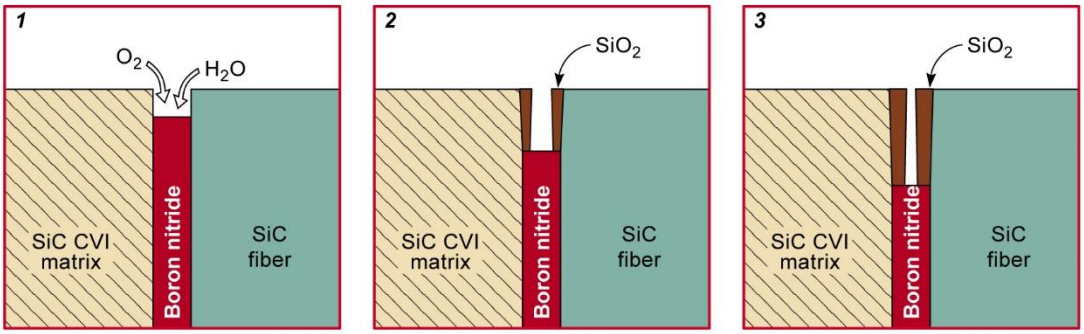

Figure 11. Model of a SiC/BN/SiC CMC undergoing oxidation, removing the BN interphase due to boria volatilization; Xu, et al.[49]

Another model of SiC/BN/SiC CMC oxidation behavior was proposed by Jacobson, et al.[33] (Figure 12). In this model, the BN and SiC phases form a borosilicate glass during oxidation at 700 and 800°C. The B_2O_3 within the borosilicate then reacts with H_2O (g) to form volatile hydroxide species. The borosilicate volatilizes slowly, creating void space in its wake. In this model, a borosilicate layer remains between the intact BN and the void, gradually moving into the interior of the composite. Over time the annular voids are sealed with SiO_2. This model is based on four experiments conducted at 700 and 800°C in 1% H_2O (g)/O_2.

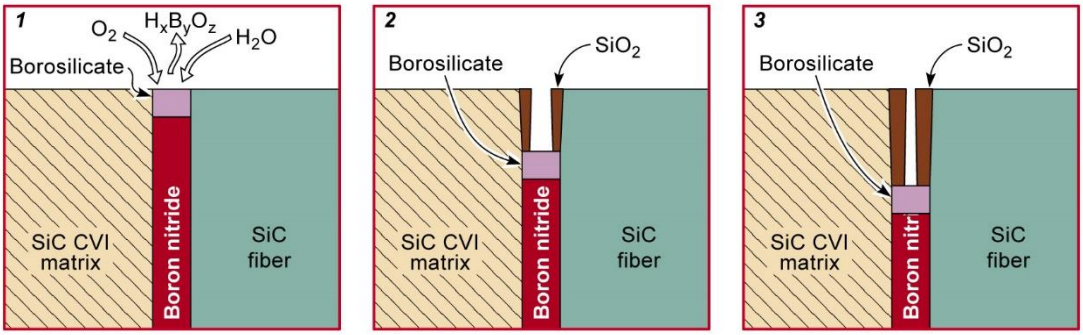

Figure 12. Model of a SiC/BN/SiC CMC undergoing oxidation, removing a borosilicate glass; Jacobson, et al.[33]

Another SiC/BN/SiC oxidation model was proposed by Przybyla, et al.[66] for temperatures of 800-1200°C. This model hypothesized that the main CMC degradation mechanisms were oxidative degradation of the fibers and the BN interphase that were exposed to the oxidant through matrix cracks that were too large to seal via oxidation of the matrix. The

fiber degradation was based on the semi-empirical model by Parthasarathy, et al.[67] that assumes grain growth, fiber recession, and oxide thickness determine the strength degradation of the fiber, and ultimately failure of the composite. Fiber failure in this manner is only relevant if a bare fiber (no interphase coating) is exposed. This was assumed to be true in the model by Przybyla, et al.[66] due to the oxidation and volatilization of the BN interphase. The BN oxidation and volatilization data were based on the data of Jacobson,[33] which was described above. No new experimental data are reported with this model. Therefore, Figure 12 also accurately represents the CMC oxidation model proposed by Przybyla, et al.

Although these models consider the individual constituents to describe CMC oxidation behavior, it will be shown in this study that the SiO_2 and B_2O_3 oxidation products form a borosilicate glass that remains intact, preventing the formation of annular voids, as predicted by the previous models. Thus it is important to understand the properties and impact of borosilicate glasses on CMC oxidation behavior. Relevant oxidation processes for the SiC/BN/SiC CMCs studied in this work will be determined in this study.

1.8.2. The Effect of Stress on CMC Oxidation

The CMC oxidation models described above primarily consider thermochemical effects. The models by Xu, et al. and Przybyla, et al. also include thermomechanical effects on CMC oxidation—primarily with respect to the matrix crack opening. This is important as CMCs will experience an applied load during operation. A stress-rupture study by Morscher, et al. showed that the magnitude of the applied load will affect CMC failure mechanisms and times.[60] Morscher, et al. found that there were two modes of CMC fracture. In the high-stress regime ($\sigma >$ 150 MPa), the CMC had a “picture frame” fracture surface with (picture frame highlighted in Figure 13a) with oxidation and embrittlement of interphase and fibers on the perimeter of the

composite and fiber pullout in the center. These results are consistent with an oxidant transport-limited mechanism (diffusion mechanism). Oxidant transport-limited behavior was also observed at high temperatures (1454°C) for a carbon-fiber/SiC CMC.[61]

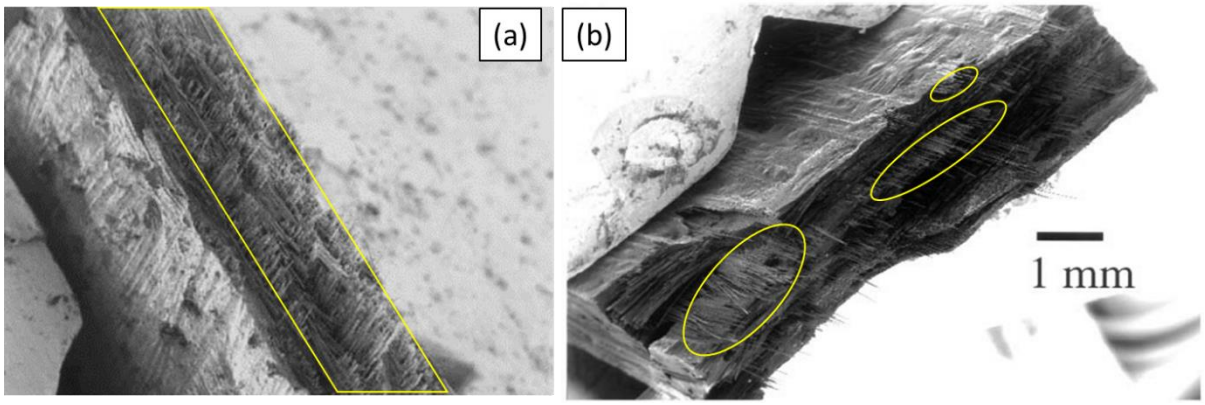

Figure 13. CMC cross-sections after failure in the a) high-stress regime, and b) in the low-stress regime; Morscher, et al.[60]

In the low-stress regime ($\sigma < 150$ MPa), the CMC had random fiber tow embrittlement, along with areas of fiber pullout on the fracture surface (fiber pullout circled in Figure 13b). This result is consistent with an oxidant reaction-rate-controlled mechanism. A similar result was observed at low temperatures (~750°C) for a C/SiC CMC.[61] For the intended application of CMCs in the hot section of turbine engines, the low-stress, slow-fracture, reaction-controlled regime is expected to dominate. However, the progression of this oxidative degradation of CMCs with an applied load has not yet been studied for SiC/BN/SiC as a function of time. The effect of stress on CMC oxidation will be studied in this work through stressed permeability tests interrupted at a series of times and prepared in cross-section for characterization of the extent of oxidation.

1.9. Gaps in Knowledge

As identified by the literature review in the previous sections, many gaps in knowledge exist related to the oxidation of dense SiC/BN/SiC CMCs and their constituents. The gaps that will be addressed by this work for the first time are outlined in the list below.

- Oxidation kinetics and behavior of SiC fibers in a significant water vapor content relevant for turbine engine environments – 50 vol% (prior work ≤ 2 vol% H_2O) have not yet been determined.
- Oxidation behavior of a stand-alone dense Slurry-SMI matrix with SiC particulates and a boron-containing phase has not been explored. Effects of matrix constituents on oxidation behavior relative to pure SiC were unknown.
- Oxidation kinetic data for dense SiC/BN/SiC CMCs over a wide range of technologically relevant conditions are lacking: The two available works primarily focus on short time behavior (< 20 hours) at 800°C.
    - Use temperatures of dense SiC/BN/SiC CMCs up to 1300°C are anticipated.
    - Microstructural characterization for interrupted oxidation exposures up to 100h have not yet been attempted.
    - A detailed comparison between oxidation behavior in dry oxygen and high water vapor partial pressures is lacking.
- A detailed understanding of effects and mechanisms of high oxidant partial pressure on external oxidation of SiC/BN/SiC CMC constituents vs effects of low oxidant partial pressure on internal oxidation of SiC/BN/SiC CMC constituents is lacking.
- Effects of applied load on internal CMC oxidation behavior as a function of load and exposure time prior to stress rupture had not been explored in prior work.

1.10. Objectives

The overall objective of this dissertation is to develop an understanding of relevant SiC/BN/SiC oxidation mechanisms and behavior over a large range of conditions, varying time, temperature, environment, and load. This was achieved by the oxidation of the stand-alone CMC constituents and CMCs as outlined below.

- The objective of Chapter 3 was to address SiC fiber oxidation in both dry and wet oxidizing environments. The dry oxidation kinetics were found to be similar to other SiC fiber oxidation studies and bulk SiC oxidation studies. This work resulted in a publication in Advanced Engineering Materials (2016) that has been internationally cited. The wet oxidation study addressed a gap in knowledge for the oxidation behavior of SiC fibers in a significant water vapor content (50 vol% H_2O) for the first time. Oxidation kinetic data were determined for temperatures ranging from 700-1300°C. At high temperatures (1200 and 1300°C) the oxide was crystalline, which resulted in *in situ* cracking and complete consumption of the SiC fibers after 100h at 1300°C. The wet oxidation kinetics and oxide cracking will result in a publication in the Journal of the American Ceramic Society.
- The objective of Chapter 4 was to address the oxidation behavior and kinetics of a stand-alone Slurry-SMI matrix material containing SiC particulates and B-containing phases in both dry and wet oxidizing environments for the first time. In all conditions, the oxidation rates were altered compared to bulk Si or SiC due to the presence of boron. These results are used as a comparison for CMC oxidation behavior described in Chapter 5.
- The objective of Chapter 5 was to address SiC/BN/SiC CMC oxidation over a large range of conditions (time, temperature, and environment, with a preliminary exploration of applied load) for the first time. This work focuses separately on CMC surface oxidation

and interior oxidation. Rapid surface-sealing due to oxidation was identified for exposed CMC surface oxidation that was nearly independent of exposure time, temperature, and environment contrary to prior observations of preferential loss of the BN interphase. This will result in a publication submitted to the Journal of the American Ceramic Society. Preferential SiC fiber oxidation relative to SiC matrix and BN oxidation was identified in the interior of the CMCs. This will result in another publication submitted to the Journal of the American Ceramic Society.

2. Test Materials and Procedures

2.1. Test Materials

CMC constituents (fibers and matrix material) and full CMCs were studied in an attempt to fully understand the oxidation behavior of the CMCs. Hi-Nicalon SiC fiber tows, (COI Ceramics, Inc., San Diego, CA) consisting of 500 individual fibers, were cut in 10 cm lengths and twisted into a lanyard shape (Figure 14a). The lanyard shape was utilized to hang the sample in the ThermoGravimetric Analysis (TGA) furnace for oxidation as described in detail below.

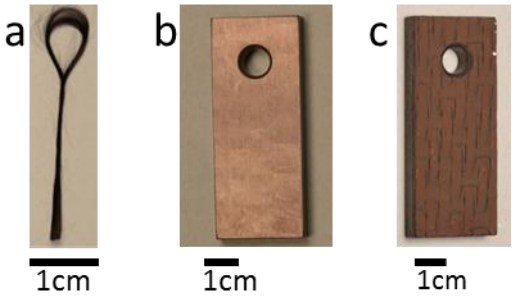

Figure 14. a) Hi-Nicalon fiber tow formed as a lanyard to hang in TGA furnace, b) SiC-based matrix material coupon, c) SiC/BN/SiC CMC coupon.

Hi-Nicalon fibers contain a crystalline β-SiC phase, amorphous free carbon, and residual amorphous Si-C-O, with stoichiometry of 62 wt% Si, 37 wt% C, and 0.5 wt% O.[27] The polyvinyl alcohol sizing on the commercial Hi-Nicalon fibers was removed prior to oxidation experiments according to the following procedure of Hay et al.[29] The lanyards were placed in a boiling deionized water bath at 100°C for one hour, then the lanyards were removed from the water bath and dried for 20 minutes at 120°C while suspended in a convection oven. The lanyards were reintroduced to the boiling water bath for another hour and the drying procedure was repeated. The desized lanyards were weighed on a bench-top balance to an accuracy of ± 0.05 mg (MS105D4, Mettler Toledo, Columbus, OH).

SiC-based matrix material coupons of size 2.54 cm x 0.95 cm x 0.32 cm (1" x 3/8" x 1/8"), were fabricated with a hole to hang in the TGA furnace (Figure 14b) by Rolls-Royce High Temperature Composites (HTC) (Cypress, CA). The matrix material consisted of SiC in a Si-continuous phase with boron-containing regions.

SiC/BN/SiC CMC coupons of size 2.54 cm x 0.95 cm x 0.32 cm (1" x 3/8" x 1/8"), were fabricated with a hole to hang in the TGA furnace (Figure 14c), by Rolls-Royce HTC. The CMCs consisted of a stacked, 2-D Hi-Nicalon fiber layup, a BN interphase, and a SiC-based matrix, which was the same as the matrix coupons. A Chemical Vapor Deposited (CVD) SiC seal coat was applied to all faces (including the hole interior) of the CMC by Rolls-Royce HTC. Prior to oxidation, the seal coat was removed from the bottom face of the CMC using 9 μm diamond polishing grit (Buehler, Lake Bluff, IL) to allow for oxygen ingress into the CMC from only one direction.

In addition to studying the oxidation behavior of CMCs and CMC constituents, the melting and viscosity behaviors of stand-alone borosilicate glasses were studied on Si-based substrates. Three substrates were used: CVD SiC (Bomas Machine Specialties, Inc., Somerville, MA), amorphous SiO_2 (99.99% pure, Ted Pella, Inc., Redding, CA), and Si (Ted Pella, Inc. Redding, CA). All substrates used were 1 cm x 1 cm squares (0.25-1 mm thickness).

Borosilicate glasses were synthesized by melting pieces of SiO_2 (99.99% metals basis, Alfa Aesar, Ward Hill, MA) and B_2O_3 (99.98% trace metals basis, Sigma-Aldrich, St. Louis, MO) glasses (total batch weights were approximately 10 g) in designated mass ratios in a box furnace at 1000-1200°C, to obtain the desired nominal glass compositions of 100, 90, 80, 70, and 60 wt% B_2O_3 (balance SiO_2). An extra 10 wt% B_2O_3 was added to each batch to account for volatilization of B_2O_3 during heating. The glasses were melted in a 95% Pt-5% Au crucible

(Heraeus Precious Metals North America, Conshohocken, PA) with at Pt foil lid. The glasses were kept at temperature in the box furnace for 30-90 minutes and then removed from the furnace at temperature to "air-quench" the glass, avoiding phase separation. After the glass cooled to room temperature, it was weighed, removed from the crucible, and ground using a mortar and pestle. Any mass loss was assumed to be due to volatility of B_2O_3 (g). For the 80 wt% B_2O_3 composition, the glass was further ground using cylindrical SiC grinding medium (Glen Mills, Inc., Clifton, NJ) in a ball mill (U.S. Stoneware, East Palestine, OH) for 24 hours. For 90, 70, and 60 wt% B_2O_3 compositions, the ground glasses were mixed by hand or by a plastic stir rod in Nalgene containers for 5-30 minutes. For all compositions, the powder was placed back in the Pt-Au crucible with the Pt lid and melted at 1000-1200°C for 30-90 minutes and removed at temperature. Once cooled, the crucible was weighed to determine the final nominal composition of the glass assuming all mass loss was due to B_2O_3 (g) volatility.

After the second melt, the glasses were formed into cylinders measuring approximately 2 mm in diameter and 3 mm in height (Figure 15) using one of the following two methods.

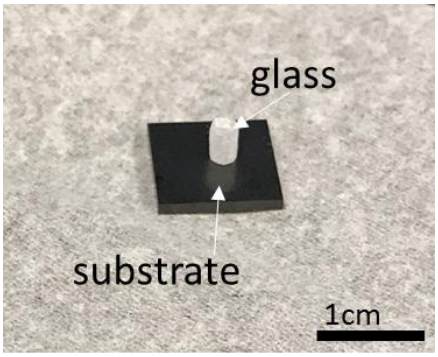

Figure 15. 100% B_2O_3 glass cylinder on SiC substrate prior to Hot Stage Microscope testing.

For high-boria content glasses (100 or 90 wt% B_2O_3), the glasses were heated to 1000°C or 1100°C, respectively, in the Pt-Au crucible and removed at temperature. A wound Pt wire was then dipped into the molten glass and pulled directly out, creating a glass strand connecting the Pt wire and the molten glass in the crucible. Glass strands of approximately 2mm in diameter

were held until the strand solidified. The strand was broken off at the base (adjoining to the glass melt) and ground using 180 grit SiC paper to approximately 3mm in height.

The lower-boria content glasses (80, 70, and 60 wt% B_2O_3) were too viscous, even at 1250°C, to be pulled into glass strands as described above. To achieve the necessary cylindrical shape, pieces of the glass composition (after the second melt) were melted on to the end of a borosilicate rod (Kimble KIMAX, Thermo Fisher Scientific, Inc., Waltham, MA) using an oxygen-acetylene torch (Smith Equipment, Watertown, SD). Additional glass of the same composition was then melted on to the end of the rod and the glass was placed back in the small tip of the flame (to avoid heating the rod). Once the glass was molten (< 1 second in the flame), it was removed and pulled into the cylindrical shape using the inside of flat, stainless steel tweezers (NovelTools, Los Angeles, CA). Figure 16 shows images depicting the cylinder formation process.

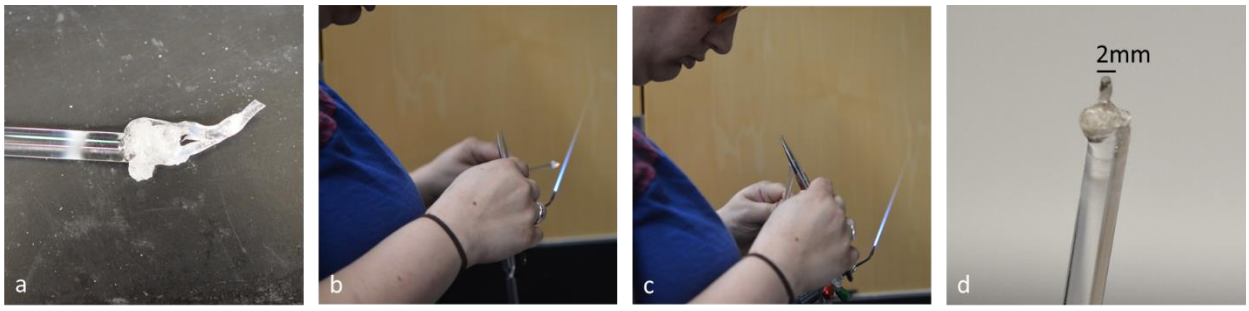

Figure 16. Formation of a borosilicate glass cylinder with oxygen-acetylene torch: a) melted borosilicate glass on the end of borosilicate rod, b) tip of glass just removed from flame, c) glass shaped by tweezers, d) final glass shape on end of borosilicate rod.

This process was repeated as few times as possible to achieve the required shape. Additional exposure to the flame increased the possibility of B_2O_3 (g) volatility, with resulting changes in the composition of the glass. Compositions were confirmed using Inductively Coupled Plasma-Optical Emission Spectroscopy as described in the characterization procedures section that follows.

2.2. Experimental Setup and Procedures

The oxidation studies of CMCs and their constituents (listed in the section above) were conducted using a vertical ThermoGravimetric Analysis (TGA) furnace. Test materials were suspended in the TGA from a SetSys 100 g microbalance (Setaram, Inc., Hillsborough, NJ) using an alumina hanger (99.5% pure, CoorsTek, Inc., Golden, CO) inside a 22 mm ID fused quartz tube (99.995% pure, Quartz Scientific, Inc., Fairport Harbor, OH). Oxidation experiments were conducted using TGA at 700-1300°C for 1, 50, or 100 hours in one of two environments: dry O_2 or wet O_2 (described below). There were three main temperatures of interest: 800, 1200, and 1300°C; 800°C represents a low temperature where BN oxidation rates dominate over SiC oxidation rates,[33] 1200°C represents a typical operating temperature for aircraft turbine engines,[68] and 1300°C represents an upper-limit future use temperature.[68] The dry O_2 experiments were conducted by flowing dry O_2 gas flowing at 100 sccm (room temperature) sequentially through a desiccant (anhydrous sodium alumina silicate, Sigma-Aldrich, St. Louis, MO) and then through the furnace. For wet O_2 experiments, a presaturator and saturator were used in conjunction with the TGA to ensure precise control of the H_2O (g) content in the gas stream (Figure 17).

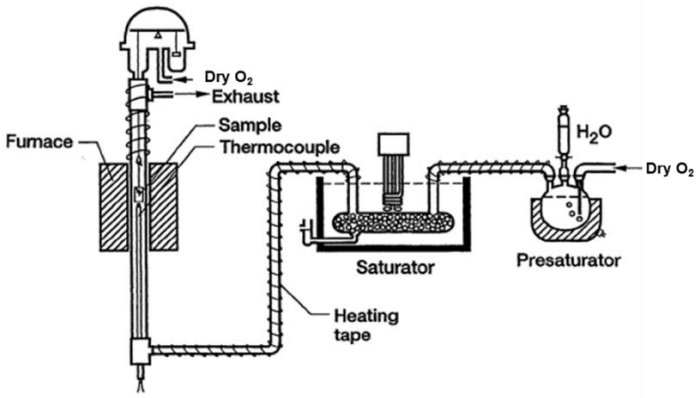

Figure 17. ThermoGravimetric Analysis (TGA) setup with H_2O saturator and presaturator.

For wet O_2, 500 sccm (room temperature) dry O_2 flowed through the anhydrous sodium alumina silicate desiccant prior to entering the presaturator. The presaturator consisted of a water bath at approximately 99°C, over-saturating the gas stream with H_2O (g). The over-saturated gas stream then flowed through the saturator which was equilibrated in a water bath at 81.7°C. Condensation of excess H_2O (g) left a 50 vol% H_2O (g) / 50 vol% O_2 (g) gas stream that flowed through the furnace. The total gas velocity (RT) over the sample was 4.4 cm/s. Additionally, a counter flow of 500 sccm (RT) dry O_2 flowed over the balance at the top of the TGA to prevent moisture condensation on the balance. Both gas streams exited the TGA as "exhaust" near the top of the setup, to avoid counter-flow effects on the sample. All tests were conducted at 1atm.

A limited number of CMC and matrix material coupons were provided by RR-HTC. Table 2 shows how each of the 64 CMCs received from RR-HTC were used. Appendix B lists the final state of each CMC coupon.

Table 2. Use of 64 CMC coupons received from RR-HTC

Test or Characterization Techniques	No. CMCs Used
TGA oxidation (3 temperatures, 3 times, 2 environments) with up to 3 repeats at each condition	49
CVD intact for baseline TGA oxidation	4
Failed TGA experiments due to power outage	3
Characterization or baseline of as-received CMCs (SEM and ICP)	5
Unused	3
Total CMCs Used	**64**

18 matrix material coupons were provided by RR-HTC. T shows how each of the 18 matrix material coupons were used.

Table 3. Use of 18 matrix material coupons received from RR-HTC

Test or Characterization Techniques	No. Matrix Material Coupons Used
TGA oxidation (3 temperatures, 2 environments) With up to 3 repeats at each condition	13
Characterization or baseline of as-received coupons (SEM and ICP)	5
Total Matrix Material Coupons Used	**18**

Hot Stage Microscope (HSM) experiments were conducted at Alfred University (Alfred, NY). A Misura HSM (HSM-ODHT M31600/80, Modena, Italy) was used with the Misura 32.2 software package. A labeled picture of the HSM is shown in Figure 18.

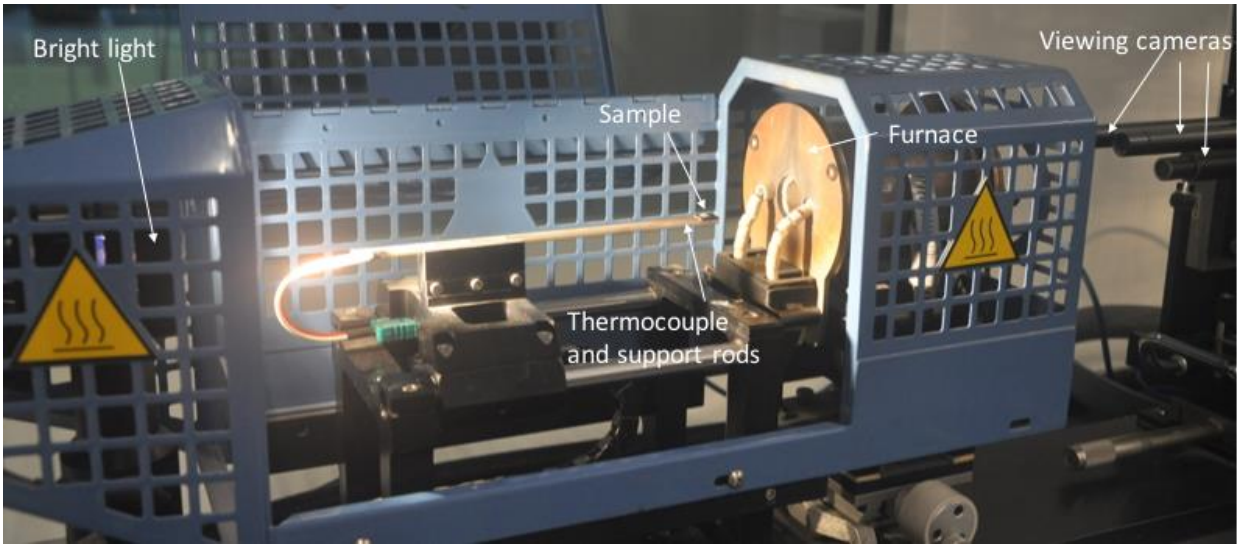

Figure 18. Hot Stage Microscope used for viscosity tests at Alfred University

HSM tests were conducted with the borosilicate glass cylinders on Si-based substrates in lab air. The starting dimensions and masses of the substrate and glass before each test were measured. The cylinder was placed on the center of the substrate to begin each experiment. For all experiments, a heating rate of 20°C/min was used to ramp to the desired temperature. Two types of heating profiles were used. A continuous ramp to 1000°C was used for one cylinder of each composition. Additionally, isothermal tests were conducted at a different temperature for each composition. Each temperature was chosen to maintain a constant viscosity (10715 Poise) at the

nominal composition, based on the data from Bruckner, et al.[40] The furnace was ramped at the same rate to the desired temperature and held for 45 minutes. Table 4 shows the quantity of tests conducted at each condition.

Table 4. Matrix of completed HSM tests

Wt% B_2O_3	Ramp to 1000°C	Hold at 500°C	Hold at 580°C	Hold at 710°C	Hold at 925°C
100	1	6			
90	1		6		
80	1			6	
70	1				6
60	1				

Droplet profiles were recorded by the three viewing cameras and analyzed with the Misura 32.2 software according to ASTM 1857.[45]

2.3. Characterization Procedures

Hi-Nicalon fiber oxidation behavior was characterized with TGA, Scanning Electron Microscopy (SEM), and X-Ray Diffraction (XRD). TGA was used to record the mass change with time for each fiber oxidation experiment. The oxidation mechanism (diffusion- or reaction-rate-controlled) was determined from the variation of the specific mass change with time (parabolic or linear relationship, respectively). Although the kinetics were determined from the TGA mass change data, the data underestimated the oxidation rate constants due to decreasing fiber surface area during oxidation. The oxides on adjacent fibers can join together, increasing the oxidant diffusion distance to the available SiC. Therefore, the oxide thickness rather than mass change was used to calculate kinetic constants.

SEM (FEI Quanta 650, Hillsboro, OR) was used to observe and measure the oxide thicknesses on fibers in cross-section after each oxidation experiment. The average measured oxide thicknesses were used to calculate oxidation rate constants in units of μm/h (for a reaction-

rate-controlled oxidation mechanism) or $\mu m^2/h$ (for a diffusion-controlled oxidation mechanism). For both dry and wet O_2, three runs were conducted at each temperature and 105 to 217 measurements were made on 35 to 54 fibers. After SEM characterization of oxides on the fibers, select samples were characterized with XRD (X'Pert Pro MPD, PANalytical, Westborough, MA) to determine the crystallinity of the oxides.

The matrix material was characterized with TGA, SEM with Energy Dispersive Spectroscopy (EDS), and XRD. The oxidation mechanisms were again determined by mass changes recorded by TGA. Additionally, rapid, transient mass changes at the beginning of each experiment were quantified by TGA. SEM and EDS were used to characterize the oxide morphology and composition in plan view after oxidation. Coupons were also sectioned in half (Figure 19), and the cut-face, shown by the thick arrow in Figure 19, was ion-polished (IM 4000, Hitachi, Tokyo, Japan) to measure oxide thicknesses on each coupon in cross-section after oxidation.

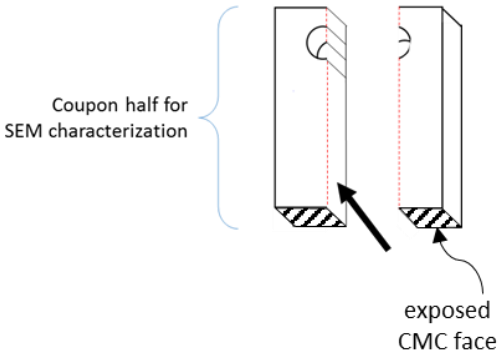

Figure 19. Diagram of matrix material and CMC coupon halves, showing half for SEM characterization. The thick arrow indicates the cut face that was polished. Hatched region shows face of the CMC for which the seal coat was removed.

EDS (AZtec Oxford XMax 150, Oxford Instruments, Concord, MA) was used to semi-quantitatively determine oxide composition. XRD was again used to determine the crystallinity of the oxides on the matrix material coupons.

The CMCs were characterized with TGA, SEM, EDS, TEM, and XRD. Because the CVD SiC seal coat was intact on all CMC faces except one, TGA was only used to quantify the rapid, transient mass changes that occurred at the beginning of each CMC oxidation experiment. The CVD SiC seal coat on all other faces was oxidizing simultaneously, affecting the total mass change recorded with TGA during oxidation. After each oxidation experiment, the exposed CMC face was characterized in plan view with SEM and EDS to characterize the oxide morphology and composition. Four CMC coupons were oxidized with the CVD SiC seal coat intact on all faces of the coupon. These were used as baseline experiments for mass gain behavior with TGA.

CMC coupons were sectioned in half and the cut face (thick arrow in Figure 19) was polished to 1 μm using diamond polishing grit for characterization of oxidation in the interior of the CMC. The oxygen ingress lengths from the exposed CMC face into the composite were observed and measured using SEM and EDS. Evidence of oxidation along the BN interphase was of particular interest. SEM micrographs along with oxygen EDS maps were used to measure oxygen ingress lengths along fiber tows parallel to the oxygen ingress direction into the CMC. Oxygen ingress length measurements were made in multiple locations on each characterized CMC. Select CMCs were ion-polished in cross-section to characterize BN interphase oxidation at the exposed CMC surface with SEM.

Thin foils were made from select CMCs for Transmission Electron Microscopy (TEM) by Focused Ion Beam (FIB) milling (NC State University, Raleigh, NC). These foils examined areas between two adjoining fibers in the CMCs after oxidation. The TEM foils were analyzed using the FEI Titan STEM (Hillsboro, OR) at UVa. In addition to TEM imaging of the foils, chemical analysis was conducted using Electron Energy Loss Spectroscopy (EELS) and Energy Filtered TEM (EF-TEM). All data acquisition was conducted by Dr. Helge Heinrich at UVa. For

EELS quantification, the Gatan Tridiem energy filter was set to a dispersion of 0.3 eV/channel and the entrance aperture was set to 2 mm. A spot size of 6 was use in STEM mode for all EELS analyses along with a camera length of 60 mm. The software used for analysis was the Quantification application in Digital Micrograph 1.85.1535. The following parameters were used for EELS analyses throughout this work (Table 5). A 1st order polynomial fit was used for all background extrapolations.

Table 5. EELS parameters used for CMC quantification

Edge Name	Background Start (eV loss)	Background End (eV loss)	Signal Start (eV loss)	Signal End (eV loss)	Hartree-Slater Cross-Sections (Barns)
Si-$L_{2,3}$	84.0	94.0	99.0	108.9	2871 ± 287
B-K	167.1	183.0	188.1	213.0	983 ± 98
C-K	252.9	278.1	284.1	309.0	412 ± 41
N-K	357.9	393.0	401.1	426.0	193 ± 19
O-K	474.0	521.1	531.9	572.1	155 ± 15

For EF-TEM quantification, the following parameters were used throughout this work (Table 6). A power law was used for all background fits from the pre-edge images.

Table 6. EF-TEM parameters used for CMC quantification

Edge Name	Pre-Edge 1 Window (eV loss)	Pre-Edge 2 Window (eV loss)	Post-Edge Window (eV loss)	Slit Width (eV)
Si-L	55-57	77-97	109-129	20
B-K	146-166	166-186	188-208	20
C-K	242-262	262-282	284-304	20
N-K	338-368	368-398	401-431	30
O-K	469-499	499-529	532-562	30

The average starting compositions of the borosilicate glass cylinders were quantified using Inductively Coupled Plasma-Optical Emission Spectrometry (ICP-OES) (iCap 6200 Duo Spectrometer, Thermo Fisher Scientific, Inc., Waltham, MA). Three cylinders of each composition were digested in an HF-H_2O solution (2 mL 48 wt% trace metal grade hydrofluoric

acid (HF) (Thermo Fisher Scientific, Inc., Waltham, MA) and 13 mL DI H_2O (l)) for 24 hours to completely digest the glass, each in its own 15mL PET centrifuge tube. The ICP-OES was calibrated with Si and B solutions prepared from known Si and B concentrations (1, 10, 100, or 500 ppm Si or B) (Inorganic Adventures, Christiansburg, VA) prior to analysis of the digested solutions. The digested solutions were then analyzed, yielding B and Si concentrations in parts per million (ppm). The B and Si concentrations were converted to wt% B_2O_3 and SiO_2 following several assumptions. First, it was assumed that the only possible oxide compositions were SiO_2 and B_2O_3. Next, it was assumed that for every 1 mol of Si detected by the ICP-OES, 1 mol of SiO_2 was dissolved in the acid solution and for every 2 mol of B detected, 1 mol of B_2O_3 was dissolved. Last, it was assumed that the composition determined from each digested glass cylinder was representative of all cylinders of that nominal composition.

Borosilicate glasses and the Si-based substrates were characterized after HSM testing using several techniques: SEM/EDS, ICP-OES, optical imaging, and ImageJ software. SEM and EDS were used to characterize the droplet profiles on the substrates, and the substrate surface once the droplets were removed. ICP-OES was used to determine the average composition of the droplet after exposure. For this analysis, the oxide droplets were removed from the substrate and digested in an HF/H_2O solution according to the procedure described above for analysis of the glass cylinders before exposure.

3. Oxidation of Hi-Nicalon SiC Fibers

3.1. Objective

The goal of this study was to determine the oxidation kinetics of stand-alone SiC fibers in both dry and wet O_2 environments. Stand-alone fiber oxidation provides a baseline for oxidation of exposed fibers in CMCs.

This chapter begins with an oxidation study of Hi-Nicalon SiC fibers in dry O_2, which are found to have similar oxidation kinetics and behavior to bulk SiC. Linear kinetics are dominant at temperatures ≤ 800°C while parabolic kinetics are dominant at temperatures of 900°C and above. Next, oxidation kinetics for SiC fibers in 50 vol% H_2O/ 50 vol% O_2 (wet O_2) are presented. Wet oxidation of the fibers at high temperatures (1200-1300°C) resulted in crystalline oxide formation which cracked *in situ*. At 1300°C, the *in situ* crack formation provided fast paths for oxidant transport to the fiber surface, which changed the dominant diffusion oxidation mechanism to a reaction-controlled mechanism. The *in situ* oxide cracking is attributed to excessive hoop stresses which exceed the strength capabilities of the crystalline phase.

3.2. Results

3.2.1. Dry Oxidation

SiC fiber oxidation kinetics were obtained by TGA oxidation and SEM characterization. Representative TGA mass change plots for dry O_2 fiber oxidation experiments conducted at temperatures from 700 to 1300°C are shown in Figure 20. TGA results are reported as a specific mass change vs. time. The mass change is normalized by an approximate surface area (SA) of the fiber tow given by Equation 19.

$$SA = (2\pi rh + 2\pi r^2)N \quad [19]$$

Where r is the fiber diameter (7 µm), h is the fiber length (10 cm), and N is the number of fibers per tow (500), yielding a surface area of 22 cm^2.

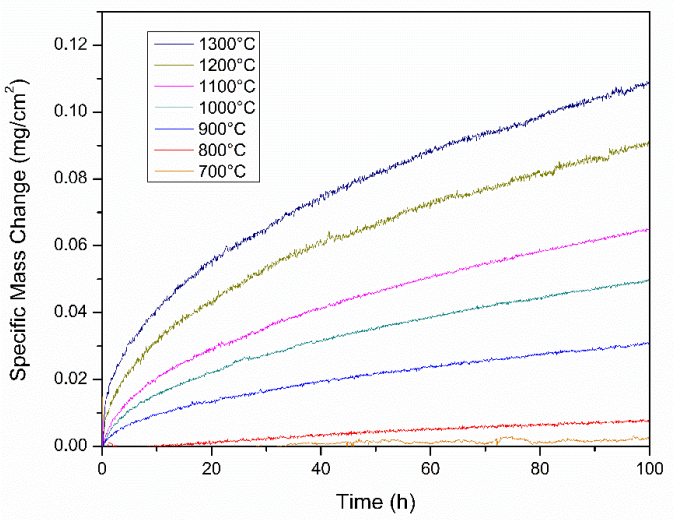

Figure 20. Example TGA specific mass change results for dry O_2 Hi-Nicalon fiber oxidation experiments, showing oxidation kinetic behavior as a function of temperature.

The oxidation mechanisms were determined from the variation of the specific mass change with time. Parabolic oxidation kinetics were observed from 900 to 1300°C. Parabolic kinetics were confirmed when the plots of the specific mass change vs. root time resulted in straight lines. An example plot obtained for a fiber lanyard oxidized at 900°C in dry O_2 for 100h is shown in Figure 21. Parabolic mass gains are indicative of an oxidant permeation-controlled mechanism.

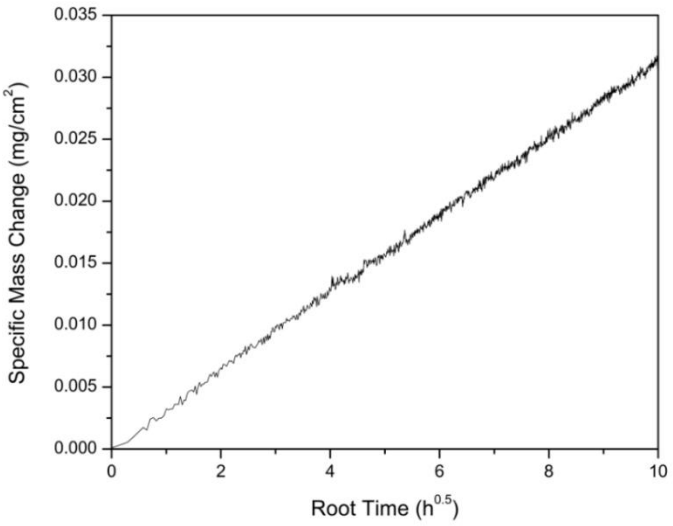

Figure 21. Specific mass change versus root time data from a TGA experiment for SiC fibers oxidized in dry O_2 at 900°C for 100h showing a line—confirming a parabolic mass change.

The oxidation mass changes results from 700 and 800°C are expanded in Figure 22. The 800°C results do not perfectly fit the linear trend, as indicated by the black line. However, the regression on this line is 0.96.

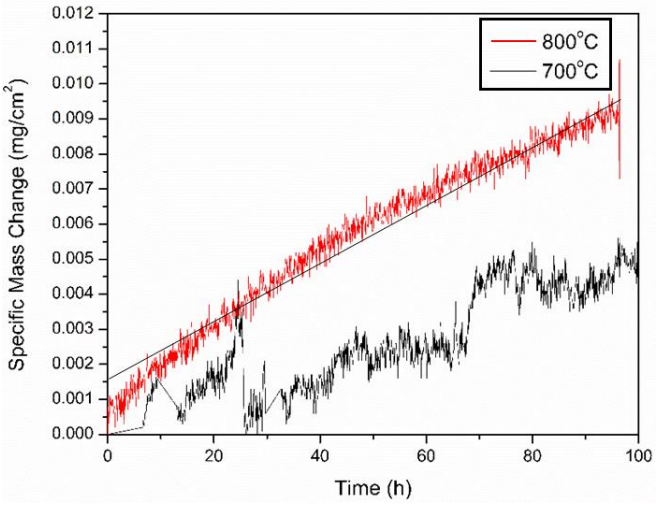

Figure 22. Linear specific mass changes for SiC fiber lanyards oxidized in dry O_2 at 700 and 800°C.

To determine if a linear-parabolic mechanism was a better fit, the TGA data were plotted with the x-axis as t/specific mass change, following the Deal and Grove method (Figure 24).

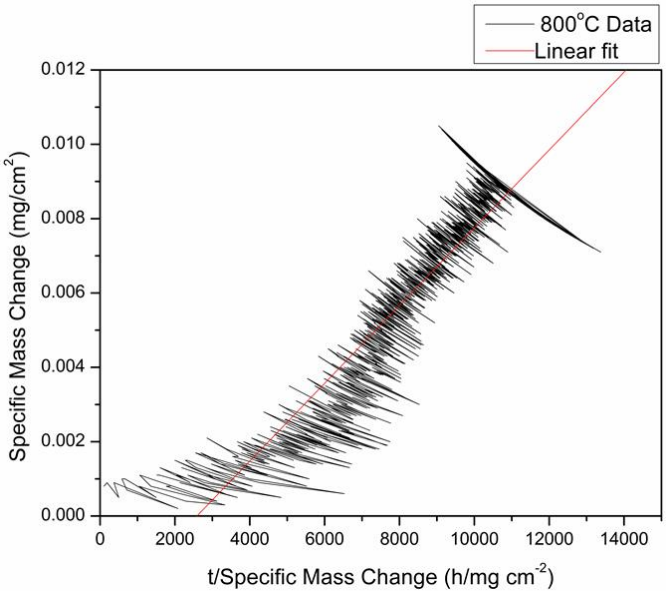

Figure 23. Specific mass change for SiC fiber lanyard oxidized at 800°C in dry O_2 as a function of time/specific mass change to determine linear-parabolic kinetic parameters.

If the linear-parabolic mechanism fit the data, the data would fit a line. The slope of the line will equal k_p while the intercept is equal to $-k_p/k_l$. However, the data are non-linear and the regression on the best-fit line for these data was 0.82. Therefore, the forced-fit to linear oxidation kinetics will be used for subsequent calculations with an added uncertainty because the linear fit is not perfect. Linear oxidation kinetics are indicative of a reaction-rate-controlled mechanism according to Reaction 3.

The 700°C data (Figure 22) contain significant scatter due to the limited sensitivity of the TGA balance and the small mass changes that occurred, but are assumed to follow linear kinetics based on the 800°C results. Mass changes for the fibers exposed at 700°C were also below the detectability limit of a bench-top balance. Quantification of oxidation rates at this temperature are best obtained from oxide thickness measurements as described later.

Although the kinetic laws were determined from the TGA mass change data, the oxidation rate constants determined from the mass change underestimate the oxidation rate due to decreasing fiber surface area occurring during oxidation. The oxides on adjacent fibers can

join together, increasing the oxidant diffusion distance to the available SiC (Figure 24f). Alternatively, the oxide thicknesses on fiber cross sections were measured with SEM after each oxidation experiment (Figure 24) and used to quantify oxidation rates.

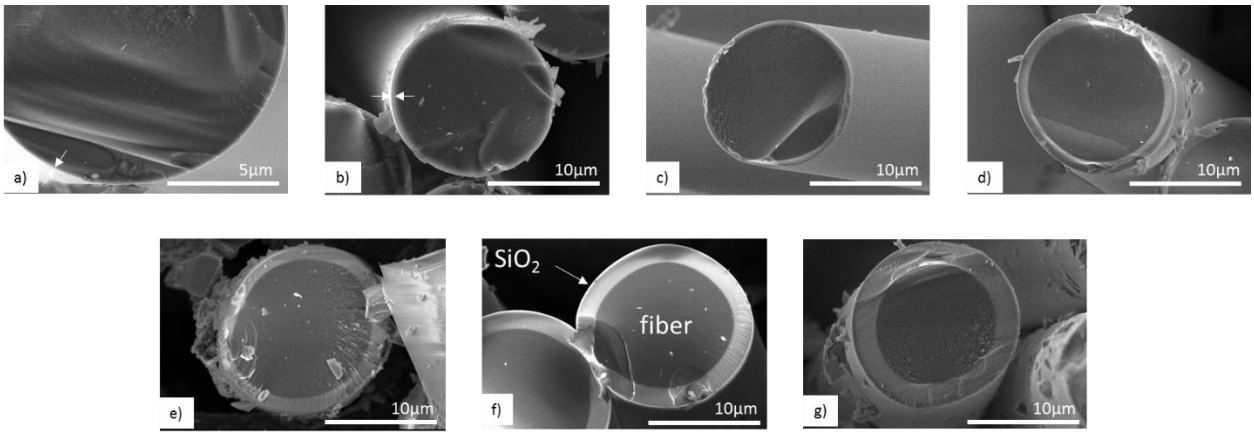

Figure 24. Typical oxide thicknesses observed with SEM after 100h exposure of Hi-Nicalon fibers in dry O_2 at 700-1300°C (a-g). Arrows indicated oxide thickness (a-b).

Oxide thicknesses after 100h at 700°C in dry O_2 were measured with high-magnification SEM, as indicated by the arrows in Figure 25.

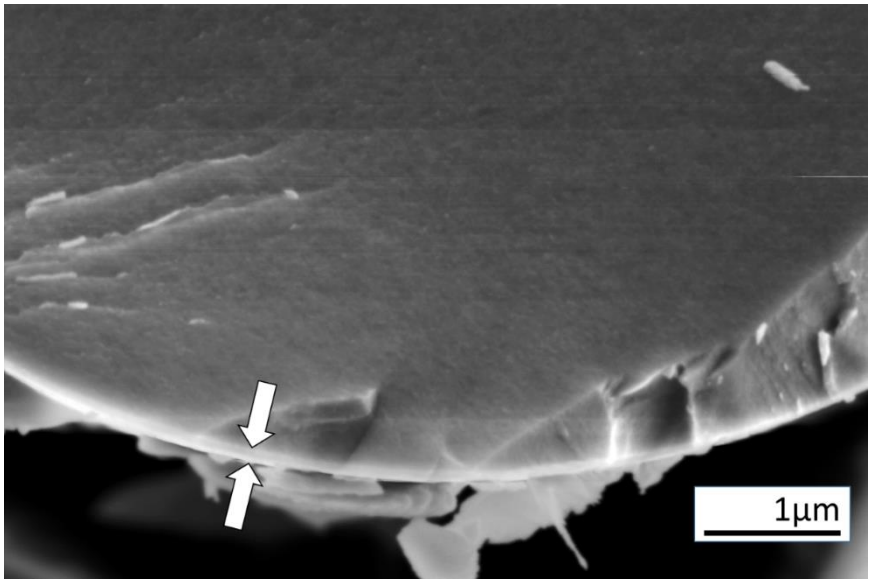

Figure 25. Oxide thickness indicated by arrows on a Hi-Nicalon fiber after oxidation for 100h at 700℃ in dry O_2.

The average measured oxide thicknesses were used to calculate linear oxidation rate constants, k_l, in units of µm/h or parabolic oxidation rate constants, k_p, in units of $\mu m^2/h$. As described above, the dominant kinetics at each temperature was determined from the shape of the TGA mass change curve. The average oxide thicknesses with standard deviation and resulting oxidation rate constants are given in Table 7.

Table 7. Average oxide thickness, standard deviation, and corresponding oxidation rate constants for Hi-Nicalon fibers in dry O_2 from 700-1300°C for 100h

Temperature (°C)	Average Oxide Thickness (µm)	No. of Measurements	k_l from Observed Thickness (µm/h)	k_p from Observed Thickness ($\mu m^2/h$)
700	0.08 ± 0.02	95	$(8.0 \pm 1.7) \times 10^{-4}$	
800	0.24 ± 0.08	81	$(2.4 \pm 0.8) \times 10^{-3}$	
900	0.53 ± 0.07	135		$(2.4 \pm 0.8) \times 10^{-3}$
1000	1.01 ± 0.09	128		$(1.0 \pm 0.2) \times 10^{-2}$
1100	1.24 ± 0.11	141		$(1.5 \pm 0.3) \times 10^{-2}$
1200	1.63 ± 0.07	110		$(2.7 \pm 0.2) \times 10^{-2}$
1300	2.10 ± 0.14	108		$(4.4 \pm 0.6) \times 10^{-2}$

Oxidation rate constants can be reported in terms of mass gain or oxide thickness. A conversion between the different units for parabolic oxidation rate constants (mg^2/cm^4h and $\mu m^2/h$) can be conducted based on SiC and SiO_2 molecular weights and densities, as given in Appendix A (Equation (5) on page 2 of the appendix).

3.2.2. Wet Oxidation

Wet O_2 (50 vol% H_2O/50 vol% O_2) Hi-Nicalon fiber oxidation experiments were conducted for 100h from 700 to 1300°C. Three experiments were conducted at each temperature. Figure 26 shows an example of the specific mass change with time for each temperature. It was observed from TGA mass change data that fibers oxidized at 700-1200°C oxidized following parabolic kinetics.

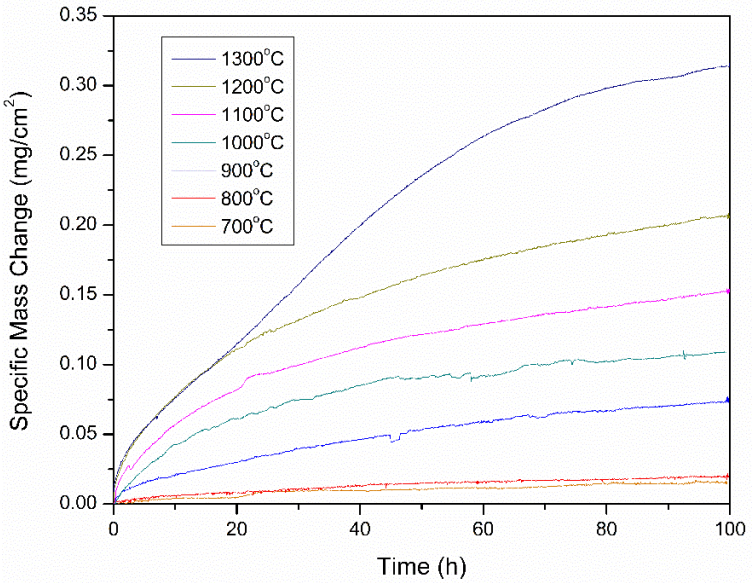

Figure 26. Example TGA specific mass change results for wet O_2 Hi-Nicalon fiber oxidation experiments, showing oxidation kinetic behavior as a function of temperature.

The mass changes at 700 and 800°C are plotted against root time in Figure 27. The resulting lines suggest a parabolic mass gain during oxidation in wet O_2, indicating an oxidant permeation-controlled mechanism dominated.

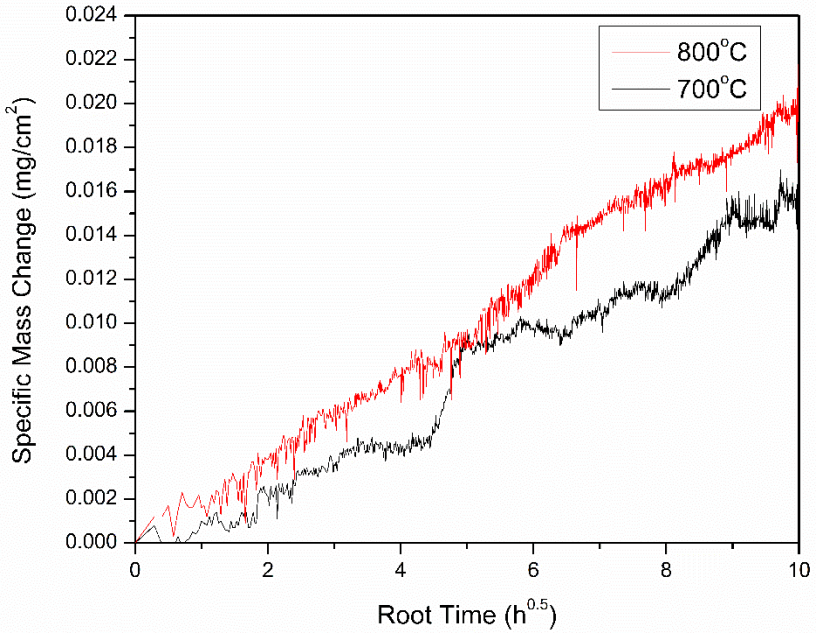

Figure 27. Specific mass change vs. root time for a Hi-Nicalon fiber lanyard oxidized in wet O_2 at 700 and 800°C showing a line—confirming a parabolic mass change.

The 700°C data show significant scatter due to the limited sensitivity of the TGA balance and the small mass gain of the fiber tow at this low temperature. Additionally, mass changes for the fibers exposed at 700°C were also below the detectability limit of a bench-top balance. None the less, the mass gain is best described by parabolic kinetics, indicating that the oxidant permeation is rate-controlling.

The mass change curve observed for oxidation at 1300°C followed parabolic kinetics for the first 16 hours (Regime 1), followed linear kinetics for the next 34 hours (Regime 2), and began to level off for the remaining 50 hours (Regime 3), as seen more explicitly in Figure 28.

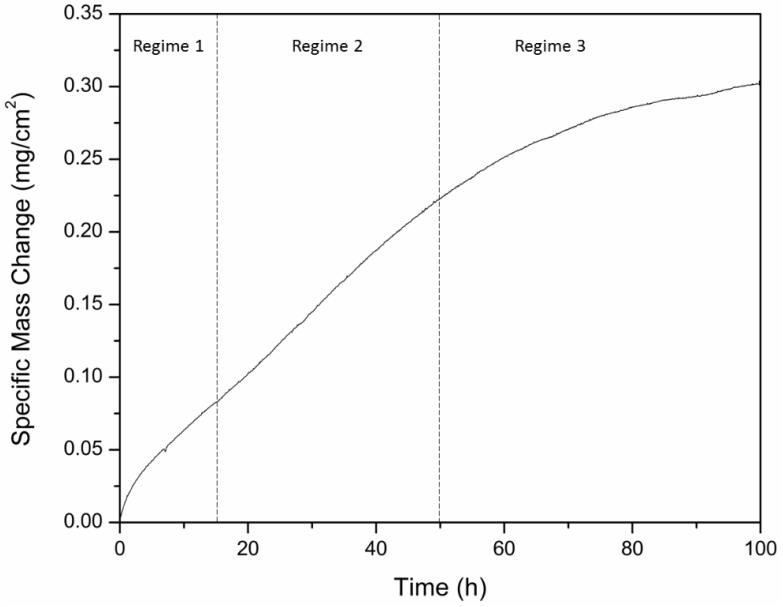

Figure 28. TGA mass change results for Hi-Nicalon fibers oxidized at 1300°C in wet O_2 for 100h showing three different mass change regimes.

The duration of Regime 1 was determined by plotting the specific mass change data against root time and shortening the upper time limit until the best linear regression was achieved. The same process was used for Regime 2 with the data plotted against time. The root time plot is shown in Figure 29. Multiple regimes indicate changes in oxidation mechanisms with time, as will be discussed below.

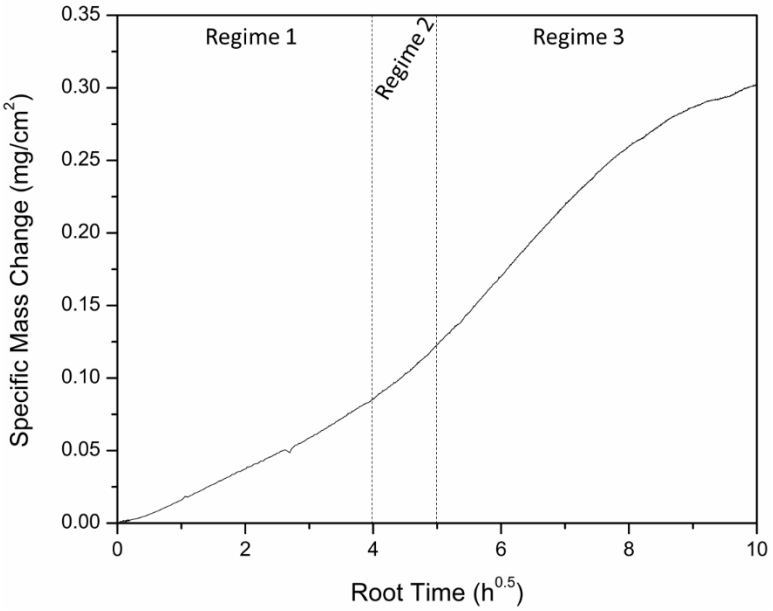

Figure 29. TGA mass change results for Hi-Nicalon fibers oxidized at 1300°C in wet O_2 for 100h plotted against root time to show linearity in Regime 1.

Significant mass loss due to $Si(OH)_4$ volatility (Reaction 10) was not observed in the TGA results at any temperature in wet O_2. This was assumed to be due to the high surface area of the fiber tow (500 fibers per tow), as described below. A fused quartz (SiO_2) coupon was tested in the TGA in the same wet O_2 environment at 1200°C for 100h. This coupon lost mass ($3.7x10^{-3}$ mg/cm^{2}h), which is consistent with the expected $Si(OH)_4$ volatility at this temperature, validating the experimental setup. See Appendix C for a calculation of the expected volatility at these conditions, based on the work of Opila and Hann.[20]

However, in the case of the fiber tow oxidation, the high surface area of SiC fibers and high surface area of thermally grown SiO_2 likely resulted in saturation of the gas stream with $Si(OH)_4$, suppressing any further volatility. Had the volatility reaction not been suppressed over the whole sample, the oxide thicknesses closer to the bottom of the lanyard would be significantly thinner due to volatility than the oxide thicknesses near the top of the lanyard where more $Si(OH)_4$ saturated the gas stream. An oxide thickness can be predicted for 100h oxidation

at 1200°C in 50 vol% H_2O (g) where $Si(OH)_4$ volatility was suppressed[15] and where paralinear kinetics were observed due to $Si(OH)_4$ volatilization.[20] For the case of $Si(OH)_4$ suppression, an oxide thickness of 4.4 μm is predicted for 100h oxidation at 1200°C in 50 vol% H_2O (g) based on the parabolic rate constant of Opila[15]. For the case of $Si(OH)_4$ volatility, an oxide thickness of 3.5 μm is predicted based on the parabolic rate constant of Opila[20]. Oxide thicknesses were measured and compared at the bottom and top of the fiber lanyards and no statistical differences in oxide thicknesses between the two locations were found. The $Si(OH)_4$ volatility contribution to the fiber oxidation kinetics is therefore negligible. The average oxide thickness on the Hi-Nicalon fibers after 100h at 1200°C in wet O_2 from this work was 5.1 ± 0.9 μm, similar to the case of bulk SiC oxidized when $Si(OH)_4$ volatility was suppressed.

Similar to the dry O_2 fiber oxidation results, the oxide thicknesses on fiber cross sections after wet oxidation were observed and measured with SEM (Figure 30) and the averages were used to calculate oxidation rate constants.

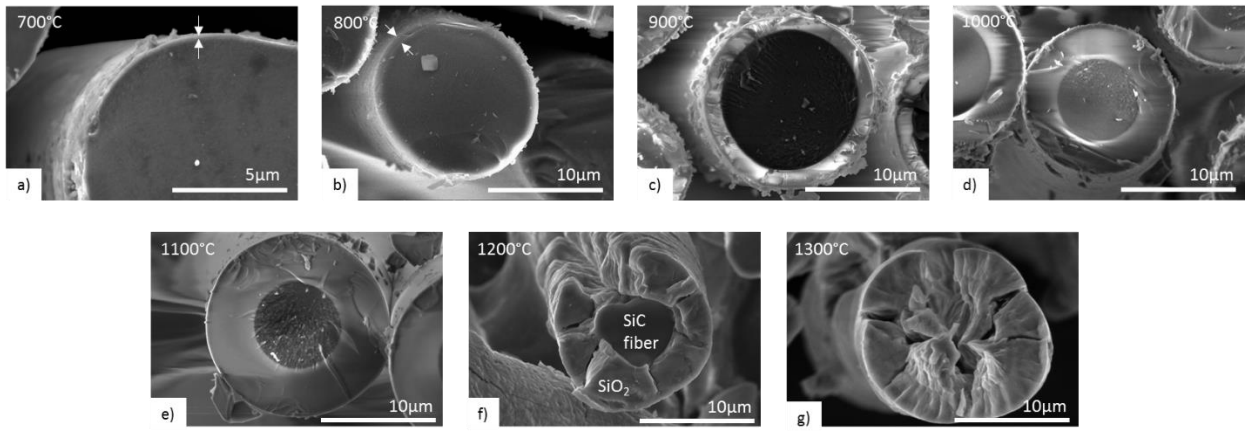

Figure 30. Typical oxide thicknesses observed with SEM after 100h exposure of Hi-Nicalon fibers in wet O_2 from 700-1300°C (a-g). Arrows indicate oxide thickness (a-b).

Fibers oxidized for 100h in wet O_2 at 700-1100°C formed an amorphous SiO_2 layer. The oxide formed at 1200 and 1300°C at 100h, however, was cracked, which is indicative of a crystalline

polymorph of SiO_2. Crystallinity was confirmed by XRD (PDF card 00-004-0379) (Figure 31); cristobalite formed at these oxidation conditions.

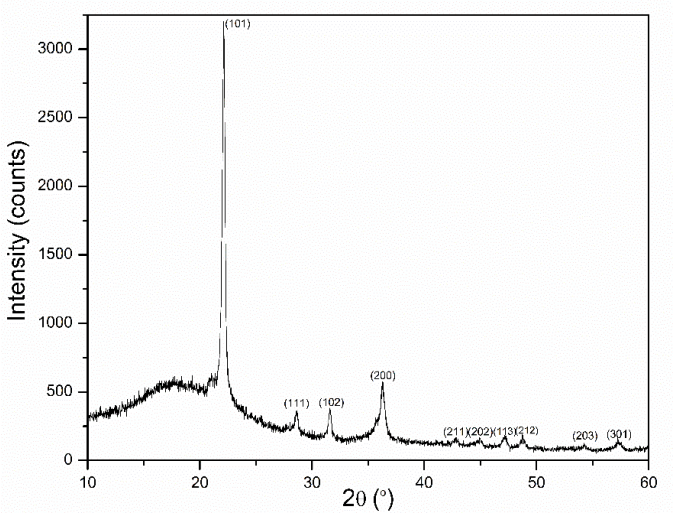

Figure 31. XRD results from a Hi-Nicalon fiber lanyard oxidized at 1300°C in wet O_2 showing labeled cristobalite peaks.

The wide amorphous peak at low 2θ was due to the scotch tape mounting medium used in the diffractometer (Figure 32).

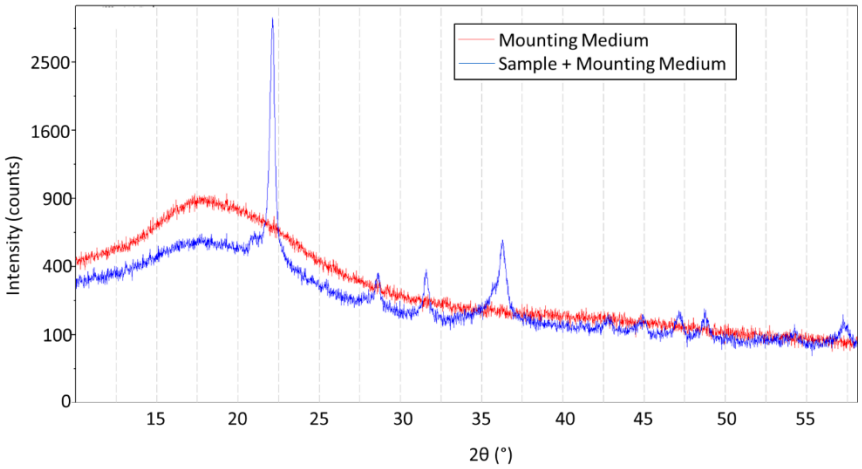

Figure 32. Comparison of XRD results from the oxidized Hi-Nicalon fiber lanyard and the scotch tape mounting medium.

After one experiment conducted at 1100°C for 100h in wet O_2, a thin crystalline layer was observed on the outer edge of the thermally grown oxides (Figure 33).

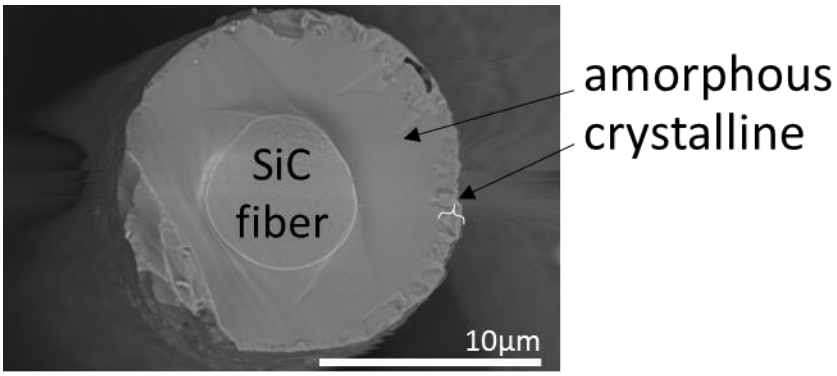

Figure 33. Hi-Nicalon fiber oxidized at 1100°C for 100h in wet O_2 with a crystalline outer layer and an amorphous inner layer in the thermally grown oxide.

A crystalline exterior is consistent with the crystallization behavior of SiO_2 on SiC observed by Presser, et al.[69; 70] and Opila.[15] Both authors observed disk-like crystal plates of cristobalite on the surface of an otherwise-amorphous SiO_2, indicating that crystallization initiates at the SiO_2/atmosphere interface and proceeds inward towards the SiO_2/SiC interface.[70] Presser, et al. reported crystallization rates of 1.5 µm/h at 1400°C in O_2, but noted that this rapid rate was influenced by impurities in the system.[70] A definitive crystallization rate of SiO_2 at 1200 and 1300°C in 50 vol% H_2O in an environment with minimal impurities (due to the 99.995% purity of the fused quartz tube used in this work) could not be determined in this work due to the majority of the oxides being either fully amorphous or crystalline at the conclusion of the 100h oxidation experiments. However, crystallinity was investigated for more exposure times at 1200 and 1300°C and a crystallization rate was estimated from the 6h, 1300°C, wet O_2 exposure (below).

Experiments of shorter duration were conducted at 1200 and 1300°C to probe the oxidation conditions necessary for the formation of both amorphous and/or crystalline oxides. The differences in appearance of the oxides in SEM (smooth for amorphous, cracked for crystalline) were used to determine oxide crystallinity. Table 8 gives the crystallinity results of

the shorter experiment durations at 1200 and 1300°C. Two or three experiments were conducted at each condition. Designation of 0.5 signifies that approximately half of the fibers (42 of 81) observed in one lanyard had a completely crystalline oxide, while half (39 of 81) had a completely amorphous oxide for the same experiment. These exposure times were likely near the onset of crystallization—where the oxides had just begun to crystalize, not achieving crystallinity in oxides for all fibers yet. Additionally, over 64% of the fibers (241 of 376) imaged after 100h oxidation at 1300°C had been completely consumed (Figure 30g).

Table 8. Comparison of 1200 and 1300°C wet O_2 fiber oxidation tests at various times, showing the formation of amorphous or crystalline oxide growth

Temperature (°C)	Test Duration (h)	No. Tests with Amorphous Oxide	No. Tests with Crystalline Oxide
1200	6	3	0
	24	2.5	0.5
	48	2	1
	100	0	3
1300	6	2	0
	24	0	3
	100	0	3

There was a statistical difference in oxide thickness for the amorphous and crystalline oxides on fibers oxidized for 24 and 48h in wet O_2 at 1200°C (Table 9). This is attributed to the assumed slower oxidant permeation through β-cristobalite than through amorphous SiO_2.[69] This assumption is based on the reduced oxide thickness observed below cristobalite spherulites, compared to adjacent areas of amorphous SiO_2.[69] The permeation of O_2 or H_2O (g) through β-cristobalite has not been measured due the necessity and difficulty of conducting high-temperature measurements. Because β-cristobalite transforms to α-cristobalite at 270°C, room-temperature permeability measurements are not possible. In addition, the β to α phase transition is accompanied by a 5% volume change which results in cracked oxides at room temperature.

Table 9. Comparison of average amorphous and crystalline oxide thicknesses, standard deviation, on Hi-Nicalon fibers oxidized in wet O_2 at 1200 and 1300°C

Temperature (°C)	Test Duration (h)	No. of Measurements	Amorphous Oxide Thickness (μm)	Crystalline Oxide Thickness (μm)
1200	6	142 (amorphous)	1.30 ± 0.07	n/a
	24	167 (amorphous) 39 (crystalline)	2.6 ± 0.2	1.9 ± 0.2
	48	96 (amorphous) 62 (crystalline)	3.5 ± 0.2	2.6 ± 0.3
	100	184 (crystalline)	n/a	5.1 ± 0.9
1300	6	90 (amorphous)	1.5 ± 0.2	n/a
	24	128 (crystalline)	n/a	2.6 ± 0.4
	100	105 (crystalline)	n/a	8.6 ± 1.3

An example of the differences in amorphous and crystalline oxide thicknesses for 24h at 1200°C in wet O_2 is shown in Figure 34.

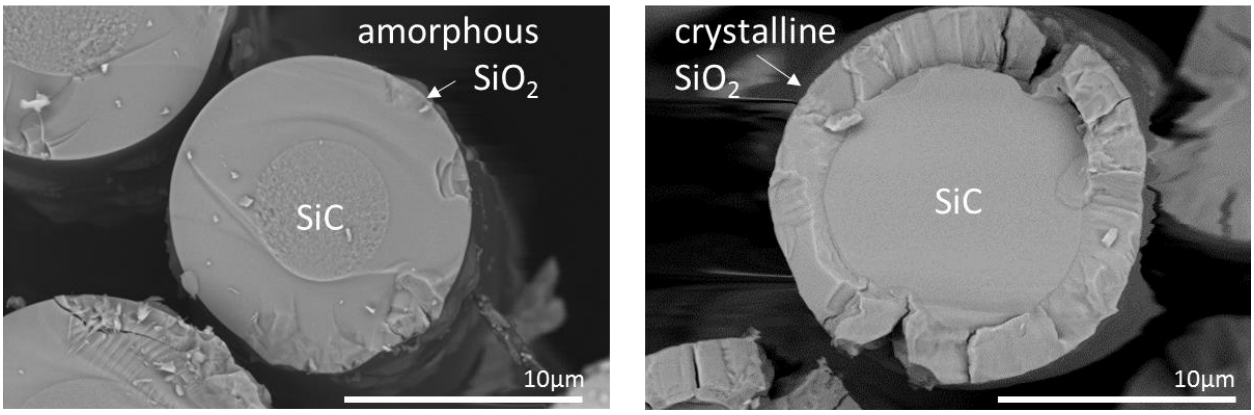

Figure 34. Two fibers oxidized at 1200°C in wet O_2 for 48h, showing oxide thickness differences between amorphous (left) and crystalline (right) SiO_2.

It was observed that the large cracks in the crystalline oxide corresponded to the areas of greatest fiber recession (Figure 35). This was true at both 1200 and 1300°C in wet O_2.

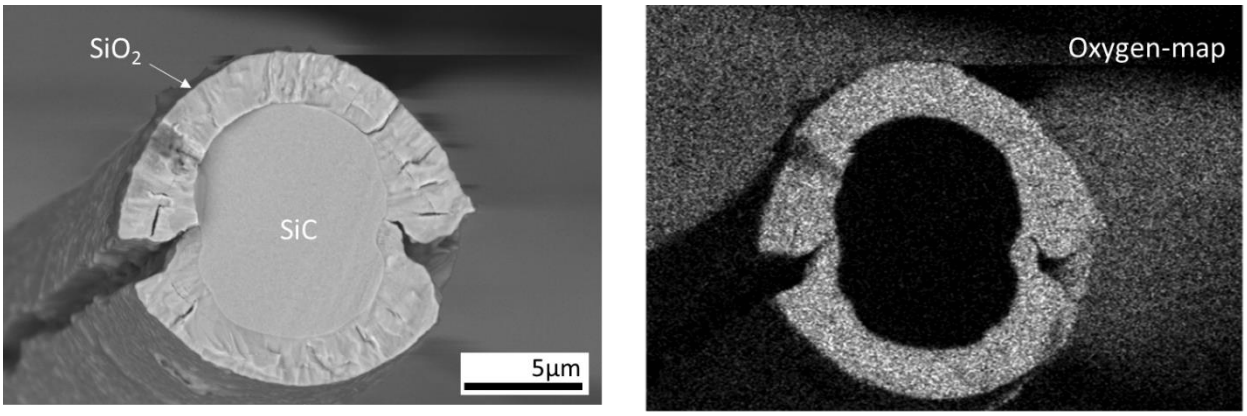

Figure 35. SEM image (left) and oxygen EDS map (right) of a Hi-Nicalon fiber oxidized in wet O_2 at 1300°C for 24h showing cracks in the oxide corresponding to areas of increased fiber oxidation.

Two 6h exposures in wet O_2 at 1300°C showed primarily amorphous oxides, with one of the tests showing some oxides with a crystalline edge (Figure 36) indicating that crystallization had just begun. The average thickness of the crystalline edge was 0.6 ± 0.1 µm, which can be used to estimate a minimum crystallization rate of 0.1 µm/h. The crystallization rate is likely more rapid that this, because the onset of crystallization occurred after the oxide was already growing. Only 2 of the 16 fibers imaged showed cracks (one example in Figure 36, right). This result showed that cracking had also just begun at this condition.

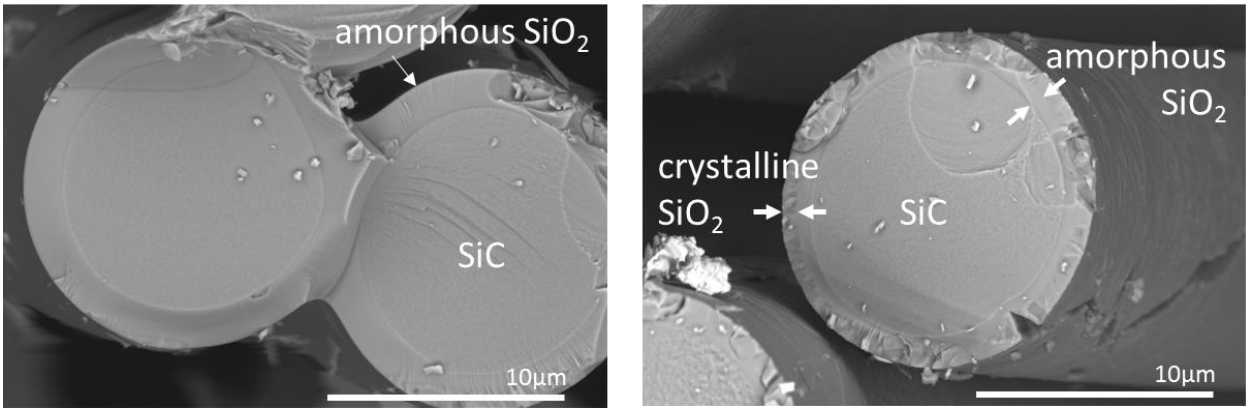

Figure 36. SEM image of Hi-Nicalon fibers with an amorphous oxide after exposure to wet O_2 at 1300°C for 6h.

The average oxide thicknesses measured on fibers after 100h oxidation exposures were used to determine the parabolic oxidation rate constants (Table 10), similar to the dry O_2 results. The parabolic rate constant reported for 1300°C was calculated from oxide thicknesses measured from the 6h tests. Results for 1300°C wet O_2 exposures will be discussed further in the following section.

*Table 10. Average oxide thickness, standard deviation, and corresponding oxidation rate constants for Hi-Nicalon fibers in wet O_2 from 700-1300°C, based on 100h exposures for 700-1200°C, *6h exposure used for k_p at 1300°C*

Temperature (°C)	Average Oxide Thickness (μm)	No. of Measurements	k_p from Observed Thickness ($\mu m^2/h$)
700	0.17 ± 0.03	108	$(2.8 \pm 0.9) \times 10^{-4}$
800	0.5 ± 0.3	217	$(2.5 \pm 2.6) \times 10^{-3}$
900	1.9 ± 0.2	164	$(3.7 \pm 0.6) \times 10^{-2}$
1000	3.1 ± 0.2	179	$(9.9 \pm 1.3) \times 10^{-2}$
1100	4.2 ± 0.3	127	$(1.8 \pm 0.3) \times 10^{-1}$
1200	5.1 ± 0.9	184	$(2.6 \pm 0.9) \times 10^{-1}$
1300	8.6 ± 1.3	105	$*(3.9 \pm 0.9) \times 10^{-1}$

3.3. Discussion

3.3.1. Dry Oxidation

The parabolic oxidation rate constants were compared to those for other SiC fibers and bulk CVD SiC in the literature, as reported by Wilson and Opila (Figure 37).

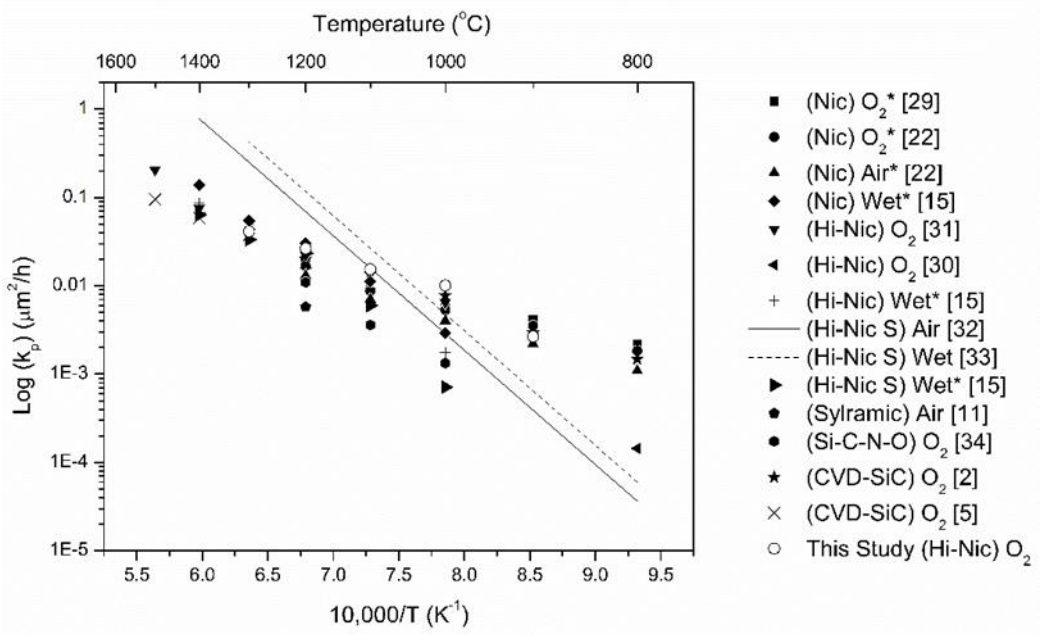

Figure 37. Parabolic rate constants for SiC fiber oxidation plotted as log(k_p) versus inverse temperature (indicates data extracted from a plot) [Plot from Wilson & Opila].*[28]

Although the plot in Figure 37 shows a variation in reported parabolic rate constants for different SiC fibers, the results from this study were not statistically different from other Hi-Nicalon fiber or bulk CVD SiC oxidation studies. As described in *Section 1.3. Bulk Si and SiC Oxidation*, parabolic kinetics result from a diffusion-controlled mechanism because the diffusion distance increases with time. Because thick, protective SiO_2 scales were observed with SEM on the fibers oxidized in dry O_2 at temperatures of 900-1300°C and parabolic kinetics were observed with TGA, a diffusion-controlled mechanism was confirmed for the Hi-Nicalon fibers at these temperatures. This is consistent with the work of Ramberg, et al., who reported parabolic oxidation kinetics for CVD SiC at temperatures of 900-1100°C.[71]

The linear oxidation rate constants for dry O_2 oxidation were also compared to the literature (Figure 38). No previous linear oxidation kinetic data were found for Hi-Nicalon fibers oxidized in dry O_2. Several studies reported both linear and parabolic rate constants for Hi-Nicalon (S) following the full Deal & Grove oxidation model.[29; 30] It was observed, however,

that the linear oxidation rates for Hi-Nicalon in this study were slightly higher, but not statistically different from those obtained for bulk CVD SiC and SiC whiskers at 800°C. Hi-Nicalon fibers showed similar oxidation kinetics to CVD SiC for both linear and parabolic kinetics. Linear kinetics (observed from TGA) along with the thin SiO_2 scale observed on the fibers with SEM confirmed the reaction-controlled mechanism (Reaction 3) for the temperatures of 700-800°C. This is, again, consistent with the Ramberg, et al., who observed only linear oxidation kinetics for CVD SiC below 900°C.[71]

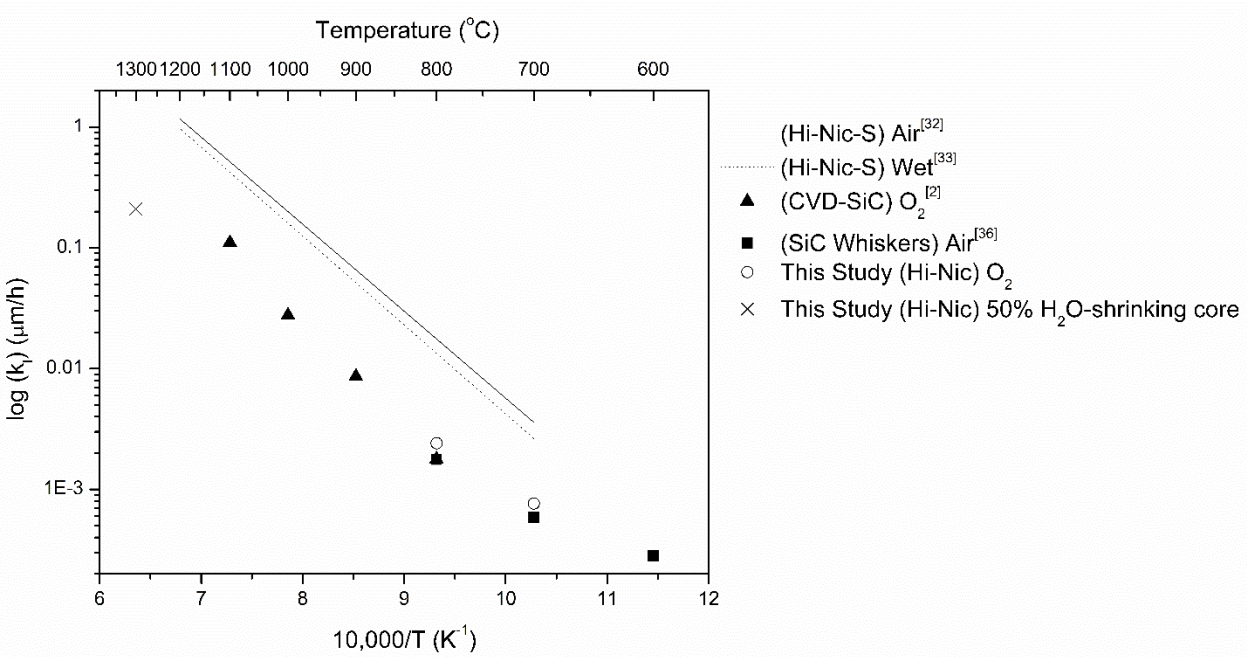

Figure 38. Linear rate constants for SiC fiber oxidation plotted as log(k_l) versus inverse temperature. Plot from Wilson & Opila[28] with wet O_2 data from this study (x).

The data from this study were plotted as log(k) versus inverse temperature and were fitted with a line to determine the pre-exponential constant and the activation energy for both parabolic and linear oxidation kinetics (Table 12) according to the Arrhenius equation:

$$k = k_o \exp\left(-\frac{E_a}{RT}\right) \qquad [20]$$

where k_o is the pre-exponential coefficient, E_a is the activation energy, R is the universal gas constant, and T is absolute temperature. The parabolic oxidation activation energy in dry O_2, 110 ± 15 kJ/mol (Figure 39), was in agreement with the range given in the literature: 107-144 kJ/mol.[58; 72; 73]

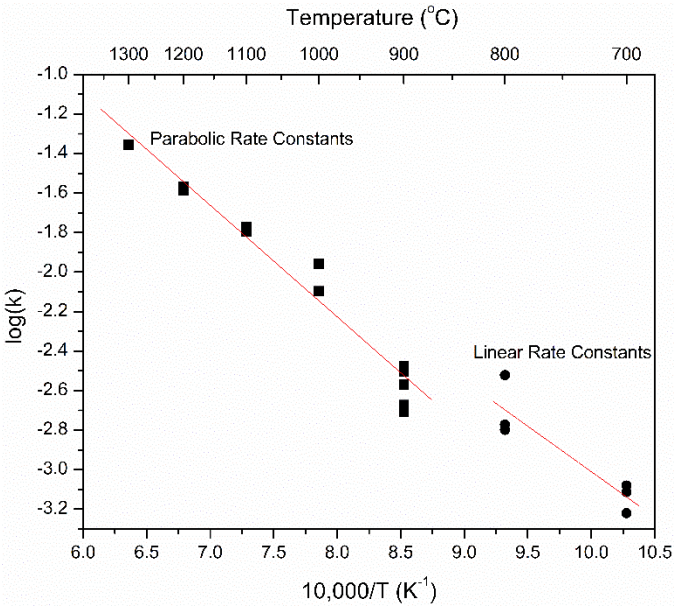

Figure 39. Linear and parabolic oxidation rate constants for Hi-Nicalon SiC fiber oxidation in dry O_2.

This activation energy is similar to that for the O_2 permeation rate through SiO_2 as determined by Norton (134 kJ/mol),[37] indicating that molecular O_2 permeation is the dominant mechanism for fiber oxidation from 900-1300°C in dry O_2 (Table 11).

Table 11. Bond strength and energy comparisons for reaction-controlled linear oxidation kinetics of Si-C and Si-Si phases

Material	Bond	Bond Strength (kJ/mol)	T_m (°C)	E_a for Linear Oxidation (kJ/mol)
CVD SiC	Si-C	368 [74]	2730	170 [71]
Single Crystal Si	Si-Si	184 [17]	1400	192 [8]
Hi-Nicalon SiC Fibers-This Work	Si-O-C	-	-	90 ± 50

The bond strength for Si-C was determined by UV irradiation of an organosilane molecule,[74] but is significantly higher than the Si-Si bond strength. This is consistent with the higher melting

temperature of SiC than Si. The activation energy for the reaction-rate-controlled oxidation mechanism corresponds to breaking of bonds. So it would be expected that the bonds with the higher energy would require a higher activation energy for oxidation. Contrary to this, however, are the activation energies for reaction-rate-controlled oxidation mechanisms of the two phases. Deal and Grove reported an activation energy of 192 kJ/mol for single crystal Si reacting with O_2[8] and Ramberg reported a slightly lower, but similar 170 kJ/mol for CVD SiC reacting with O_2[71]. The similarity of these two activation energies imply similar mechanisms for the linear oxidation behavior.

The activation energy determined for Hi-Nicalon SiC fibers in this work was 90 ± 50 kJ/mol, lower than either Si or SiC. If this activation energy corresponds to breaking of bonds during reaction of the fiber with O_2, then it is likely that the bonds are different than Si-Si or Si-C. This is possible for the Hi-Nicalon fibers that contain excess C and primarily consist of an amorphous Si-O-C phase. Therefore, the lower activation energy compared to bulk SiC or Si is due to breaking of the Si-O-C bonds in the fiber.

Table 12. Arrhenius rate equation data for Hi-Nicalon SiC fibers in dry and wet O_2

Oxidation condition	Activation energy (kJ/mol)	Pre-exponential coefficient (μm/h for linear, μm²/h for parabolic)
Dry O_2, parabolic oxidation kinetics (900-1300°C)	110 ± 15	200 ± 30
Dry O_2, linear oxidation kinetics (700-800°C)	90 ± 50	40 ± 500
Wet O_2, parabolic oxidation kinetics (900-1300°C)	88 ± 10	365 ± 14

3.3.2. Wet Oxidation

In the wet O_2 fiber oxidation studies parabolic oxidation kinetics were observed for 700-1200°C from TGA (Figure 26). Additionally, it was noted that the parabolic oxidation rate constants for 900-1300°C in wet O_2 (Table 10) were approximately an order of magnitude

greater than those for the same temperature in dry O_2 (Table 7), consistent with results observed for CVD SiC[15] and Si[8], due to the greater solubility of H_2O (g) in SiO_2, compared to O_2 (g).

The parabolic oxidation rate constants were plotted vs. inverse temperature to determine the Arrhenius rate equation parameters (Equation 20) for fibers oxidized in wet O_2 (Figure 40). Two different lines were fit to the data. The first (solid line, Figure 40) was fit to the parabolic oxidation rate constants determined from average oxide thicknesses for temperatures that showed parabolic kinetics for 100h exposures (700-1200°C). The slope and intercept were used to calculate an activation energy (167 ± 25 kJ/mol) and pre-exponential coefficient (410,000 ± 110 $\mu m^2/h$), respectively. The large value and error (95% confidence) for the pre-exponential coefficient were due to the apparent change in slope between 700 and 900°C (Figure 40).

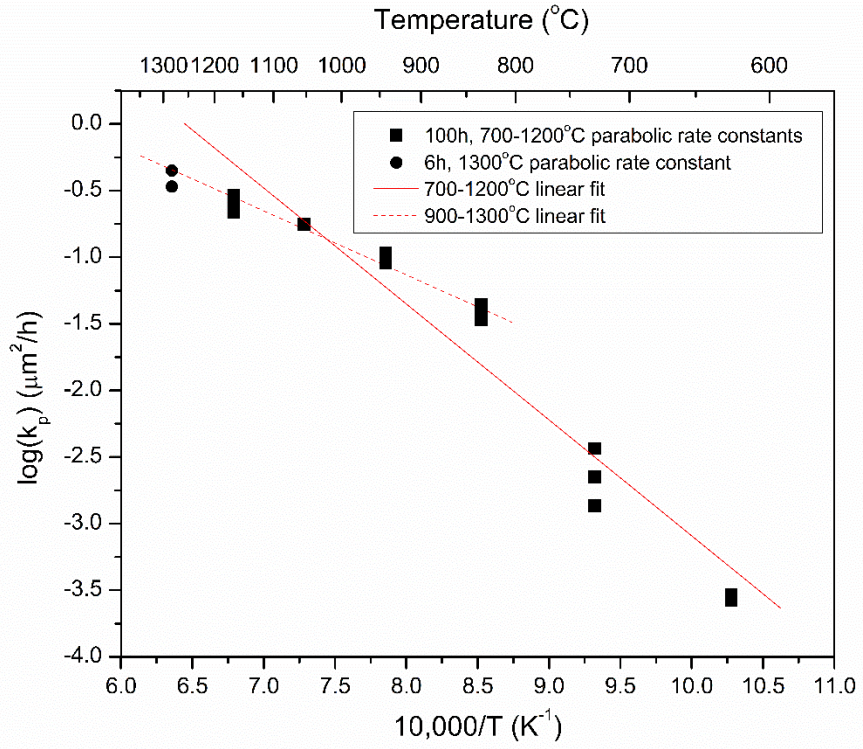

Figure 40. Parabolic oxidation rate constants for Hi-Nicalon SiC fiber oxidation in wet O_2.

If it is assumed that this change in slope correlates with a change in mechanism, the 700 and 800°C data should not be included in the linear fit. Although the TGA data from the 700 and

800°C wet O_2 exposures show parabolic mass gain with time, it is possible that a different mechanism other than diffusion-controlled growth dominated at this temperature. A possible mechanism could be a linear-parabolic fit, as described by Deal and Grove.[8] Additional oxide thickness data is required at 700 and 800°C in wet O_2 as a function of time, to determine if a linear-parabolic fit is appropriate.

Additionally, the parabolic oxidation rate constant determined from average oxide thicknesses for 1300°C, 6h exposure was included in Figure 40 because the TGA results showed parabolic oxidation kinetics for these conditions. When a second line (dashed line, Figure 40) was fit through the 900-1300°C data, an activation energy of 88 ± 10 kJ/mol and a pre-exponential coefficient of 365 ± 14 $\mu m^2/h$ were calculated and resulted in a smaller error and a more reasonable value for k_o (Table 12). Therefore, these parameters are recommended for use in the Arrhenius expression. The activation energy for parabolic oxidation of SiC in wet O_2 from this study falls in the range reported for Si (68 kJ/mol[8]) and SiC (28-156 kJ/mol[13; 15; 20]) in wet O_2 conditions. This indicates that molecular H_2O (g) permeation is the dominant mechanism at these conditions, as described for Si by Deal and Grove.[8] No other Hi-Nicalon wet O_2 studies have been conducted.

3.3.2.1. Hi-Nicalon Fiber Oxidation Kinetics at 1300°C in Wet O_2

Total fiber consumption after 100h at 1300°C was observed in SEM with > 64% of fibers being completely oxidized (example in Figure 30g). The oxidation mechanisms for the Hi-Nicalon fibers oxidized at 1300°C in wet O_2 were affected by the presence of cracks in the oxide, rapid oxidation, formation of a crystalline oxide, and a shrinking SiC core (leading to a reduction in SiC surface area). These factors resulted in changes in the mass gain rate with time (Figure 28).

Figure 28 shows that Regime 1 corresponded to parabolic oxidation kinetics, the kinetics expected for SiC in wet O_2 at 1300°C.[15] The average oxide thickness (amorphous and crystalline) from the 6h exposures (1.53 ± 0.17 μm) was used to calculate the parabolic oxidation rate constant reported for 1300°C in Table 10. This rate constant (3.88 x 10^{-1} $\mu m^2/h$) is similar to the parabolic oxidation rate constant of (3.2 ± 0.7) x 10^{-1} $\mu m^2/h$ reported in the literature for oxidation of CVD SiC under the same conditions.[15]

Figure 28 shows that Regime 2 corresponded to linear mass gain. This change in behavior can be explained by a transition of the oxide from amorphous to cristobalite, and the resulting cracking of the cristobalite. An oxygen EDS map (Figure 35, right) shows that the locations of the cracks corresponded to areas of increased fiber oxidation, indicating that the cracks were present during exposure and did not form during the beta-to-alpha transition of the cristobalite phase on cooling. The increased fiber oxidation in the vicinity of the cracks led to the increased oxidation rates of the fibers at 1200 and 1300°C in wet O_2. Greater oxide thicknesses near cracks in crystalline oxide scales were also observed on Hi-Nicalon-S fibers by Hay, et al.[75] Another study by Hay, et al. reported a deviation from parabolic oxidation kinetics for Hi-Nicalon-S fiber oxidized in $Si(OH)_4$-saturated steam at 1300°C,[76] which was attributed to the cylindrical geometry of the fibers.

The rapid oxidation rate at 1300°C resulted in cracking at times greater than 6 hours and therefore ready access of the oxidant to the SiC fiber surface, where a reaction-rate-controlled mechanism would dominate (according to Reaction 4). The mechanism for cracking will be discussed in the following sub-section. The duration of the linear oxidation kinetics of Regime 2 was approximately 34h (Figure 28). The linear oxidation rate of Regime 2 was determined from the TGA data (Figure 28) to be 0.022 $mg/cm^2/h$ or 0.21 μm/h SiO_2 growth. This is greater than

two orders of magnitude faster than the linear growth rate at 700°C in wet O_2 (Figure 38), as expected for an increase in temperature. This oxidation rate is also of the same order of magnitude as other linear oxidation rates reported for SiC (Figure 38).

After 50 hours (Regime 1 + Regime 2), the mass gain of the fibers began to level-off during oxidation at 1300°C in wet O_2 (Regime 3). The fibers at this stage had a reduced radius and the reaction of the oxidant with the fiber can be considered as a shrinking core substrate with a cylindrical shape.[77; 78] The mass gain rate would continue to decrease with time until all of the SiC reacted to form SiO_2. This decreasing rate could be approximated through an iterative calculation, similar to the method used by Opila,[79] described as follows.

The mass gain due to SiO_2 growth is assumed to be dependent on the available SiC surface area, which would decrease with time. The mass change for a given time increment was determined based on the linear rate from TGA. The rapid SiO_2 growth rate is equivalent to 0.14 µm/h of SiC loss, as calculated using SiC and cristobalite densities and molecular weights. This mass change, however, caused a change in fiber diameter (R_1 to R_2, Figure 41), and therefore reduced the available SiC surface area.

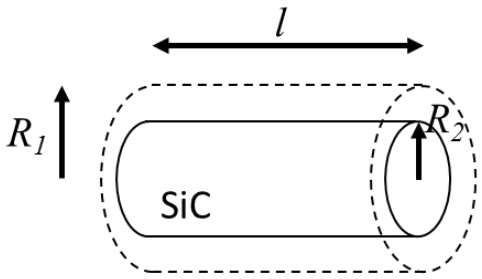

Figure 41. Schematic drawing of a SiC fiber shrinking radially with time due to its reaction with oxidizing gases to for SiO_2.

Subsequently, a new surface area was calculated based on R_2. This calculation was repeated iteratively using a time increment of 0.1h until the SiC fiber had been completely consumed.

Table 13 shows the time steps for the first hour, the subsequent SiO_2 growth, and the reduced radius (R_2) after each time step.

Table 13. The First Hour of Time Steps in the Shrinking Cylinder Calculation for Hi-Nicalon SiC Fibers Oxidized in Wet O_2 at 1300°C.

t (h)	Mass of New SiO_2 (mg)	Total SiO_2 Mass (mg)	R_2 SiC (μm)
0	0	0	7
0.1	0.047	0.076	6.5
0.2	0.090	0.17	6.0
0.3	0.12	0.29	5.2
0.4	0.14	0.43	4.3
0.5	0.15	0.58	3.4
0.6	0.14	0.72	2.5
0.7	0.12	0.84	1.7
0.8	0.097	0.94	1.1
0.9	0.071	1.0	0.70
1	0.048	1.1	0.40

The results from this calculation can be seen graphically in Figure 42. These calculations predicted rapid consumption of the fiber (~2h), compared to the 50h observed for the decreasing mass gain rate with time observed for the 1300°C test (Figure 28). This discrepancy could be due to an overestimation of the linear oxidation rate from the TGA data since the surface area of the fibers during Regime 2 is unknown.

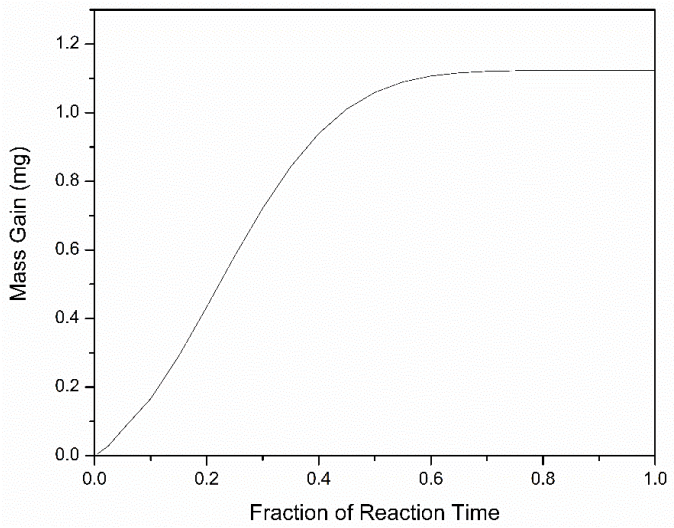

Figure 42. A plateau in mass gain due to decreasing SiO_2 growth with decreasing SiC surface area according to a shrinking cylinder geometry.

Based on the shrinking core model and the small mass gain in Regime 3 (shown in Figure 28), the fibers oxidized for 100h at 1300°C in wet O_2 have not all been completely consumed. This was consistent with the fiber cross-sections, showing 36% of the cross-sections (135 of 376 fibers) had unreacted SiC fiber cores (example of remaining SiC core in Figure 43).

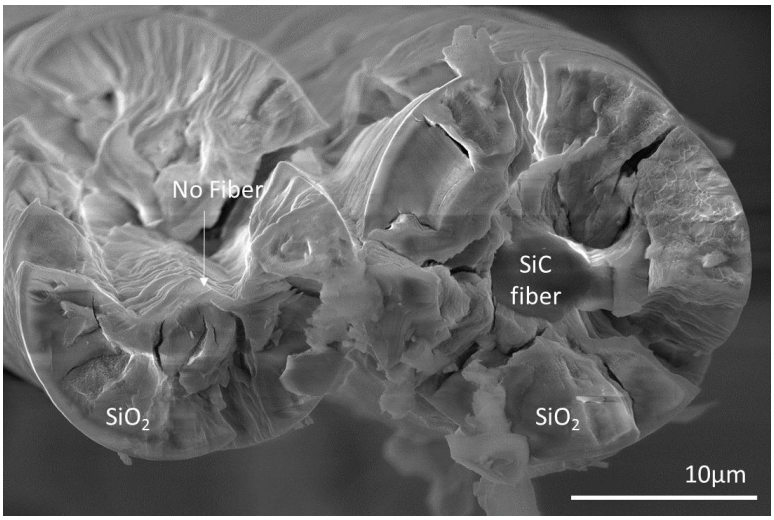

Figure 43. Small remaining Hi-Nicalon SiC fiber core (right) and completely oxidized fiber (left) after oxidation at 1300°C in wet O_2 for 100h.

3.3.2.2. Crack Formation in Crystalline Oxides

Crystallization and cracking of the oxide during 1300°C, wet O_2 exposures caused changes in the oxidation mechanism with time. It was proposed that the cracks in the oxide formed *in situ* at 1200 and 1300°C, resulting in increased fiber oxidation in the vicinity of the cracks. These cracks formed due to stresses in the oxide due to the curvature of the substrate, as explained by a model by Hsueh and Evans.[80] Other authors have also observed cracked oxides due to growth stresses from the cylindrical or curved substrates.[75; 76; 81; 82] However, no stress calculations have been conducted for crystalline SiO_2 on a cylindrical SiC fiber.

In the model by Hsueh and Evans for interfacial oxidation of a curved substrate, a tensile hoop stress (σ_θ) is induced in the old oxide when new oxide grows beneath it. There is a ~2x volume increase associated with growing SiO_2 from SiC. Figure 44 shows a schematic for the stress state of the oxide during growth by Hsueh and Evans.[80]

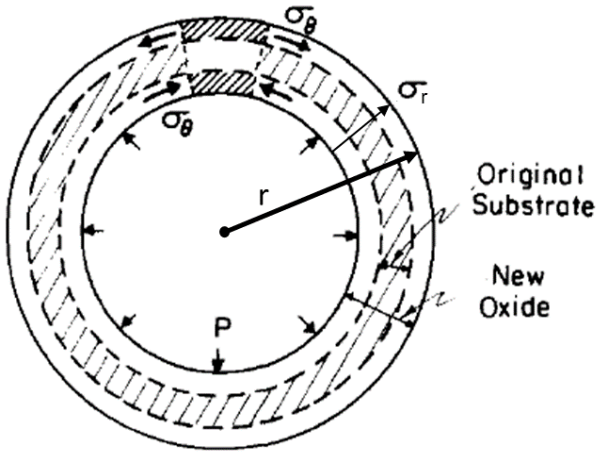

Figure 44. Radial oxidation strain during interfacial oxidation of a cylindrical substrate, as described by Hsueh and Evans.[80]

From it can be seen that a state of compression exists at the fiber/oxide interface, but that a state of tension exists at the exterior of the oxide (oxide/atmosphere interface). The radial (σ_r) and

hoop stresses were modeled for both the fiber and oxide using equations, from Hsueh and Evans[80] and are included in Appendix D.

Hoop stresses in the oxide were calculated for two bounding cases: using the largest possible and smallest observed crack lengths based on the 1300°C wet O_2 results in Appendix D. High tensile hoop stresses at the oxide/atmosphere interface would rest in cracking of the crystalline oxide. The stresses calculated in Appendix D are unrealistically high, even for the smallest crack length used. Possibilities for this result include: *i)* an alternative mechanism causes crack propagation at much lower stresses; *ii)* brittle fracture occurs for crystalline oxide thicknesses significantly smaller than those measured in this work; or *iii)* the values assumed in the model are inaccurate.

A possible additional mechanism for crack extension could be stress-corrosion due to water vapor, as first described by Wiederhorn[83] and reviewed by Gy[84] and Ciccotti.[85] This mechanism is observed for silicate glasses under load and in the presence of H_2O (g or l). Under a stressed condition, dissociative hydrolysis of SiO_2 is enhanced at the crack tip, allowing for rapid crack propagation. This mechanism is shown schematically in Figure 45.

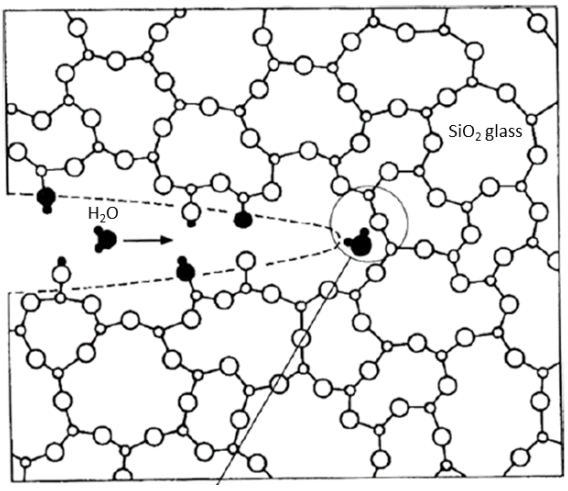

Figure 45. Stress-corrosion/static fatigue mechanism in SiO_2 glass from Ciccotti.[85]

It is also possible, however, that sub-micron-sized flaws on the oxide surface initiate brittle fracture when the oxide scale is thin, following the work of Griffith.[86] Once the brittle fracture was initiated, the crack would continue to grow as the oxide grew. Hay, et al., observed cracked, crystalline oxides on SiC fibers oxidized in dry air,[87] not in H_2O (g). This suggests that cracking is due to brittle fracture when a high hoop stress is reached in the oxide, rather than propagated by stress-corrosion due to H_2O (g).

It should be noted that cracking via either mechanism was not observed in the amorphous SiO_2 layers observed after 100h at temperatures of 1100°C and below even for thicker oxides in some cases. This indicates that the stresses in the amorphous oxide exposed to these temperatures are relaxed by viscoelastic flow or creep.[88] At high pressure (180 psi) and temperature (1300°C) SiO_2 glass was reported to have a creep rate 3 to 5 orders of magnitude higher than polycrystalline oxides that have similar cubic crystal structures to β-cristobalite at the same conditions.[22] The creep rate at lower pressure (10psi) at 1300°C is only reported for the glass (0.001 h^{-1}), and not for crystalline oxides so no direct comparison can be made for cristobalite, but it is likely that a lower creep rate exists for cristobalite at lower pressures too.

The viscoelastic flow in amorphous SiO_2 must significantly reduce the hoop stresses in the oxide because amorphous oxide thicknesses observed after 100h at 1100°C in wet O_2 (4.2 ± 0.3 μm) did not crack while some of the oxides from a 6h, 1300°C exposure (average oxide thickness from this test 1.43 ± 0.15 μm) that had crystalline edges cracked (example shown in Figure 36). This is an indication that the phase of the oxide plays a role in the oxide cracking, in addition to oxide thickness.

These results indicate that the hoop stresses in the crystalline oxides thermally grown at 1200 and 1300°C can cause *in situ* cracking due to the cylindrical shape of the fibers, consistent with the post-exposure SEM observations.

3.4. Conclusions

Hi-Nicalon fibers oxidized in 100% dry O_2 followed parabolic oxidation kinetics at temperatures of 900-1300°C consistent with oxidation limited by oxygen permeation through the scale dominating at these temperatures. Linear oxidation kinetics were observed at 700-800°C which may be attributed to oxidation limited by the reaction of the amorphous Si-O-C phase in the fibers with oxygen. These results were consistent with other studies of Hi-Nicalon fibers and bulk CVD SiC oxidized in dry environments described in the literature.

Hi-Nicalon oxidation kinetics in 50 vol% H_2O/ 50 vol% O_2 were determined for the first time. Linear oxidation kinetics (reaction-rate-controlled mechanism following Reaction 4) likely occurred at 700°C and parabolic oxidation kinetics (oxidant permeation-controlled mechanism) dominated in the range of 800 to 1200°C. Kinetic parameters were reported for parabolic oxidation in a high water vapor content.

Changing mechanisms for fibers oxidized at 1300°C were deciphered and reported for the three regimes. The multiple oxidation regimes existed due to the formation of cristobalite, which cracked *in situ* due to stresses generated in the oxides around the cylindrical fiber substrates. Regime 1 followed parabolic oxidation kinetics prior to significant oxide cracking. Once formed, the cracks in the oxide allowed for direct-access of the oxidant to the fiber, which allowed for reaction-rate-control to dominate (Regime 2) until the amount of available fiber for oxidation decreased due to the shrinking-core (Regime 3).

3.5. Recommendations for Future Work

A more rigorous calculation of the stresses causing cracking in crystalline oxide should be conducted that incorporates crystallization rates in SiO_2 and the creep behavior of amorphous SiO_2. This calculation would give a better understanding of the conditions necessary for oxide cracking on Hi-Nicalon fibers when exposed to wet O_2 environments.

Stand-alone Hi-Nicalon fiber oxidation results provide a baseline for fiber oxidation behavior in CMCs. However, fibers in the composite will not be directly exposed to the oxidants due to the presence of the BN interphase and SiC matrix. For a better representation of the effects of BN on fiber oxidation behavior in CMCs, Hi-Nicalon fibers should be coated in a BN layer and oxidized in the TGA. The study would include characterization of mass change curves from TGA and SEM/EDS analysis after oxidation. Both dry and wet O_2 environments should be studied over low temperatures (500-800°C) and high temperatures (900-1300°C) to expose any differences in BN oxidation behavior on the SiC fibers with temperature.

4. Matrix Material Oxidation

4.1. Objective

The goal of this aspect of the study was to understand the oxidation behavior of stand-alone matrix material in both dry and wet O_2 environments. Stand-alone matrix oxidation behavior provides a baseline for interpreting matrix oxidation in CMCs.

This chapter begins with a description of the as-received matrix material, followed by the TGA oxidation results and determination of oxidation kinetic data. Then the crystallinity and relative compositions of the oxides are determined. Finally, the effects of the boron-containing regions on the oxidation mechanisms are identified.

4.2. Results

4.2.1. As-Received Matrix Material

The as-received matrix material coupons (manufactured by RR-HTC) were characterized with SEM and EDS to understand the starting microstructure. The matrix consisted of SiC particulates and boron-containing regions in a continuous Si matrix. No porosity was observed. Strips of Si containing no SiC particulates were observed throughout each matrix coupon, as shown in the lower right of Figure 46.

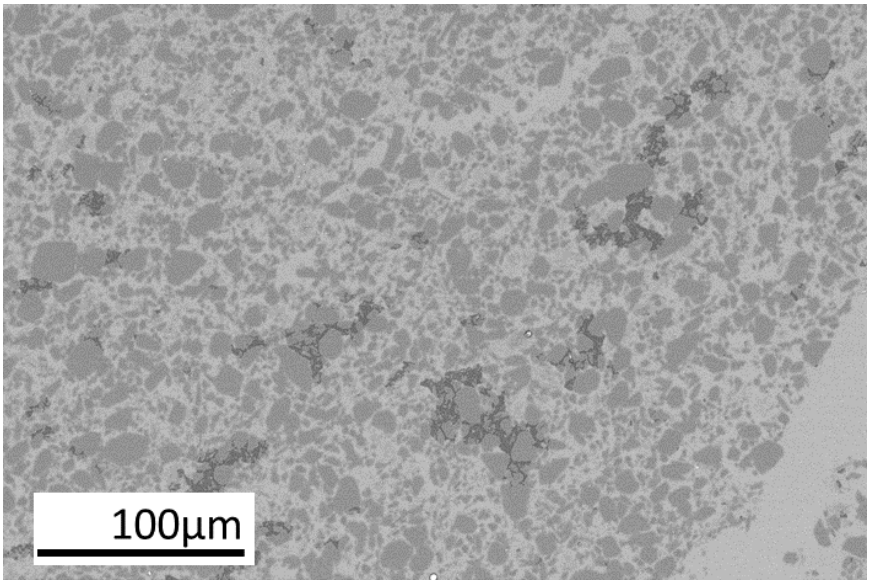

Figure 46. As-received matrix material in SEM (back-scattered) showing SiC particulates in a continuous Si phase (bright phase).

The matrix material coupons were uncoated, so all exposed faces had the same microstructure for oxidation testing.

4.2.2. TGA Oxidation of Matrix Material

Matrix material coupons were characterized by TGA and with SEM after 100 hour oxidation exposures at 800, 1200, or 1300°C in dry or wet O_2. From the TGA data, it was observed that matrix material coupons followed parabolic kinetics when oxidized at 1200 and 1300°C in both dry and wet O_2. Figure 47 shows examples of the specific mass changes vs. root time from the TGA data for matrix coupons oxidized in dry and wet O_2 at 1200 and 1300°C for 100 hours. The linear relationships of specific mass gain vs. root time indicate parabolic oxidation kinetics.

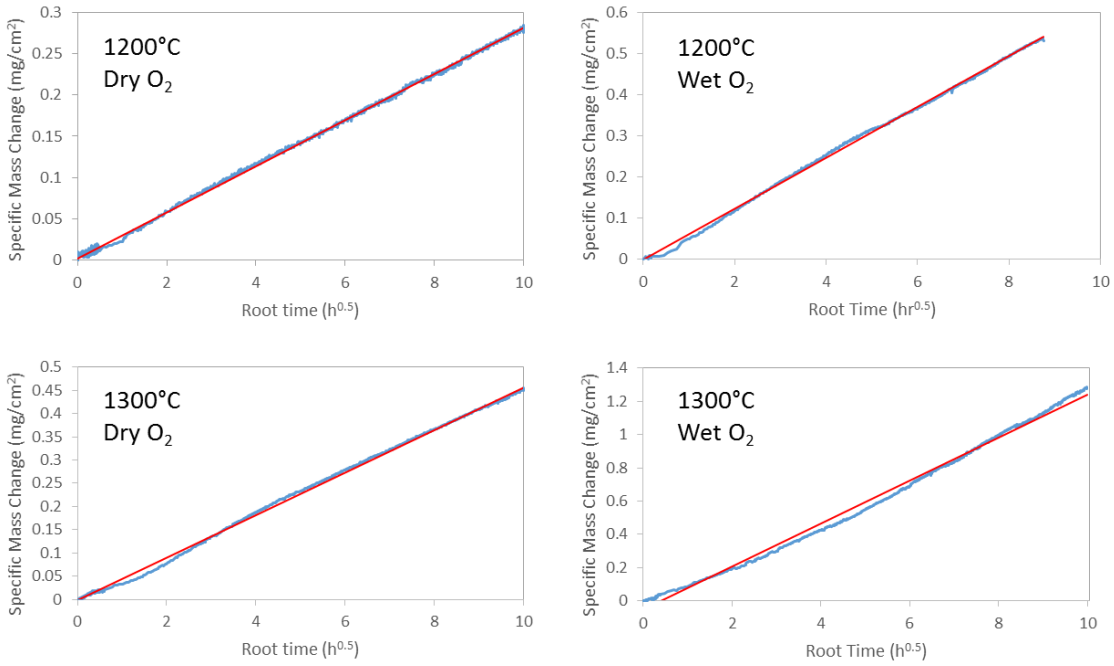

Figure 47. TGA data from matrix material coupons showing parabolic oxidation kinetics (red line) in dry (left) and wet (right) O_2 at 1200 and 1300°C.

Parabolic rate constants were calculated from the benchtop specific mass gain for coupons oxidized at 1200 and 1300°C and are compared to high purity CVD SiC oxidation rates from the literature (Table 14).

Table 14. Parabolic oxidation rate constants for matrix material in dry and wet O_2 compared with the literature[10; 15] for CVD SiC

Oxidation Condition	Average Experimental k_p (mg^2/cm^4h)	SiC Literature k_p (mg^2/cm^4h)
Dry O_2, 1200°C	3.2×10^{-4}	1.1×10^{-4} [10]
Dry O_2, 1300°C	1.6×10^{-3}	2.3×10^{-4} [10]
Wet O_2, 1200°C	1.5×10^{-3}	1.2×10^{-3} [15]
Wet O_2, 1300°C	6.8×10^{-3}	1.9×10^{-3} [15]

The parabolic rate constants in Table 14 are averages from 2 or 3 experiments and were 1.3 to 7 times greater than the parabolic rate constants reported in the literature[10; 15] for CVD SiC. The increased parabolic rate constants are attributed to increased oxidation due to the presence of boron in the matrix, as will be discussed below.

Matrix material coupons oxidized at 800°C did not follow linear or parabolic oxidation kinetics. Figure 48 (top) shows the specific mass change data for a matrix material coupon oxidized in dry and wet O_2 at 800°C for 100 hours showing non-linearity in the specific mass change with time, indicating linear oxidation kinetics were not observed. Figure 48 (bottom) shows the specific mass change data plotted vs. the square root of time for the same coupons. If parabolic kinetics held, the specific mass change vs. root time data would result in a line. The data are non-linear at short times in dry O_2 and over 100h in wet O_2, indicating parabolic oxidation kinetics were also not observed. This complex behavior is again attributed to the presence of boron in the matrix, which will be discussed in the following section.

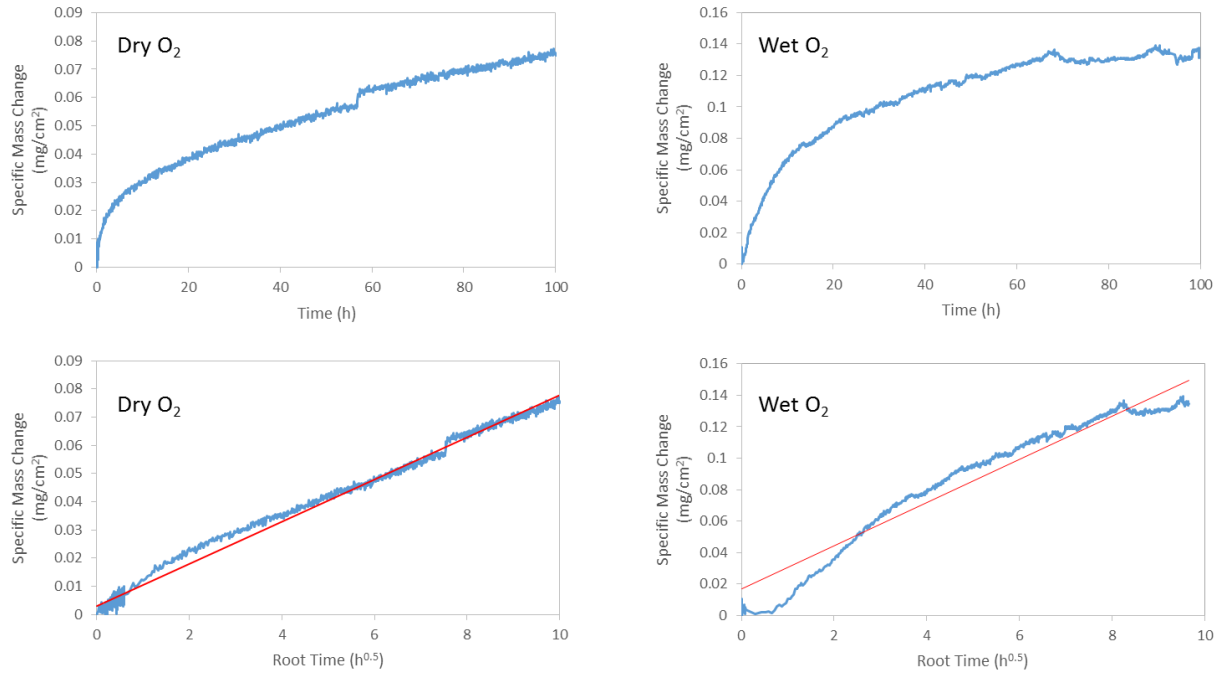

Figure 48. Specific mass change data from TGA for matrix material coupons oxidized in dry (left) and wet (right) O_2 at 800°C vs. time (top) and vs. root time (bottom). Red lines highlight the deviation of the mass change curve from linearity.

4.2.2.1. SEM Characterization after Oxidation

To better understand the oxidation behavior of the matrix material, SEM was used to characterize the oxides in both plan view and cross-section. It was clear from the plan view images (Figure 49) that a smooth, continuous oxide did not form on the matrix material.

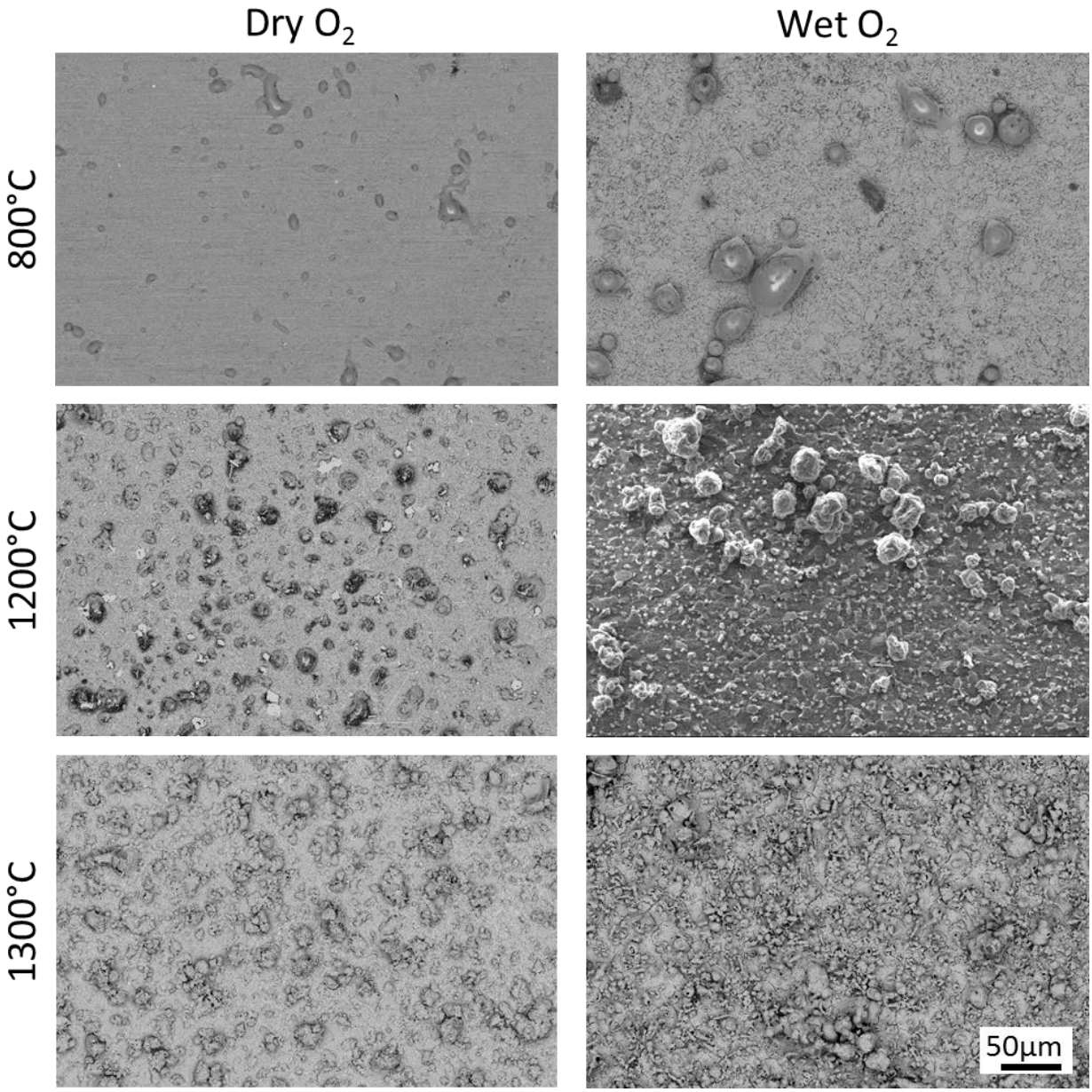

Figure 49. SEM plan view images of matrix material coupons after oxidation for 100h in dry and wet O_2 as a function of temperature.

Oxide droplets were observed on the surface of the coupons after all oxidation conditions. The formation of oxides droplets is attributed to the B-containing regions in the matrix, as will be discussed below.

The oxides formed at 1200 and 1300°C appeared cracked and crystalline for both gas environments (Figure 49). The crystalline oxides were confirmed to be cristobalite from XRD (Figure 50, bottom). No crystalline B-containing species were detected with XRD, likely due to boron volatility at the high temperatures. Peaks corresponding to SiC and Si from the underlying matrix material are observed.

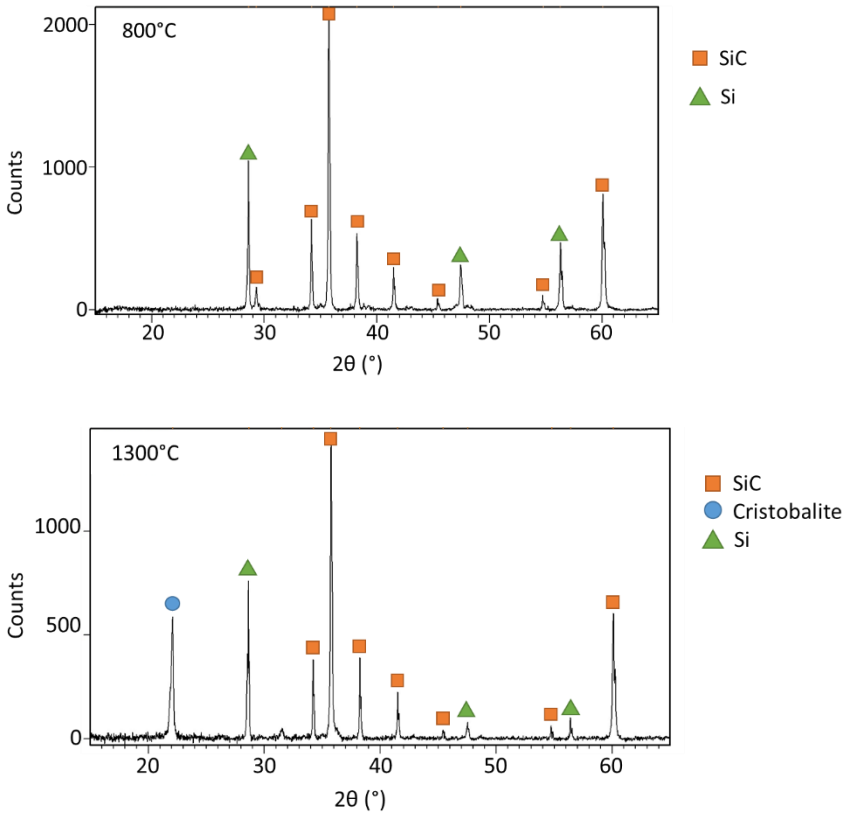

Figure 50. XRD spectra from matrix material coupons oxidized in dry O_2 at 800 (top) and 1300°C (bottom) for 100h.

A matrix material coupon oxidized at 800°C in dry O_2 was also characterized in XRD (Figure 50, top). Only peaks from SiC and Si were observed—no crystalline oxide peaks, indicating that

the oxide was amorphous. The broad peak due to an amorphous oxide is minimal in this spectrum due to the relative amounts of the amorphous oxide compared to the SiC and Si in the underlying matrix material. A cross-section of the thin oxide is discussed later.

SEM characterization of ion-polished coupon cross-sections showed that the oxide layers were porous after wet O_2 oxidation at 1200 and 1300°C and after dry O_2 oxidation at 1300°C (example in Figure 51).

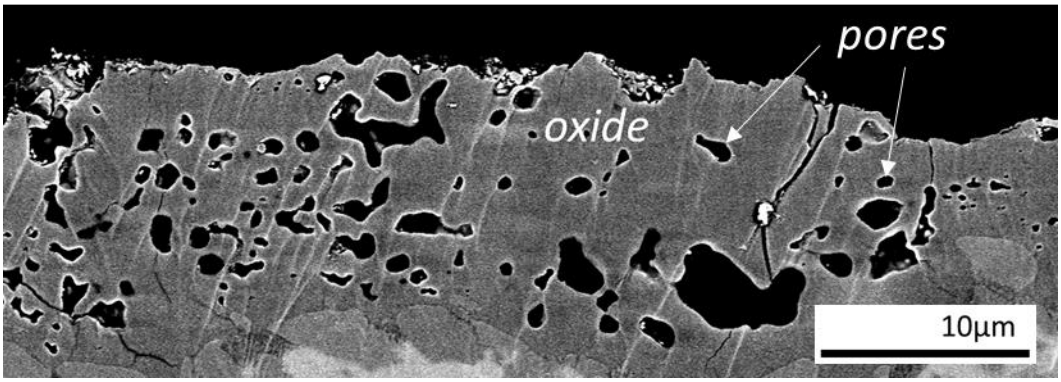

Figure 51. Porous oxide on matrix material coupon oxidized at 1300°C in wet O_2 for 100h.

It was also observed that oxide droplets were present near boron-containing regions (arrow in Figure 52) in the matrix material at all three temperatures studied.

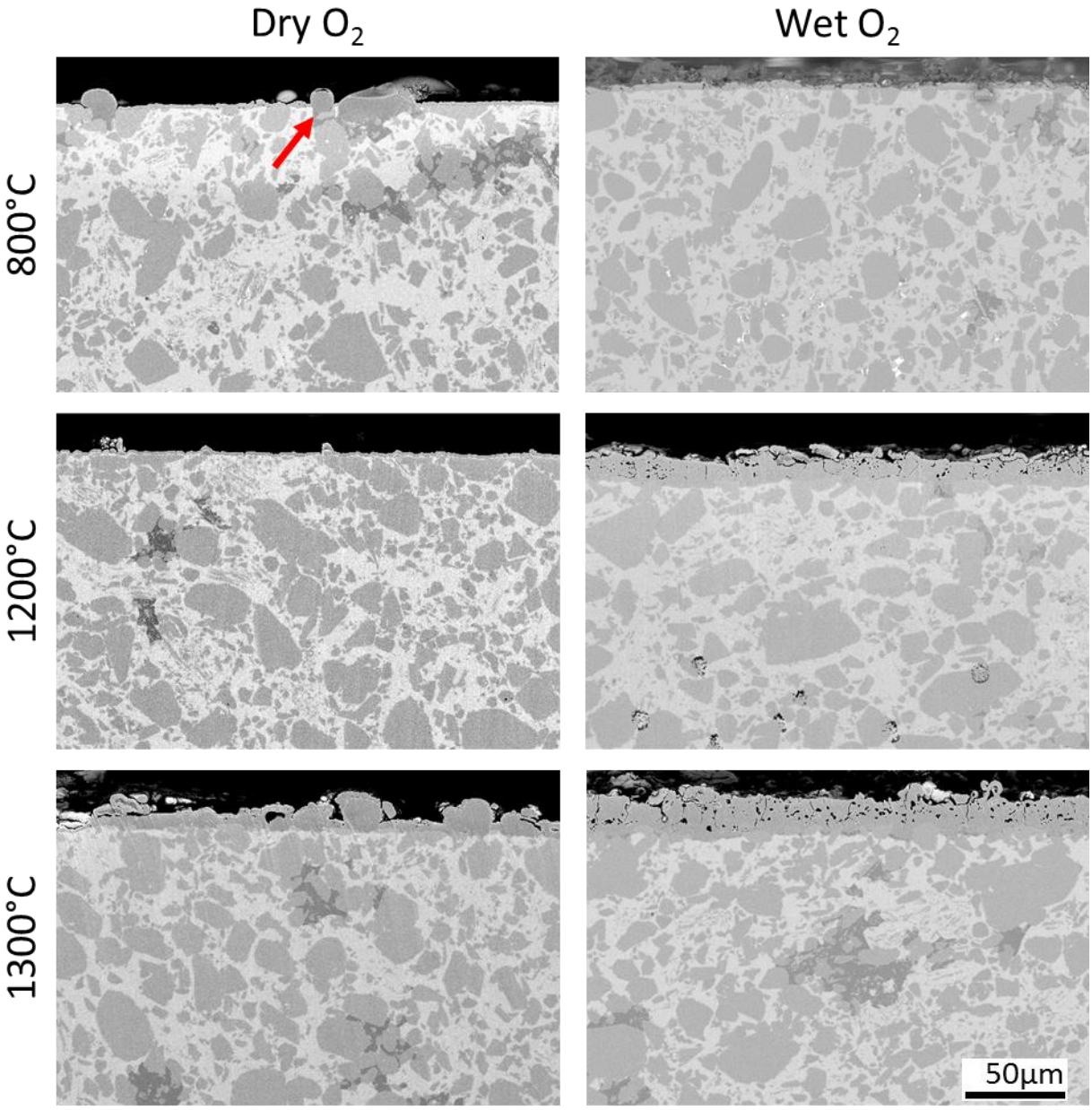

Figure 52. SEM cross-sections of matrix material coupons after oxidation in dry and wet O_2 as a function of temperature. Arrow indicates an oxide droplet formed near boron containing regions.

EDS point analyses of cross-sectioned droplets from an 800°C, dry O_2 exposure showed B, Si, O, and C signals (Figure 53, top left), indicating that the oxide droplets were a borosilicate phase. A similar composition was detected in a droplet from an 800°C, wet O_2 exposure (Figure 53, top right).

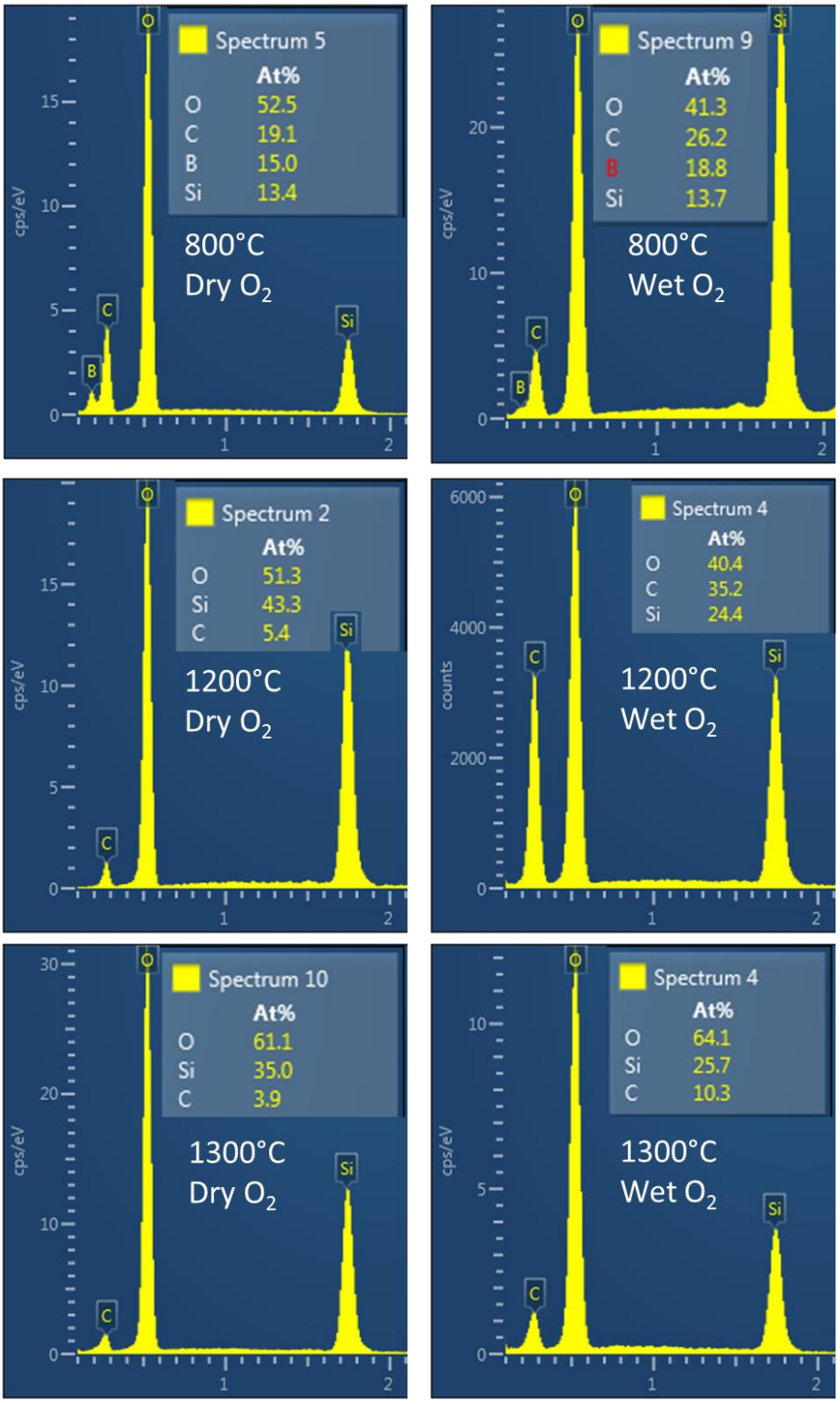

Figure 53. EDS spectra from point analyses of oxide droplets after dry O_2 (left) and wet O_2 (right) oxidation at 800, 1200, and 1300°C for 100h.

Oxide droplets characterized with EDS point analyses from 1200 and 1300°C exposures in both dry and wet O_2 did not show a B-signal (Figure 53middle and bottom). The droplets occurred in the vicinity of boron containing regions in the matrix, indicating that the droplets formed as borosilicate glasses. Because the volatility of B-hydroxide species in H_2O (g) or of B_2O_3 (g) in dry O_2 are expected to increase with temperature,[32] the boron likely volatilized from the droplets at the higher temperatures. Figure 54 shows the increasing activities of gaseous B-containing species as a function of temperature, as calculated using the FactPS database in the FactSage equilibrium module with inputs of 0.5 mol H_2O (g) and 0.5 mol O_2 (g).[35]

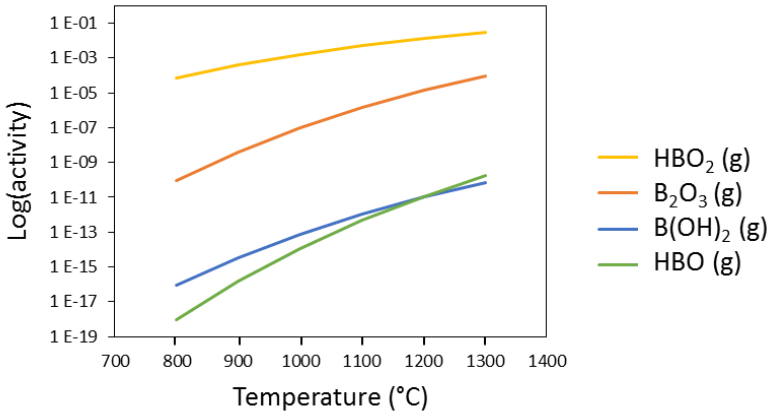

Figure 54. Increasing activities of B-hydroxide species with temperature, as calculated by FactSage.[35]

4.3. Discussion

The presence of boron had three effects on the oxidation of the matrix material coupons as observed by SEM, EDS, and TGA: 1) oxide droplets, 2) pores in the oxides, and 3) change in oxidation kinetics. The oxide droplets that were observed on the matrix material coupon surfaces formed in the vicinity of boron containing regions in the material. Locally enhanced oxidation rates in these regions due to the presence of boron[50; 51] likely allowed for the droplets to form rapidly. Oxidant diffusivities are higher in borosilicate glasses than in SiO_2, allowing for a more

rapid oxidation rate.[33; 38; 51] Borosilicate droplets were observed with EDS for the 800°C exposures, but only silica was detected with EDS for 1200 and 1300°C (Figure 53) due to increased boria volatility at higher temperatures.

The second effect observed with SEM as a result of the oxidation of boron in the matrix material was the formation of pores in the oxide (Figure 51) at the higher temperatures (1200-1300°C). The pores were likely a results of increased product gases (Reactions 1-4 and 12-13) due to the boron-enhanced oxidation rates. In the wet O_2, additional product gases were formed due to oxide volatility (Reactions 10 and 14-16). Porous oxides were not observed on CVD SiC materials oxidized in the same conditions[20] (Figure 55a). However, a porous oxide with similar morphology to the porous matrix material oxides was observed on CVD SiC after 500 hours oxidation at high pressure (10 atm)[89] (Figure 55b).

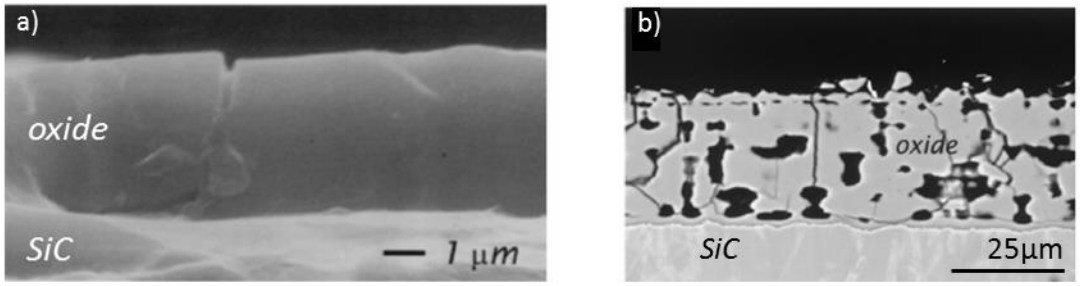

Figure 55. CVD SiC materials from oxidation studies in the literature for two conditions: 1300°C, 50% H_2O, 100h at 1 atm[20] *(a) and 1300°C, 15% H_2O, 500h at 10 atm*[89] *(b).*

The lower viscosity of the liquid borosilicate glass, relative to pure SiO_2,[40] in this study likely allowed for the coalescence of the gases, creating pores. Borosilicate viscosity as a function of composition and temperature is an important parameter to consider during CMC oxidation and will be the focus of the free-standing borosilicate glass study in *Chapter 6. Viscosity and Melting Behavior of Borosilicate Glasses*.

The final effect of the boron was on the oxidation kinetics of the matrix material. At 800°C the kinetics observed with TGA were not linear, as expected for bulk SiC oxidized in the

same conditions. Instead, the boron in the matrix material had a dual effect that resulted in complex oxidation kinetics (poor fit to simple linear or parabolic kinetics). As discussed above, the regions containing boron experienced enhanced oxidation rates due to the boron, while areas without boron experienced slow oxidation of Si and SiC due to the low temperature. Additionally, boria volatility could be occurring simultaneously, resulting in a mass loss. The interplay of these simultaneous processes could not be deciphered from the TGA data.

The rates for the 1200 and 1300°C exposures were also affected by the presence of boron. The pore coalescence and boria effects on the glass network structure both increased oxidant transport through the glass and could account for the slightly higher (1.3-7x) parabolic oxidation rates, compared to CVD SiC. The pores, however did not appear to be connected (from SEM) and parabolic kinetics were observed (from TGA), so the oxide scales were still protective in these conditions. Although B_2O_3 volatility likely occurred at these temperatures as well, the Si and SiC oxidation rates were higher, due to the initial presence of B_2O_3 and the higher temperatures, resulting in parabolic mass gains during oxidation. Because the oxide remains protective, an O_2 (g) or H_2O (g) diffusion-limited oxidation mechanism is valid.

4.4. Conclusions

Oxidation of a stand-alone matrix material composed of SiC-Si with a small boron content was conducted for the first time and resulted in oxide morphologies not previously observed on CVD SiC materials. The B-containing regions altered the oxide morphologies and kinetics at all temperatures studied, as compared to CVD SiC oxidized at the same conditions. Borosilicate oxide droplets formed on the surface in the vicinity of boron-containing regions in the matrix material. These regions experienced increased oxidation rates, resulting in increased gaseous species that were trapped in the oxide at 1200 and 1300°C. Parabolic oxidation rate

constants reported for 1200 and 1300°C were 1.3-7 times greater than CVD SiC oxidized at the same conditions due to the presence of boron.

Because the CMCs contain the same SiC-Si matrix constituent as these coupons studied, the oxidation behavior of the matrix material can be used as a baseline for understanding matrix oxidation behavior in the CMCs. The oxide droplets, increased oxidation rates, and porous oxide could affect the lifetime of CMC components.

4.5. Recommendations for future work

It should be understood how the amount and distribution of boron in the matrix affects the oxide morphology. To understand the importance of these factors, an experiment should be conducted where concentration and distribution are varied. Boron levels above and below the studied matrix material should be studied in both dry and wet O_2 atmospheres at temperatures of 800 and 1200°C, and other temperatures of interest. Results from these studies could inform the ideal phase fraction and distribution of boron in the matrix material for CMCs.

5. Ceramic Matrix Composite Oxidation

5.1. Objective

The goals of this study were to characterize CMC oxidation behavior in both dry and wet O_2, to provide kinetic data for a CMC life prediction model, and to inform an overall description of CMC oxidation mechanisms. The oxidation kinetics of the BN interphase was of critical interest, as this phase is needed to maintain the desired mechanical properties of the CMCs. Oxidation studies of CMC coupons were conducted using TGA, as described in *Section 2.2. Experimental Setup and Procedures*.

Note that it was attempted to obtain oxidation kinetic data by many analysis methods, yet none of the oxidation results were found to be significantly dependent on time. In addition, many of the observed oxidation kinetics were also independent of temperature or oxidant. These analyses include TGA weight change, overall weight change, TGA transient weight change, surface oxide phase distribution and morphology, oxidant ingress in porosity pipes, oxidant ingress along internal composite interfaces, loss of BN interphase, oxidant ingress under applied load.

This chapter begins with an overview and characterization of the as-received CMC materials, followed by baseline oxidation exposures of CMC coupons with the CVD SiC seal coat intact on all faces. Oxidation of CMC coupons with an exposed face are analyzed with respect to the effects of high oxidant partial pressure (sealing of the surface due to oxidation) in both plan view and cross-section. Oxidized CMCs are also analyzed with respect to the effects of low oxidant partial pressure (oxidation within the composite). This analysis consists of oxide thicknesses over the BN interphase, oxide composition determination, and SiC/BN interface

characterization. Finally, the effect of an applied load on internal CMC oxidation behavior is described.

5.2. Results

5.2.1. As-Received CMCs

CMC coupons were fabricated with a CVD SiC seal coat on all surfaces. As described in *Chapter 2. Test Materials and Procedures*, the bottom face of each coupon was ground to expose all the constituents (fibers, interphase, and matrix) to the oxidizing environment in the TGA. The exposed CMC faces, as well as cross-sections of the CMCs, were characterized by SEM/EDS, and TEM/Energy Filtered TEM (EF-TEM) before and after oxidation.

The as-received CMC coupons provided by RR-HTC for TGA testing were first characterized with SEM to gain an understanding of the structure and phase distribution within the CMCs. There were three main constituents in the CMCs: the commercially available Hi-Nicalon^{TM} SiC fiber tows in a 2-d weave, the BN interphase surrounding each fiber, and the Si/SiC matrix that consisted of a Chemically Vapor Infiltrated (CVI) SiC layer surrounding the BN interphase and a Slurry (SiC particulates)/Melt (Silicon) Infiltrated (Slurry-SMI) Si/SiC matrix phase (Figure 56) with some boron-containing regions. The Hi-Nicalon SiC fibers were the same as those studied in *Chapter 3. Oxidation of Hi-Nicalon SiC Fibers*.

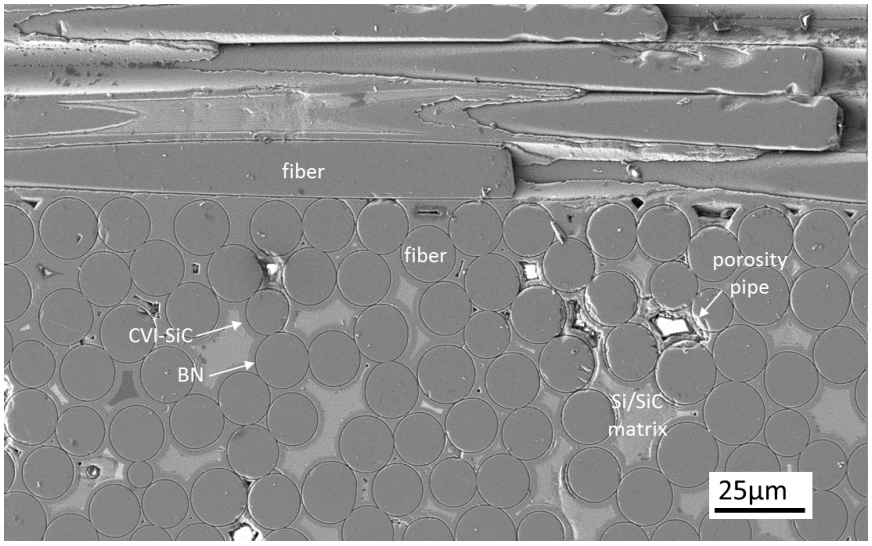

Figure 56. Cross-section of an as-received TGA CMC coupon showing all CMC constituents.

Both 0° and 90° plies in the [0/90] CMC lay-up can be seen in Figure 56 with the 0° ply coming "out" of the page and the 90° ply going across the image. The 0° plies were of primary interest to this work to examine oxidation penetration into the longest direction of the composite. All reported penetration rates will be for the 0° direction.

EF-TEM maps obtained from as-received CMCs were used to characterize the SiC/BN/SiC interfaces and showed phase compositions as expected: BN interphase, SiC fiber and matrix (Figure 57). The oxygen EF-TEM map shows a slight signal along the SiC/BN interfaces (Figure 57, top right), indicating that a small amount of oxygen exists at the interface before oxidation. This could be due to a small gap at the interface that oxidized in the laboratory air, but no gap is observed in the TEM image (Figure 57, top left). The oxygen could also be due to the processing method. Details of the proprietary processing method are not known. The oxygen signal provides a reference to compare with CMCs after oxidation.

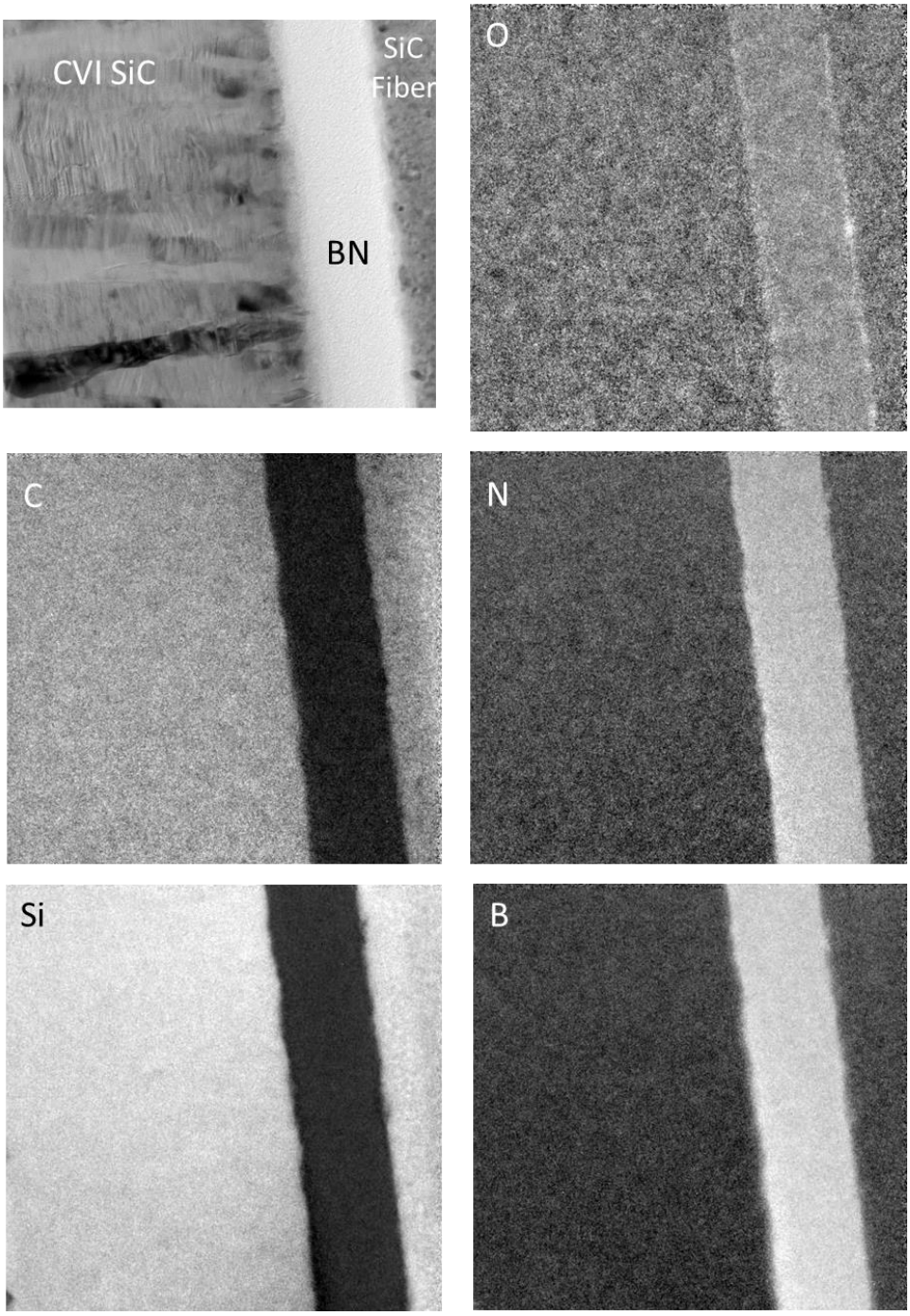

Figure 57. As-received CMC in TEM (top left) and corresponding EF-TEM maps. Length scale omitted intentionally due to RR Intellectual Property (IP).

5.2.2. TGA Exposures

5.2.2.1. Baseline Coupon Oxidation

Four CMC coupons with the CVD SiC seal coat intact on all faces were oxidized for 100 hours in different exposure conditions: 800 and 1200°C in dry O_2, and 800 and 1300°C in wet O_2. These tests were conducted as baselines for the TGA and specific mass change data for CMCs oxidized with an exposed face. The baseline coupons achieved steady-state linear kinetics at 800°C in dry O_2 and parabolic kinetics at 1200 and 1300°C in both dry and wet O_2 (Figure 58). The wet O_2, 800°C data (Figure 58, top right) is unusable, with the observed noisy signal possibly due to the sample touching the furnace tube wall. However, note the small mass change observed at 800°C in both environments, confirmed with a bench-top balance. No repeat experiments with the CVD SiC seal coat intact were conducted due to limited number of samples available. However, due to the small mass change over 100h (< 0.1 mg as measured using a bench top balance), the coupon exposed in 800°C wet O_2 was assumed to follow linear oxidation kinetics consistent with prior results for SiC.[71; 90]

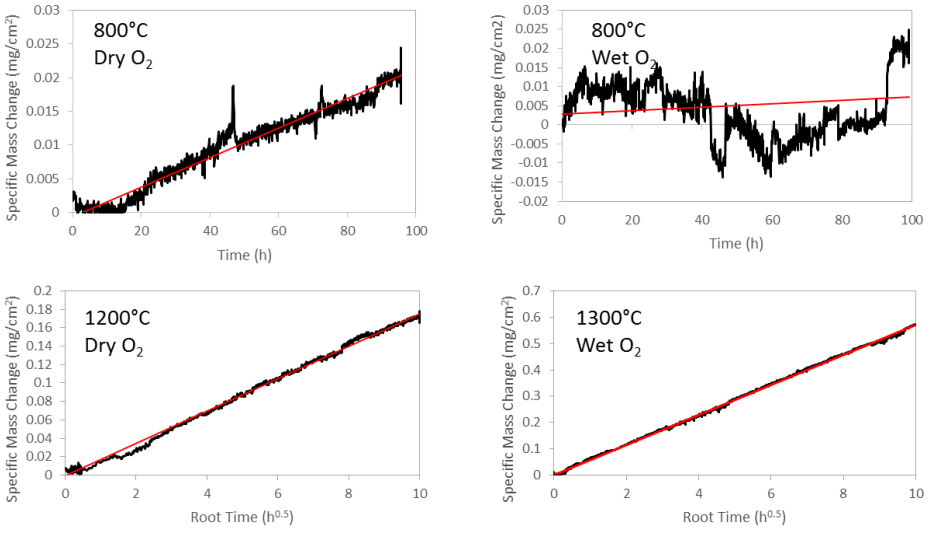

Figure 58. Specific mass change vs. root time for a CMC with the CVD SiC seal coat intact oxidized in wet O_2 at 1300°C for 100h. Black: TGA data, Red: linear fit.

In addition to analyzing the TGA data, the total specific mass change (from a benchtop balance) was calculated for each baseline CMC coupon (Table 15). Table 15 also contains the average specific mass changes for CMCs exposed at the same conditions, but with an exposed face. In the case of the CMCs with an exposed face, it should be noted that 5 of the 6 faces were still coated with CVD SiC during oxidation (~95% of the surface area still coated with CVD SiC). Any differences in the mass change between the baseline and exposed face coupons were due to oxidation of the exposed CMC constituents on the exposed face instead of oxidation of CVD SiC only. There was no statistical difference in specific mass changes between the baseline CMCs and the exposed face CMCs oxidized in dry O_2. At 800°C in the wet O_2, the baseline CMC gained a small amount of mass while the exposed face CMCs lost mass, possibly due to B_2O_3 volatility. At 1300°C in the wet O_2, the exposed face CMCs had a large uncertainty due to one coupon gaining mass and two losing mass, again likely due to increased volatility in the wet O_2 environment. Statistically, there was no difference between the baseline and the exposed face CMCs at 1300°C in the wet O_2. Thus, coupon mass change could not be used to reliably assess differences in oxidation behavior of the exposed faces.

Table 15. Specific mass changes of CMCs oxidized for 100h with the CVD seal coat intact vs. with an exposed face

Temperature (°C)	TGA Environment	Seal coat CMC baseline specific mass change (mg/cm^2)	Average exposed face CMC specific mass change and standard deviation (mg/cm^2)
800	Dry O_2	0.012	0.010 ± 0.002
1200	Dry O_2	0.13	0.12 ± 0.02
800	Wet O_2	0.004	-0.030 ± 0.004
1300	Wet O_2	0.3	0.1 ± 0.3

5.2.2.2. Exposed Face Sealing

Exposed CMC faces were imaged in plan view with SEM after oxidation to characterize the oxide morphology and distribution relative to the CMC constituents. The resulting surface

microstructures were compared as a function of oxidation time, temperature, and environment. Areas of unoxidized BN interphase (dark rings) were observed after exposure at 800°C for 1 hour in both wet and dry O_2 (Figure 59), indicating that the BN interphases were not all covered after one hour oxidation.

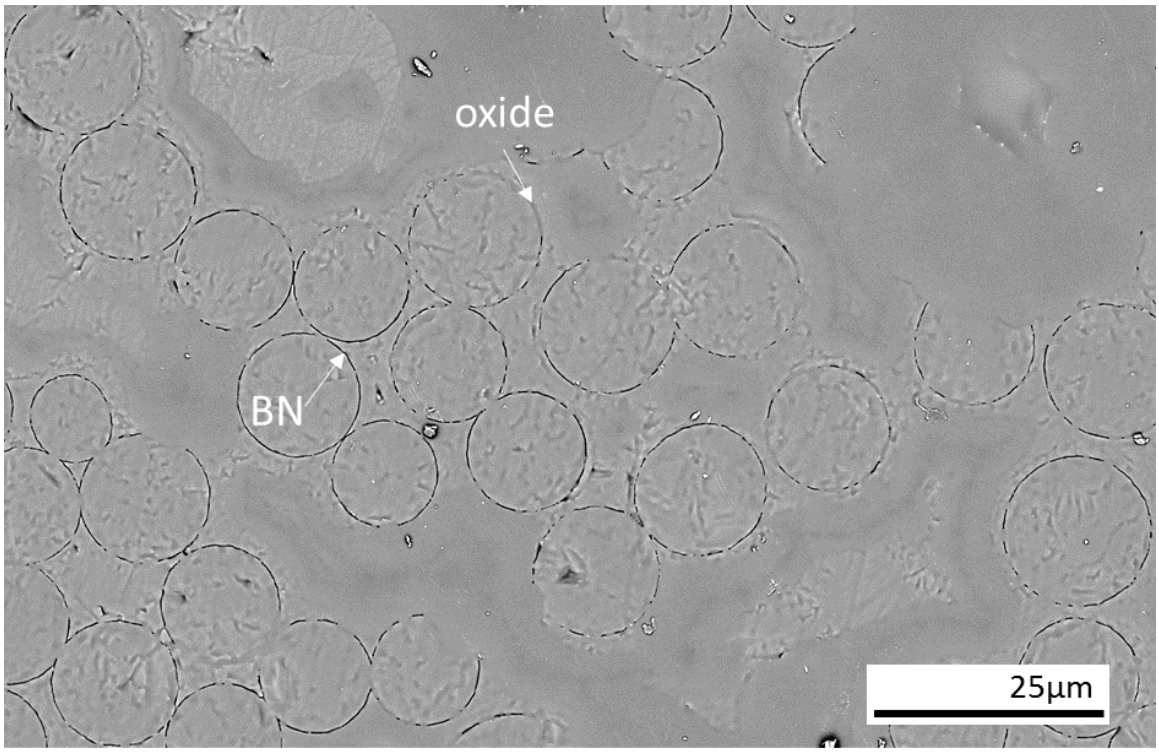

Figure 59. SEM image of an exposed CMC face after oxidation in dry O_2 at 800°C for 1 hour showing unoxidized BN and some oxide on the interphase.

However, as time and temperature were increased, the BN and SiC phases further oxidized, sealing all BN interphases in both dry O_2 and wet O_2. Figure 60 shows exposed CMC surfaces after oxidation in dry O_2 at all three temperatures studied for 1 and 100h. The BN interphases are covered with oxide, which sealed them against further rapid oxidation.

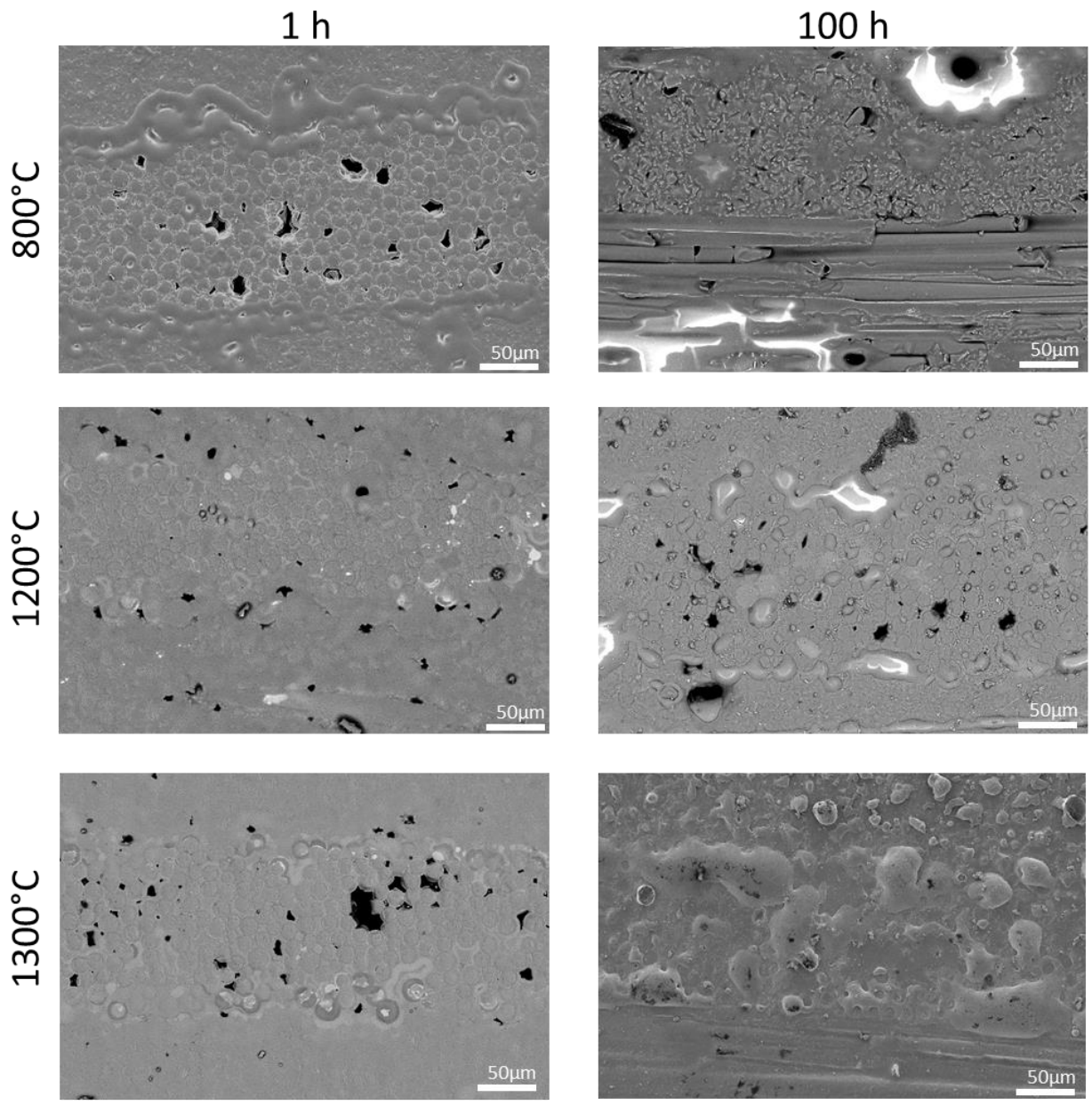

Figure 60. SEM images of exposed CMC faces after oxidation in dry O_2 as a function of time and temperature.

Figure 61 shows exposed CMC surfaces after oxidation in wet O_2 at all three temperatures studied for 1 and 100h. Again, the BN interphases are covered with oxides.

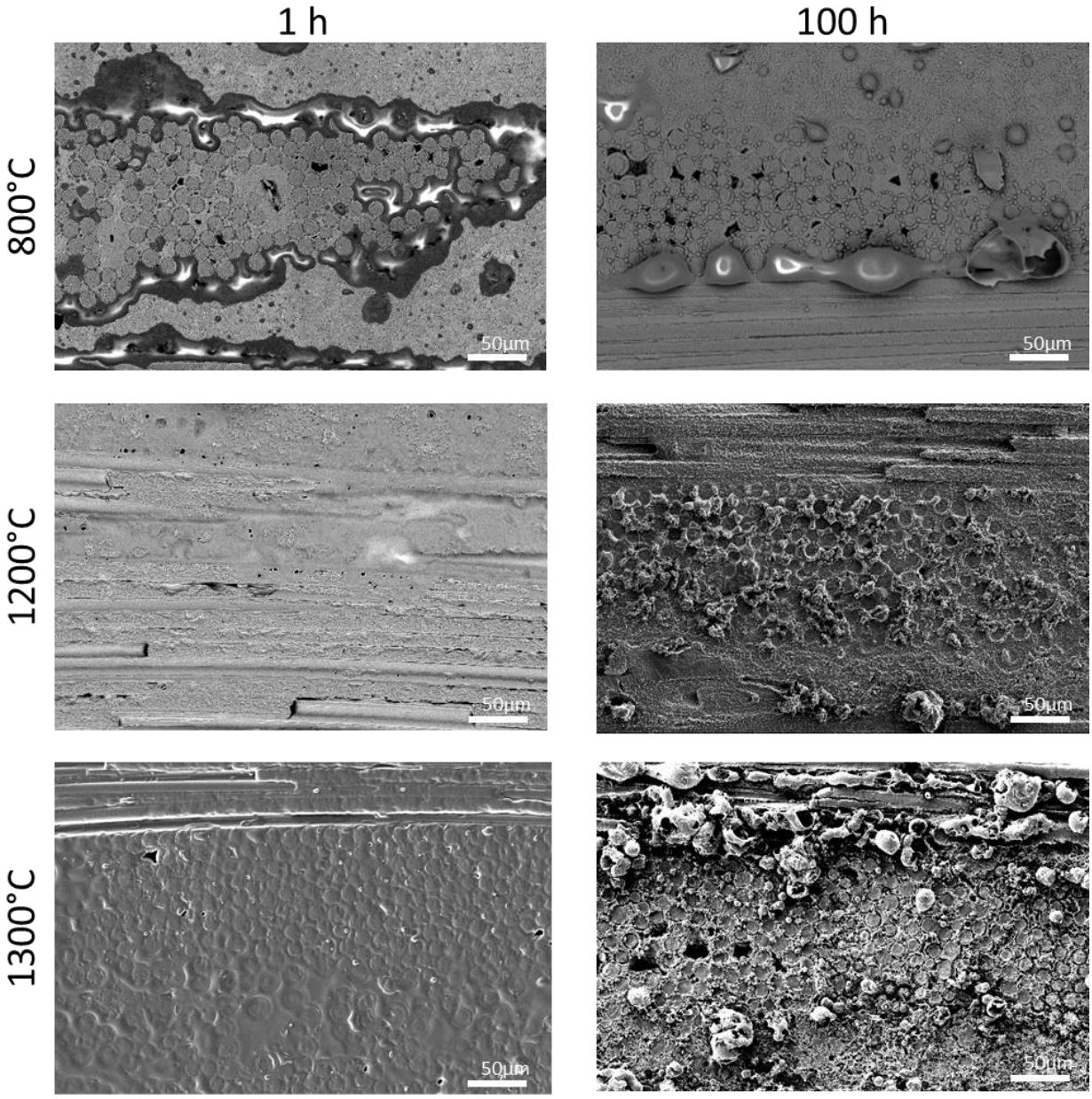

Figure 61. SEM images of exposed CMC faces after oxidation in wet O_2 as a function of time and temperature.

In addition to sealing the surface, pronounced oxide droplets were observed on the BN interphase after oxidation (arrows in Figure 62).

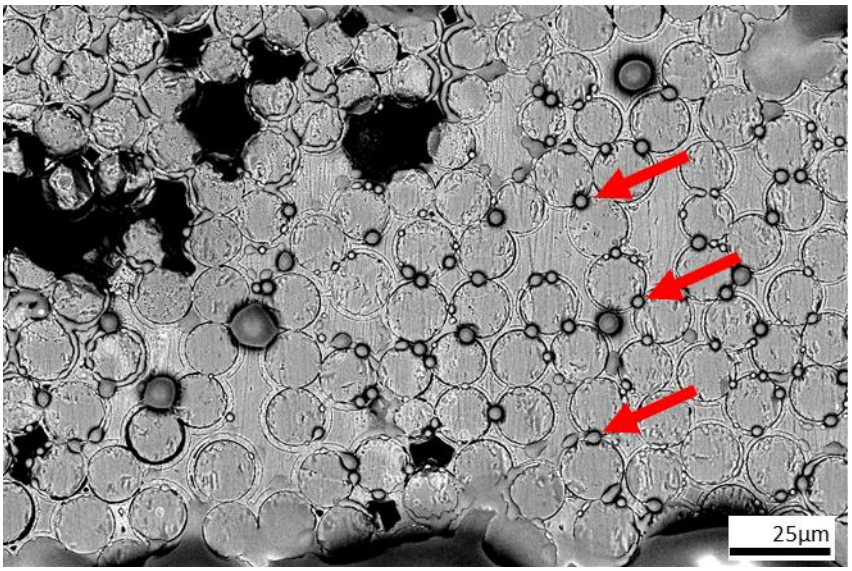

Figure 62. SEM image of an exposed CMC face after oxidation in wet O_2 at 800°C for 50h showing oxide droplets (arrows) on the interphase.

Oxide droplets were observed in both dry and wet O_2 after all one hour exposure conditions except 800°C in the dry O_2. For 800°C dry O_2, oxide droplets were observed on the exposed face after 50 hours of exposure (Figure 63).

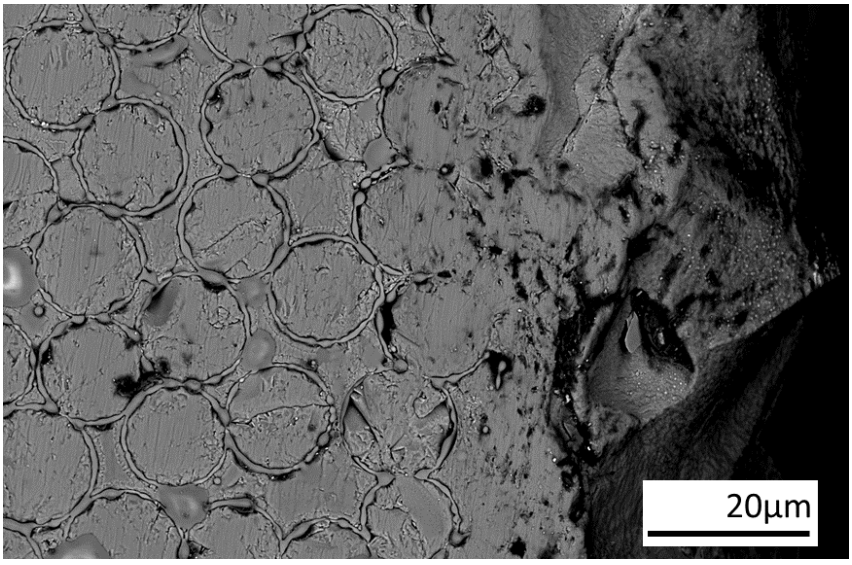

Figure 63. SEM image of an exposed CMC face after oxidation in dry O_2 at 800°C for 50h showing oxide droplets on the interphase.

After 100h at 1200°C and after 50h at 1300°C in dry O_2, the oxides that sealed the interphases on the surface were crystalline. These oxides appeared cracked and "frosty" in SEM,

rather than smooth and continuous like the amorphous oxides. Oxides were observed to be crystalline after a shorter exposure time in wet O_2—just 50h at both 1200 and 1300°C. Figure 64 shows the crystalline oxide in plan view on an exposed CMC face oxidized in wet O_2 at 1300°C for 50h.

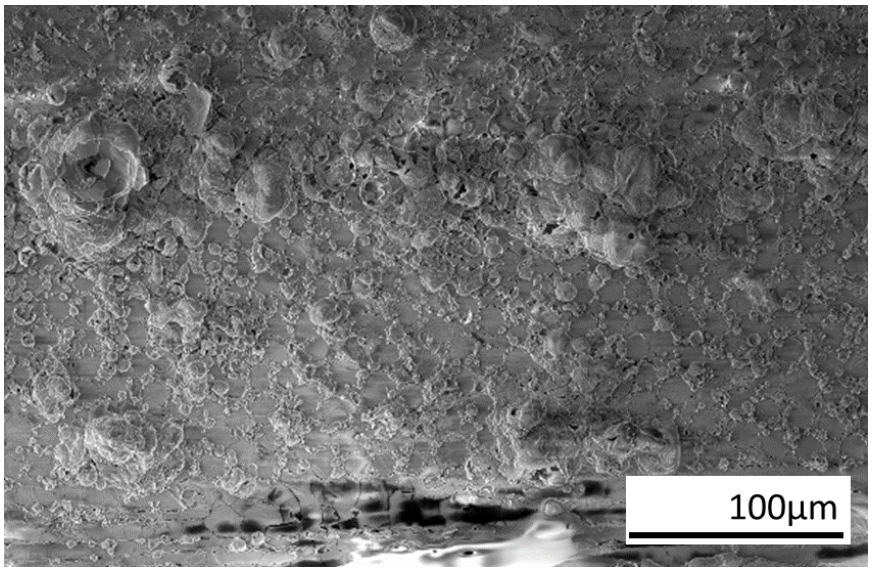

Figure 64. SEM image of an exposed CMC face after oxidation in wet O_2 at 1300°C for 50h showing crystalline oxide.

Crystallinity was confirmed by XRD (Figure 65, Table 13), showing cristobalite as the oxide phase. Crystallinity observed at the lower temperature (1200°C in wet O_2 and 1300°C in dry O_2) is in agreement with the crystallization times and temperatures observed for stand-alone Hi-Nicalon fibers (*Section 3.3.2. Wet Oxidation*).

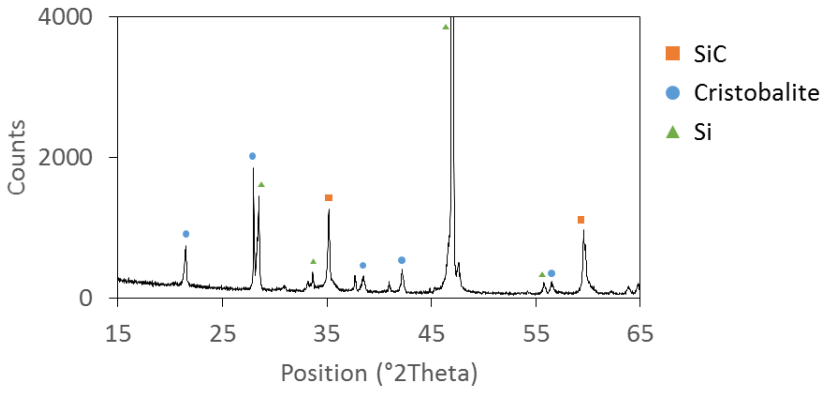

Figure 65. XRD pattern for an exposed CMC surface after oxidation in wet O_2 at 1200°C for 100h showing cristobalite, SiC, and Si peaks.

Other crystalline phases detected were Si and SiC from the substrate material (Table 16). No crystalline B-containing phase was observed with XRD. Possible reasons for this result are discussed in a following section

Table 16. 2Theta peaks detected by XRD and the corresponding phase

Peak Position (°2Theta)	Relative Intensity (%)	Phase	PDF Card #
21.5	2.6	Cristobalite	96-900-8111
28.0	7.2	Cristobalite	96-900-8111
28.5	6.2	Si	96-901-1057
33.5	0.4	Si	96-901-1057
35.2	5.3	SiC	96-900-8857
37.7	0.8	Cristobalite	96-900-8111
42.2	1.4	Cristobalite	96-900-8111
46.9	100	Si	96-901-1057
55.8	0.4	Si	96-901-1057
56.5	0.6	Cristobalite	96-900-8111
59.5	3.9	SiC	96-900-8857

Analysis of oxide composition was attempted with ICP-OES but was unsuccessful due to challenges in determining an appropriate acid digestion solution. A description of the attempted procedures and results are given in Appendix E.

5.2.2.2.1 Sealing Kinetics Determined by TGA

SEM was used to characterize oxide microstructures that sealed BN interphase on exposed CMC faces. TGA was used to quantify the time for sealing due to oxidation. The TGA data showed transient mass changes during the initial hour of each oxidation experiment. Note, this transient mass change was not observed for the CVD SiC coated coupons shown in Figure 53. Following the transient mass change, the CMCs achieved steady-state mass gains (Figure 66). CMCs oxidized at 1200 and 1300°C oxidized with near parabolic kinetics after the transient mass changes in both dry and wet O_2.

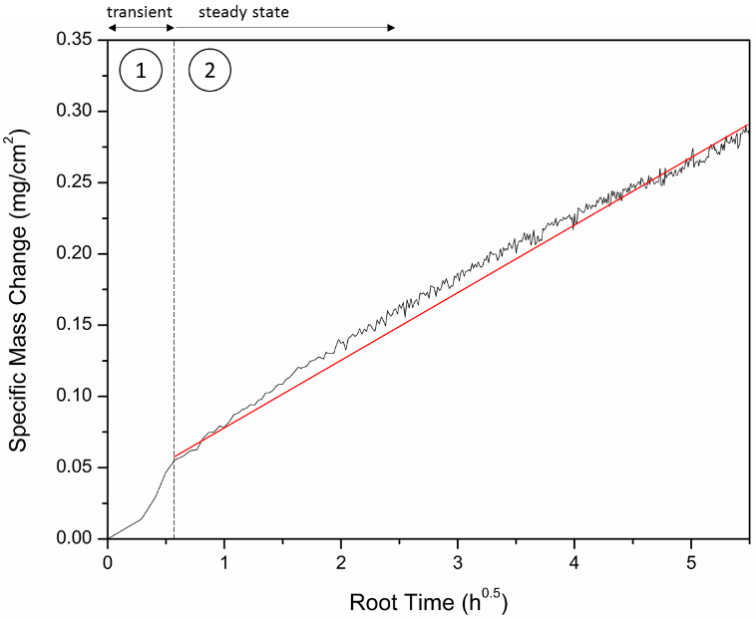

Figure 66. TGA data for a CMC with an exposed face oxidized at 1300°C in wet O_2 showing a transient mass gain followed by near parabolic oxidation kinetics.

The transient stage (Regime 1) was a rapid mass gain that was assumed to be due to the rapid sealing of BN interphase on the exposed CMC face through oxidation. This was confirmed by comparing the duration of Regime 1 to the formation time for oxide droplets on CMCs, which will be discussed below. The TGA data were utilized to quantify the time and amount of mass change in Regime 1 for each oxidized CMC.

CMCs oxidized in wet O_2 typically gained more mass compared to those oxidized in dry O_2 during the rapid mass gain period (Figure 67), especially clear at 800°C, due to increased oxidation rates in the presence of H_2O (g).

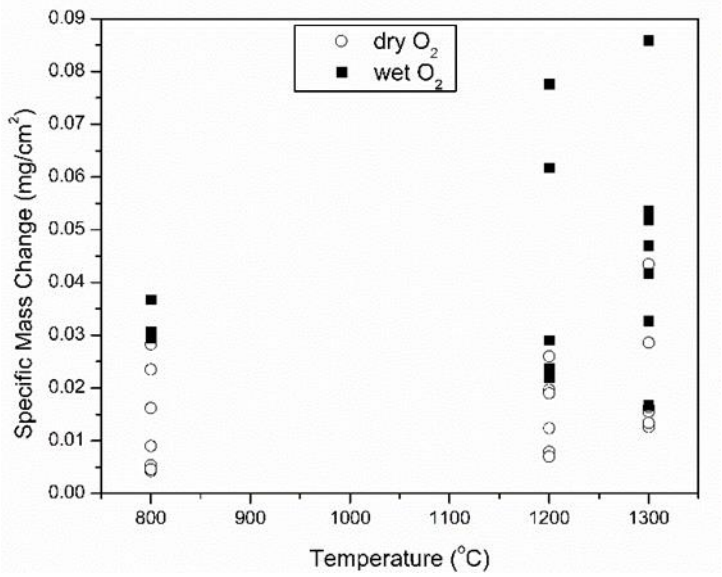

Figure 67. Transient specific mass gain of CMCs oxidized in wet O_2 was twice that of CMCs oxidized dry O_2 during the initial transient mass gain period (Regime 1).

On average, CMCs oxidized in wet O_2 gained 2.2, 2.6, or 1.6 times more mass than the CMCs oxidized in dry O_2 at 800, 1200 or 1300°C, respectively, during the transient Regime 1 (Table 17). However, the difference in the specific mass change between dry and wet O_2 at 1200 and 1300°C was not statistically significant.

Table 17. Specific mass changes in Regime 1 for dry and wet O_2

Temperature (°C)	Regime 1 Specific Mass Change in Dry O_2 (mg/cm^2)	Regime 1 Specific Mass Change in Wet O_2 (mg/cm^2)
800	0.015 ± 0.010	0.032 ± 0.003
1200	0.015 ± 0.007	0.04 ± 0.02
1300	0.03 ± 0.02	0.05 ± 0.02

The mass gain transient *time* was not statistically different at each temperature for the two environments (Table 18, Figure 68).

Table 18. Time for specific mass changes in Regime 1 for dry and wet O_2

Temperature (°C)	Time for Regime 1 Specific Mass Change in Dry O_2 (h)	Time for Regime 1 Specific Mass Change in Wet O_2 (h)
800	0.4 ± 0.2	0.4 ± 0.1
1200	0.3 ± 0.2	0.3 ± 0.3
1300	0.2 ± 0.1	0.2 ± 0.2

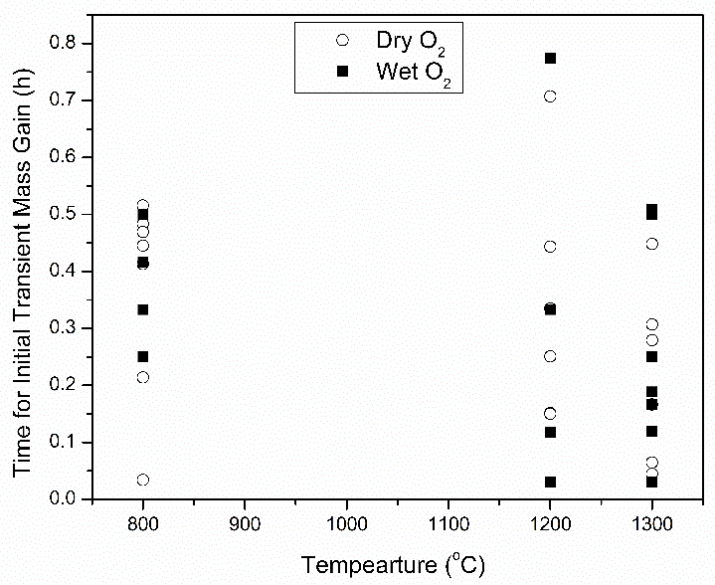

Figure 68. Time for initial transient mass gain (Regime 1) was not statistically different for wet or dry O_2.

In addition to the rapid initial mass gain for each exposed CMC (Regime 1, example in Figure 66), there was a furnace startup time associated with each exposure. Because the hot furnace moved to surround the hanging sample in the tube, buoyancy effects in the gas caused artifacts in the initial mass change readings in the TGA. These were obvious and not included in the mass change analysis (circles in Figure 69).

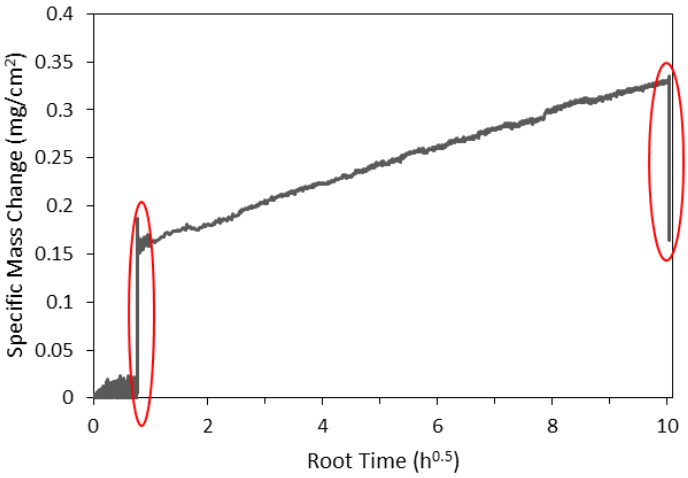

Figure 69. Specific mass change vs. root time from TGA for a CMC with the CVD seal coat intact oxidized in dry O_2 at 1200°C for 100h showing large, obvious buoyancy effects (circles).

The duration of the furnace startup time varied by temperature and with gas environment. The furnace startup times (buoyancy equilibration times) ranged from 0.01-0.1 hour and 0.1-0.6 hour for dry and wet O_2 tests, respectively. Each CMC was exposed to the oxidizing conditions during this time, so it must be considered in addition to Regime 1 when determining the total sealing time for the BN interphase. Therefore, the total sealing time was the sum of Regime 1 and the furnace startup time for each test. The average durations of Regime 1, furnace startup times, and the resulting total sealing time are given in Table 19.

Table 19. Average Total Sealing Time for CMCs with Exposed Faces.

Environment	Temperature (°C)	Average Duration of Regime 1 (h)	Average Furnace Startup Time (h)	Average Total Sealing Time (h)
Dry O_2	800	0.4 ± 0.2	0.05 ± 0.04	0.4 ± 0.1
	1200	0.3 ± 0.2	0.06 ± 0.04	0.4 ± 0.2
	1300	0.2 ± 0.1	0.03 ± 0.03	0.2 ± 0.1
Wet O_2	800	0.4 ± 0.1	0.4 ± 0.2	0.8 ± 0.2
	1200	0.3 ± 0.3	0.2 ± 0.1	0.5 ± 0.3
	1300	0.2 ± 0.2	0.14 ± 0.03	0.4 ± 0.2

The duration of the total sealing times was greater in wet O_2 than dry O_2 for CMCs oxidized at 800°C. This could be due to a combination of the greater B_2O_3 volatility in H_2O (g) compared to O_2 and relatively slow SiC oxidation rate due to the lower temperature. The range of total sealing times was not significantly different at 1200 or 1300°C (Figure 70).

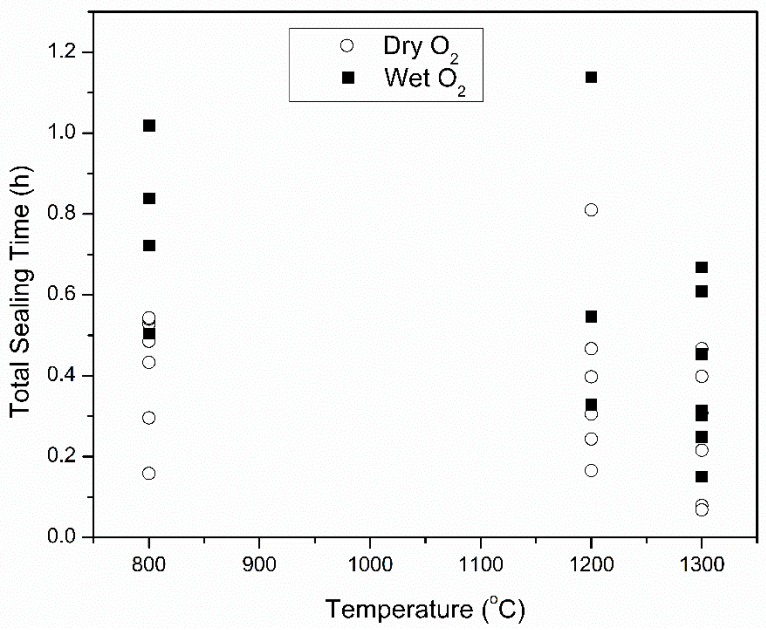

Figure 70. Total time for sealing of exposed CMC faces (Regime 1 + furnace startup).

Despite differences in sealing rates at 800°C between dry and wet O_2, all 35 oxidation experiments in Figure 70 were compared. The sealing durations ranged from 5-68 minutes. This suggested *i)* a rapid sealing of the BN interphase on the exposed CMC faces at all oxidizing conditions and *ii)* CMC oxidation kinetics could not be determined from the short time TGA results.

5.2.2.3. Cross-Sectional Characterization

After SEM characterization of the oxidized exposed CMC faces, the CMCs were sectioned along the length of the coupon to characterize the oxidation in the interior of the composite (Figure 19). Three types of information were gathered: *i)* surface oxide composition and thickness above the BN interphase region *ii)* oxygen ingress into porosity pipes; *iii)* extent of oxidation in the interior of the CMC at the BN/SiC fiber interface where BN is preserved but SiC is oxidized. Each of these features is described below.

5.2.2.3.1. Oxide Droplets in Cross-Section

The oxide droplets originally observed with SEM on the surface of the CMCs were observed in cross-section with SEM and TEM. Similar to the oxide droplets observed on the matrix material, the oxide droplets on the CMCs were adjacent to B-containing regions: in the case of Figure 71 the BN interphase.

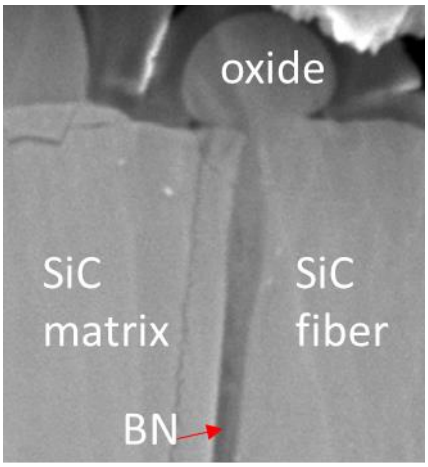

Figure 71. SEM cross-section of an oxide droplet on a CMC oxidized in wet O_2 at 800°C for 100h. Length scale omitted intentionally due to RR IP.

Oxide droplet formation adjacent to the BN interphase indicated rapid initial BN oxidation. Two oxide droplets were also observed with TEM. Figure 72 (top left) shows the TEM image of an oxide droplet in cross-section from a CMC oxidized in wet O_2 at 800°C for 100h with corresponding Energy Filtered TEM (EF-TEM) compositional maps (Figure 72 top right and bottom 4 maps).

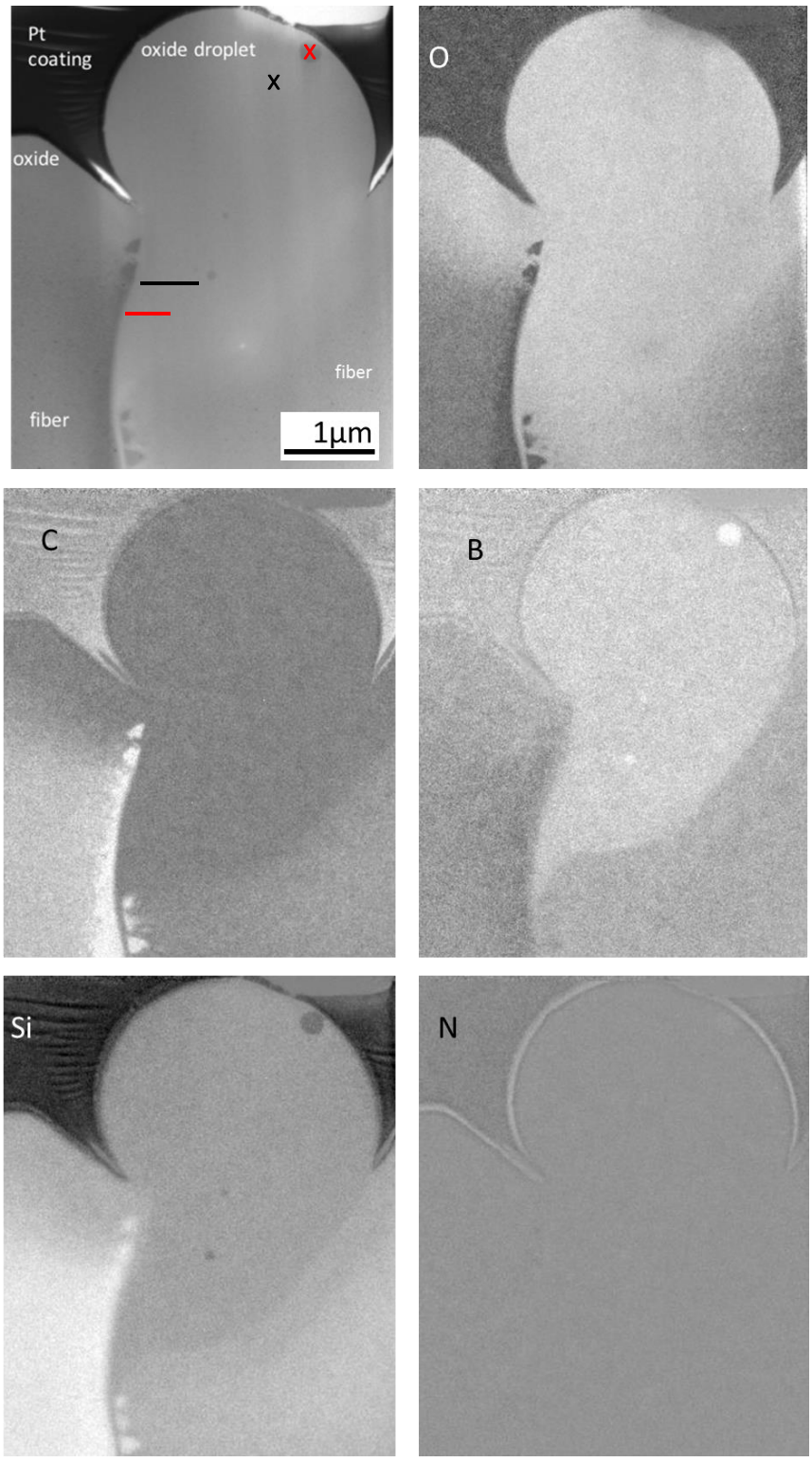

Figure 72. Cross-section of an oxide droplet from a CMC oxidized in wet O_2 at 800°C for 100h with imaged with bright-field TEM (top left) and EF-TEM maps.

From these EF-TEM maps, it was seen that there was a distinct compositional difference between the oxide droplet and the oxide that formed on the surface of the SiC fibers. The white signal of the boron map was only present in and directly below the oxide droplet, indicating that the droplet is a borosilicate glass. The Si and O signals (Figure 72, bottom left and top right, respectively) show that a Si-rich oxide formed on the top of the fibers. These two distinct oxide compositions indicated that there was minimal mixing of the oxides after formation.

Compositional analyses of the droplet were conducted with Electron Energy Loss Spectroscopy (EELS) (Table 20) due to difficulties quantifying B with EDS.

Table 20. EELS Compositional Analyses in the B-Rich Oxide Droplet

EELS Analysis	Wt% B_2O_3	Wt% SiO_2
Line average (78 points) (black line below droplet in Figure 72)	22	78
Line average (18 points) (red line below droplet in Figure 72)	42	58
Point, top of droplet (black x in Figure 72)	11	89
Point, dark spot (red x in Figure 72)	28	72

The first three analyses in Table 20 came from locations that had the same Si and B intensities in the corresponding EF-TEM maps. Although the EF-TEM maps are qualitative, the brightness of each map correlates with the relative amount of the element present. It was therefore expected that the amount of B_2O_3 would be consistent in each analysis. However, the compositions ranged from 11 to 42 wt% B_2O_3 and the fourth analysis in the bright spot of the B-map showed only 28 wt% B_2O_3. The EELS spectra corresponding to these analyses are given in Appendix F.

Another oxide droplet was imaged in cross-section with TEM and corresponding EF-TEM maps from a CMC oxidized in wet O_2 at 1300°C for 100h. This droplet was damaged during FIB sample thinning, creating holes in the droplet, and the substrate is not visible in the images. Figure 73 shows a schematic of the oxide droplet, with the red square outlining the location of the high-magnification image and EF-TEM maps shown in Figure 74.

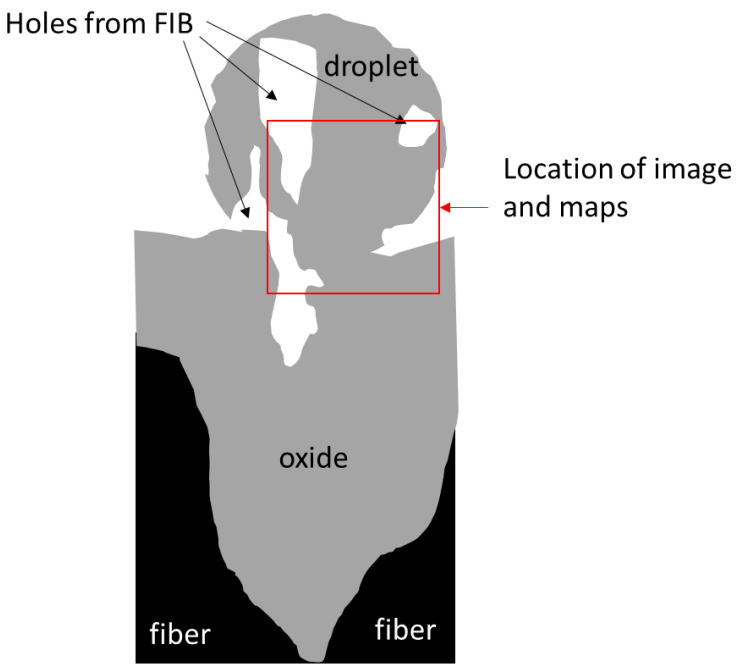

Figure 73. Schematic diagram of the oxide droplet on a CMC oxidized at 1300°C for 100h in wet O_2.

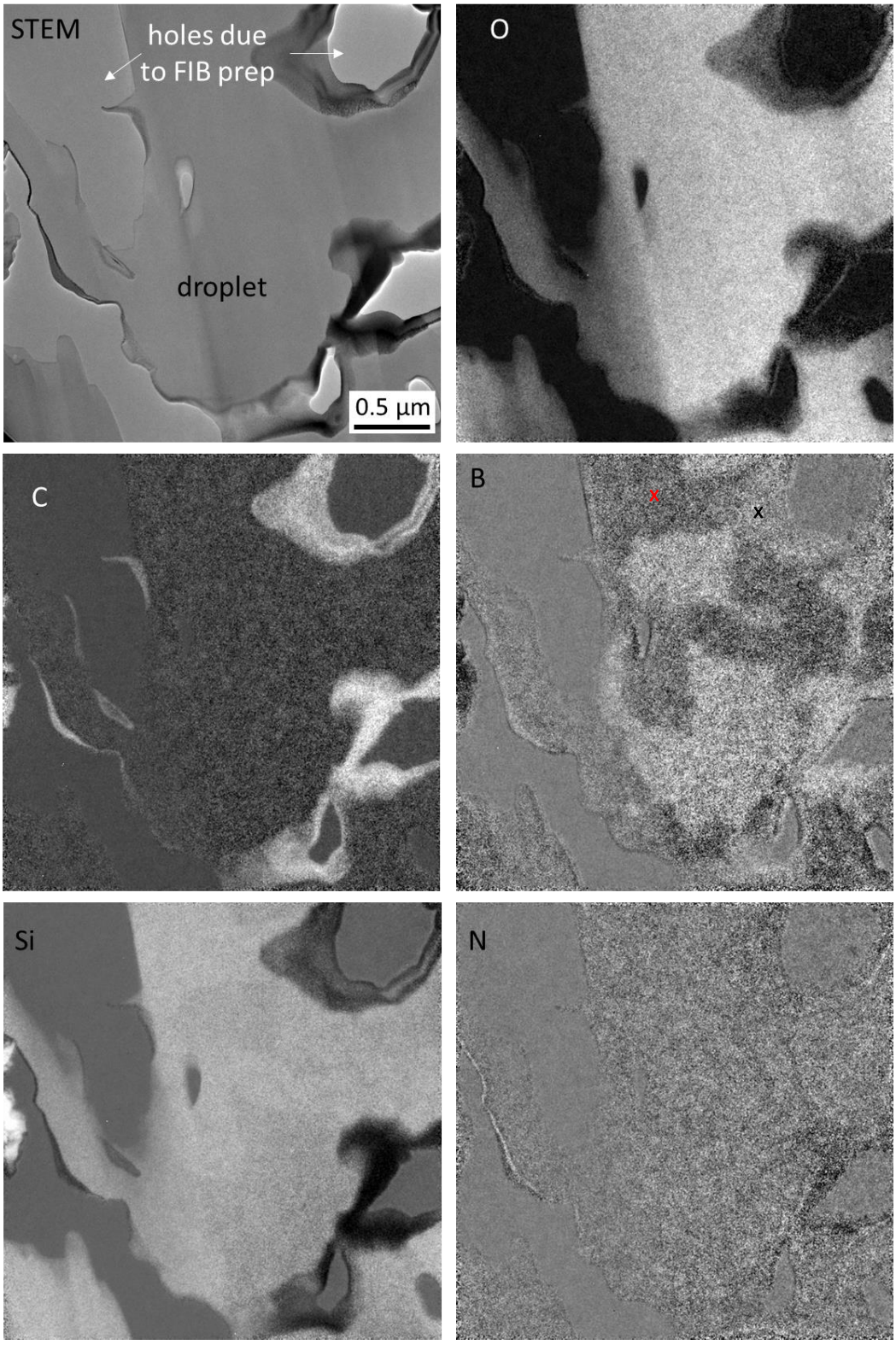

Figure 74. Oxide droplet (no substrate) from a CMC oxidized in wet O_2 at 1300°C for 100h with TEM (top left) and EF-TEM maps.

It was expected from the SEM/EDS analysis of oxide droplets after 100h oxidation at high temperatures (1200 and 1300°C) that the all boron would have volatilized from the oxide, according to Reactions 14-17 (similar to Figure 53). However, from the Si- and B-maps in Figure 74 it can be seen that boron still exists in the oxide but the droplet composition is not uniform. There are areas that are Si-rich (Figure 74, bottom left) that correspond with areas of B-depletion (Figure 74, middle right). This could be due to partial volatilization of B_2O_3 from the borosilicate droplet. However, EELS point analyses in the B-rich and B-depleted regions (given by the black and red x's, respectively) yielded similar compositions (20 wt% B_2O_3 in the B-rich and 13 wt% B_2O_3 in the B-depleted). The EELS spectra corresponding to these analyses are given in Appendix F.

These compositions are within the same range as the droplet from the 800°C exposure (Table 20. EELS Compositional Analyses in the B-Rich Oxide Droplet), which is inconsistent with the expectation for B_2O_3 volatilization. These inconsistencies were likely due to the EELS quantification technique, which will be discussed in the following section in detail.

In addition to forming oxide droplets, oxidation of the BN interphase near the surface caused increased product gases to form, similar to the effect on the oxide from the B-containing regions in the matrix material. A difference from the matrix material oxide, however, is that the pores in the CMC oxides formed directly above noticeable sources of B (the BN interphase). Figure 75 shows pores trapped in the oxide on the exposed face of a CMC oxidized in wet O_2 for 100h at 1300°C. As will be discussed below, the BN interphase remains surrounded by glass. The BN surrounded by glass was also observed in CMCs oxidized in dry O_2 (Figure 75).

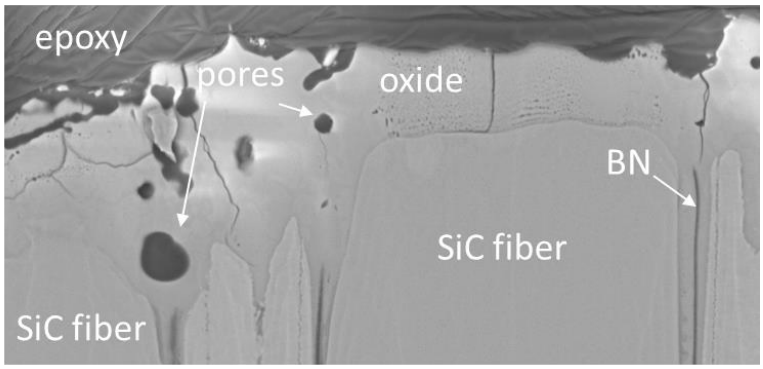

Figure 75. Pores in the oxide directly above the BN interphase regions in a CMC oxidized in wet O_2 at 1300°C for 100h. Length scale omitted intentionally due to RR IP.

5.2.2.3.2. Oxidation Near SiC Fiber Intersection Points

In addition to oxidation along SiC/BN interfaces, oxidation near fiber intersection points was also of interest. In the as-received CMCs, areas of greater BN thickness were observed adjacent to these fiber intersection points, as shown in Figure 76. These areas were of interest due to observations of increased SiC oxidation at these locations by Ogbuji,[51] as will be discussed in the following section.

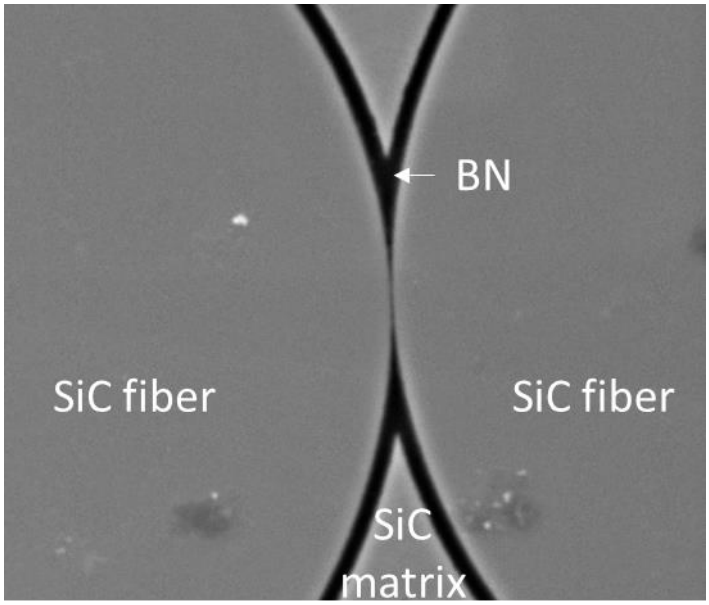

Figure 76. SEM image of a fiber intersection point in the as-received CMC material, showing increased BN thickness adjacent to the intersection (arrow). Length scale omitted intentionally due to RR IP.

A TEM cross-section of two intersecting fibers in a CMC after oxidation in wet O_2 at 1300°C for 100 hours is shown in Figure 77. There is a large amount of oxide between the fiber intersection point and the tip of the BN interphase. This large area of oxide corresponded to the area of greater BN thickness prior to oxidation. This phenomenon was also observed after oxidation in dry O_2.

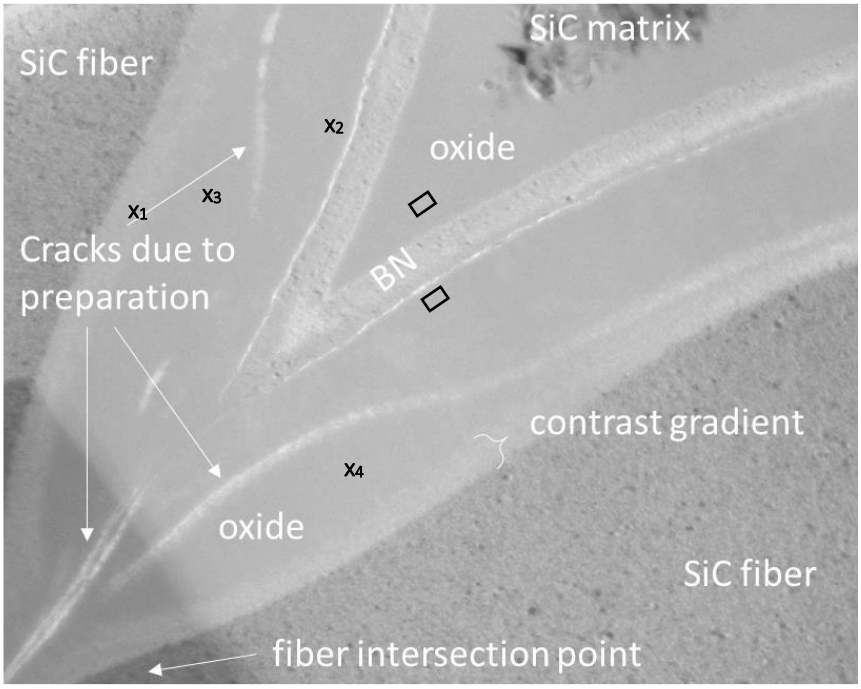

Figure 77. TEM image of a CMC after oxidation in wet O_2, 1300°C for 100h showing increased oxidation near fiber intersection point. Length scale omitted intentionally due to RR IP.

This TEM foil was oriented approximately parallel to the exposed CMC surface and was taken ~10 µm below the exposed face. Quantification of EELS point analyses in the oxide (corresponding to the black x's and squares in Figure 77) resulted in B_2O_3 contents in the range of 13-31 wt% B_2O_3. EELS spectra corresponding to these point analyses are given in Appendix F. Cracks in the oxide appear bright in the TEM image because they are the thinnest areas of the foil. The cracks were assumed to be due to foil preparation and will not be considered further in the analysis of the micrograph. This micrograph shows the BN interphase

surrounded by oxide on both sides. The contrast gradient along the edge of the oxide, adjacent to each fiber, was likely due to the thickness of the TEM foil and the 3D architecture of the fibers in the CMC. The oxide thickness between the SiC fiber and the BN interphase is greater than the oxide thickness between the BN interphase and the SiC matrix, again indicating preferential fiber oxidation over matrix oxidation.

To further characterize the area of increased fiber oxidation (or fiber recession) near the fiber intersection points, the oxide formed on a CMC in wet O_2 at 1200°C for 50 hours was chemically removed by a 1:4 HF:H_2O solution during a 16.5 hour digestion (Figure 78).

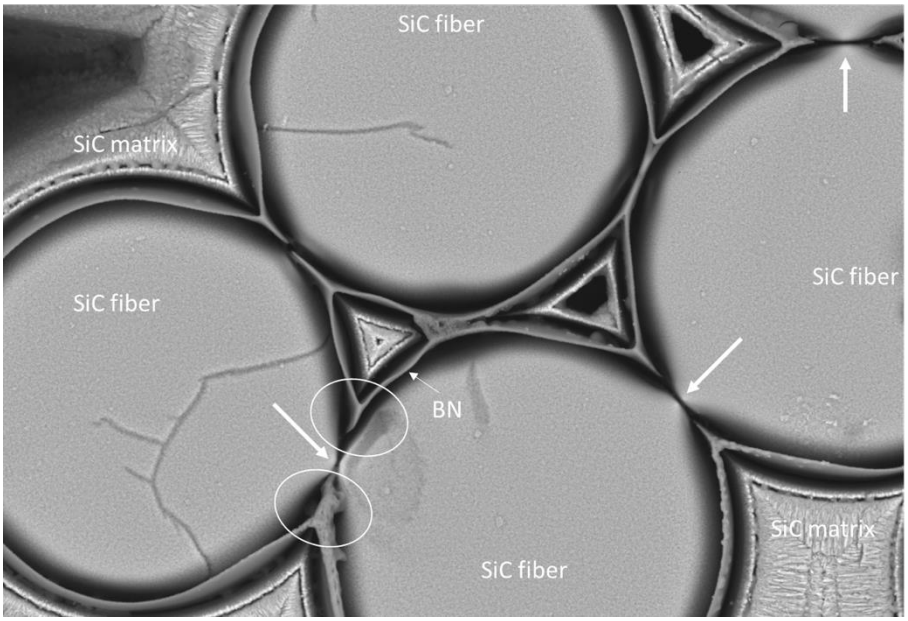

Figure 78. BSE-SEM image of fiber intersection points (arrows) in a CMC after oxidation in wet O_2, 1200°C for 50h with the oxide chemically removed, showing increased SiC fiber recession (circles) near intersection points. Length scale omitted intentionally due to RR IP.

Cracks due to surface grinding prior to oxidation are observed in several fibers. These cracks did not affect the oxidation of the CMC. With the oxide removed, thin, pointed BN films that surround the perimeter of the fibers were observed, indicating that some BN interphase remained surrounded by oxide, as previously observed in cross-sections. The intact fiber intersection points were also observed (arrows, Figure 78) adjacent to areas of greater fiber recession

(circles). The circles show explicit examples of greater fiber recession local to areas where thicker BN interphases were present prior to oxidation. Other examples can be seen adjacent to other fiber intersection points in Figure 78. Implications of the increased oxidation near the fiber intersection points will be discussed further in a following section.

5.2.2.3.3. Oxide Thickness over the BN Interphase

Oxide thicknesses over the BN interphase were measured in the select number of CMCs that were ion-polished, covering a wide range of oxidation conditions. These data are critical, since the external oxide presumably protects the underlying BN interphase. These thicknesses are defined by the distance "A" in Figure 84.

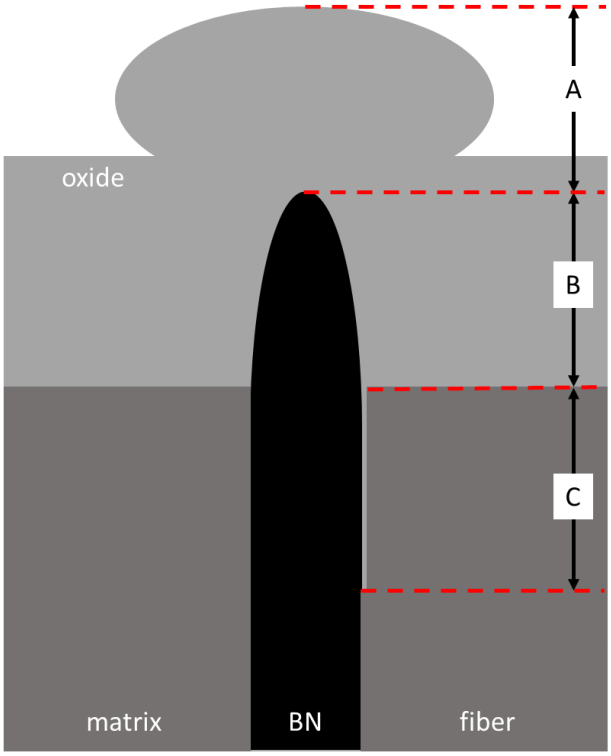

Figure 79. A schematic of a CMC in cross-section after oxidation showing the external oxide thickness (A) and internal oxidation (B + C).

Table 21 shows the oxide thicknesses above the remaining BN interphase. The measured oxide thickness above the BN interphase is extremely variable since oxide droplets are observed in some cases but not in others.

Table 21. Average oxide thicknesses above BN (region "A") from ion-polished CMC cross-sections.

Environment	Temperature (°C)	Time (h)	No. Coupons	No. Measurements	Average Oxide Thickness above BN (μm)
Dry O_2	800	1	1	8	0.7 ± 0.7
		100	1	12	1.8 ± 0.5
	1200	50	1	5	3 ± 2
		100	1	3	1.3 ± 0.5
	1300	1	1	2	0.84 ± 0.02
		100	1	7	5 ± 2
Wet O_2	800	1	1	1	3.8
		100	1	4	4.0 ± 0.8
	1200	100	1	5	10 ± 3
	1300	1	1	10	0.8 ± 0.2
		100	1	6	8 ± 4

These data show that there were minimal trends observed with time, temperature, and environment. In both dry and wet O_2, the average oxide thicknesses were statistically different between 1h and 100h only at 1300°C. However, there was an apparent difference between dry and wet O_2 for 100h at both 800 and 1200°C. These minimal trends could not be used to determine oxidation kinetic data and indicate that the CMCs had a high oxidation resistance at all conditions. However, a limited number of ion-polished samples were available for these measurements.

5.2.2.3.4. Porosity Pipe Oxidation

Low-magnification SEM images and corresponding EDS maps of CMC cross-sections were used to measure the average oxygen ingress lengths along fiber tows that intersected the exposed CMC face (Figure 70). It will be shown, however, that the oxygen ingress lengths that were observed and measured were due to oxidation along porosity pipes in the fiber tows, not

due to BN interphase oxidation. BN interphase oxidation was characterized in cross-section near the exposed face.

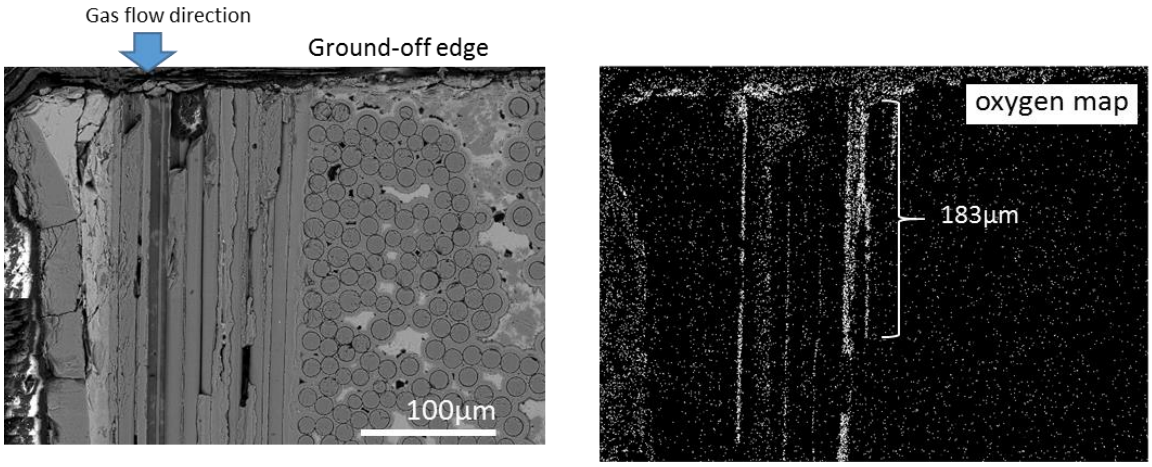

Figure 80. SEM image and corresponding oxygen EDS map of a CMC cross-section after oxidation in dry O_2 at 1300°C for 100h.

The oxygen ingress lengths were measured from the oxygen EDS maps and an average was calculated for each cross-sectioned CMC. There were no trends in the average oxygen ingress lengths with variations in time, temperature, or environment, nor was there repeatability between tests conducted at the same conditions (Table 22).

Table 22. Average oxygen ingress lengths for all characterized oxidized CMC coupon halves

Temperature (°C)	Oxidizing Environment	Time (h)	Average Oxygen Ingress Lengths (μm)	# Tows, # Tows w/ Oxygen, # Measurements
800	Dry O_2	100	390 ± 340 170 ± 140	10, 7, 21 9, 8, 19
		50	40 ± 40 130 ± 110	9, 8, 26 9, 7, 22
		1	70 ± 80	9, 3, 3
	Wet O_2	100	180 ± 190	9, 9, 53
		50	230 ± 190	9, 8, 29
		1	150 ± 110	10, 7, 29
1200	Dry O_2	100	260 ± 310 130 ± 140	12, 10, 20 11, 9, 24
		50	150 ± 220	8, 5, 9
		1	80 ± 40	10, 8, 14
	Wet O_2	100	190 ± 130	4, 4, 13
		50	320 ± 270	11, 11, 34
		1	120 ± 110	9, 9, 32
1300	Dry O_2	100	100 ± 90 280 ± 390	8, 4, 9 6, 6, 15
		50	270 ± 100	7, 3, 6
		1	80 ± 60	10, 3, 6
	Wet O_2	100	120 ± 60	11, 10, 24
		50	100 ± 120	4, 4, 33
		1	350 ± 550	9, 5, 22

After further examination of the cross-sections, it was determined that the detected oxide formed along connected pores inside fiber tows—these were given the term porosity pipes. Porosity pipes exist in nearly every fiber tow in the CMCs and are formed during processing when the slurry and melted matrix materials do not infiltrate the spaces between some fibers in the tows, as shown in Figure 82. SEM images of the as-received materials showed the presence of these porosity pipes (Figure 56).

Two sequential cross-sections of an oxidized CMC were examined to understand the oxidation behavior in the porosity pipes. First, the CMC surface (with the oxide mechanically

removed by grinding and polishing with SiC and diamond grit) was characterized with SEM and EDS. Then, a parallel surface, 80 µm below the surface was characterized (Figure 81).

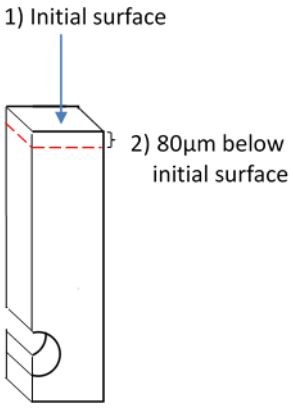

Figure 81. Oxidized CMC cross-sections analyzed for porosity pipe oxidation.

At the initial surface (with the oxide mechanically removed), porosity pipes were observed with SEM after oxidation. The corresponding oxygen EDS map (Figure 82, right) showed oxidation of the CVI SiC layer that was in contact with the porosity pipes. The BN interphase regions adjacent to the oxidized CVI SiC layers were not oxidized.

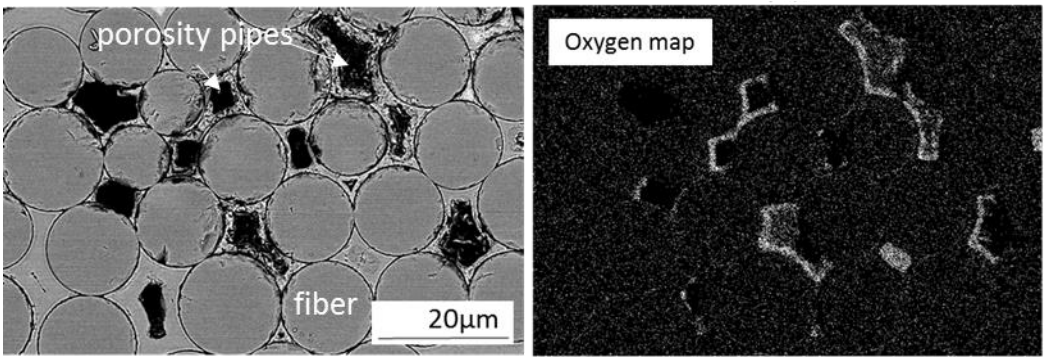

Figure 82. Fiber tow at the initial CMC surface after oxidation in dry O_2, 1200°C, for 100h (with the oxide removed) showing porosity pipes in SEM (left) with oxidized CVI SiC seen with EDS (right).

After an additional 80 µm was removed parallel to the initial exposed surface, the same fiber tow was examined with SEM and EDS (Figure 83). The shape of the porosity pipes was changed slightly, but it is evident that these oxidized paths are the same porosity pipes that existed 80 µm

above. Again, the CVI SiC layers in contact with the porosity pipes were oxidized, as seen with the oxygen EDS map, while the BN interphase remained intact.

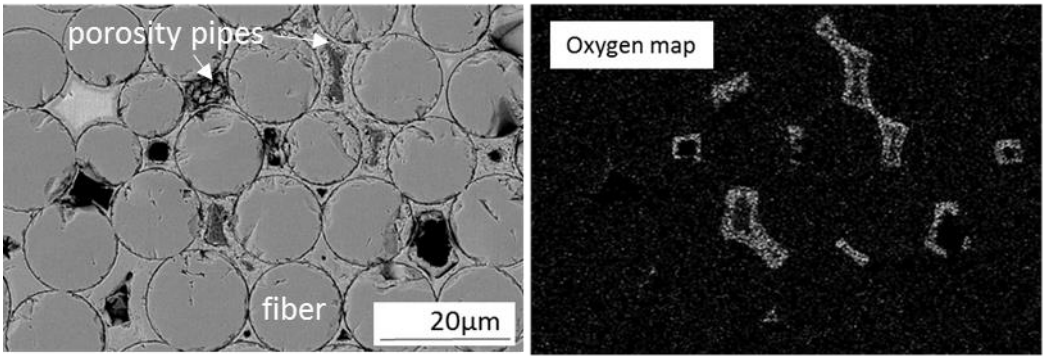

Figure 83. Same fiber tow (Figure 82) 80 µm below the initial surface after oxidation in dry O_2, 1200°C, for 100h showing porosity pipes in SEM (left) with oxdizied CVI SiC seen with EDS (right).

Oxidation of the CVI SiC layer along the porosity pipes indicated that the porosity pipes must be connected to the exposed CMC surface. These porosity pipes oxidized and extended down the length of the CMC as observed in cross-section. The oxygen ingress lengths measured were the lengths of the porosity pipes that ended either when the porosity pipe was pinched closed, or when it continued out of the plane of the cross-section. The average oxygen ingress lengths along the porosity pipes can therefore not be used to determine the rate of BN oxidation in the interior of the CMC, but do prove that fast paths for oxygen transport into the interior of the composites. Contrary to expectation, CMC oxidation kinetics could not be determined from the oxygen ingress results along the BN interphase because there were very few instances where this was observed, as described below.

5.2.2.3.2. BN Oxidation in CMCs

At the exposed CMC face, it was observed that oxide droplets initially formed over regions where BN intersected the surface (Figure 79, left), but once the sealing oxide was thick (~0.5 µm or larger), SiC preferentially oxidized, leaving remaining BN surrounded by the glass (Figure 79, right).

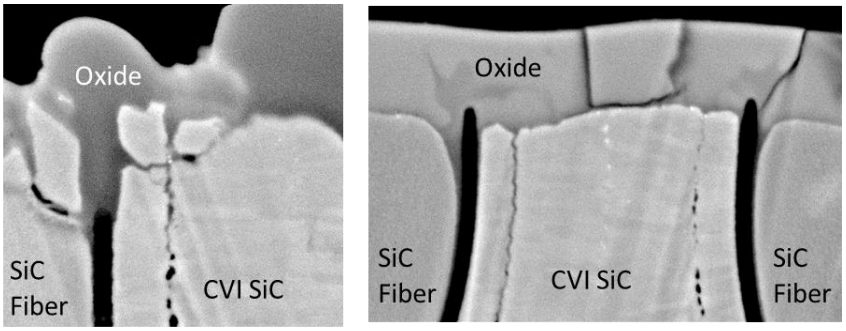

Figure 84. Unoxidized BN (dark phase) surrounded by glass after dry O_2 oxidation at 800°C for 100h (left) and 1200°C for 50h (right). Length scale omitted intentionally due to RR IP.

Remaining BN surrounded by glass was also observed with TEM. Figure 85 shows an example of unoxidized BN surrounded by oxide 2 μm below the oxidized surface, as determined by the EF-TEM maps. BN remained surrounded by oxide after all oxidizing conditions (examples in Figure 84 and Figure 85), so this result could not be used to determine CMC BN oxidation kinetic data.

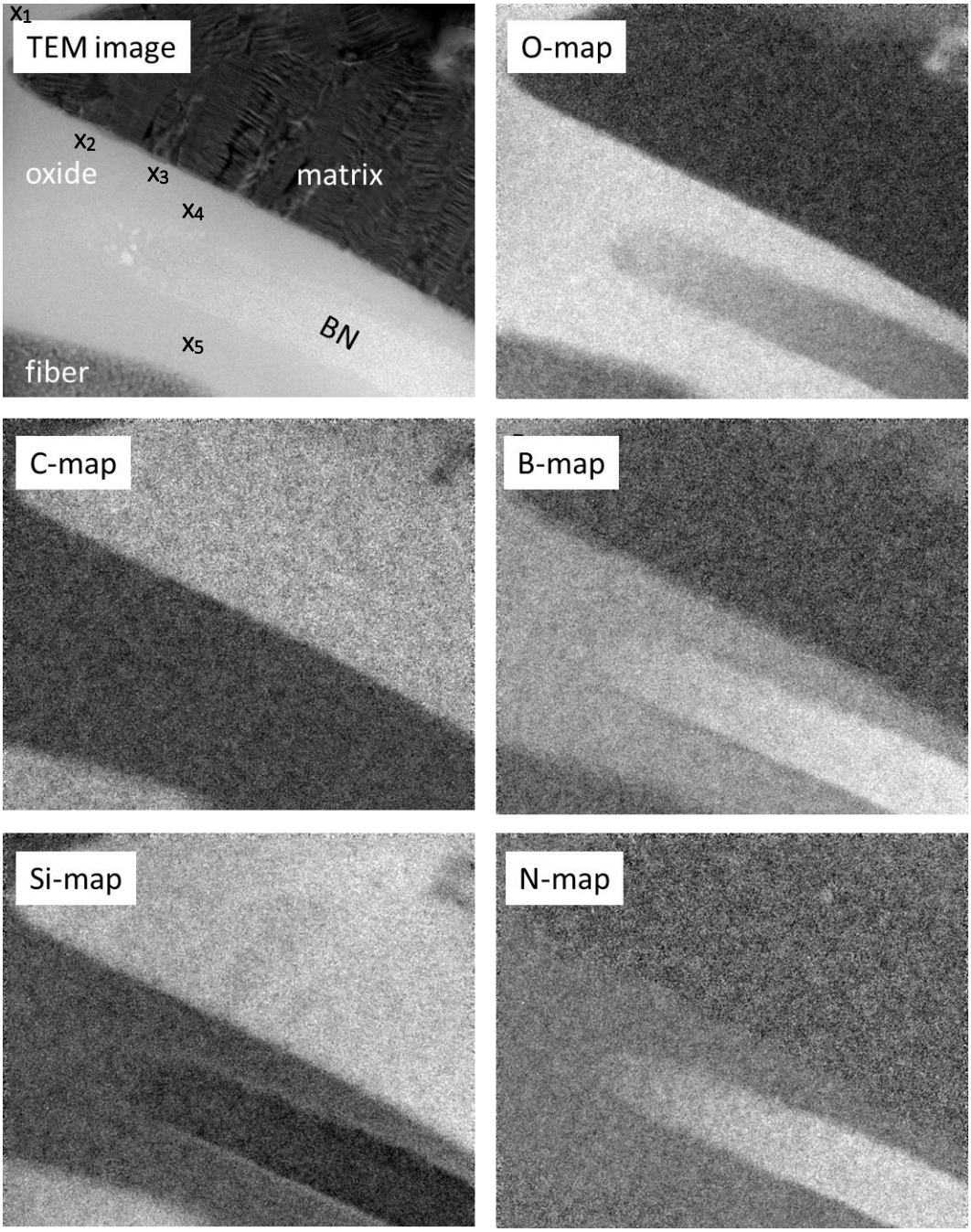

Figure 85. TEM image (top left) and corresponding EF-TEM maps of unoxidized BN surrounded by oxide 2 µm below the surface after dry O_2 oxidation at 800°C for 100h. Length scale omitted intentionally due to RR IP.

Quantification of EELS point analyses in the oxide (given by the black x's in Figure 85) resulted in B_2O_3 contents in the range of 8-13 wt% B_2O_3. The EELS spectra corresponding to these analyses are in Appendix F.

5.2.2.3.3. Oxidation Along the SiC/BN Interfaces

Instances of BN/SiC interface oxidation occurred in less than 8% of the CMC cross-sections characterized by SEM (27 CMC coupons were characterized in cross-section). Only one TEM specimen (~135 µm below the surface) of the five prepared by FIB (ranging 33-280 µm below the surface) showed evidence of oxidation along the fiber/BN interface (Figure 86). Note the oxide layer observed here is significantly thicker than that observed in the EF-TEM oxygen map in the as-received composite shown in Figure 52. The composition of this oxide layer was not discernable with EELS due to the electron beam probe size limitations. No oxide layer was observed at the BN/matrix interface. This indicates preferential SiC fiber oxidation over SiC matrix. Potential reasons for preferential fiber oxidation will be a topic of the discussion section below.

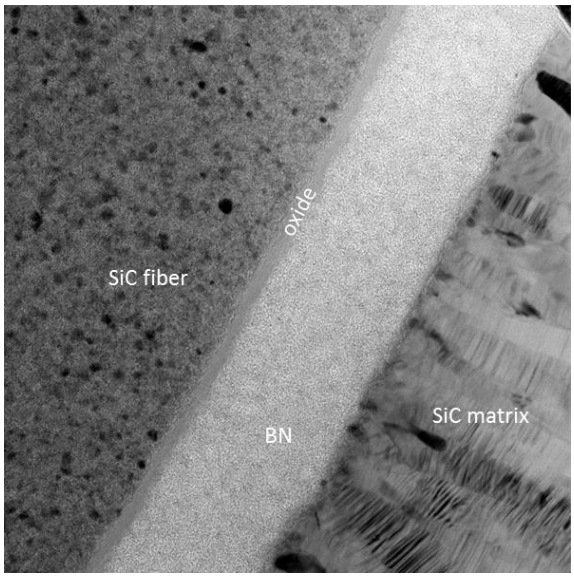

Figure 86. TEM image showing preferential oxidation along the fiber/interphase interface in a CMC oxidized in wet O_2 at 800°C for 100h. Length scale omitted intentionally due to RR IP.

Preferential SiC oxidation occurred below the exposed CMC surfaces, due to the reduced Po_2. However, at a certain point below the sealed CMC surface, oxidation progresses inward to

the composite parallel to the SiC/BN interface, rather than expanding outward into the SiC (labeled as “interphase/interface oxide” in Figure 87).

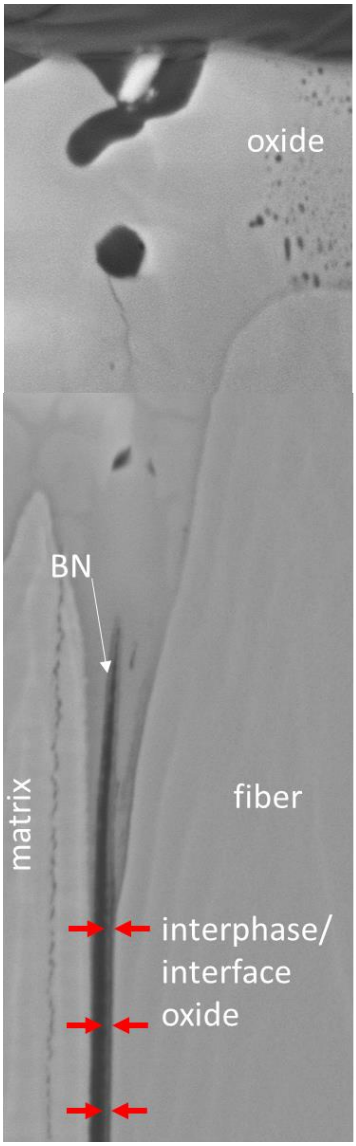

Figure 87. Interphase/interface oxide along the fiber/BN interface below the surface oxide.

This oxide will be referred to as “interphase/interface” oxide meaning it is observed at the SiC/BN interface. This oxide was not observed to grow into either the SiC fiber or the BN interphase, effectively providing inert walls allowing further oxidation into the composite. Figure 88 (top) and Figure 90 show other examples of the oxidation along the BN/fiber interface. Figure 88 (top) comes from ~30 µm below the exposed surface while Figure 86 is from ~135 µm below

the surface. The interphase/interface oxide was observed along only 9 BN/fiber interfaces (from 73 imaged interfaces in 11 ion-polished coupons). The interphase/interface oxide thicknesses were independent of oxidation conditions (time, temperature, or environment).

Further into one CMC (up to 30 µm from the exposed surface) oxidized at 1200°C for 100h in dry O_2, evidence of oxidation along the BN/SiC interfaces was observed with SEM (Figure 88).

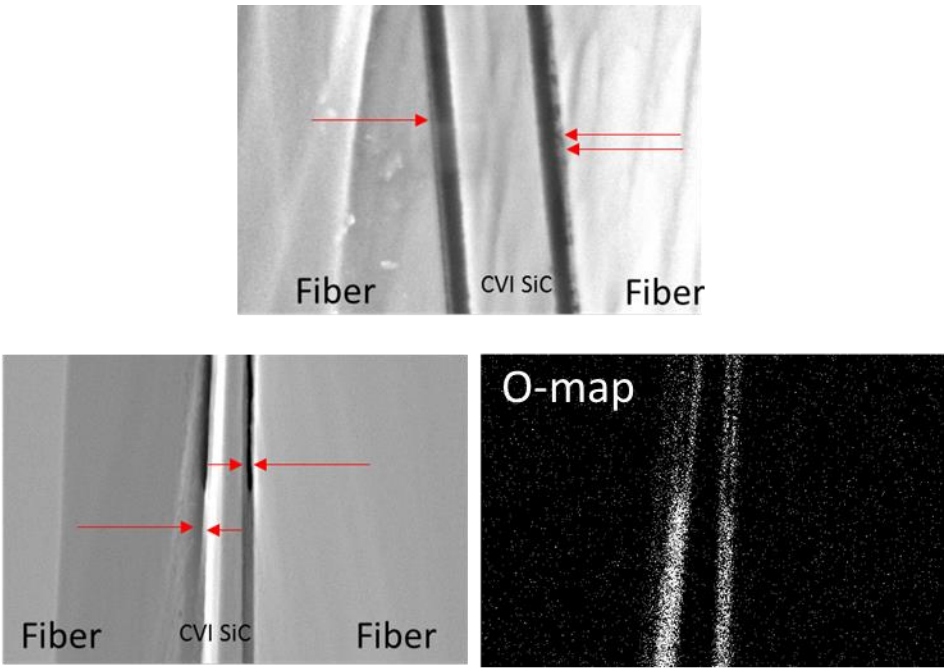

Figure 88. Oxidation at BN/SiC interfaces (arrows) in CMCs oxidized at 1200°C for 100h in dry O_2 (top) and wet O_2 (bottom) with a corresponding oxygen EDS map. Length scale omitted intentionally due to RR IP. Exposed coupon faces are oriented toward the top of images.

The composition of the oxide was not discernable with the EDS due to the electron beam probe size limitations of the SEM. Oxidation was observed along both BN/fiber and BN/matrix interfaces with SEM and EDS (Figure 88, bottom). It was also observed in some cases that the oxide was non-uniform in composition (Figure 88, top, double arrow) based on phase contrast in BSE imaging mode. Two hypotheses for oxidation mechanisms along the SiC/BN interphase are presented in the discussion section below.

5.2.3. Stressed Permeability Testing

CMCs tested with TGA (*Sections 5.2.2.2. Exposed Face Sealing* and *5.2.2.3. Cross-Sectional Characterization*) were highly oxidation resistant and oxidation kinetics could not be determined. Prior work by Morscher, et al.,[60] indicated that oxidizing CMCs under load would increase the amount of oxidation and potentially allow for the determination of oxidation rates. However, this was a stress rupture study, so intermediate extents of oxidation were not determined, preventing kinetic analysis. To elucidate the effect of stress on CMC oxidation behavior, stressed permeability tests were conducted on eleven slotted CMC coupons (shown in Figure 89) at Southern Research (Birmingham, AL) and characterized at UVa. This is the first known study to explore stressed oxidation kinetics in CMCs. The CMC coupons used for this study were manufactured by RR-HTC and had similar starting microstructures to the CMC coupons tested with TGA. However, no CVD SiC seal coat was applied to the exterior of the stressed permeability coupons. The coupons were machined to shape by RR-HTC.

Permeability testing procedures and parameters can be found in Appendix G, provided by James Hawbaker, a collaborator at Southern Research. Several parameters were varied throughout the stressed permeability testing: starting coupon permeability (measured during stressed permeability testing at Southern Research, Appendix G), the pre-exposure stress (used to induce CMC cracking at room temperature), and the exposure time in the stressed state. Normalized parameters for the eleven tested coupons are given in Table 23.

All permeability tests were conducted at 800°C in lab air and were pre-stressed to induce cracking before stressed permeability testing. Stresses normalized to the maximum load are reported here, with a value of 1 indicating the maximum load applied. Normalized Pre-Stresses (NPS) of 1 or 0.8 were used and a Normalized Exposure Stress (NES) of 0.8 was used for all

tests. A pressure gradient was established across the coupon with 2 atm air used on the front of the coupon (2 slots) and 1 atm air on the back side (1 slot) (Figure 89). The starting permeabilities were normalized to the coupon with the highest permeability in Table 23.

Table 23. Normalized initial coupon parameters and exposure conditions for 11 stressed permeability CMC tests

Coupon No.	Normalized Starting Permeability	Normalized Pre-Exposure Stress	Exposure time at NES of 0.8 (h)
1	0.70	0.8	1
2	0.83	0.8	8
3	0.92	1	8
4	0.72	0.8	20
5	0.80	0.8	20
6	0.89	1	20
7	0.82	1	53.2
8	0.81	0.8	100
9	0.91	0.8	100
10	0.91	1	100
11	1	1	8 + 92

Of primary importance to this dissertation were the results from SEM and EDS characterization used to elucidate the oxidation behavior during the stressed permeability testing. This characterization was performed on the CMC coupons at UVa after stressed permeability testing at Southern Research. Three cross-sections from the stressed permeability coupons (dashed lines in Figure 89) were characterized with SEM and EDS to determine extent of oxidation.

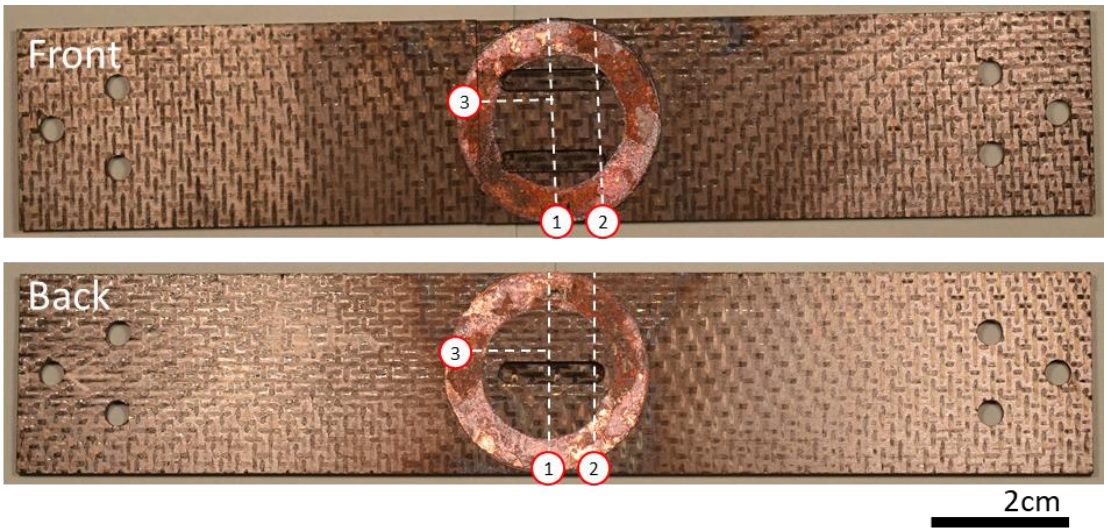

Figure 89. Permeability/stressed-oxidation coupon showing locations of three cross-sections characterized with SEM and EDS.

Cross-section 1 was made through the center of the slots. A schematic drawing of this cross-section with oxygen permeability path is shown in Figure 90. This in-plane permeability path was formed due to the pressurized air that was applied to the two slots in the center of the front face of the coupon. The air then flowed in the in-plane direction (as identified by Southern Research) and exited the specimen through the one slot on the reverse side. Cross-section 2 was also made through the slots, near the slot edge, where the stress concentration was highest.

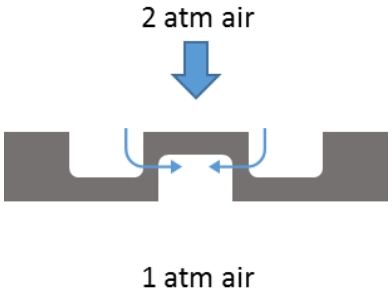

Figure 90. Schematic drawing of Cross-sections 1 and 2 through a permeability/stressed-oxidation coupon showing oxygen permeability path. Load was applied in the direction in and out of the page.

Cross-section 3 was made between the 2-atm (front) and 1-atm (back) slots, exposing an area that experience forced airflow. Results from Cross-section 3 (Figure 91) were the most relevant and are reported.

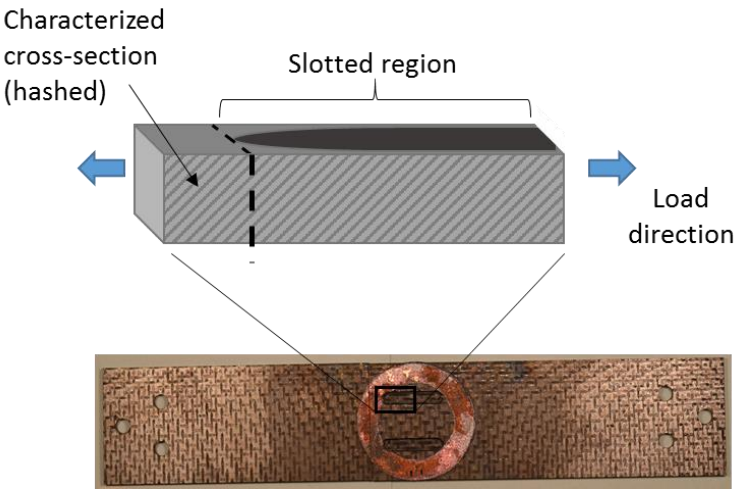

Figure 91. Schematic drawing of cross-section 3 in a permeability/stress-oxidation CMC showing the slotted and non-slotted regions (top) and its location in the composite (bottom). Air flow with respect to the schematic was out of the page.

Several microstructural features were observed in the CMC cross-sections after test. Small cracks in the CVI SiC layer surrounding the BN layer were observed (red lines, Figure 92). These cracks terminated at the BN/SiC interfaces and the CVI/matrix interfaces.

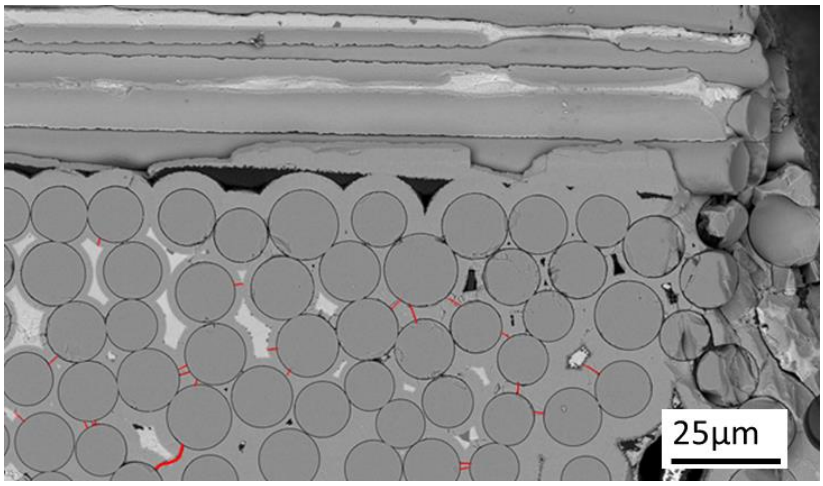

Figure 92. Cracks in the CVI SiC layer (indicated by red lines) in a cross-section of a CMC (normalized permeability of 0.70) exposed for 1h at a normalized exposure stress of 0.8 in the 800°C permeability/stressed-oxidation testing in air. From Cross-section 1.

In addition, large cracks penetrated the fiber tows and extended into the matrix. In five of the six samples that showed matrix cracking, the cracks were oxidized, as determined by EDS

compositional mapping. Figure 93 shows a matrix crack (highlighted in red) and a corresponding oxygen EDS map showing that oxidation followed the crack path.

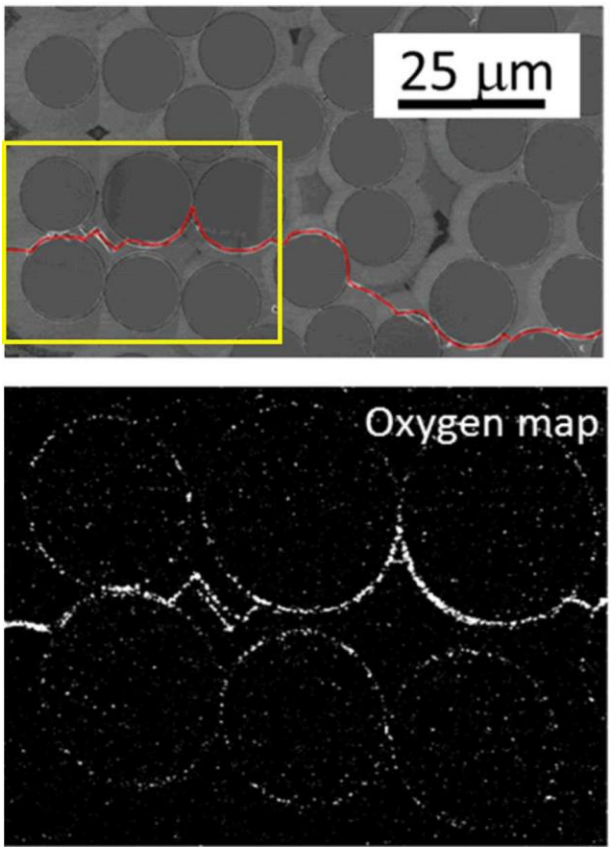

Figure 93. SEM (top) and corresponding oxygen EDS map (bottom) of the oxidized interphase along the matrix crack in a CMC (normalized permeability of 0.72) exposed for 20h at a n of 0.8 in the 800°C permeability/stressed-oxidation testing in air. From Cross-section 3.

The matrix cracks observed were perpendicular to the load direction applied to the CMC during the permeability testing. The cracks in each cross-section were mapped with red lines to show the quantity and location of the cracks. Figure 94 shows an example.

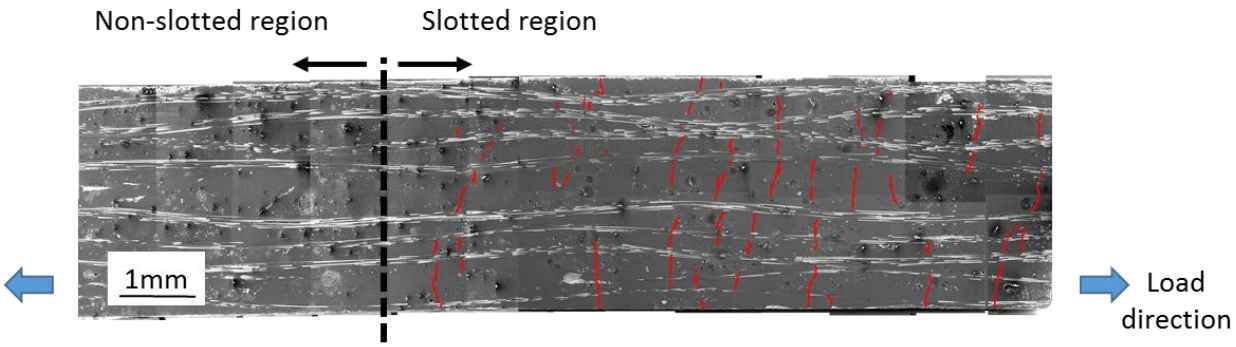

Figure 94. Cross-section of a CMC (normalized permeability of 0.72) pre-stressed to a normalized pre-stress of 0.8 and exposed for 20h at a NES of 0.8 at 800°C during permeability/stressed-oxidation testing in air, showing matrix cracks (red lines) perpendicular to the load direction. From Cross-section 3.

One CMC specimen intended for a 100 hour test failed after 53.2 hours (Figure 95).

Oxidation was observed along the interphase surrounding fibers in the fracture surface (Figure 96).

Figure 95. Stressed permeability coupon no. 7 after failure at 53.2 hours.

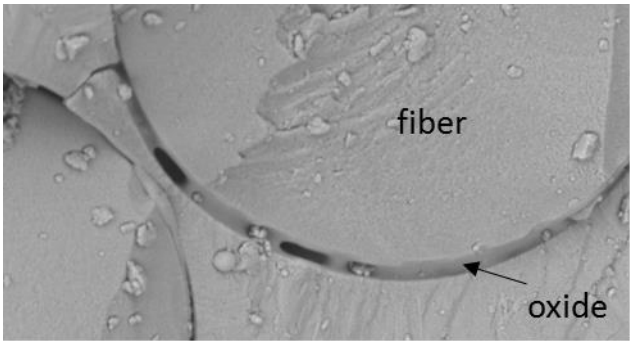

Figure 96. Oxidized interphase surrounding a fiber on the fracture surface of the CMC (normalized permeability of 0.82) that failed after 53.2h of the 800°C permeability/stressed-oxidation testing in air at a normalized exposure stress of 0.8.

In addition to cracks caused by the stressed state of the CMCs during the permeability exposures, large pores (Figure 97) and porosity pipes (similar to Figure 81) were observed in the cross-sections.

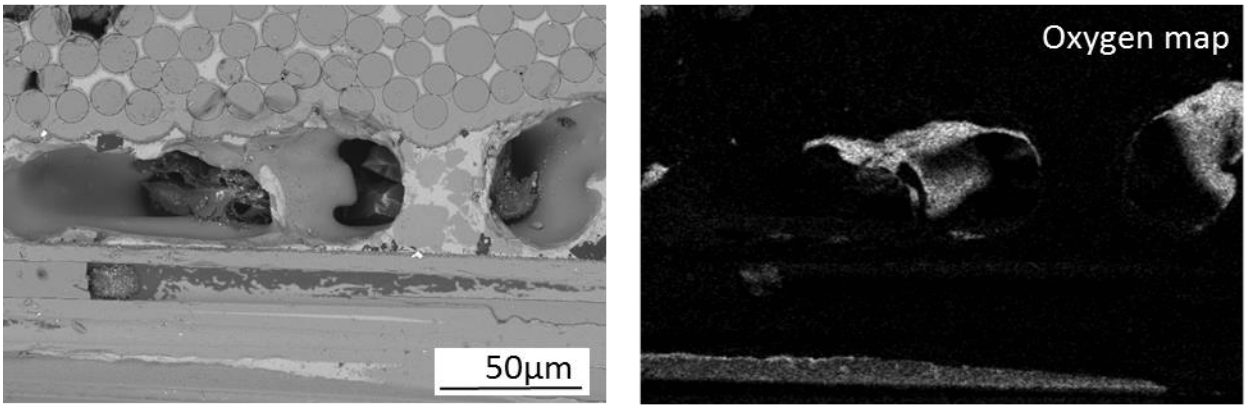

Figure 97. Large pores in the matrix of a CMC (normalized permeability of 0.72) observed in cross-section (left) and the corresponding oxygen EDS map (right) after exposure for 20h at a normalized exposure stress of 0.8, 800°C permeability/stressed-oxidation testing in air. From Cross-section 1.

The large pores and porosity pipes existed in all stressed-oxidation CMC specimens. Ten of the eleven stressed permeability CMCs showed oxidation of large pores in cross-section and seven of eleven showed oxidation of porosity pipes. Table 24 summarizes all of the features that were present (P) and were oxidized (O) in each 800°C stressed permeability CMC specimen tested in air. All specimens were tested at a NES of 0.8 for the exposure duration.

Table 24. Oxidation results determined by SEM for CMCs after 800°C permeability/stressed-oxidation testing in air; P represents the Presence of a feature, O represents the feature was Oxidized

Coupon No.	Normalized Starting Permeability	Exposure time at NES of 0.8 (h)	Normalized Pre-Exposure Stress	CVI SiC cracks	SMI Matrix cracks	Large pores	Porosity Pipes
1	0.70	1	0.8	P		O	O
2	0.83	8	0.8			P	P
3	0.92	8	1			O	P
4	0.72	20	0.8		O	O	O
5	0.80	20	0.8	P	P	O	P
6	0.89	20	1		O	O	O
7	0.82	53.2	1		O	O	O
8	0.81	100	0.8			O	O
9	0.91	100	0.8			O	P
10	0.91	100	1		O	O	O
11	1	8 + 92	1		O	O	O

Cross-sections of CMCs pre-stressed to at NPS of 1 were compared to characterize the number and location of the matrix cracks (Figure 98) as a function of time at temperature. The CMC that failed after 53.2h was not cross-sectioned.

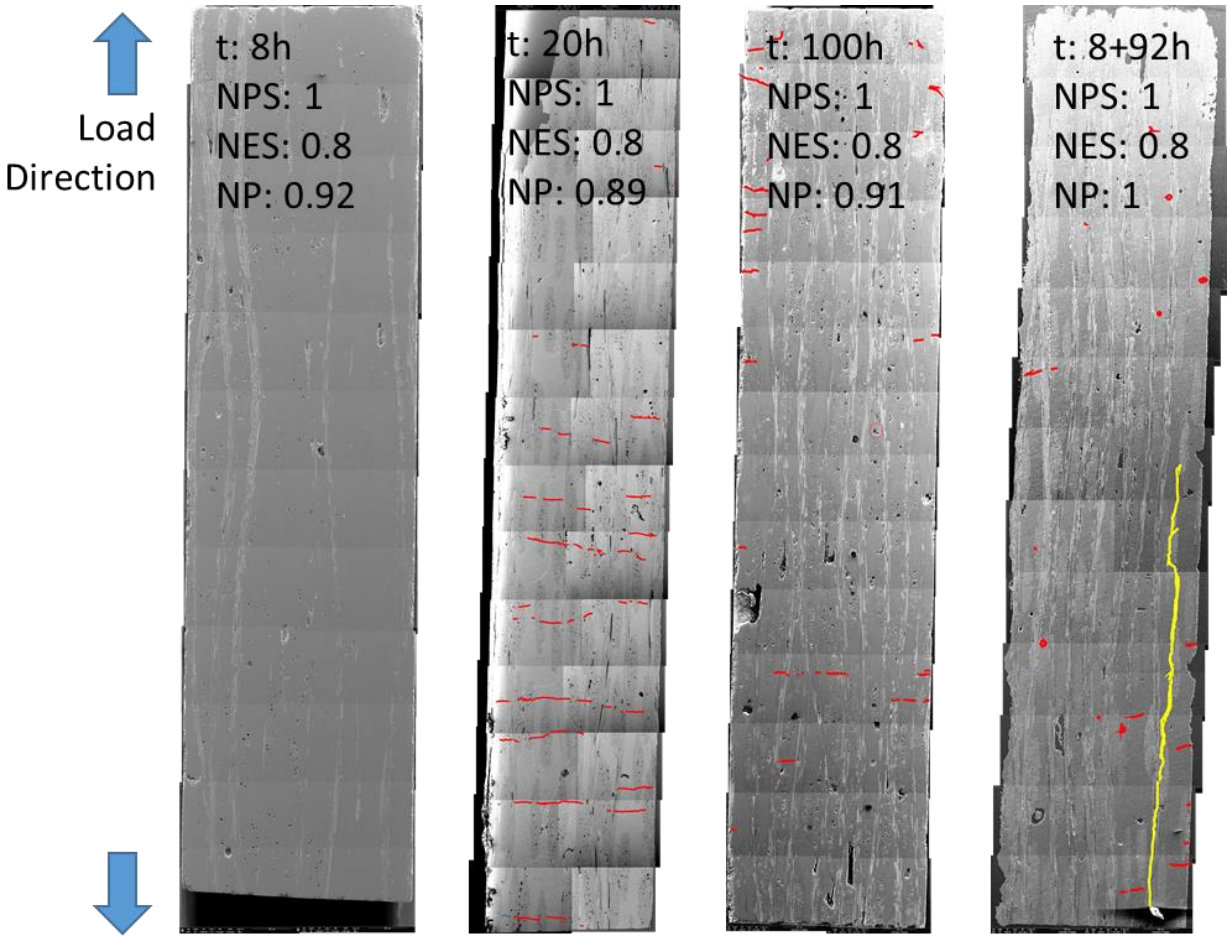

Figure 98. Cross-sections of four CMCs pre-stressed to a normalized pre-stress of 1 and oxidized at 800°C in air at a normalized exposure stress of 0.8 for 8, 20, or 100h with permeability/stressed-oxidation testing. Red lines show matrix cracks, yellow lines show processing damage.

The 8h test had no matrix cracks in this cross-section. The 20h exposure had the most matrix cracks and the cracks spread across the width of the coupon. The 100h exposures primarily had small cracks along the edges of the coupons. There was no obvious trend in location or number of matrix cracks with increasing time.

The oxidized features (large pores, porosity pipes, and matrix cracks) in samples tested at the same conditions were not repeatable. This variation was attributed to the large variation in starting CMC permeabilities (0.70 to 1 Normalized Permeabilities (NP) from the log Darcy Coefficients, ranging 4 orders of magnitude), as will be discussed below. Because there were no

trends observed with increasing time, the results could not be used to determine CMC oxidation kinetic data.

5.3. Discussion

5.3.1. TGA Exposures

This section will begin with a discussion of the external surface oxidation and sealing, followed by a discussion of the internal oxidation. The boundary between external and internal oxidation in the CMC is defined by the BN/B_2O_3 equilibrium Po_2. This can be seen visually in CMC cross-sections as the point where remaining BN is surrounded by oxide. Above this point, external oxidation occurs because the Po_2 is above the BN/B_2O_3 equilibrium value.

5.3.1.1. Exposed Face Sealing

It was observed with SEM that sealing of the BN interphase occurred during oxidation (Figure 61). Sealing due to the oxide droplets and continuous oxides that formed at BN interphase indicated that the exposed BN interphases were protected against further rapid oxidation, preventing major oxidative damage to the BN interphase or SiC fibers. This was unexpected, especially at 800°C, based on the previous CMC oxidation models that existed in the literature.[33; 49; 66] The sealing of the BN interphase is critical for mitigating oxidation-induced degradation of theses RR-HTC CMCs. However, kinetic data related to the sealing rate could not be determined due to the rapid sealing of the BN interphase at all conditions studied.

As discussed in *Chapter 4. Matrix Material Oxidation*, oxide droplets were observed in the SiC matrix materials over the boron containing regions. The droplets formed on CMCs were also found directly above B-containing components (this time on the BN interphase), suggesting the droplets were borosilicate glasses. The borosilicate composition was qualitatively confirmed with EF-TEM compositional mapping that showed a clear B-signal in the cross-section of an

oxide droplet formed at 800°C. The distinct interface between the B-rich oxide and the Si-rich oxide (Figure 72) suggested that these two phases formed independently. This is consistent with the rapid formation of the B-rich oxide droplet, concurrent with the slower oxidation of neighboring SiC fibers and matrix. The rapid formation of droplets on CMCs helped to seal the BN interphase against further oxidation. Morscher, et al. observed that SiO_2-rich borosilicate sealed exposed interphases in mini-composites, significantly reducing further oxidation, however, the composition of the sealing borosilicate was only determined to be "high SiO_2 content glass" by XPS with EDS only showing Si and O signals.[52] There was no B_2O_3-rich oxide observed by Morscher, et al.

5.3.1.1.1 Quantitative Borosilicate Compositional Analysis

The average compositions (with standard deviations) of the thermally grown borosilicates in this work were determined by EELS with TEM (Table 25).

Table 25. Borosilicate compositions as determined from EELS with TEM

Temperature (°C)	Environment	Morphology	Average Wt% B_2O_3	Maximum Wt% B_2O_3	Minimum Wt% B_2O_3	No. Analyses
800	Dry O_2	Below Surface	7 ± 6	13	0	5
800	Wet O_2	Droplet	26 ± 13	42	11	4
1300	Wet O_2	Droplet	16 ± 4	20	13	2
1300	Wet O_2	Below Surface	23 ± 5	31	16	11

The boria content in the oxides ranged from 0 to 42 wt% B_2O_3. Even within one sample that indicated a constant boron composition *qualitatively* with the EF-TEM map (800°C wet O_2 droplet, Figure 72), the *quantitative* analysis of composition using EELS varied by 30 wt% B_2O_3. The variation could be due, in part, to the EELS quantification technique. The quantifications of the EELS analyses are based on background fits for each elemental ionization "edge". The Si $L_{2,3}$-edge (99 eV) is used for EELS quantification of Si instead of the K-edge (1839 eV) that is at

a high energy loss. The Si $L_{2,3}$-edge occurs at lower energy losses than the K-edges used to quantify B (188 eV), C (284 eV), N (401 eV) and O (532 eV). The quantification of Si $L_{2,3}$-edge is especially prone to modulations of the pre-edge background due to (multi-)plasmon excitations. Background fits using the standard 1st or 2nd order log-polynomial, or power law models for EELS quantification do not accurately account for plasmon-induced pre-edge modulations. While it is possible to identify the best fitting model (1st order log-polynomial for the Si $L_{2,3}$-edge) the pre-edge modulations still cause significantly different results depending on the choice of pre-edge and post-edge windows. With access to a standard borosilicate sample with known composition, appropriate windows for pre- and post-edges could be chosen. However, a borosilicate standard was not available when this analysis was conducted. An example of broad Si $L_{2,3}$-edge and B K-edge that led to a poor background fit is shown in Figure 99. Other EELS spectra are given in Appendix F.

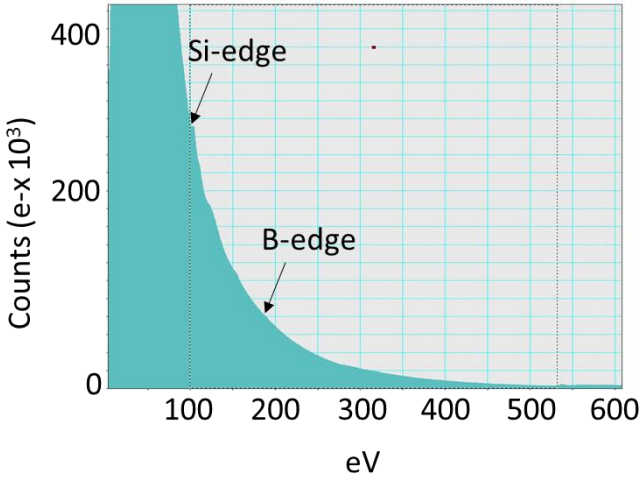

Figure 99. EELS Spectrum from a borosilicate showing a broad Si $L_{2,3}$-edge.

To analyze the impact of these parameters on the quantification results, the boron and silicon contents in an area of 1 µm x 0.3 µm in the oxide from Figure 85 was quantified with EELS using 2 different fits, 2 different edge models (using Hartree-Slater or hydrogenic models for the calculation of ionization-edge cross-sections[91]), and 2 different energy windows for Si

and B. The compositions in this selection ranged from 16-25 wt% B_2O_3. Without a compositional standard, it is impossible to know which combination of fit parameters yields the most accurate results. Due to this complication in the EELS quantification technique for these elements, the EELS data will only be considered qualitative.

5.3.1.1.2. Rapid Sealing Rates

It was hypothesized that the rapid mass gain at the beginning of the TGA data for all exposed CMCs was due to the sealing of BN interphase with the oxide droplets. The total time for the transient mass changes was < 1.2h in all cases, which correlated with the observation that oxide droplets were observed on exposed CMC face after only 1 hour at all three temperatures in wet O_2 and after 1 hour at 1200 and 1300°C in dry O_2. It is therefore likely that the rapid mass gains observed were the result of the formation of the oxide droplets. Although rapid oxidation is not typically considered a beneficial behavior for CMCs, the case of rapidly forming oxide droplets to seal BN interphase prevented further oxidation of the BN interphase and SiC fibers. Protecting these constituents from oxidative degradation is a key factor in extending the thermochemical life of the CMCs.

5.3.1.1.3. Composition of the Crystalline Oxide

There were no B-containing crystalline phases detected with XRD; there are several possible explanations: *i)* the boron atoms could be incorporated into the cristobalite structure, *ii)* the boron could have volatilized from the system according to Reactions 14-17, or *iii)* the boron that initially oxidized could be incorporated in an amorphous oxide phase.

When B_2O_3 is incorporated into the SiO_2 network, it modifies the network structure,[38] making a periodic, crystalline structure unlikely. It is then unlikely that boron atoms are incorporated into cristobalite.

A large amount of the boron in the glass could have volatilized during the oxidation process, as observed in another study.[33] This is consistent with the prediction of B_2O_3 volatility at higher temperatures (Figure 54). However, the compositions of the oxide droplets as determined by EDS (Figure 53) and EELS (Table 20) showed a significant boron content. Therefore, B_2O_3 volatility does not account for the lack of B-containing phases detected with XRD.

It is possible that a majority of the B_2O_3 exists in the amorphous droplet phase. However, because no broad diffuse signal near the low 2Theta values of the XRD spectrum of a CMC oxidized in wet O_2 at 1200°C for 100h was observed (Figure 65), it is unlikely that any B-containing amorphous oxide droplets constituted a significant phase fraction of the surface oxide. None the less, the presence of a boron-rich oxide droplet near the BN interphase and SiC fibers (no matter how small a phase fraction) will affect the constituent oxidation resistance.

5.3.1.2.1. Porosity Pipe Oxidation

The useful lifetime of a CMC would be compromised if the BN interphase was significantly oxidized below the exposed surface. The porosity pipes that intersected the exposed surface of the CMC did not seal during oxidation due to their several-micron wide open cross-section, allowing a direct path for the oxidant into the CMC. What was observed, however, was that the primary phase that oxidized was the CVI SiC that lined the porosity pipes. Although the oxygen ingress lengths along the porosity pipes were hundreds of microns (Table 22), they had little effect on the overall degradation of the CMC and could not be used to determine oxidation kinetic data. It should be noted, however, that if a load was applied to the CMCs and a crack initiated in the matrix a few hundred microns from the exposed surface, the porosity pipes in the vicinity of the crack would create a fast-path for oxygen to reach the crack.

5.3.1.2.2. Preferential Fiber Oxidation

There are several possible causes for preferential fiber oxidation over matrix oxidation. The first is that there could be a faster path along the fiber/BN interface than the matrix/BN interface. However, no gaps were observed with SEM or TEM along either SiC/BN interface.

Another possible reason for preferential fiber oxidation could be differences in composition. Hi-Nicalon fibers are non-stoichiometric (containing excess carbon) and contain residual oxygen (0.6 mol%).[27] The non-stoichiometry and non-crystallinity of the fiber could increase the oxidation rate compared to the CVI SiC in the matrix if a reaction-limited mechanism dominated in the interior of the composite. The Po_2 is likely below that of BN/B_2O_3 equilibrium (10^{-19} atm at 1300°C) because preferential SiC oxidation is observed over BN oxidation. Several considerations can be made regarding the effect of chemistry.

Thermodynamic considerations of compositional differences are considered. If SiC is non-stoichiometric (excess C or excess Si) the activity of C and Si will be altered, changing the free energy for reaction with O_2 to form SiO_2. Reactions 21 and 22 show potential reactions of a C-rich or Si-rich SiC phase, respectively.

$$\frac{1}{2}SiC + \frac{1}{2}C + O_2(g) = \frac{1}{2}SiO_2 + CO(g) \quad [21]$$

$$\frac{2}{5}SiC + \frac{2}{5}Si + O_2(g) = \frac{4}{5}SiO_2 + \frac{2}{5}CO(g) \quad [22]$$

Reaction 22 has a lower free energy per mole of oxygen than Reaction 20, as calculated using the FactSage Reaction Module with the FactPS database for temperatures of 800-1300°C. However, Reaction 22 is not representative of the Hi-Nicalon fibers that contain excess carbon. Therefore, the thermodynamic consideration cannot explain the observed behavior of preferential fiber oxidation over matrix oxidation.

Finally, a kinetic consideration. The Hi-Nicalon SiC fibers had an increased linear rate constant at 800°C compared to CVD SiC (Figure 38). However, the difference between the two is not statistically significant: $(2.4 \pm 0.8) \times 10^{-3}$ µm/h for SiC fibers vs. 1.7×10^{-3} µm/h for CVD SiC.[71] Neither consideration provides a conclusive explanation for preferential fiber oxidation and the reason for this observation remains unresolved. Table 26 summarizes the considerations for preferential fiber oxidation over matrix oxidation due to the chemistry of the fiber.

Table 26. Possible considerations for preferential fiber oxidation over matrix oxidation below the exposed CMC surface

Consideration	Method of Determination	Explain Preferential Fiber Oxidation?	Comments
Thermodynamics Lower ΔG for Reaction	FactSage Reaction Module	X	Reaction with lower ΔG not representative of fiber
Increased k_l	This study	✓	K_l of fiber and CVD SiC are not statistically different

5.3.1.2.2. Constituent Oxidation Below the Exposed Surface

Pores in the oxide were observed in the wet O_2. As described for porous oxides on the matrix material specimen, the pores in the oxide on the CMC likely resulted from increased product gases from the combined BN and SiC oxidation, because pores were observed in the vicinity of the BN interphase (Figure 75). Oxidation of both SiC and BN (Reactions 3-4 and 12-13, respectively), the presence of boron in the glass, and the presence of pores in the glass all increased the SiC oxidation rates.

Another effect of BN oxidation was increased fiber oxidation in the vicinity of thicker BN found at fiber intersection points. Increased oxidation of BN near fiber intersections was first observed by Ogbuji, who observed “pin hole” pores in these areas.[51] That work proposed that the area of thicker BN interphase oxidized to B_2O_3 (l) which reacted with the adjacent SiC (s), according to Reaction 23:

$$B_2O_3(l) + SiC(s) = B_2O_3 \cdot SiO_2(l) + CO(g) \quad [23]$$

The gas created from this reaction caused the pin hole pores to form, which then led to increased oxidation of SiC near the pores, and eventually failure of the CMCs in the vicinity.[51] This result had two implications for this dissertation. First, pores were observed near the BN interphase in the oxide, as previously discussed (Figure 75). Secondly, the mechanism proposed by Ogbuji suggested increased SiC oxidation in the vicinity of BN near fiber intersection points. Evidence of this was observed in this work with TEM and SEM for CMCs oxidized in various conditions (Figure 77and Figure 78). These micrographs showed minimal oxidation of fibers directly at the intersection points (with initially thin BN interphase) and increased fiber oxidation immediately adjacent to the intersection points. The areas of increased BN thickness were also the locations of 40% of the borosilicate droplets (Figure 62). These observations are consistent with rapid, initial BN oxidation at the exposed CMC surface. Where there was a greater amount of BN, a greater amount of B_2O_3 was produced during oxidation, increasing neighboring SiC oxidation according to Reaction 23.

The SiC fibers and BN interphase directly below the sealing oxide experienced small amounts of oxidation but did not show significant trends with temperature in wet O_2 and a small trend with temperature in dry O_2. As shown in Figure 84and Figure 85 the BN readily and preferentially oxidized at short times (even at 800°C), forming the sealing oxide at the CMC surface. However, when the oxide was thick, the Po_2 was reduced below the surface. With a reduced Po_2, the more thermodynamically favorable oxide will form. In the case of BN and SiC exposed to a low Po_2 oxidant, SiC oxidation is thermodynamically favorable (Figure 6).[50] Evidence of this was observed as unoxidized BN was surrounded by the oxide near the surface with both SEM (Figure 84and Figure 85) for all oxidizing conditions.

Even with the BN-enhanced oxidation, the oxidation depth of the BN interphase was not extensive. From 12 ion-polished CMC cross-sections from coupons exposed to varying oxidation conditions, the greatest oxygen ingress length at the SiC/BN interface measured was 30 μm. One instance of oxidation at the SiC/BN interface was observed with TEM from 135 μm below the surface. In both environments, no time dependence was observed for the BN oxidation depth in the CMCs at 800 or 1200°C, with minimal dependence at 1300°C. While this is a promising result for the use of these materials in high-temperature applications, it prevented the determination of oxidative degradation rates necessary for CMC life prediction.

Additionally, several instances of a "interphase-interface" oxide along the SiC/BN interface were observed. Two hypotheses are presented for the formation of this thin oxide layer. First, it is possible that a small gap exists at the BN/SiC interface that would allow for gas-phase transport of the oxidant along the interface. No such gap was observed in TEM for the as-received CMC or the oxidized CMCs. However, only a limited number of observations were made (6 CMCs) due to the necessity of TEM to observe any gap.

Second, it is possible that oxidant permeation in the SiO_2 occurred along the SiC/BN interface as the depth of oxide growth is consistent with transport in condensed phases. A discussion of preliminary evidence for this mechanism is given in Appendix H. However, the "interphase-interface" oxide was not observed in a majority of SiC/BN interfaces. It is therefore likely that special interfaces existed in the CMC which allowed for the interphase-interface oxide to form. But once again, no evidence of a special interface was observed by TEM, so no definitive conclusion can be made regarding the oxidant transport mechanism along the SiC/BN interfaces in CMCs.

5.3.2. Stressed Permeability Testing

The impact of an applied load on a CMC's oxidation behavior was first studied by Morscher, et al.[60]through a stress rupture study (test to failure). The current work featured interrupted stressed oxidation to explore the time dependence of CMC oxidation under applied load for the first time. Oxidized features observed in the interrupted stressed-oxidation testing in this work included large pores, porosity pipes, and matrix cracks. Each will be discussed in turn.

The large pores and porosity pipes were clearly connected to the surface, which resulted in their oxidation. Similar to porosity pipe oxidation in CMCs oxidized with TGA, oxidation of the large pores and porosity pipes in the stressed permeability coupons did not result in oxidation of the BN interphase or SiC fibers. The oxidation of these features, therefore, would only affect oxidative lifetime of the composites when providing a pathway to the interphase through matrix cracks.

The oxidized matrix cracks, however, did result in oxidation of the BN interphase, which will affect the lifetime of the CMCs. Oxidation of BN to B_2O_3 will cement the fibers to each other or the matrix, preventing fiber pull-out necessary for CMC toughness. Effects of exposure time, pre-stress load, and starting permeability of the CMCs on the matrix cracking were each considered. The exposure times for the 800°C stressed air permeability tests ranged from 1 to 100 hours. However, as can be seen from Table 24 and Figure 98 no trends were observed with increasing exposure time. It is assumed that this is due to other contributing factors (pre-stress load and starting permeability). Therefore, no oxidation kinetic information was determined from the effect of exposure time.

Two pre-stress loads were used in this study: NPS of 0.8 and 1. It was hypothesized that increasing the pre-stress load at room temperature prior to the 800°C stressed permeability tests

in air would increase the starting damage to the composites. This appeared to be true, as CMCs that experienced the higher initial load (NPS of 1) also experienced more matrix cracking (Table 24), however this effect could not be further explored due to *i)* the limited number of samples available and *ii)* the inability to deconvolute the effects of variable CMC permeability, discussed below, from applied load. Oxidation kinetic data could not be determined by varying the pre-stress load.

The inherent structural variability of the CMC coupons resulted in starting permeabilities that ranged over four orders of magnitude, from NP (Log Darcy Constant) of 0.70 to 1. When the starting permeability was the only factor that differed between two stressed permeability exposures, such as the two 20h tests with NPS of 0.8, the oxidation behavior was different. Oxidized matrix cracks were not observed in the specimen with the higher starting permeability (NP of 0.80), compared to the coupon with a lower starting permeability (NP of 0.72), which did have oxidized matrix cracks. It is therefore hypothesized that oxidation in matrix cracks might occur more readily in low permeability CMCs. However, no more than two specimens were tested at each stressed oxidation condition, so a clear effect of permeability on oxidation behavior could not be determined. The small test population and structural variability in CMC starting materials prevented determination of oxidation kinetic data for the 800°C stressed air permeability tests.

5.4. Conclusions

CMC oxidation kinetics could not be determined for CMC coupons with an exposed face oxidized in dry and wet O_2 at 800, 1200, and 1300°C. Attempts in quantifying the oxidation kinetics of the BN interphase included analysis of the composition and phase-distribution of the surface oxide, oxide thickness measurements over the BN interphase, rapid transient mass

changes, porosity pipe oxidation, and oxidant ingress under an applied load. No trends were observed with time, temperature, or environment for the sealing of the BN interphase on the exposed faces. However, CMC oxidation mechanisms were identified from the large quantity of data collected.

The external CMC surfaces sealed with thermally grown borosilicates formed on the exposed composite face that showed compositional variation over the BN interphase and adjacent SiC fiber and matrix. Local variations in composition will result in local variations in oxide viscosity and oxidant permeability. The borosilicate droplet compositions were characterized semi-quantitatively with EELS giving a range of 0-42 wt% B_2O_3 (balance SiO_2) after 100h exposures. High B_2O_3 contents in the glass will result in reduced oxidant viscosity as compared to SiO_2. However, reliable permeability data for binary borosilicate glasses as a function of composition do not exist.

The phases in the interior of the CMCs oxidized following a process that was independent of temperature or environment: the SiC fibers oxidized first, followed by the SiC matrix, and last the BN interphase. The preferential oxidation of SiC over BN indicated that the Po_2 must be lower than the BN/B_2O_3 equilibrium oxygen partial pressure (10^{-19} atm at 1300°C). Estimated diffusivities from limited oxidation ingress length measurements along SiC/BN interfaces indicated that diffusion along the interface is consistent with permeation through an amorphous solid.

CMCs experienced matrix cracking with applied loads from the stressed-permeability tests as compared to the TGA specimen. The CMCs that experienced higher initial loads (normalized pre-stress of 1) experienced more cracking compared to those with the lower initial load (normalized pre-stress of 0.8). However, oxidation kinetic data could not be determined

from the stressed-permeability work due to *i)* the limited number of specimens available, and *ii)* the inability to deconvolute the effects of variable CMC starting permeability from applied load.

5.5. Recommendations for Future Work

Because oxidation kinetics could not be determined from this study, it is recommended that future CMC studies modify the testing conditions. From the stressed permeability work with Southern Research (Birmingham, AL), it was evident that a CMC under an applied load at high temperatures will experience greater damage due to oxidation than a CMC without load. It is suggested that CMC oxidation tests be conducted with a range of applied loads that induce matrix cracking, but do not cause failure, so crack propagation and sealing rates can be determined as a function of time, temperature, environment, and applied load. This study could yield relevant data necessary to explore the synergy between oxidation and cracking as well as to determine CMC oxidation rates that can be used in a lifetime prediction model

6. Viscosity and Melting Behavior of Borosilicate Glasses

6.1. Motivation

There was an expectation prior to starting this work that a thermally grown borosilicate glass formed during oxidation of a CMC would wet an exposed surface or crack to seal the CMC against further oxidation due to its low viscosity. However, it was observed in this work that although the BN interphases are sealing rapidly, the oxide droplet morphology of the borosilicate phase is forming, contrary to expectation, with minimal wetting of surfaces. This unique morphology was observed in both dry and wet O_2 at all temperatures studied (800, 1200, and 1300°C).

Similarly, it was expected that the composition of the oxide would be constant across the exposed CMC surface. Contrary to this expectation, it was observed that borosilicate droplets formed near the BN interphase on the exposed CMC surfaces while SiO_2-rich oxide was observed above the SiC phases. These unexpected results prompted the following work with borosilicate glasses to understand their influence on CMC oxidation behavior.

6.2. Objectives

The goal of this study was to explore the viscosity and melting behavior of borosilicate glasses as a function of glass composition, towards understanding the observed morphology and non-uniform sealing of exposed CMC surfaces. Another goal was to compare the stand-alone glasses to the thermally grown oxide droplets formed on CMCs during oxidation. A third goal was to incorporate the composition-viscosity-morphology correlation results from these stand-alone borosilicate glasses into the mechanistic description of CMC oxidation behavior.

This chapter reviews the thermally grown borosilicate droplet morphologies before discussing the melting behavior of stand-alone borosilicate glasses. The temperature and

compositional dependence of the stand-alone borosilicate glass melting resulted in estimates for thermally grown droplet initial compositions. The chapter concludes with the impact of glasses of these compositions on CMC oxidation.

6.3. Results

6.3.1. Borosilicate Glass Droplets on CMCs

As described in the *CMC Oxidation chapter*, oxide droplets were observed on the BN interphase after oxidation of exposed CMC surfaces in both dry and wet O_2. In dry O_2, oxide droplets were observed after 50h at 800°C and after 1h at 1200 and 1300°C. In wet O_2, oxide droplets were observed after 1h at all temperatures studied (800, 1200, and 1300°C). Representative droplet morphologies were shown in plan view (Figure 62) and cross-section in *Chapter 5. Ceramic Matrix Composite Oxidation*. Figure 100 and Figure 101 show additional examples of the droplet morphology in profile in SEM images.

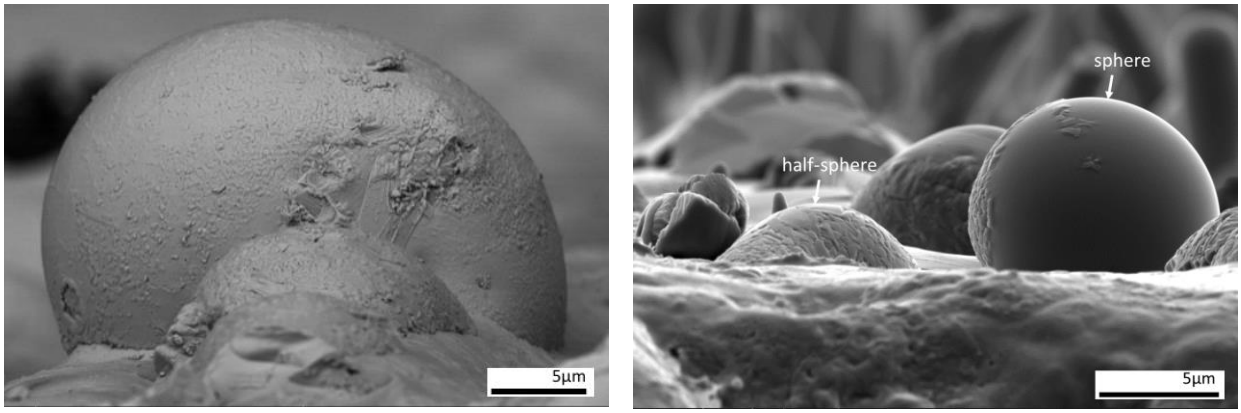

Figure 100. Spherical borosilicate droplets observed on exposed CMC faces after oxidation in dry O_2 for 50h at 1300°C (left) and 1200°C (right).

As can be seen in Figure 100 and Figure 101, oxide droplets formed half-sphere or sphere shapes.

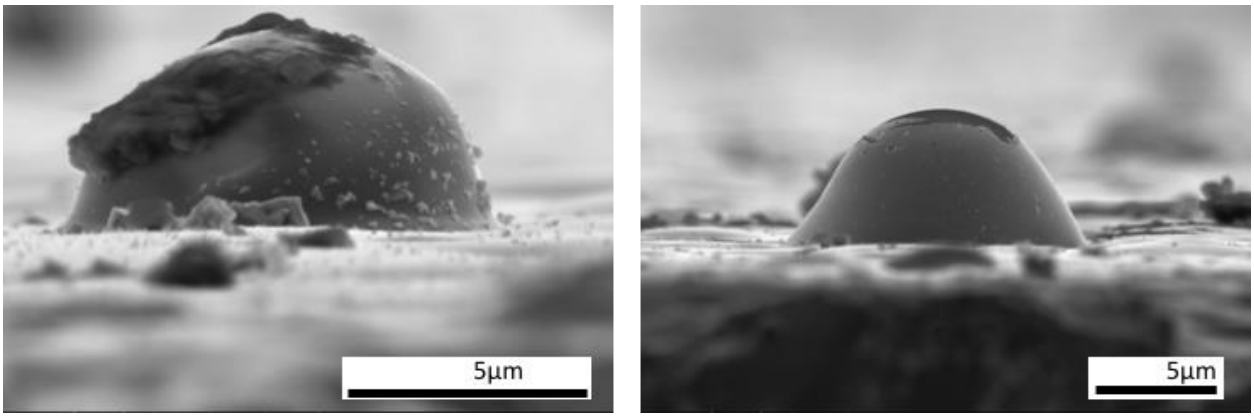

Figure 101. Half-sphere shape borosilicate droplets observed on exposed CMC faces after oxidation in wet O_2 for 1h at 1200°C.

Although instances of the half-sphere morphology were observed, the spherical morphology is thought to be representative of the first temperature, time, and composition required for the thermally grown borosilicate droplets. The half-sphere morphology is likely to result at higher temperatures and therefore not indicative of conditions required for initial non-wetting oxide formation. Therefore, the properties of borosilicate glasses (composition and viscosity) that result in the spherical shape morphology are the focus of this study.

6.3.2. Starting Glass Compositions

As described in *Section 2.1. Test Materials* and summarized again in Table 27, four borosilicate glass compositions were used in this work. Each composition was made in a separate batch. Three glass cylinders of each starting composition were digested with an HF-H_2O solution, as described in *Section 2.3. Characterization Procedures*. The digested solutions were analyzed using ICP-OES to determine the average starting composition of each batch of glasses. The average starting compositions are given in Table 27.

Table 27. Average starting compositions for each batch of glasses as determined by ICP-OES

Batch #	Nominal Wt% B_2O_3	Wt% B_2O_3	Wt% SiO_2
1	100	99.6 ± 0.8	0.4 ± 0.8
2	90	98.5 ± 0.7	1.5 ± 0.7
3	80	85 ± 11	15 ± 11
4	70	85 ± 5	15 ± 5

The starting compositions of Batches 3 and 4 show significant variability and were not statistically different from each other despite initial nominal composition differences. However, the four batches were treated as four distinct compositions for Hot Stage Microscope (HSM) testing. The HSM results are reported with respect to batch. The average starting glass compositions will be compared to the final glass compositions in a following section.

6.3.3. Hot Stage Microscope Testing and Results

Each borosilicate glass cylinder was heated on a Si-based substrate relevant for CMCs (Si, SiC, or SiO_2) in the Hot Stage Microscope (HSM) at Alfred University (Alfred, NY), as described in the *Section 2.2. Experimental Setup and Procedures*. The masses of each glass cylinder and the corresponding substrate were taken before and after each test. It was assumed that the substrate mass stayed constant. Each cylinder lost mass during testing. Mass changes for the glass cylinders are reported in Table 28.

Table 28. Mass change of each borosilicate glass cylinder tested with hot stage microscopy

Batch #	Substrate	Initial Mass (mg)	Final Mass (mg)	Mass Change (mg)
1	SiC	15.8	15.5	- 0.3
		14.8	14.7	- 0.1
	SiO_2	23.4	23.1	- 0.3
		11.9	11.6	- 0.3
	Si	15.9	15.9	- 0.0
		20.8	20.5	- 0.3
2	SiC	10.2	9.9	- 0.3
		11.4	11.3	- 0.1
		14.8	14.6	- 0.2
	SiO_2	8.8	8.6	- 0.2
	Si	11.5	11.3	- 0.2
		16.2	16.2	- 0.0
3	SiC	16.8	16.4	- 0.4
		17.8	17.6	- 0.2
		17.4	17.2	- 0.2
		18.1	17.8	- 0.3
	SiO_2	19.8	19.4	- 0.4
		16.7	16.6	- 0.1
	Si	17.0	16.5	- 0.5
4	SiC	18.2	17.9	- 0.3
		16.6	15.9	- 0.7
		16.6	16.2	- 0.4
		19.8	19.5	- 0.3
	SiO_2	19.6	19.1	- 0.5
	Si	14.0	13.5	- 0.5
		12.8	12.5	- 0.3

The mass losses were assumed to be due to B_2O_3 volatility. Bubbles were observed to be trapped in the glass droplets after testing (Figure 102) which were consistent with the formation of gaseous species.

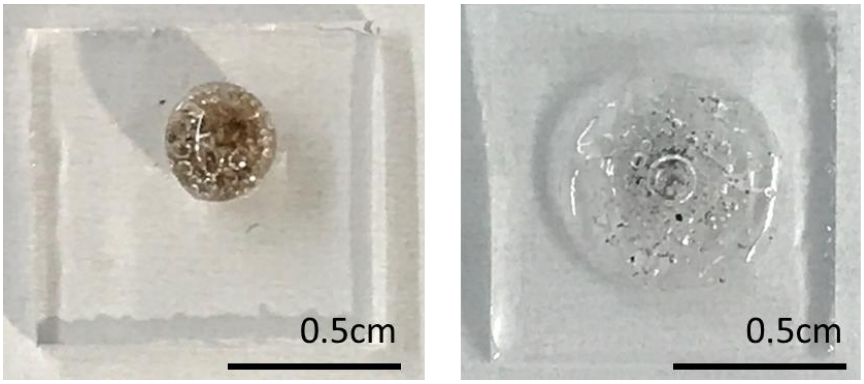

Figure 102. Glass drops with trapped gas bubbles after 45 minutes holds at temperature on SiO_2 substrates; Batch 1, hold at 500°C (left) and Batch 3, hold at 710°C (right).

Discoloration of the glass droplets (brown and black features) was not visible in the cylinders before testing, but was assumed to be due to impurities in the glasses. These impurities were observed in all compositions after HSM testing. Trapped bubbles were also observed in all glass compositions on all substrates. However, not all bubbles remained trapped in the glass. It was observed from sequential silhouette images of the glasses that bubbles would rise to the surface, burst, and then new bubbles would form in the glass. An example is shown for 100 wt% B_2O_3 (Batch 1) on SiC in Figure 103.

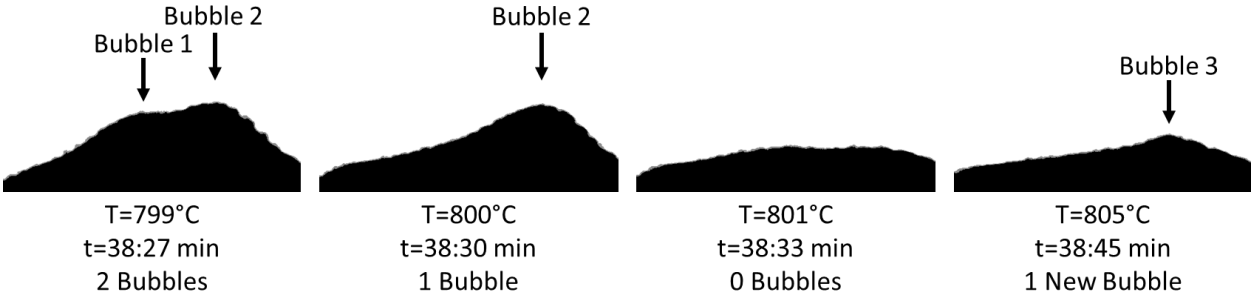

Figure 103. Sequential silhouette images of a 100 wt% B_2O_3 glass on SiC showing bubbles in glass, bursting through surface, and a new bubble forming.

In addition to measuring the mass changes, several outputs from the Misura 32.2 software were recorded for each exposure. These outputs consisted of silhouette images of the glass cylinder, temperature, % sintering (% of initial height), contact angle, viscosity, and silhouette

area variation, all with respect to time. The silhouette images and viscosity results will each be discussed in turn.

Four specific silhouettes were identified for each melting cylinder: softening, sphere, half-sphere, and melting. Figure 104 shows an example of the four silhouettes as well as the starting cylindrical shape. The SiC substrate is also in the frame of view. A fifth silhouette, sintering, is typically identified by ASTM 1857,[45] but could not be identified for these materials because the cylinders were already fully dense, not made of powder that could sinter together.

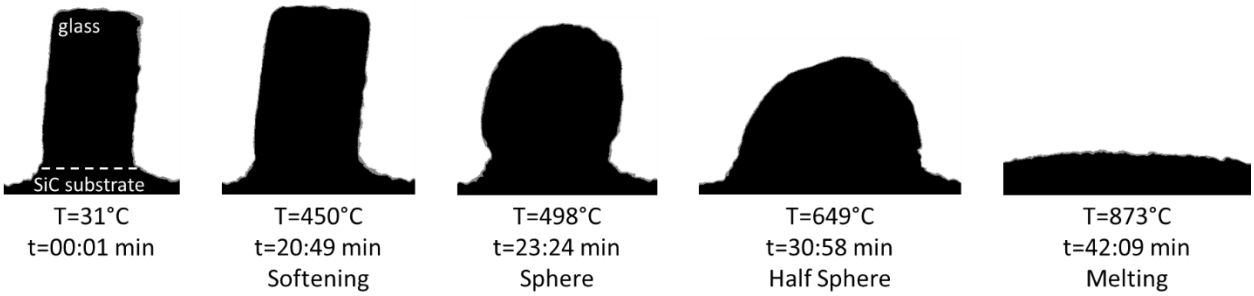

Figure 104. The starting borosilicate glass cylinder silhouette and four distinct silhouettes identified by Misura hot stage microscope software for 100 wt% B_2O_3 heated to 1000°C on a SiC substrate in laboratory air.

The temperatures corresponding with the sphere shape (T_{sphere}) and the half sphere (T_{HS}) were identified for nearly every sample (Table 29). The Misura software malfunctioned during or after three sample runs, so T_{sphere} and T_{HS} were not recorded for those experiments. These runs were not included in Table 28 or Table 29.

*Table 29. T_{sphere} and $T_{HS\ (half\ sphere)}$ for each borosilicate glass cylinder tested with hot stage microscopy. * indicates a heating rate of 60°C/min; all other tests conducted with heating rates of 20°C/min*

Batch #	Substrate	T_{sphere} (°C)	T_{HS} (°C)	Max. T of test (°C)
1	SiC	498	649	1000
		502	500	500
		501*	500*	500*
	SiO_2	502	500	500
		502	500	500
	Si	501	500	500
		501	500	500
2	SiC	528	580	580
		520	580	580
		520	632	1000
	SiO_2	511	580	580
	Si	509	580	580
		537	580	580
3	SiC	677	675	675
		578	672	710
		710	710	710
		615	665	1000
	SiO_2	571	646	710
		603	666	710
	Si	604	662	710
		614	662	710
4	SiC	637	693	780
		670	692	925
		636	713	925
		683	750	1000
	SiO_2	606	680	925
	Si	622	702	925
		568	635	925

It should be noted that for many of the tests from Batches 1 and 2, the half sphere shape was achieved during the 45 minute hold at the maximum temperature. For Batch 2, the glasses reached the half sphere shape after 0.75-5 minutes at the hold temperature. For Batch 1, the glasses achieved the half sphere shape after 12-45 minutes at the hold temperature. As a

reminder, the maximum temperature (hold temperature) for Batch 1 was selected based on a 1000°C ramped exposure (20°C/min) where the sphere shape was observed at 498°C. All tests were held at the maximum temperature for 45 minutes except tests with a maximum temperature of 1000°C, which immediately began cooling after the maximum temperature. Discrepancies within T_{sphere} for each glass composition could be due to variations in starting composition, maximum heating temperature, substrate, or starting cylinder shape, as will be discussed in the following section. The average T_{sphere} (and standard deviation) is given for each composition in Table 30.

Table 30. Average T_{sphere} with standard deviation for each batch of glasses as determined by hot stage microscopy

Batch #	T_{sphere} from HSM (°C)
1	500 ± 1
2	520 ± 10
3	620 ± 50
4	630 ± 40

The Misura software follows ASTM D1587,[45] which uses the softening, half-sphere, and melting silhouettes to calculate a viscosity curve (with time or temperature). This ASTM standard was originally based on the method of Scholze.[42] The Scholze method determined constant viscosities that correlated with specific glass shapes formed on heating, for any glass composition. Scholze did not identify a viscosity that corresponded to the sphere shape in glasses, so this silhouette was not used in the software analysis. The determination of the viscosity for a sphere was made in this work by interpolation.

An example of a viscosity curve from a sample from Batch 4 is shown in Figure 105, along with the corresponding viscosity points determined by HSM images. The three glass shapes used to determine the viscosity curve (softening, half-sphere, and melt) are marked on the

curve, along with the location of the sphere shape (red box). Scholze stated that the surface tension of the glass did not affect the results[42] and Pascual, et al. stated that the effect of the glass surface tension on the viscosity results was within the error of the measurement technique.[43] Therefore the curve determined by the fixed viscosity points is essentially independent of glass surface tension.

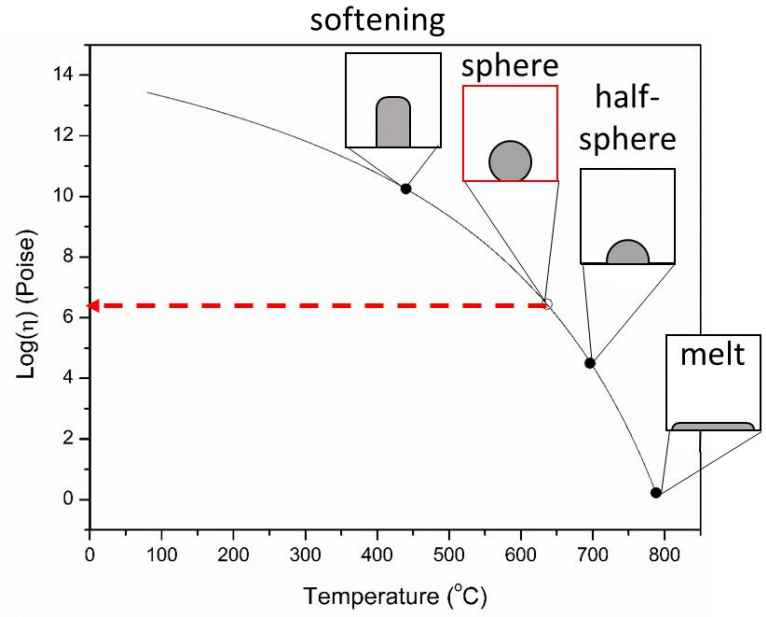

Figure 105. Changes in viscosity of a Batch 4 borosilicate glass with temperature (heated at 20°C/min). The specific viscosity points are labeled on the curve and a schematic is shown for each point. The black boxes indicate values used to determine the viscosity curve. The red box indicates the formation of a sphere shape.

The sphere shape was identified by the HSM software, but did not correspond to a specific viscosity. Instead, the temperature that resulted in the sphere shape was used to extract the corresponding viscosity from the HSM data by interpolation of the viscosity curve. Examples curves for Batches 2-4 are in Figure 106.

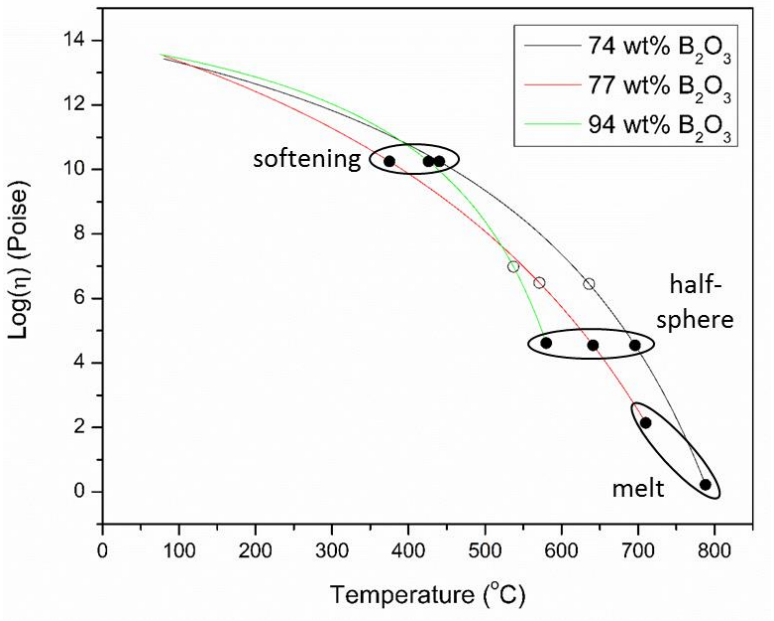

Figure 106. Viscosity curves from HSM software for Batches 2-4 showing softening, half-sphere, and melting fixed points.

The HSM software used log(η) = 10.25 for softening and log(η) = 4.55 for half-sphere fixed viscosity points. The sphere point (open circles, Figure 106) are approximately all the same viscosity as well.

The log(η) for the sphere and half sphere shapes determined in this work are reported in Table 31, along with values from the literature. The standard deviations are also reported for each value. Log(η) for a sphere was calculated separately for Batch 1 (100% B_2O_3) and Batches 2-4 because T_{sphere} was below the melting temperatures for Batches 2-4, but above the melting temperature for Batch 1. Because the thermally grown borosilicate glasses contain SiO_2, the results from Batch 1 (100 wt% B_2O_3) will be ignored in favor of the results from Batches 2-4 (containing both SiO_2 and B_2O_3 in varying ratios).

Table 31. Average log(η) (Poise) for sphere and half sphere shapes from this work and comparisons to results from the literature

Glass Shape	Log(η) HSM	Log(η) Scholze[42]	Log(η) Pascual[43]	Log(η) Pascual[44]
Half Sphere	4.5 ± 0.6	4.6 ± 0.1	4.5 ± 0.1	4.1 ± 0.1
Sphere	4.1 ± 0.3 (Batch 1) 6.75 ± 1.1 (Batches 2-4)	-	-	5.4 ± 0.1

Pascual's first study[43] was conducted to validate the method of Scholze.[42] The second study by Pascual modified the technique and identified the corresponding viscosity for sphere shapes in glasses.[44]

$Log(\eta)_{sphere}$ from the HSM for Batches 2-4 was barely statistically different from Pascual[44], because of the large standard deviation. However, several experimental factors could contribute to the order of magnitude difference between the HSM value and the value from Pascual[44] for $Log(\eta)_{sphere}$. Identification of the softening, half-sphere, and melting silhouette shapes are critical to determine the viscosity curve. Any uncertainty associated with the selection of these fixed points could lead to skewing the viscosity curve. In this work, the rapid (20°C/min) heating rate, compared to the ASTM standard method of 5°C/min,[45] could have resulted in misidentification of $T_{softening}$, T_{HS}, and $T_{melting}$, due to the lag of the glass response to the rapid heating, skewing the temperature readings. Additionally, the ASTM standard also uses the "sintering" silhouette shape to create the viscosity curve.[45] However, in this work, the glass was fully dense prior to heating, so no sintering shape was observed.

The rapid heating rate and use of three silhouettes instead of four could cause uncertainty in the value for $log(\eta)_{sphere}$. However, because no other heating ramp was used, and because only one other study provided a characteristic value for $log(\eta)_{sphere}$, the $log(\eta)_{sphere} = 6.75 \pm 1.1$ from HSM in this study will be used for subsequent analysis and calculations.

6.3.4. Glass Compositions after HSM

After completion of each test, the glass droplet was mechanically removed from its substrate with tweezers and digested in an HF-H_2O solution. The digested solutions were analyzed using ICP-OES to determine the average final composition of each glass (Table 32).

Table 32. Average final compositions for each batch of glasses as determined by ICP-OES

Batch #	Wt% B_2O_3	Wt% SiO_2
1	100.0 ± 0.1	0.0 ± 0.1
2	94 ± 6	6 ± 6
3	77 ± 18	23 ± 18
4	74 ± 12	26 ± 12

The differences between the final and initial glass compositions were not statistically significant for all glass compositions, but the scatter is larger for Batches 3 and 4. Due to the higher number of samples used to determine the average final glass compositions (7-8 glasses per batch), the final compositions were used for calculations involving viscosity, as discussed below.

6.3.5. Viscosity and Temperature Comparisons

If two of the three glass viscosity parameters (temperature, composition, and viscosity) are known, the third can be determined. So, in addition to extracting the viscosity data for each glass from the HSM software, the viscosity was calculated two different ways. First, viscosities were calculated by interpolating from the temperature-composition data of Bruckner, et al.[40] Second, viscosities were determined using the viscosity module of the FactSage database.[35] Both of these calculations used the final glass compositions (Table 32) and corresponding T_{sphere} (Table 30) to determine the viscosities. Results from the two calculation methods are in Table 33.

Table 33. Viscosities interpolated and calculated based on T_{sphere} determined by hot stage microscopy for each composition

Wt% B_2O_3	T_{sphere} from HSM (°C)	Log(η) HSM	Calculated Log(η) Bruckner, et al.[40]	Calculated Log(η) FactSage[35]
94 ± 6	520 ± 10	6.75 ± 1.1	4.2	4.9
77 ±18	620 ± 50		4.9	5.4
74 ± 12	630 ± 40		5.3	5.6

The values for $\log(\eta)_{sphere}$ interpolated from the data of Bruckner, et al., were 1.45-2.55 times lower than the $\log(\eta)_{sphere}$ determined from HSM. The values of $\log(\eta)_{sphere}$ calculated from the viscosity module in the FactSage database were 1.15-1.88 times lower than the $\log(\eta)_{sphere}$ determined from HSM.

Another calculation was made to determine the temperature required for the glass sphere shape using the viscosity (Table 31) at each final composition (Table 32). Temperatures calculated from the data from Bruckner, et al., and the viscosity module of the FactSage database are given in Table 34.

Table 34. Temperatures required for the sphere shape viscosity for each composition

Wt% B_2O_3	Log(η) HSM	T_{sphere} (°C) HSM	Calculated T (°C) Bruckner, et al.[40]	Calculated T (°C) FactSage[35]
94 ± 6	6.75 ± 1.1	520 ± 10	260	400
77 ± 18		620 ± 50	415	510
74 ± 12		630 ± 40	460	530

According to the calculations based on the data from Bruckner, et al., the temperatures required for log(η) of 6.75 are 170-260°C lower than the temperatures recorded by the HSM. The temperatures determined by the viscosity module in FactSage were 100-117°C lower than the temperatures recorded by the HSM. These differences will be discussed below.

6.4. Discussion

6.4.1. Boria Volatility

The mass losses of the borosilicate glasses ranged from 0.1-0.7 mg (from initial masses of 10-20 mg), with 17 of 26 cylinders having mass losses in the range of 0.1-0.3 mg (Table 28). It is assumed that mass loss occurred due to boria volatility from both the surface and the B_2O_3 (g) bubbles that burst through the surface of the droplets. Bubbles were observed in glasses on all three Si-based substrates (Si, SiC, and SiO_2). It appeared that the substrate composition (and oxidation of the substrate material) did not affect bubble formation.

It is hypothesized that several factors did affect boria volatility and bubble formation: glass composition, temperature, and therefore, viscosity. The viscosity of a borosilicate glass increases with increased SiO_2 content and decreases with increasing temperature.[40] Bubble formation will likely decrease with increasing viscosity. However, in this study, as the SiO_2 content increased, so did the exposure temperatures. The viscosity of all glasses studied must have been low enough to allow bubbles to form, consistent with the lack of trend in mass loss with glass composition (Table 28). More bubbles were observed to burst (with silhouette images) for the 100% B_2O_3 glasses heated to 1000°C than the other compositions heated to the same temperature, presumably due to the lower viscosity of this composition. Assuming all of the mass loss was due to B_2O_3 volatility, there was < 2 wt% decrease in B_2O_3 content during HSM testing (Table 28). The ICP-OES analysis showed no significant changes in composition in glasses after HSM testing (Table 32). The final compositions were used for all calculations.

Bubbles were not observed in the thermally grown oxide droplets on CMC interphases (Figure 72). This suggests that there was a lower B_2O_3 content in the thermally grown borosilicate droplets than the stand-alone glasses studied: a lower boria content in the glass

would reduce the B_2O_3 available to volatilize, as well as increase the viscosity of the glass, making it more difficult for gases to coalesce to form bubbles. The thermally grown borosilicate droplets in the TGA were exposed to higher temperatures (800-1300°C) for up to 100h and exposed to H_2O (g) in some cases, all of which increases B_2O_3 volatility. This is consistent with the EDS results discussed previously where B was only detected with EDS for oxide droplets after the 800°C exposures. However, B was detected with EF-TEM and EELS. However, the glass viscosity could be high, even when containing B_2O_3.

6.4.2. Hot Stage Microscopy Results

As seen in Table 29, T_{sphere} varied within each batch of glasses. These variations could be due to the starting composition, maximum heating temperature, or substrate. Each possibility will be discussed. There was likely variation in the starting glass compositions from each batch, but these could not be determined prior to HSM testing due to the destructive nature of the ICP technique.

The maximum heating temperature, while different for each batch of glasses, exceeded T_{sphere} for all batches except Batch 1 (100 wt% B_2O_3). Because the maximum temperature was greater that T_{sphere}, it was assumed to have no effect on the average T_{sphere} for each batch.

There were also no statistical differences in T_{sphere} between the different substrates (Si, SiC, or SiO_2) for each batch of glasses. This could be due to the native SiO_2 layer that likely existed on each substrate prior to HSM testing, or to the size of the borosilicate spheres. The borosilicate spheres in the HSM study were 2-3 mm in diameter, which was about 3 orders of magnitude larger than the oxide droplets observed on exposed CMC faces (several μm in diameter). It is possible that the mass of the HSM oxide spheres overcame the surface energy

effects. This can be determined by calculating the capillary length, L_c, which is the characteristic length scale for a liquid subject to both surface tension and gravity[92] (Equation 24):

$$L_c = \sqrt{\frac{\gamma_{LV}}{\Delta\rho g}} \quad [24]$$

where γ_{LV} is the surface tension between the liquid (B_2O_3) and the gas (air), $\Delta\rho$ is the difference in densities of the two medium, and g is the gravitational constant. Drops smaller than L_c will remain spherical due to the dominance of surface tension, while drops larger than L_c will flatten due to gravity.[92] The following parameters (Table 35) were used to calculate L_c for 100% B_2O_3.

Table 35. Parameters used to calculate the capillary length for B_2O_3

Parameter	Value
γ_{LV}	7.59 dyne/cm [93]
$\Delta\rho$ (B_2O_3 - air)	1.8 g/cm^3 [94]
L_c	*0.66 mm*

The resulting capillary length was 0.66 mm, which is smaller than the drop diameters from the HSM study. Therefore, it is likely that the mass of the spheres overcame the surface tension, causing the liquid drops to flatten when held at or above T_{sphere} independent of substrate. This is also consistent with some of the thermally grown glass droplets keeping their spherical shape because the diameter was less than the capillary length. Based on these analyses, the most likely source of variation in T_{sphere} was the starting glass composition, rather than the other factors.

6.4.3. Viscosity and Temperature Comparisons

Several calculations were made in the previous section to compare the HSM results (T_{sphere} and log(η) values) to results predicted by other sources (Bruckner, et al.[40] and FactSage[35]). In all cases, the calculations predicted decreased temperatures or increased viscosity necessary to achieve the sphere shape at each composition. The temperature calculations were based on a fundamental assumption: log(η)=6.75 was the viscosity at which

the sphere shape formed for all glasses heated with HSM. However, as described previously, determination of viscosity of a glass by HSM is not as rigorous as by other equipment, such as the rotational viscometer used by Bruckner, et al.[40] There is also uncertainty in the value for $\log(\eta)_{sphere}$, due to the rapid heating rate of 20°C/min and the use of three silhouette shapes instead of four. The viscosities measured precisely by Bruckner, et al.[40] are likely more reliable than the viscosities determined by this HSM study. Assuming the value for $\log(\eta)_{sphere} = 5.4$ from Pascual[44] is more reliable than $\log(\eta)_{sphere}$ determined by HSM in the present work, an additional value for the borosilicate composition can be estimated for each T_{sphere}. These calculations are described in the following section.

The temperatures for sphere shapes predicted by Bruckner, et al.[40] and FactSage[35] to achieve the sphere viscosity of $\log(\eta)=6.75$ were lower than the T_{sphere} values determined by the HSM work in this study. It is possible that the thermally grown glass droplets on the CMCs formed at these low temperatures. However, no CMC oxidation tests were done in this low temperature range (260-530°C, from Table 34). A hypothesis about the formation temperature for the thermally grown oxide droplets will be outlined in the following section.

6.4.4. Incorporation of Borosilicate Glass Sphere Formation for Understanding CMC Oxidation

In the CMC oxidation experiments, oxide droplets were observed after 50h at 800°C in dry O_2, the lowest test temperature, but not after 1h in the same conditions. Oxide droplets had been previously observed on the B-doped C and BN interphases of CMCs oxidized at 600°C (but not at 950°C).[64] This is consistent with the oxide droplets forming at lower temperatures. However, the BN interphase used in that study contained approximately 20 at% oxygen,[64] which could lower the oxidation temperature of BN due to impurities.[32] BN interphases with reduced oxygen content would likely have increased droplet formation temperatures. This is

likely the case for the BN interphase used for the present study, which had low oxygen content as detected with EELS and TEM. Therefore, it is not unreasonable to assume oxide droplets formed at temperatures near 800°C in all CMC oxidation tests for this work.

The maximum T_{sphere} determined in this stand-alone borosilicate glass study was 630°C (Table 30) for a composition of 74 ± 12 wt% B_2O_3. To achieve a T_{sphere} of 800°C, the borosilicate glass must have < 74 wt% B_2O_3, as a bounding value. The composition required to achieve log(η)=6.75 at 800°C was determined two ways. First, a line was fit to the T_{sphere} vs. composition data from HSM (Figure 107).

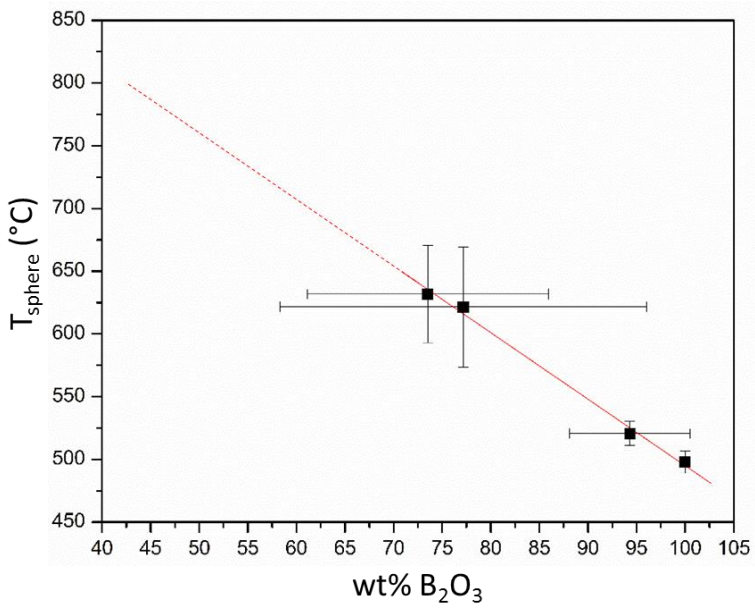

Figure 107. Linear fit of T_{sphere} with B_2O_3 composition.

The equation for the linear fit is:

$$T_{sphere} = -5.38x + 1032 \quad [25]$$

where x is wt% B_2O_3. Figure 107 shows the error (standard deviation) along the x-axis according to the ICP data for final glass composition (Table 32) and the error (standard deviation) along the y-axis according to the T_{sphere} determined by HSM for the different batches of glasses (Table 30). Using the equation for the linear fit, at 800°C, the glass would contain 43 wt% B_2O_3.

No mathematical relationship (theoretical or empirical) exists to relate viscosity and composition for a general glass. There does exist a relationship between viscosity and temperature, as established by Vogel, Fulcher, and Tammann (the VFT equation)[95]:

$$\log(\eta) = A + \frac{B}{T - T_0} \quad [26]$$

where A and B are constants, as is T_0, the correlation temperature, for each glass composition. These constants have no physical significance for the glasses.[95] This relationship, however cannot be used to explain the linear relationship between T_{sphere} and borosilicate composition.

The borosilicate viscosity data collected by Yan, et al.[39] and Bruckner, et al.,[40] however, can be examined with respect to the temperature required for a constant viscosity at each composition. Figure 108 shows the temperature required for a constant viscosity of log(η)=6.75 at each composition studied in these two works, as well as the linear fit to the data.

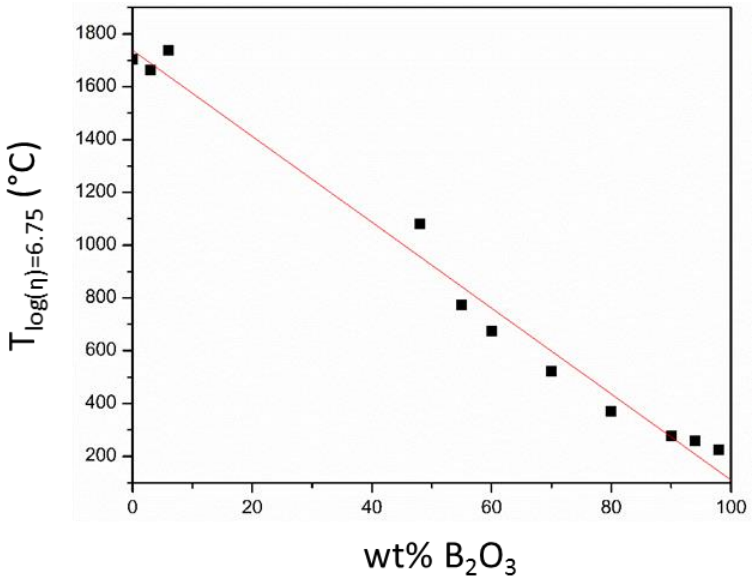

Figure 108. Linear relationship between temperature for a constant viscosity and composition.

The reasonable linear fit to the data in Figure 108 gives confidence for the linear relationship shown in Figure 107. The equation for the linear fit in Figure 108 is:

$$T_{\log(\eta)=6.75} - 16.3x + 1738 \quad [27]$$

Equation 27 can be used to calculate the composition when $T_{\log(\eta)=6.75}$ = 800°C. This results in a composition of 58 wt% B_2O_3. From these two calculations, it can therefore be hypothesized that the required B_2O_3 composition in the borosilicate glass droplets formed at 800°C would be between 43 and 58 wt% B_2O_3.

The composition required to achieve log(η)=6.75 at 800°C was also determined by interpolating from the data of Bruckner, et al.[40] Using this method, at 800°C, the glass would contain 54 wt% B_2O_3. This is within the range of compositions estimated by the linear relationships above.

Alternatively, the value for $\log(\eta)_{sphere}$ = 5.4 from Pascual[44] could also be used to interpolate the glass composition at 800°C, from the data of Bruckner, et al.[40] This results in a value of 63 wt% B_2O_3 (balance SiO_2) to form the sphere shape at 800°C. This will be considered as the upper bound of the borosilicate composition range instead of the 58 wt% determined from the linear relationship given by Equation 27. The borosilicate composition interpolated from FactSage lies between these values of 43 to 63 wt% B_2O_3.

The composition of the thermally grown borosilicate glasses in the present study were measured qualitatively using EELS/TEM (Table 20). The average compositions ranged from 7 ± 6 to 26 ± 13 wt% B_2O_3 with a maximum composition of 42 wt% B_2O_3. However, these compositions were from oxides on CMCs that had been exposed at high temperatures (800 or 1300°C) for 100h. It is likely that B_2O_3 volatility occurred during the 100h, reducing boria content in the borosilicate, especially at 1300°C. Therefore, the predicted starting borosilicate droplet composition range of 43 to 63 wt% B_2O_3 is plausible.

Attempts were also made to remove the thermally grown oxides from the CMCs with acid etching for ICP-OES analysis of the composition (Appendix E), but were unsuccessful due

to the acid digestion of the substrate material along with the glasses. However, thermally grown borosilicates on Sylramic iBN were able to be digested by an HF-H_2O solution in a previous study by McFarland[96] and the glasses ranged from 11-45 wt% B_2O_3 after 1h of oxidation in dry O_2 at temperatures of 900-1300°C, with decreasing boria content with time and temperature.[96] This range of borosilicate compositions is closer to the 43-63 wt% B_2O_3 predicted in this work than the 7-26 wt% determined from EELS of the thermally grown borosilicates after 100h. Although the amount of SiC and BN available, the temperature range, and the oxidizing environment in the work by McFarland varied from the present CMC study, the results indicate that thermally grown borosilicate glasses could contain a significant fraction of B_2O_3.

If the thermally grown borosilicate droplets on CMCs contain 43-63 wt% B_2O_3, the oxidation of BN and SiC in the vicinity of the borosilicate would increase. The permeation of H_2O (g) and/or O_2 (g) through the scale increases with boron content in a borosilicate glass, due to boron modifying the SiO_2 network.[38] However, boria depletion due to volatility increases with time and temperature, reducing the boron modifications to the SiO_2 network and slowing the oxidant permeation with time. The protective capability of the borosilicate droplets near the BN interphase and SiC fibers is critical to retain the integrity of the composite properties. Knowing the borosilicate composition is therefore critical to determining the CMC oxidation rates, as will be discussed in the next chapter.

6.5. Conclusions

ICP-OES analysis of stand-alone borosilicate glasses indicated boria contents varying from 74 to 100 wt% B_2O_3. Values for T_{sphere} and the corresponding log(η) were determined with hot stage microscopy as a function of composition. These parameters were used to estimate the composition of borosilicate droplets thermally grown at 800°C to be in the range of 43 to 63 wt%

B_2O_3. This high boria content will result in rapid oxidant permeation in the glass, increasing the oxidation rate near the critical CMC constituents (BN interphase and SiC fiber). However, the boria volatilization from the oxide would then result in reduced oxidant permeation through the droplet with time, limiting degradation of these critical constituents.

6.6. Recommendations for Future Work

Several changes could be made to improve the precision and accuracy of this study. First, a more-repeatable glass cylinder formation method should be used to create glass cylinders of a more-consistent composition. It is recommended that a mold of the desired cylinder shape be filled with a fine, well-mixed borosilicate powder of the desired composition and heated in a box furnace to melt and quench into a solid shape. This would avoid the inconsistent boria volatility inevitable with the torch formation method. Second, the method of Scholze[42] should be followed more closely during HSM testing. Specifically, a heating ramp rate of 5°C/min should be used instead of the 20°C/min that was used in this study. This would avoid a delay in realizing T_{sphere} due to the fast heating, allowing the glass to equilibrate more at each temperature.

7. Implications for Life Prediction of CMCs

7.1. Objective

The goal of this final chapter is to synthesize the results from the previous chapters to identify mechanisms important for incorporation in an overall CMC oxidation model. This chapter will also provide a summary of key parameters that should be considered when developing a rigorous thermochemical life prediction model for CMCs.

7.2. Considerations for a CMC Oxidation Model

From the results presented in the previous chapters, two simultaneous processes are of interest during oxidation of Ceramic Matrix Composites: exposed surface oxidation and internal oxidation. Both processes will be considered separately, followed by a relevant mechanistic description of CMC oxidation.

7.2.1. Summary of Exposed CMC Surface Oxidation

When a CMC surface is exposed to an oxidizing environment, all of the constituents (SiC fiber, BN interphase, and SiC matrix) can react with the oxidizing species (H_2O (g) or O_2). It was observed with SEM and TEM that all three constituents did oxidize on the surface. The SiC fibers showed minimal oxidation on the surface, in contrast to the stand-alone fiber oxidation results from *Chapter 3. Oxidation of Hi-Nicalon SiC Fibers*. This occurred because the fibers in the CMCs were protected by the surrounding interphase and matrix. The oxidation behavior of the SiC matrix in the CMC was similar to the behavior of the stand-alone matrix material that was presented in *Chapter 4. Matrix Material Oxidation*. However, the impact of the matrix material oxidation behavior (slightly elevated oxidation rates, compared to bulk SiC, due to boron incorporation) is reduced in the composite material, because the matrix material contributes less than 50 area% of the total CMC. Additionally, the degradation of the interphase

and fibers are of primary concern, rather than the matrix, since these constituents are required to maintain the requisite strength and toughness of the CMCs.

The phase that oxidized most rapidly at the surface of the CMC was the BN interphase, which formed borosilicate glass droplets on the surface of the exposed interphase. These borosilicate droplets were observed with SEM after oxidation at all three temperatures (800, 1200, and 1300°C) in both environments (dry and wet O_2). Because the droplets were observed after 1 hour, it was hypothesized that the rapid mass gain observed with TGA for all CMCs with exposed faces was due to the rapid formation of the borosilicate phase.

A range of compositions of these droplets was qualitatively determined to be 7 to 26 wt% B_2O_3 with EELS from 100h exposures. However, it was noted that the borosilicate composition will likely change with time due to B_2O_3 volatility, especially at higher temperatures and/or in the wet O_2 environment. Because of this, the initial composition of the thermally grown borosilicate droplets that sealed the exposed BN interphases on the CMC surfaces could not be determined.

To better understand the borosilicate composition and viscosity required for initial formation of the droplet morphology, stand-alone borosilicate glasses of known compositions were melted with HSM, as described in *Chapter 6. Viscosity and Melting Behavior of Borosilicate Glasses*. From this study, it was determined that borosilicate glasses likely contain between 43-63 wt% B_2O_3 (balance SiO_2) to form a spherical shape at 800°C. It is critical to know the composition of the borosilicates to predict the oxidant permeation rate though the glass, which will increase with increasing boria content.

7.2.2. Summary of Internal CMC Oxidation

Different oxidation behavior was observed in the interior of the CMCs. Below the exposed surface, the Po_2 in the vicinity of the oxidizing phases is decreased below the BN/B_2O_3 equilibrium. As discussed in *Chapter 5. Ceramic Matrix Composite Oxidation*, the more thermodynamically stable oxide will form under these conditions. In this case, SiO_2 will form from SiC instead of B_2O_3 from BN.[50] Evidence of this behavior was observed with SEM and TEM when BN remained intact, surrounded by oxide that progressed down the SiC/BN interfaces into the interior of the composite (Figure 86 and Figure 87). Oxidation along the SiC/BN interfaces likely occurred by oxidant permeation through a condensed phase process.

When comparing the oxidation of the two SiC phases in the interior of the CMC (fiber and matrix), evidence was found both with SEM (Figure 87) and TEM (Figure 86) suggesting preferential fiber oxidation over matrix oxidation. However, oxidation of both SiC phases in the CMCs was minimal: the longest oxide ingress measured (from 12 ion-polished samples of varying oxidation conditions) was 30 μm below the exposed surface in the most extreme test condition (1300°C, wet O_2, 100h). One example of oxidation along the SiC/BN interface was observed with TEM 135 μm below the surface. Nonetheless, both internal and surface oxidation of CMCs must be considered to develop a CMC oxidation model.

7.3. A Relevant Mechanistic Description of CMC Oxidation

The robust oxidation resistance of the CMCs studied in this work (oxidation depths less than ~20 μm in 100h) is a promising result for the use of these materials in high-temperature applications. However, the lack of temperature and oxidant dependence makes life prediction based on oxidative degradation rates challenging. Although CMC oxidation rates could not be determined, an overall mechanistic description of CMC oxidation was developed by synthesizing

the results summarized in the previous sections. The mechanistic description is independent of oxidizing atmosphere or temperature for the oxidants and temperatures used in this study.

The first step of rapid oxidation of the BN interphase to form a boria-rich droplet was concurrent with the slower oxidation of the SiC phases (fibers and matrix) on the exposed faces to form a silica rich glass. Relatively little mixing of the two oxide phases was observed. The borosilicate and SiO_2 phases rapidly sealed the BN interphase, minimizing further oxidation.

In the interior of the composite, preferential oxidation of the Hi-Nicalon SiC fiber was followed by oxidation of the SiC matrix, leaving unoxidized BN surrounded by the oxide below the surface. BN oxidation initiated in the areas of greater BN thickness adjacent to fiber intersection points. Surface borosilicate droplets were found over these fiber intersection points. The fibers near the intersection points were more susceptible to greater SiC consumption due to B_2O_3-enhanced SiC oxidation. A schematic for this mechanistic description is shown in Figure 109. Not included in the schematic due to scale is the possibility of an ultra-thin oxide layer at the SiC/BN interfaces, as observed in a TEM cross-section of the as-received CMC material (Figure 57).

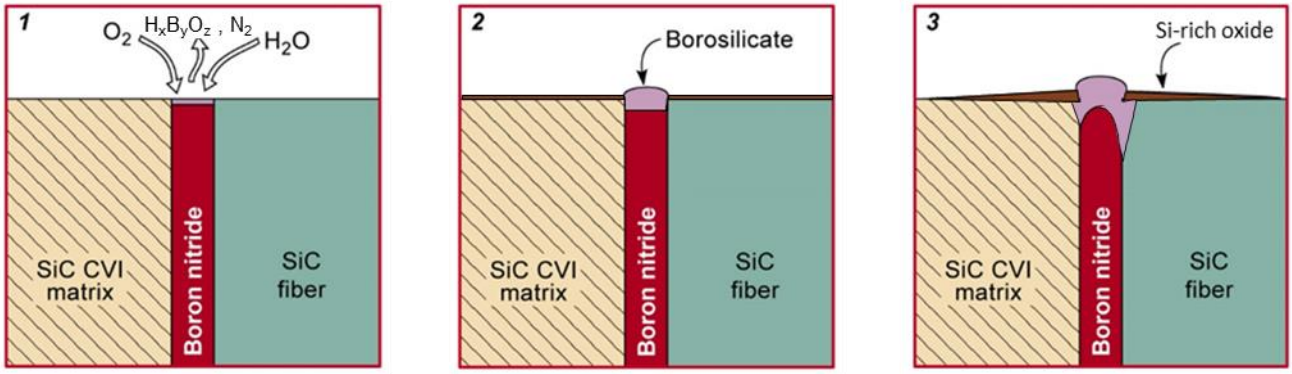

Figure 109. Schematic of the proposed mechanistic description of CMC oxidation.

This schematic shows the differences between the mechanistic description from this work and the CMC oxidation models that were previously proposed by Xu, et al.[49] (Figure 11),

Jacobson, et al.[33] (Figure 12), and Przybyla, et al.[66] The most significant difference is the presence of a condensed-phase oxide between the two SiC phases as the interphase reacts. The condensed phase oxide remained intact, unlike in the previously proposed models,[33; 49] increasing the diffusion path inward for the oxidant and preventing formation of an annular void. It should be noted that the temperature range for annular void formation begins at 700°C in the models by Xu, et al.[49] (modeled 700-1000°C) and Jacobson, et al.[33] (modeled 700-800°C), while Przybyla[66] modeled 800-1200°C. All three models reported annular void formation over the entire temperature range. Although the current study did not examine CMC oxidation at 700°C, no annular voids were observed at temperatures ≥ 800°C, and a condensed phase oxide was observed at all conditions.

Additionally, the B-rich oxide and Si-rich oxides were observed to be non-mixing, forming two compositionally distinct phases, rather than a homogeneous borosilicate phase covering the exposed CMC face. The lack of mixing could be attributed to borosilicate's propensity for phase separation, a possibility indicated by the curvature of the liquidus line in the SiO_2-B_2O_3 phase diagram (Figure 3). Distinct B-rich and Si-rich regions within the borosilicate droplet were observed in one of the two droplet TEM cross-sections. This could be due to phase separation or non-mixing of the oxides. However, because it was only observed in one example, it was not included in Figure 109.

The differences between the oxidation results of this work and the previously described models is likely due the structure of the CMC itself, including interphase thickness, crystallinity, and composition of the BN interphase, and matrix density. The condensed phase oxide that formed at the BN interphase enabled the robust oxidation behavior observed in this work.

7.4. Implications for Future Life Prediction Models

From the results of this work and the mechanistic description of CMC oxidation depicted in Figure 109, several key parameters should be considered when developing a rigorous thermochemical life prediction model appropriate for these CMCs that are not currently accounted for in the existing CMC oxidation models. The presence of an intact borosilicate instead of an annular void will affect the subsequent oxidation behavior below the surface of the CMC. The composition of the borosilicate droplets will affect its viscosity, which will affect how the glass spreads across the surface of the CMC. The initial composition of the thermally grown borosilicate droplets was predicted to be in the range of 43-63 wt% B_2O_3 at 800°C, which can be used to estimate the borosilicate viscosities from the data and Yan, et al.[39] and Bruckner, et al.[40]

However, the presence of an intact borosilicate glass will also have a significant impact on the oxidation behavior of the CMC constituents. The oxidant diffusion rate through the borosilicate will be slower than through an annular void, but will be faster than through pure SiO_2. The presence of boria in the borosilicate has been observed by other authors to increase the oxidant permeation compared to silica. Schlichting observed up to 10^4x increase in O_2 permeation rate compared to SiO_2 with varying amounts of B_2O_3 in the oxide,[38] while McFarland observed a ~4x increase in the parabolic oxidation rate for SiC fibers with a BN coating.[96] The large increase reported by Schlichting was not repeatable by McFarland,[96] but the significance of the composition on the oxidant permeation is made evident by both authors. Oxidant permeation through an intact borosilicate phase is a key parameter that must be considered in a CMC life prediction model.

Despite the many attempts in this work, no kinetic data for CMC oxidation could be determined over the conditions studied in the work, and a quantitative kinetic model related to the proposed CMC oxidation mechanisms could not be developed. As an alternative, the existing CMC oxidation models are again reviewed, below, with consideration of the impact of the intact borosilicate phase and the parameters needed to apply to the RR-HTC CMCs studied in this work. The parameters related to the intact borosilicate phase will be discussed as they relate to each available current CMC oxidation models in the following sections.

7.4.1. Comparison to the CMC Oxidation Model by Xu, et al.

As described in *Chapter 1. Introduction*, the model by Xu, et al. predicts volatilization of the borosilicate that forms from BN/SiC oxidation, leaving annular voids surrounding the fibers (Figure 11).[49] This model is not based on experimental results of CMC oxidation tests, but developed by extracting miscellaneous information from the literature to predict CMC life. Comparison of the theoretical model to the large body of experimental data from this work shows the significant differences compared to the RR-HTC CMCs.

Although no temperature range was explicitly described for this model, results were shown for the range of 700-1000°C. However, it was shown for the overlapping temperature range studied in the present work (800-1300°C) that the condensed borosilicate phase remains intact in the RR-HTC composite. Therefore, some of the input parameters used by Xu, et al. should be changed to better represent the observations for the RR-HTC composite. As described above these observations of an intact borosilicate phase would result in significantly different CMC oxidation behavior. Suggested new parameters (or a range) for this model are listed in the last column of Table 36.

Table 36. Parameters used in the model by Xu, et al.[49] and suggestions for new parameters to represent oxidation of a RR-HTC CMC

Parameter	Description	Value used by Xu, et al.[49]	New Suggested Value
E	Young's modulus for SiO_2	70 GPa [81]	~52-63 GPa [97; 98]
v	Poisson's ratio for SiO_2	0.17 [81]	0.2 [97]
ε^T	Linear transformation strain for SiC -> SiO_2	0.22	*ok*
Ω	Molar volume ratio for SiO_2/SiC	1.8	1.8 (SiC to SiO_2) – 2.0 (BN to B_2O_3)
η	Viscosity of SiO_2	$\eta=\eta_o(\tau/\tau_c)/\sinh(\tau/\tau_c)$	Log(η)=6.75
η_o	Reference viscosity for SiO_2	$\eta_o=3.8x10^{-14}$ exp(712/RT) Pa*s [99]	Depends on B_2O_3:SiO_2 ratio, Bruckner, et al. [40]
τ_c	Reference stress that is above deviation for Newtonian viscosity for SiO_2	100 MPa	*ok*
B	Parabolic rate constant from D&G model, SiC in dry O_2	$3.01x10^{-15}$ exp(-94.3/RT) m^2/s [71]	4x $B_{SiC\text{-}H2O}$ [96] – 10^4x $B_{SiC\text{-}H2O}$ [38]
A	From D&G model, SiC in dry O_2	$1.9x10^{-10}$ exp(75.7/RT) m [71]	Changes with P_{H2O} [15]
K_I	Stress intensity of SiC fiber based on SiO_2 scale	1.4 MPa $m^{1/2}$	Change due to η, v, E, for BSO instead of SiO_2
T	Temperatures of interest	700-1000°C	800-1300°C

A majority of the suggested parameters in Table 36 come from the literature, not directly determined in the present work. However, these parameters represent property changes, due to the incorporation of a condensed phase borosilicate glass in the model (determined by the results in this work for the RR-HTC CMCs), rather than annular voids filled with pure SiO_2.

No known mechanical property data exist for the binary borosilicate glass. So, the proposed Young's modulus and Poisson's ratio for borosilicate come from bulk borosilicate glasses, which can contain other oxides (Na_2O, K_2O, Al_2O_3). The additional oxides could affect these properties, but they are likely a better approximation for the thermally grown glass than pure SiO_2. The viscosity of the borosilicate glass will also vary from SiO_2 by several orders of magnitude depending on the boria composition.[40] These variations could be used to determine

η_o. The viscosity (η) reported in Table 36, however, is fixed based on the viscosity determined to form the sphere shape.

The new parameter with the largest variation is the parabolic rate constant, which would be increased compared to SiC due to the presence of boron. As described above, McFarland observed a ~4x increase in the parabolic oxidation rate for SiC fibers with a BN coating,[96] while Schlichting observed up to 10^4x increase in O_2 permeation rate compared to SiO_2 with varying amounts of B_2O_3 in the oxide. In this work, the matrix material coupons that contained boron experienced parabolic oxidation rates 1.3-3.6x or 2.9-7x SiC for temperatures of 1200-1300°C in wet or dry O_2, respectively. Although these rate data were obtained outside the temperature range of the model by Xu, et al., this variation in k_p indicates that an increased oxidation rate due to boron should be included in the model. Additionally, the work by McFarland and Schlichting were conducted in dry O_2. It was found in this study, along with other work,[8; 9; 15] that wet O_2 increases the oxidation rate of Si and SiC due to a ~10x increase in H_2O (g) permeability in SiO_2, compared to O_2 (g). Therefore, the recommended parabolic oxidation rates in Table 36 are 4x-10^4x the oxidation rate of SiC in H_2O (g). Future work should be conducted to better define boria effects on k_p for a more accurate CMC oxidation model.

7.4.2. Comparison to the CMC Oxidation Model by Jacobson, et al.

Similar to the model by Xu, et al., the CMC oxidation model by Jacobson, et al. results in annular voids surrounding the SiC fibers due to volatility of the borosilicate glass (Figure 12).[33] This model is based on six experimental conditions for oxidation of CMCs and minicomposites at temperatures between 500 and 816°C. The limited results were used to develop a model over the temperature range of 700-800°C. It should be noted that the highest temperature of interest in the model by Jacobson, et al. (800°C) overlaps with the lowest temperature used in the present

study. However, in the large volume of data from the present work, a condensed-phase borosilicate glass remained intact at 800°C (and 1200 and 1300°C).

To modify the model to accurately represent the results from the RR-HTC CMCs used in this work, several input parameters used by Jacobson, et al. should be changed. Relevant oxidation parameters used by Jacobson, et al. are listed in Table 37, along with suggested values in the last column. Parameters that were also included in Table 36 are not described in detail in this section.

Table 37. Parameters used in the model by Jacobson, et al.[33] and suggestions for new parameters to represent oxidation of a RR-HTC CMC

Parameter	Description	Value used in by Jacobson, et al.[33]	New Suggested Value
J_{HxByOz}	Flux of $H_xB_yO_z$ gases outward	Function of D_{HxByOz}, P_{HxByOz}, and T	Not rate limiting
y_{HxByOz}	Recession distance of BN due to $H_xB_yO_z$ volatilization	Function of J_{HxByOz} and molar volume of BN	Minimal BN recession observed
k_{HxByOz}	Recession rate of BN due to $H_xB_yO_z$ volatilization	Function of D_{HxByOz}, P_{HxByOz}, and T	Minimal BN recession observed
D	BN/annular void width	0.2-0.5 μm	No annular void formation
x	Mol fraction of B_2O_3 in borosilicate layer	0.5	0.43-0.63
B	Parabolic rate constant from D&G model	Table IV to start (SiC in dry O_2), then modified until model fits data	4x $B_{SiC\text{-}H2O}$ [96] – 10^4x $B_{SiC\text{-}H2O}$ [38]
A	From D&G model	Table IV for SiC to SiO_2 in dry O_2	Changes with P_{H2O} [15]
T	Temperatures of interest	700, 800°C	800-1300°C
x'	Molar volume change due to SiO_2 from SiC	~2	1.8 (SiC to SiO_2) – 2.0 (BN to B_2O_3)

The study by Jacobson, et al. stated that volatilization of an $H_xB_yO_z$ species (different species, depending on temperatures and environment) was the rate-limiting flux for BN recession.[33] In the present study for the RR-HTC CMCs, however, if volatilization did occur, it removed B_2O_3 from the borosilicate phase, leaving SiO_2, rather than a void. As described above,

changes in borosilicate composition will result in changes in oxidant permeation through the glass.

The BN recession reported by Jacobson, et al. resulted in annular void formation. The BN recession rate was dependent on the partial pressure and diffusion rates of the $H_xB_yO_z$ (g).[33] Additionally, the BN thickness and mole fraction of B_2O_3 in the borosilicate were used to calculate the annular void diameter and equilibrium vapor pressure of $H_xB_yO_z$, respectively. These parameters should instead be used to calculate the volume of borosilicate formed and the permeation rate of the oxidant through the borosilicate glass formed on the RR-HTC CMCs. As discussed for the previous model, oxidation rate constants for SiC in H_2O (g) should be used to predict increased oxidant permeation in a borosilicate glass.

A significant difference between the model by Jacobson, et al. and the results of this work, is the application temperature. For the most accurate application of the model by Jacobson, et al. to the RR-HTC CMCs, determination of new parameters for Table 37 could be determined after additional CMC oxidation experiments are conducted at lower temperatures (< 800°C), where annular void formation could be possible.

7.4.3. Comparison to the CMC Oxidation Model by Przybyla, et al.

The model by Przybyla, et al. is also constructed assuming the formation of annular voids around fibers, due to volatilization of BN/B_2O_3.[66] A temperature range reported in this model (800-1200°C) is similar to the temperature range extensively studied in the present work (800-1300°C). In the Przybyla model, the main CMC degradation mechanisms are described as the degradation of the fibers and the BN interphase due to oxidation. These mechanisms do not come from whole-composite oxidation experiments. The fiber degradation is based on a semi-empirical model by Parthasarathy, et al.[67] that assumes grain growth, fiber recession, and oxide

thickness determine the strength degradation of the stand-alone fiber, and ultimately failure of the composite. However, fiber degradation is only relevant when matrix cracks intersect fiber tows and lead to BN volatilization, exposing bare SiC fibers, which is predicted in this model.

In the model by Przybyla, et al., BN volatilization rates were calculated from the data of Jacobson, et al.,[33] which was described above. No new experiments of CMC oxidation were conducted by Przybyla, et al. Matrix cracks were assumed to be sufficiently large so that oxidation of the matrix itself did not seal the cracks. Parameters for the model by Przybyla are listed in Table 38. It should be noted that while these parameters are listed as important, numerical values are not provided for most parameters (marked with a question mark (?) in the table).[66] Parameters that were also included in Table 36 and Table 37 are not described in detail in this section.

Table 38. Parameters used in the model by Przybyla, et al.[66] and suggestions for new parameters to represent oxidation of a RR-HTC CMC

Parameter	Description	Value used in by Przybyla, et al.[66]	New Suggested Value
P_{HxByOz}	Equilibrium vapor pressure of $H_xB_yO_z$ (g) on B_2O_3-rich scale	Same as Jacobson, et al. [33]	Not rate limiting
V_{scale}	Molar volume of BSO scale	?	*ok*
$\Pi_{O2\text{-}SiO2}$	Permeability of oxygen in silica	10^{-12} exp(-172998/RT) mol/m-s-Pa	Based on BSO composition
H	Parameter to account for increased permeability due to P_{H2O}	25	10x ($\Pi_{O2\text{-}SiO2}$) [8]
$\Pi_{O2\text{-}scale}$	Permeability coefficient of oxygen in BSO scale	?	Unknown
$\Pi_{O2\text{-}scale(H2O)}$	Permeability coefficient of oxygen in scale in the presence of moisture	?	Unknown
$J_{O2\text{-}scale}$	Flux/permeation rate of oxygen through BSO scale	Same as Jacobson, et al. [33]	*ok*
L_{deg}	Length of interphase degradation/pore length	?	No void formation
$Po_{2,i}$, $P_{H2O,i}$	Partial pressure of oxygen or water vapor at the B_2O_3-rich scale/$H_xB_yO_z$ interface	?	0.5-1 atm
k_f	Oxidation rate of SiC fibers	From Parthasarathy [67]	Not applicable due to condensed BSO
k_m	Oxidation rate of matrix	k_f for CVI matrix, $2k_f$ for PIP or B-containing matrix	1.3-7x $k_{SiC\text{-}H2O}$
T	Temperature of interest	800-1200°C	800-1300°C
Δ_{COD}	Crack opening available for gaseous diffusion along the matrix crack	Large, so crack doesn't seal due to oxidation	*ok*
L_{surf}	Distance of the fiber tow from the free surface	?	Unknown
F_{tow}	Force on the fiber tow	Function of external stress and stress due to oxidation	Stress due to oxidation should be based on borosilicate properties, not SiO_2 properties

Several parameters listed in Table 38 are related to the borosilicate glass, but primarily to determine the equilibrium vapor pressure of $H_xB_yO_z$. The permeability of O_2 through the borosilicate scale is a key parameter, but no value is listed. This value would change based on the borosilicate composition, and is critical to determining CMC degradation due to oxidation for

the RR-HTC CMCs, as described above. It would be useful to compare the permeability of O_2 through the borosilicate from the Przybyla[66] model to the work by McFarland[96] and Schlichting[38] to determine the magnitude of the change due to boron, should that value become available in the future.

7.4.4. Stressed Oxidation Considerations

Although not included in the thermochemical mechanistic description developed in this work, the impact of applying a load to a CMC during oxidation was observed with SEM and EDS, as described in *Section 5.2.3. Stressed Permeability Testing*. Cracks and interphase oxidation were observed after some of the stressed permeability test conducted by Southern Research. This differed from the robust oxidation resistance of the unstressed, TGA-tested CMCs. However, as described in *Section 5.2.3. Stressed Permeability Testing*, not all CMCs tested in the stressed permeability conditions experienced matrix cracking and interphase oxidation. It was hypothesized that this variation was due, at least in part, to the variable starting permeabilities of the CMCs. Therefore, in future CMC life prediction models that include both thermochemical and thermomechanical effects, the applied load and the permeability of the CMC should be considered.

7.5. Recommendations for Future Work

Additional work must be conducted to supply accurate parameters outlined in the sections above. Oxidation tests should be conducted with CMC specimens (of known permeabilities) under load, to develop the relationship between thermochemical and thermomechanical oxidation behaviors. Oxidation tests with thermal cycling should also be conducted to understand the effect of cycling on the adhesion of the oxide.

Oxidation experiments should also be conducted with TGA at low temperatures ($\leq$ 700°C) with subsequent characterization to determine the conditions necessary for annular void formation in the RR-HTC CMCs. This would allow for direct comparison of the RR-HTC CMC oxidation results to the models by Xu, et al. and Jacobson, et al., which model oxidation as a result of annular void formation[33; 49] at low temperatures (700-1000°C).

Additionally, work should be conducted to understand oxidant permeation through borosilicates as a function of composition. Schlichting[38] and McFarland[96] reported drastically different increased O_2 permeation rates compared to SiO_2, ranging from 4x (McFarland) to 10^4x (Schlichting). A better understanding of oxidant permeability through borosilicate glasses as a function of boria content could improve the modeling of SiC and BN oxidation rates in CMC oxidation models if the relevant borosilicate compositions is known. To study the relevant borosilicate compositions, a quantitative technique to determine the composition of thermally grown borosilicate glasses is required.

Finally, effects of gas velocity on CMC sealing should be investigated. Volatilization reactions are known to increase in high velocity conditions due to reduced gas boundary layer thicknesses. Increased gas velocities could affect BN, B_2O_3, and SiO_2 stability.

8. Contributions and Conclusions

8.1. Original and Significant Contributions

New and significant contributions were made to the field of CMC and constituent oxidation through the work presented in this dissertation. Novel contributions are described here. Important scientific conclusions are described in the next section. The oxidation of SiC fibers in a significant water vapor content relevant for turbine applications (50 vol%) was conducted for the first time and oxidation mechanisms and kinetic data were determined for temperatures of 700-1300°C.

The oxidation of a Slurry-SMI matrix with SiC particulates and boron-containing regions in both dry and wet oxidizing environments was conducted for the first time. Kinetic data were determined for the high temperatures (1200-1300°C). Oxidation mechanisms varied from bulk SiC or Si due to the presence of boron.

Dense SiC/BN/SiC CMCs were oxidized over a large range of conditions (time, temperature, and environment) for the first time. Oxidation mechanisms were identified for surface oxidation and internal oxidation and found to be independent of temperature or environment over the conditions studied. A preliminary study of oxidation with applied load to study oxidation with crack formation was also conducted. Microscopy was conducted after interrupted exposures prior to rupture to probe the possible correlation between load and oxidation degradation.

8.2. Conclusions

The overall objective of this dissertation was to develop an understanding of SiC/BN/SiC oxidation mechanisms and behavior over a large range of conditions, varying time, temperature, environment, and load to address existing gaps in knowledge. This was achieved by the

oxidation of the stand-alone CMC constituents and CMCs with TGA, which resulted in the following conclusions.

- Oxidation of Hi-Nicalon SiC fibers in 50 vol% H_2O resulted in increased SiO_2 formation, as compared to dry O_2 oxidation of the fibers, as expected. However, at the high temperatures (1200-1300°C) a crystalline oxide (cristobalite) formed and cracked *in situ* due to tensile hoop stresses that developed in the oxide due to the cylindrical nature of the fiber. The cracks in the oxide led to increased SiC fiber oxidation, increasing the oxidation rates and resulting in complete fiber oxidation after 100h at 1300°C. Three oxidation mechanisms were identified for the fibers oxidized at 1300°C in wet O_2: i) oxidant permeation-control (parabolic kinetics) at short times (< 6h), ii) reaction-rate-control (linear kinetics) at intermediate times (6h < t < 50h) due to *in situ* cracking of the oxide, and iii) shrinking-cylinder-control (slowing rate with time) as the available fiber surface area was reduced to zero. Mechanisms (ii) and (iii) were not previously identified for SiC oxidation in wet O_2 prior to this study. The rapid oxidation of SiC fibers under wet O_2 conditions will be detrimental to strength of CMCs if bare fibers are exposed in the CMCs.
- Oxidation of a Slurry-SMI matrix with SiC particulates and boron-containing regions resulted in different oxidation behavior in both dry and wet O_2 as compared to bulk Si or SiC due to the presence of boron. Three effects due to the presence of boron were identified: i) rapid formation of borosilicate droplets in the vicinity of boron-containing regions, ii) formation of a porous oxide at high temperatures (1200 and 1300°C) due to increased product gases from the boron-enhanced oxidation rates, and iii) increased oxidation rates due to increased oxidant permeability in a porous borosilicate glass

compared to dense SiO_2. The oxidation behavior of the stand-alone matrix material can be used as a comparison for CMC oxidation behavior for the first time, rather than comparisons to bulk SiC.

- The external CMC surfaces sealed with an oxide of non-uniform composition that has not been characterized in prior studies. B_2O_3-rich oxide droplets rapidly (< 1.2h) sealed the BN interphase independent of temperature and environment while SiO_2 formed on the surrounding SiC phases. The non-uniformity of the oxide composition will lead to non-uniform properties, including oxide viscosity and oxidant permeabilities. The borosilicate droplet compositions were characterized semi-quantitatively with EELS giving a range of 0-42 wt% B_2O_3 (balance SiO_2) after 100h exposures. The temperature and compositional dependence of stand-alone borosilicate glass melting resulted in estimates for initial droplet compositions in the range of 43-63 wt% B_2O_3. High B_2O_3 contents in the glass will result in reduced oxidant viscosity as compared to SiO_2. However, reliable permeability data for binary borosilicate glasses do not exist.
- The observed oxidation mechanisms of phases in the interior of the CMCs were independent of temperature or environment in the conditions studied: the SiC fibers oxidized first, followed by the SiC matrix, and last the BN interphase. The preferential oxidation of SiC over BN indicated that the Po_2 must be lower than the BN/B_2O_3 equilibrium oxygen partial pressure (10^{-19} atm at 1300°C). Interphase-interface oxides observed at a minority of BN/SiC interfaces were hypothesized to form by either of two mechanisms. In the first, transport of oxidants down a gap between the BN interphase and the SiC fiber was considered; however, such gaps were not observed in TEM of a limited number of samples. A second possibility is that interphase occurred by transport of

oxidant through a condensed phase oxide. Estimated diffusivities from limited oxidation ingress length measurements along SiC/BN interfaces were the same order of magnitude as H_2O (10^{-9} cm^2/s) and O_2 (10^{-8} cm^2/s) through SiO_2. This result indicates that a condensed phase oxide with a composition close to SiO_2 could exist along the SiC/BN interfaces in the interior of the CMC. However, the observations of interphase-interface oxides were rare, making this hypothesis only tentative.

In summary, the findings in this dissertation identify new and critical oxidation mechanisms for dense SiC/BN/SiC CMCs that must be considered in the development of any accurate CMC oxidative life prediction model.

8.3. Future Work

Many suggestions for future work were proposed throughout this dissertation. This section serves to prioritize the suggestions that would result in the most significant impact to the field of CMC oxidation. Oxidation of CMCs is thought to be more beneficial than of the stand-alone constituents. It should be noted that the oxidation behavior of CMCs fabricated by alternative processes will be different, and the recommended work pertains to CMCs with a dense matrix and a thin BN interphase (BN thickness << fiber diameter), similar to the CMCs studied in this work. Additionally, for all CMC oxidation studies, sufficient numbers of specimens should be studied to allow for statistical interpretation of results due to typical stochastic variation in CMC microstructures.

First, it is suggested that CMC oxidation tests be conducted with a range of applied loads that induce matrix cracking, but do not cause failure, so crack propagation and sealing rates can be determined as a function of time, temperature, environment, and applied load. This study

could yield relevant data necessary to explore the synergy between oxidation and cracking as well as to determine CMC oxidation rates that can be used in a lifetime prediction model.

Effects of gas velocity on CMC sealing should be investigated. Volatilization reactions are known to increase in high velocity conditions due to reduced gas boundary layer thicknesses. It is therefore recommended that a high-velocity steam-jet furnace be used to oxidize these CMCs. Increased gas velocities could affect BN, B_2O_3, and SiO_2 stability, reducing the protective nature of the thermally grown oxide on the CMCs.

Work should be conducted to understand oxidant permeation through borosilicates as a function of composition. Other authors have reported drastically different increased O_2 permeation rates in borosilicate glasses, ranging from factors of 4 to 10^4 times greater than SiO_2. An understanding of oxidant permeability through borosilicate glasses as a function of boria content and temperature is critical to the accurate modeling of SiC and BN oxidation rates in CMCs. In addition, identification or development of methods for the accurate and spatially resolved determination of thermally grown borosilicate compositions is needed.

Low temperatures ($\leq 700°C$) oxidation of CMCs with subsequent characterization is needed to determine the conditions necessary, if any, for annular void formation due to oxidation/volatilization of the BN interphase. This would allow for direct comparison of experimental low temperature CMC oxidation results to existing CMC oxidation models, which assume annular void formation.

Annular void formation will also be affected by the thickness and crystallinity of the BN interphase. Oxidation experiments of composites of Hi-Nicalon fibers with controlled variations in BN thickness and crystallinity within a SiC matrix should be conducted to systematically understand the resulting differences in oxidation behavior in CMCs.

Last, it is recommended that short time (< 1h) oxidation tests be conducted in a horizontal tube furnace at similar temperatures to this work (800-1300°C) to determine the kinetics of BN interphase sealing due to oxidation as a function of temperature and environment.

8.4. Challenges Associated with Borosilicate Glasses

There are many challenges associated with studying borosilicate glasses. Quantitative determination of borosilicate compositions is challenging for several reasons. First, many techniques such as EDS can only detect boron qualitatively (or not at all) due to its low atomic number. EELS is often used to quantify light elements, but higher atomic number elements (such as Si) have high K-electron energy losses or L-electron energy losses that can be challenging to fit due to plasmon excitations. For either of these techniques, use of a compositional standard could help to determine the best analysis conditions. However, true quantification of both Si and B with the same technique will likely continue to be challenging. Additionally, B_2O_3 can be challenging to quantify due to its high volatility in O_2 and H_2O (g) environments.

In addition to difficulties in quantifying borosilicate compositions, very little property data exist for binary borosilicates. Viscosity data do exist, but mechanical property data (Young's modulus, etc.) and kinetic data (O_2 and H_2O permeabilities) relevant for CMC oxidation are unknown. Determination of these properties at relevant high temperatures (≥ 800°C) is challenging, again due to the high volatility of B_2O_3 at these temperatures. These difficulties associated with determining borosilicate glass properties (composition, permeability, etc.) make it a challenging material to study quantitatively.

Appendix A. A Review of SiC Fiber Oxidation with a New Study of Hi-Nicalon SiC Fiber Oxidation, *Advanced Engineering Materials*

(See PDF attachment)

Appendix B. Final State of CMC Coupons

				Post-test Status					
CMC	**Environ.**	**Temperature (°C)**	**Duration (h)**	**1/2 in epoxy**	**1/2 Ion-Polished**	**1/2 in ICP tube**	**Intact**	**Cut for XRD**	**TEM**
1.1	AR			x	**x**				
1.2	dry	1200	100	x		x (#3)			
1.3	wet	1200	100	x		x (#3)			
1.4	wet	1200	100	x		x (#2)			
1.5	dry	1200	100	x	x				x
1.6	dry	1300	100	x	x				x
1.7	dry	800	100	x					
1.8	dry	800	100	x	x				x, x
1.9	dry	800	100	x		x (#3)			
1.10	wet	1300	100	x		x (#2)			x
1.11	wet	800	100		x		x		x
1.12	wet	800	100		x	x (#2)			x
1.13	wet	800	50	x			x		
1.14	dry	800	50	x			x		
1.15	wet (open face)	800	100	x			x		
1.16	AR					x (#3) x (#3)			x
2.1	wet	1300	100		x	x (#2)			x
2.2	dry	1200	100	x		x (#3)			
2.3	dry	1200	50		x	x (#3)			x
2.4	dry	1300	100			x (#3)			
2.5	dry	1300	50	x		x (#3)			
2.6	dry	1300	50			x (#1)			
2.7	dry	1200	50				x (whole)		
2.8	dry	800	50	x		x (#2)			
2.9	dry	800	1		x	x (#3)			x
2.10	dry	1200	1	x		x (#3)			
2.11	dry	1300	1		x	x (#3)			
2.12	wet	1200	1	x		x (#3)			
2.13	wet	1200	50	x		x (#3)			
2.14	wet	800	1		x	x (#3)			
2.15	wet	1300	38+6				x (whole)		
2.16	AR (CTE)								

3.1	wet	1300	1		x	x (#3)			
3.2	wet	1300	50	x		x (#3)			
3.3	dry	800	1				x (whole)		
3.4	dry	1200	1				x (whole)		
3.5	wet	800	50	x		x (#2)			
3.6	dry	1300	1			x (#1) x (#3)			
3.7	wet	800	1				x (pieces) , x		x
3.8	wet	1300	40			x (#1) x (#2)			
3.9	wet	1300	1			x (#1) x (#2)			
3.10	wet	1200	50			x whole			
3.11	wet	1200	31				x (whole)		
3.12	wet	1200	1			x (#3) x			
3.13	wet	1200	100				x	x	
3.14	dry	1200	100			x (#1) x (#2)			
3.15	AR								
3.16	AR					x (#2) x (#3)			
4.1	dry	1300	100			x (#1) x (#2)			
4.2	wet	1300	100			x (#1) x			
4.3	wet	800	100			x (#1) x (#2)			
4.4	wet	1300	100			x (#1) x (#2)			
4.5	dry	800	100			x (#1) x (#2)			
4.6	wet	1200	1			x (#2)	x		
4.7	dry	1300	1			x (#2)	x		
4.8	wet	1300	1			x (#2)	x		
4.9	dry	1300	50			x (#2)	x		
4.10	wet	1300	50			x (#2)	x		
4.11	dry	800	12				x (whole)		

4.12	Unused								
4.13	Unused								
4.14	Unused								
4.15	unused								
4.16	AR					x (#1) x (#2)			

Appendix C. $Si(OH)_4$ Volatility Calculation for a SiO_2 Coupon in TGA

The text from this section can be used for calculations in Mathcad.

First, define the system and sample parameters:

Gas parameters:

Gas Composition:

50% H_2O

50% O_2

$P := 1 \cdot atm$

$T := 1473 \cdot K$

(1200C)

$v := 1000 \cdot \frac{cm^3}{min}$

$RT := 293 \cdot K$

sample length:

$L := 2.5 \cdot cm$

Tube geometry:

$r := 1.1 \cdot cm$

$A := 3.801 \cdot cm^2$

Assume the boundary layer of oxygen and water vapor at the surface of the SiC coupon is rate controlling and calculate the Reynold's number.

First determine the density of the gas mixture:

$M_A := 32 \cdot \frac{gm}{mole}$

The product ρv in the Reynold's number represents the flux through the reaction tube. Room temperature values are used in this case since v is only known at room temperature. The flux will be the same in the hot zone but ρ will be lower and v will be higher due to gas expansion. *The product of the two terms is independent of temperature.*

$$M_B := 18 \cdot \frac{gm}{mole}$$

$$X_A := 0.5$$

$$X_B := 0.5$$

$$R := 82.06 \cdot \frac{cm^3 \cdot atm}{mole \cdot K}$$

$$\rho := \frac{P \cdot \left(X_A \cdot M_A + X_B \cdot M_B \right)}{R \cdot RT}$$

$$\rho = 1.04 \times 10^{-3} \frac{gm}{cm^3}$$

Calculate the linear gas velocity in this system:

$$v_l := \frac{v}{A}$$

$$v_l = 4.385 \frac{cm}{sec}$$

η (T) is the viscosity of the H_2O - O_2 gas mixture. Individual viscosities are from NASA Technical Report R-132 by R.A. Svehla

$$\eta_A := 6.17 \cdot 10^{-4} \cdot \frac{gm}{cm \cdot sec}$$

viscosity for oxygen

$$\eta_B := 5.13 \cdot 10^{-4} \cdot \frac{gm}{cm \cdot sec}$$

viscosity for water vapor

This expression is valid when the molecular weights of A and B are not too different.

$$\eta := \frac{X_A \cdot \eta_A \cdot \sqrt{M_A} + X_B \cdot \eta_B \cdot \sqrt{M_B}}{X_A \cdot \sqrt{M_A} + X_B \cdot \sqrt{M_B}}$$

$$\eta = 5.724 \times 10^{-4} \frac{gm}{cm \cdot sec}$$

Finally, the Reynold's number:

$$Re_l := \frac{\rho \cdot v_l \cdot L}{\eta}$$

$$Re_l = 19.912$$

Calculate the interdiffusion coefficient for the oxygen/water vapor mixture and $Si(OH)_4$ gases.

Calculate this for $Si(OH)_4$ in water vapor. The collision diameter, σ, and collision integral, Ω, must be calculated first. A useful reference for these values is NASA Technical Report R-132 by R.A. Svehla.

$$\sigma_A := 2.641$$

collision diameter for H_2O in angstroms

$$\sigma_B := 4.880$$

collision diameter for SiF_4 in angstroms as an approximation

for $Si(OH)_4$

$$\sigma_{AB} := \frac{\sigma_A + \sigma_B}{2}$$

$$\sigma_{AB} = 3.76$$

$$\varepsilon_A := 809.1 \cdot K$$

This value is ε/κ for water vapor

$\varepsilon_B := 171.9 \cdot K$

This value is ε/κ for SiF_4

$\varepsilon_{AB} := \sqrt{\varepsilon_A \cdot \varepsilon_B}$

$\varepsilon_{AB} = 3.729 \times 10^2\ K$

$T' := \frac{T}{\varepsilon_{AB}}$

$T' = 3.95$

Ω is then picked from a table on p. 20 of Mass Transfer by Sherwood et al. based on the value of T`.

$\Omega := 0.88$

The interdiffusion coefficient can now be calculated using the Chapman-Enskog Equation:

$M_A := 18$

The values are all entered without units here because the equation is formulated with the constant .0018583 and P(atm), T(K), σ(angstroms), M(gm/mole).

$M_B := 96$

$T := 1473$

$P := 1$

$$D_{AB} := .0018583 \cdot \sqrt{\frac{1}{M_A} + \frac{1}{M_B}} \cdot T^{\frac{3}{2}} \cdot \left(\frac{1}{P \cdot \sigma_{AB}^{\ 2} \cdot \Omega} \right)$$

$D_{AB} = 2.154$

$D_{AB} := 2.154 \cdot \frac{cm^2}{sec}$

The Schmidt number can now be calculated:

The gas density must be recalculated at the sample temperature

$T := 1473 \cdot K$

$P := 1 \cdot atm$

$M_A := 32 \cdot \frac{gm}{mole}$

$M_B := 18 \cdot \frac{gm}{mole}$

$X_A := 0.5$

$X_B := 0.5$

$R := 82.06 \cdot \frac{cm^3 \cdot atm}{mole \cdot K}$

$\rho := \frac{P \cdot (X_A \cdot M_A + X_B \cdot M_B)}{R \cdot T}$

$\rho = 2.068 \times 10^{-4} \frac{gm}{cm^3}$

$Sc := \frac{\eta}{\rho \cdot D_{AB}}$

$Sc = 1.285$

The pressure and concentration of $Si(OH)_4$ are now needed:

This information is taken from Hashimoto's data, Geochimica et Cosmochimica Acta Vol. 56, pp. 511-532.

$T := 1473$

$LogK := -.2963 \cdot \frac{10^4}{T} - 3.4563$

$LogK = -5.468$

$$K_{eq} := 10^{LogK}$$

$$K_{eq} = 3.405 \times 10^{-6}$$

$$P_{SiOH4} := K_{eq} \cdot X_B^{2}$$

$$P_{SiOH4} = 8.513 \times 10^{-7}$$

$$P_{SiOH4} := 8.513 \cdot 10^{-7} \cdot atm$$

The concentration of $Si(OH)_4$ is then:

$$M_B := 96 \cdot \frac{gm}{mole}$$

$$T := 1473 \cdot K$$

$$\rho_{SiOH4} := \frac{P_{SiOH4} \cdot M_B}{R \cdot T}$$

$$\rho_{SiOH4} = 6.761 \times 10^{-10} \frac{gm}{cm^3}$$

Now the flux of $Si(OH)_4$ from a flat plate can be calculated:

$$J := \frac{0.664 \cdot Re_l^{\frac{1}{2}} \cdot Sc^{\frac{1}{3}} \cdot D_{AB} \cdot \rho_{SiOH4}}{L}$$

$$J = 1.876 \times 10^{-9} \frac{gm}{cm^2 \cdot sec}$$

$$J = 6.755 \times 10^{-3} \frac{mg}{cm^2 \cdot hr}$$

$$J_{SiO2} := J \cdot \frac{60}{96}$$

$$J_{SiO2} = 4.222 \times 10^{-3} \frac{mg}{cm^2 \cdot hr}$$

Appendix D. Oxide Hoop Stress Calculations

The following Equations (D1-D6) from Hsueh and Evans[80] were used to calculate radial and hoop stresses in the SiO_2 thermally grown on a SiC fiber.

$$\sigma_r^{oxide}(r) = \frac{e^T E_{oxide}}{2(1-\nu_{oxide}^2)}\left[\ln\left(\frac{r}{a}\right) - \frac{\left(1-\frac{a^2}{r^2}\right)}{2}\right] + \frac{E_{oxide}}{(1+\nu_{oxide})}\left[\left(\frac{1}{(1-2\nu_{oxide})} + \frac{a^2}{r^2}\right)p^{oxide} - \frac{q^{oxide}}{r^2}\right] \quad [D1]$$

$$\sigma_\theta^{oxide}(r) = \frac{e^T E_{oxide}}{2(1-\nu_{oxide}^2)}\left[\ln\left(\frac{r}{a}\right) + \frac{\left(1-\frac{a^2}{r^2}\right)}{2}\right] + \frac{E_{oxide}}{(1+\nu_{oxide})}\left[\left(\frac{1}{(1-2\nu_{oxide})} - \frac{a^2}{r^2}\right)p^{oxide} + \frac{q^{oxide}}{r^2}\right] \quad [D2]$$

$$\sigma_r^{fiber}(r) = \sigma_\theta^{fiber}(r) = \frac{E_{fiber}p^{fiber}}{\left[(1+\nu_{fiber})(1-2\nu_{fiber})\right]} \quad [D3]$$

$$q^{oxide} = \frac{\frac{e^T}{2(1-\nu_{oxide})}\left(\frac{1}{2\left(1-\frac{a^2}{b^2}\right)} - \ln\left(\frac{b}{a}\right)\right)}{\frac{1}{2(1-\nu_{oxide})}\left(1+\frac{(1-2\nu_{oxide})a^2}{b^2}\right)\left(\frac{E_{fiber}(1+\nu_{oxide})}{E_{oxide}(1+\nu_{fiber})(1-2\nu_{fiber})}+1\right)\frac{1}{a^2}-\frac{1}{b^2}} \quad [D4]$$

$$p^{fiber} = \frac{q^{oxide}}{a^2} \quad [D5]$$

$$p^{oxide} = \frac{1-2\nu_{oxide}}{2(1-\nu_{oxide})}\left(\frac{E_{fiber}(1+\nu_{oxide})}{E_{oxide}(1+\nu_{fiber})(1-2\nu_{fiber})} + 1\right)\frac{q^{oxide}}{a^2} \quad [D6]$$

The parameter definitions and values used to calculate these stresses for a fiber oxidized at 1300°C in wet O_2 for 100h are in Table 39.

Table 39. Parameters used to calculate radial and hoop stresses via equations in Hsueh and Evans[80] for a fiber and the thermally grown oxide after 100h at 1300°C in wet O_2

Parameter	Value	Reference
Radial expansion tensor e^T	1.27	[100]
Young's modulus of the oxide (SiO_2) E_{oxide} (GPa)	66	[101]
Poisson's ratio of the oxide ν_{oxide}	0.18	[101]
Young's modulus of the fiber (SiC) E_{fiber} (GPa)	270	[102]
Poisson's ratio of the fiber ν_{fiber}	0.16	[81]
Initial fiber radius b (μm)	7	[102]
Final fiber radius a (μm)	2.86	This Study
Final radius (fiber + oxide) x (μm)	11.45	This Study

Young's modulus (E_{oxide}) and Poisson's ratio (ν_{oxide}) for the oxide were taken from Jaccodine, et al., where Si was oxidized to SiO_2 from 875-1200°C.[101] Jaccodine determined the Young's modulus from a SiO_2 "balloon" technique at room temperature once the oxides had been thermally grown. This technique was proven to be more accurate than the bending-beam technique used in the same work[101] and is appropriate for determining strains in thermally grown amorphous silica. Although the SiO_2 in this work was amorphous, the mechanical property values are used as estimated for the values for β-cristobalite due to experimental difficulties associated with direct measurements in the β-cristobalite phase. β-cristobalite transforms to α-cristobalite around 270°C (with a resulting 4.9% volume decrease), so mechanical properties (Young's modulus, Poisson's ratio) and kinetic properties (oxidant

diffusivities) cannot be measured at room temperature. To measure these parameters, the β-cristobalite would have to be thermally grown at high temperatures (≥1200°C) and direct measurements would have to take place before the sample is cooled. Property values for β-cristobalite are therefore unavailable and the use of the values for amorphous SiO_2 in Table 39 are the most appropriate estimations for β-cristobalite needed for this work.

Stresses normalized by E_{fiber} and a position (r) normalized by the final (fiber + oxide) radius (x) were used to plot hoop and radial stresses for the fiber and the oxide after 100h at 1300°C (Figure 110). The interface between the fiber and oxide is labeled at a value of a/x. The radial stress switches from compressive to tensile approximately halfway through the oxide layer, but the maximum radial stress is less than one-third of the maximum hoop stress. If radial stresses dominated in the oxide, cracking or delamination would occur parallel to the fiber/oxide interface. Delamination of that nature was not observed with SEM after SiC fiber oxidation, so the radial stress will be neglected and the hoop stress will be the primary focus of this analysis.

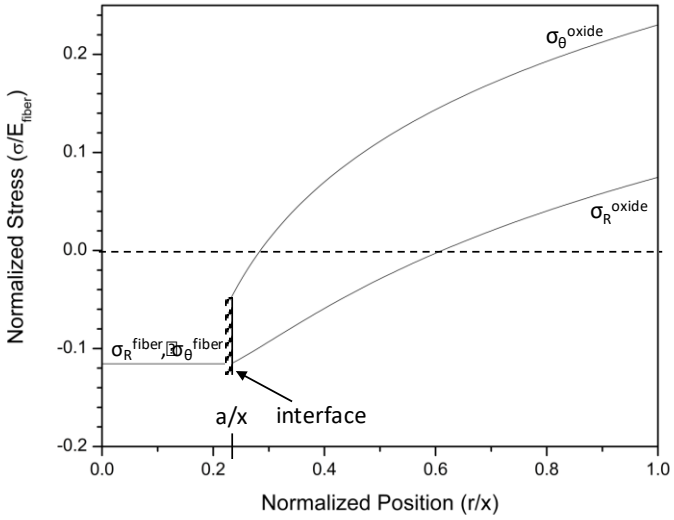

Figure 110. The radial (r) and hoop (θ) stresses of the fiber and oxide after 100h, wet O_2 exposure at 1300°C, as calculated by Equations C1-C6 (from Hsueh and Evans).

The fiber/oxide interface is shown at the position a/x. At positions > a/x, the normalized oxide stresses are increasing. The normalized hoop stress in the oxide quickly changes from

compression ($\sigma < 0$) to tension ($\sigma > 0$). For the example plotted in Figure 110, the hoop stress switches from compression to tension 0.64 μm from the fiber/oxide interface. The stresses in the oxide are calculated for the situation where no cracks have formed. It is likely that such large stresses do not actually exist in the oxide, but that cracks form with a thinner crystalline oxide *in situ* and that cracks continue to grow as the oxide itself grows. This is consistent with the observation of cracks beginning after 6h at 1300°C in wet O_2. The calculation based on the work of Hsueh and Evans was therefore used as an approximation of the maximum stress that would exist in the oxide if no cracking occurred.

The parameters in Table 39 were also used to calculate the stress for the fiber oxidized at 1100°C using appropriate values of a = 5.08 μm for final fiber radius and x = 9.28 μm for final radius of fiber + oxide (Figure 111). The normalized tensile stress at the exterior of the oxide after 100h in wet O_2 at 1100°C is about half that of the normalized tensile stress at the exterior of the oxide at 1300°C.

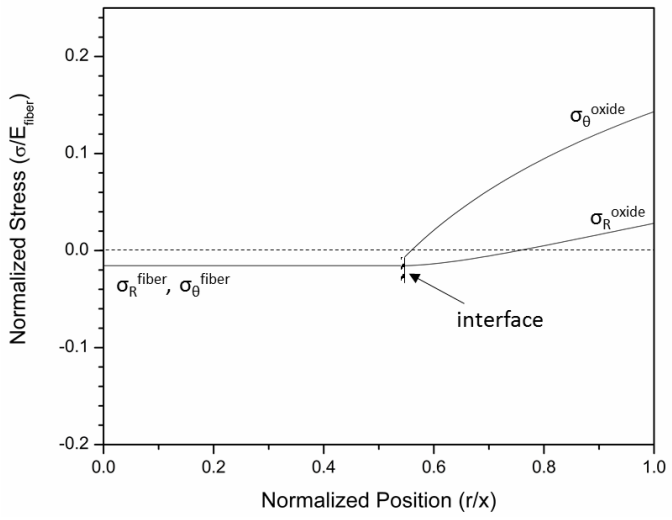

Figure 111. The radial (r) and hoop (θ) stresses of the fiber and oxide after 100h, wet O_2 exposure at 1100°C, as calculated by Equations C1-C6 (from Hsueh and Evans).

Although the tensile stress for the 1100°C condition is about half that of the 1300°C condition, it is still high (near 40 GPa). This high of a stress is also unrealistic in the amorphous oxide. However, because the SiO_2 is amorphous at these conditions, the stresses in the amorphous oxide exposed to these temperatures are relaxed by viscoelastic flow or creep.[88] The mechanism for creep would be different in cristobalite due to its crystalline nature. The viscoelastic flow in amorphous SiO_2 must significantly reduce the hoop stresses in the oxide because amorphous oxide thicknesses observed after 100h at 1100°C in wet O_2 (4.2 ± 0.3 μm) did not crack. At high pressure (180 psi) and temperature (1300°C) SiO_2 glass was reported to have a creep rate 3 to 5 orders of magnitude higher than polycrystalline oxides that have similar cubic crystal structures to β-cristobalite at the same conditions.[22] The creep rate at lower pressure (10psi) at 1300°C is only reported for the glass (0.001 h^{-1}), so no direct comparison can be made for cristobalite.

It should also be noted that the average crystalline oxide thickness observed at 24h in wet O_2 at 1300°C (2.7 ± 0.5 μm) was cracked, which was less than the average continuous, amorphous oxide thickness observed after 100h at 1100°C in wet O_2 (4.2 ± 0.3 μm). This is another indication that the phase of the oxide plays a role in the oxide cracking, in addition to oxide thickness. Because no known creep data are available for crystalline SiO_2, it is neglected in the remainder of this analysis.

When creep is neglected, a critical stress level (σ_F) based on the Griffith relation can be estimated. Hoop stresses were calculated for a normalized position (r/x) of 1 for 100h wet O_2 oxidation experiments for 800-1300°CGiven that a continuous amorphous oxide formed after 100h at 1100°C in wet O_2 and cracks formed in the 1300°C crystalline oxides, there is likely a critical stress level between the two that causes a brittle fracture in the oxide.

To determine the critical stress level (σ_F) for this system, the Griffith relation[86] for brittle fracture was used:

$$U = 4ct\gamma_{oxide} - \frac{\pi\sigma^2 c^2 t}{E_{oxide}} + U_o \quad [D7]$$

where U is the potential energy of the oxide with a crack, U_o is the potential energy of the oxide without a crack, c is half of the crack length, γ_{oxide} is the surface energy of cristobalite, σ is the stress state in the oxide and t is the oxide thickness. The equality accounts both for the increase in surface energy from forming the crack as well as the decrease in potential energy that results from the release of stored elastic energy. At equilibrium, the partial derivative of U with respect to the crack length is zero, yielding the following relationship:

$$\sigma_F = \sqrt{\frac{2\gamma_{oxide}E_{oxide}}{\pi c}} \quad [D8]$$

Therefore, if the hoop stress in the oxide (σ_θ) is > σ_F as determined from the equation above, the oxide will crack. The Griffith criterion gives the amount of energy required to grow an existing crack. Because the initial crack length was not determined in this study, two bounding cases are proposed in this section as first estimations. The first bounding case uses the 100h test oxide thicknesses at each temperature as the crack lengths. The second bounding case uses the smallest observed oxide thickness showing cracks. For all fracture stress calculations, a surface energy of 72 erg/cm^2 was used for cristobalite,[103] and the same value for E_{oxide} was used from Table 39. For the first case, the 100h oxide thicknesses reported in Table 10 were used for the crack length, c, and the resulting critical stress levels, σ_F, for the 100h exposures for temperatures of 800-1300°C are reported in Table 40.

Table 40. Calculated fracture stresses (σ_F) based on the Griffith criterion and hoop stresses in the oxide layer (σ_θ) by the Hsueh and Evans method for 100h wet O2 fiber oxidation tests

Test Temperature (°C)	Oxide Thickness/Crack Length (μm)	σ_F (GPa) Eqn. 27	σ_θ (GPa) Eqn. 20-25
800	0.51	77.0	3.9
900	1.93	39.6	13.5
1000	3.20	30.8	26.2
1100	4.2	26.8	38.7
1200	5.1	24.4	44.5
1300	8.6	18.8	62.1

When $\sigma_\theta > \sigma_F$, fracture of the oxide scale is possible. Figure 112 shows the values from Table 40 graphically.

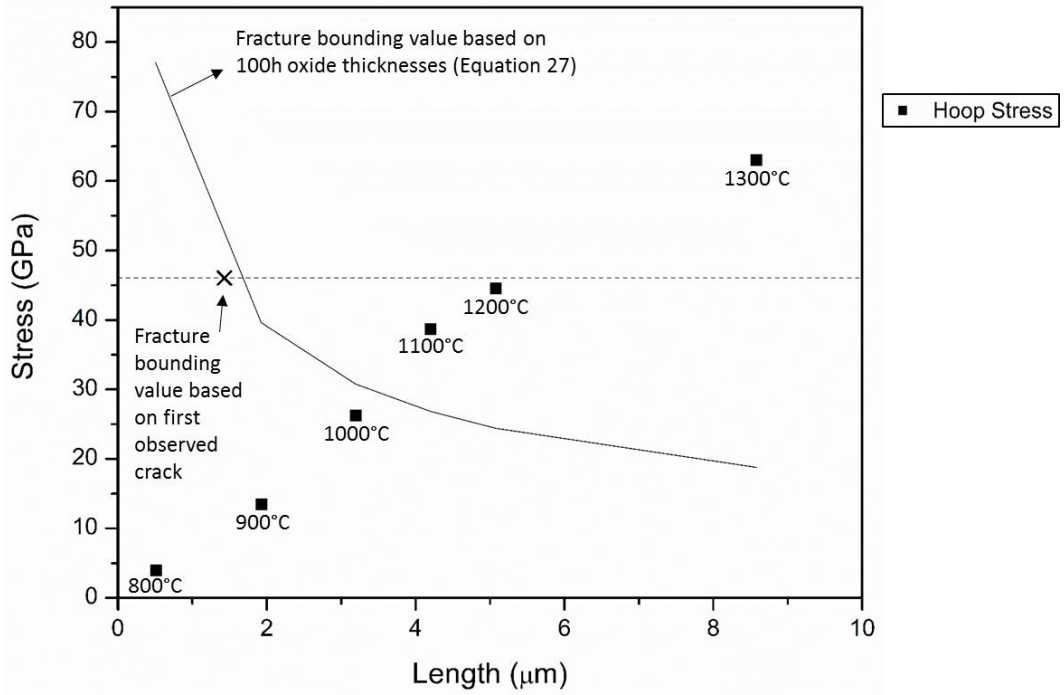

Figure 112. Fracture stresses calculated using the Griffith criterion for 100h cracks (solid line), first observed crack (dashed line), and hoop stresses calculated using the Hsueh and Evans model (points) calculated for measured oxide thicknesses after 100h in wet O_2.

It can be seen from Table 40 and Figure 112 that oxide thicknesses after 100h in wet O_2 at temperatures of 1100-1300°C could fracture due to the hoop stresses. It is important to note,

that the calculated stresses do not account for creep that likely occurred in the amorphous oxides, which would likely change the fracture requirements.

The second case is considered because oxide cracking was observed before 100h in wet O_2 at 1200 and 1300°C, as summarized in Table 9. The shortest time where cracks were observed was for a 6h, 1300°C, wet O_2 exposure where some of the oxides had crystalline edges and two fibers had oxide cracks (one fiber shown in Figure 36). The average oxide thickness from this test (1.43 ± 0.15 μm) was used as the crack length, *c*, to calculate a fracture stress of 46.0 GPa using the Griffith equation (Equation D8). This fracture stress value is less than the hoop stress for the 100h, 1300°C, wet O_2 exposure (62.1 GPa) and nearly the same as the 100h, 1200°C, wet O_2 exposure (44.5 GPa), indicating that fracture in the oxide at these conditions is still possible, and provides a more likely bounding value for cristobalite fracture. However, it is acknowledged that even this stress is unrealistically high, and that other fracture mechanisms could be at play, as described in *Chapter 3. Oxidation of Hi-Nicalon SiC Fibers*.

Appendix E. ICP-OES Digestions and Complications for CMC Oxides

E.1. Background

Inductively Coupled Plasma-Optical Emission Spectroscopy (ICP-OES) is a quantitative analysis tool that can be used to detect elemental concentrations on the order of parts-per million (ppm) in solutions. ICP-OES has been used to determine compositions of oxides after the oxides were digested in H_2O (l) or acidic solutions if the substrate is inert in the H_2O or acid solutions.[104; 105; 106] In this work, oxidized CMCs were digested in H_2O (l) and HF/H_2O solutions to determine the B and Si concentrations to determine the composition of the borosilicate glass by calculating B_2O_3:SiO_2 ratios. Several digestion procedures were used. The procedures, results, and complications due to interference from baseline interphase and matrix dissolution are presented below. The Si and B concentrations determined from ICP-OES should not be used to calculation mol% B_2O_3 in the surface oxide due to the reactions of the baseline interphase and matrix phases with the digestion solutions.

It is important to note that in prior work in this laboratory (by Hagan), baseline CMCs fabricated by different processes were stable in H_2O and HF solutions.[107]

E.2. General ICP-OES Procedure

For oxide compositional analysis by ICP-OES (iCap 6200 Duo Spectrometer, Thermo Fisher Scientific, Inc., Waltham MA), oxidized CMC coupon halves (Figure 113) were digested in H_2O and HF/H_2O solutions.

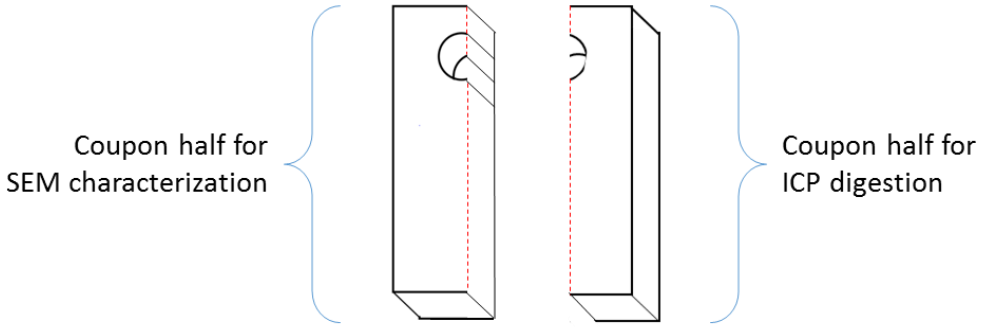

Figure 113. Diagram of CMC coupon halves, showing half for SEM characterization and half for analysis with ICP-OES.

The ICP-OES was calibrated with Si and B solutions prepared from known Si and B concentrations (1, 10, 100, or 500 ppm Si or B) (Inorganic Adventures, Christiansburg, VA) prior to analysis of the H_2O/HF solutions. The spectrometer was operated in an Ar plasma. Three (208.8, 249.6, and 249.7 nm) and five (185.0, 221.6, 250.6, 251.6, 288.1 nm) emission lines were used for detecting B and Si, respectively. All emission lines were referenced to the Indium 230.6 (II) nm line. A 10 ppm Indium standard was used during all analyses. Three repeats were measured per emission line, then used to calculate average concentrations using the AutoView Plasma View software.

The average B and Si concentrations (ppm) were converted to mol% B_2O_3 and SiO_2. Several assumptions were made for the analysis. First, it was assumed that the only possible oxide compositions were SiO_2 and B_2O_3. Next, it was assumed that for every 1 mol of Si detected by the ICP-OES, 1 mol of SiO_2 was dissolved in the acid solution and for every 2 mol of B detected, 1 mol of B_2O_3 was dissolved.

E.3. Oxidized CMC Digestions

E.3.1. Digestion Procedure #1

A majority of the oxidized CMC coupon halves (48 of 50) were digested in 2.5 mL of 48 wt% trace metal grade hydrofluoric acid (HF) (Thermo Fisher Scientific, Inc., Waltham, MA)

and 5 mL deionized H_2O (l) to dissolve the oxide, based on similar procedures used for SiO_2 and borosilicate glasses.[96; 107; 108; 109] These coupons were digested for 1-7 days. After the CMC was removed, the solution was further diluted with 7 mL DI H_2O (l). Five unoxidized coupon halves of the same geometry were digested following the same procedure as a baseline. The concentrations of B and Si detected for the 48 CMC coupon halves (oxidized and as-received) are given in Table 41, along with the duration of digestion.

Table 41. ICP-OES results for 48 digested CMC coupon halves

CMC Oxidation Conditions	# Days Digesting	Si Concentration (ppm)	B Concentrations (ppm)
dry O_2, 800°C, 1h	2-3	100	95
dry O_2, 800°C, 50h	2-3	103	95
dry O_2, 800°C, 100h	2-3	320	102
dry O_2, 1200°C, 1h	2-3	160	66
dry O_2, 1200°C, 1h	6	173	58
dry O_2, 1200°C, 50h	2-3	350	66
dry O_2, 1200°C, 100h	1	1910	80
dry O_2, 1200°C, 100h	2-3	181	76
dry O_2, 1300°C, 1h	6	149	48
dry O_2, 1300°C, 1h	7	565	115
dry O_2, 1300°C, 1h	2-3	10	5
dry O_2, 1300°C, 1h	2-3	166	99
dry O_2, 1300°C, 50h	6	214	28
dry O_2, 1300°C, 50h	7	913	116
dry O_2, 1300°C, 50h	2-3	125	10
dry O_2, 1300°C, 100h	6	144	35
dry O_2, 1300°C, 100h	7	372	92
wet O_2, 800°C, 1h	2-3	92	101
wet O_2, 800°C, 50h	2-3	120	110
wet O_2, 800°C, 100h	2-3	106	94
wet O_2, 1200°C, 1h	2-3	69	33
wet O_2, 1200°C, 1h	7	1435	136
wet O_2, 1200°C, 50h	2-3	274	74
wet O_2, 1200°C, 100h	2-3	225	70
wet O_2, 1200°C, 100h	1	1890	66
wet O_2, 1300°C, 1h	1	85	57
wet O_2, 1300°C, 1h	6	108	40
wet O_2, 1300°C, 1h	2-3	48	31
wet O_2, 1300°C, 1h	7	167	106
wet O_2, 1300°C, 40h	7	1180	133
wet O_2, 1300°C, 50h	6	220	33
wet O_2, 1300°C, 50h	1	177	51
wet O_2, 1300°C, 50h	2-3	134	37
wet O_2, 1300°C, 100h	6	125	33
wet O_2, 1300°C, 100h	7	235	93
wet O2, 1300°C, 100h	2-3	160	43

dry O_2, 800°C, 100h, CVD seal coat intact	6	41	67
dry O_2, 800°C, 100h, CVD seal coat intact	7	82	149
dry O_2, 1200°C, 100h, CVD seal coat intact	7	163	94
dry O_2, 1200°C, 100h, CVD seal coat intact	6	174	34
wet O_2, 800°C, 100h, CVD seal coat intact	7	84	103
wet O_2, 800°C, 100h, CVD seal coat intact	6	46	34
wet O_2, 1300°C, 100h, CVD seal coat intact	7	157	40
As-received	2-3	7	9
As-received	1	1764	62
As-received	1	19	12
As-received	7	84	128
As-received	6	28	46

In the oxidized samples, the B-concentration ranged from 5-136 ppm and the Si-concentrations ranged from 10-1907 ppm. From analysis of these concentrations, it was determined that the sealing oxides contained 14-55 mol% B_2O_3 for CMCs oxidized in dry O_2 and 16-58 mol% B_2O_3 for CMCs oxidized in wet O_2.

However, it was also noted that the baseline as-received coupon halves (no oxidation treatment) and CMCs with the CVD SiC seal coat intact during oxidation (no exposed CMC face, only CVD SiC seal coat oxidized) had significant B and Si signals (9-149 ppm B and 7-1764 ppm Si). The CMCs were characterized with SEM after digestion to determine the source of B and Si for the baseline materials. An example from an unoxidized CMC is given in Figure 114.

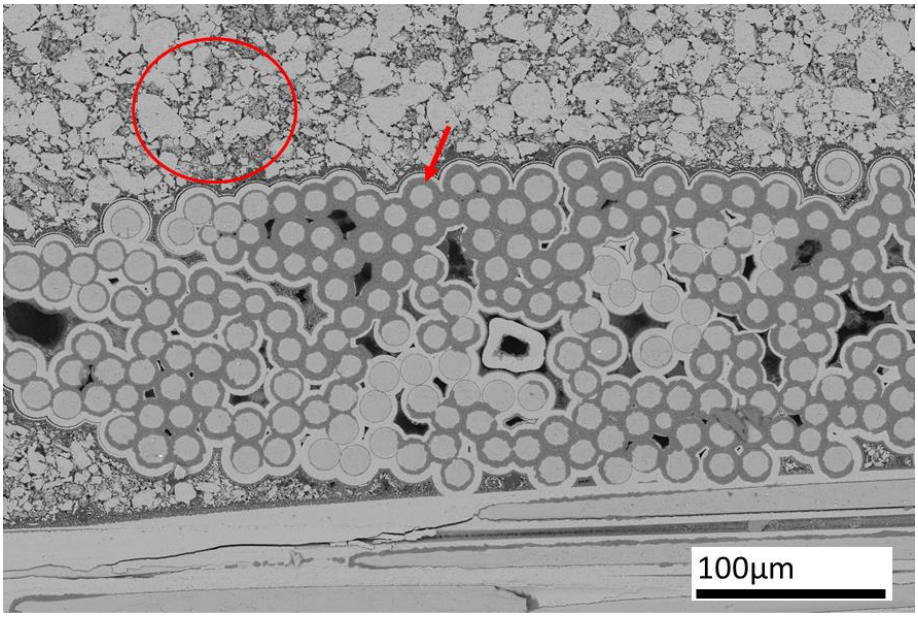

Figure 114. Backscatter SEM image of an as-received CMC coupon half after digestion in a HF/H_2O solution for 2-3 days showing a deposit along the BN interphase (arrow) and depletion of Si in the matrix (circle).

There are two features to note in Figure 114, indicated by the circle and the arrow. The circle shows a region in the matrix that was depleted in Si; only SiC particulates remain (light gray phase) while the Si continuous phase was digested by the HF/H_2O solution. This was observed across the entire cut surface of the coupon half, as well as along the exposed CMC face. This was likely the source of Si in the as-received CMC coupon halves that were digested for ICP-OES analysis.

The second feature to note was the reaction product located on top of the BN interphase (arrow in Figure 114). It was determined from EDS that this product contained B, N, and F—likely the result of a reaction of the HF with the BN interphase. Although the exact composition was not confirmed by EDS, several possible reactions (D1-D4) are listed below.

$$BN + 2HF(l) = BF_2(g) + \frac{1}{2}N_2(g) + H_2(g) \quad \text{[E1]}$$

$$3BN + 6HF(l) = B_3H_6N_3(l) + 3F_2(\text{g}) \quad \text{[E2]}$$

$$BN + 4HF(l) = {BF_4}^-(Aq) + {NH_4}^+(Aq) \quad \text{[E3]}$$

$$BN + 4HF(l) = FH_4N(s) + BF_3(g) \quad \text{[E4]}$$

These or similar reactions were likely the source of B in the "as-received" CMC coupon halves that were digested. Free energy minimization of these reactions using the FactSage equilibrium module[35] did not predict any B-N-F compounds.

Similar results were observed for CMCs that were oxidized (Figure 115), indicating that the underlying substrate was not inert with respect to the HF/H_2O digestion solution, in contrast to prior work by Hagan[107] on different CMCs digested in more concentrated HF solutions.

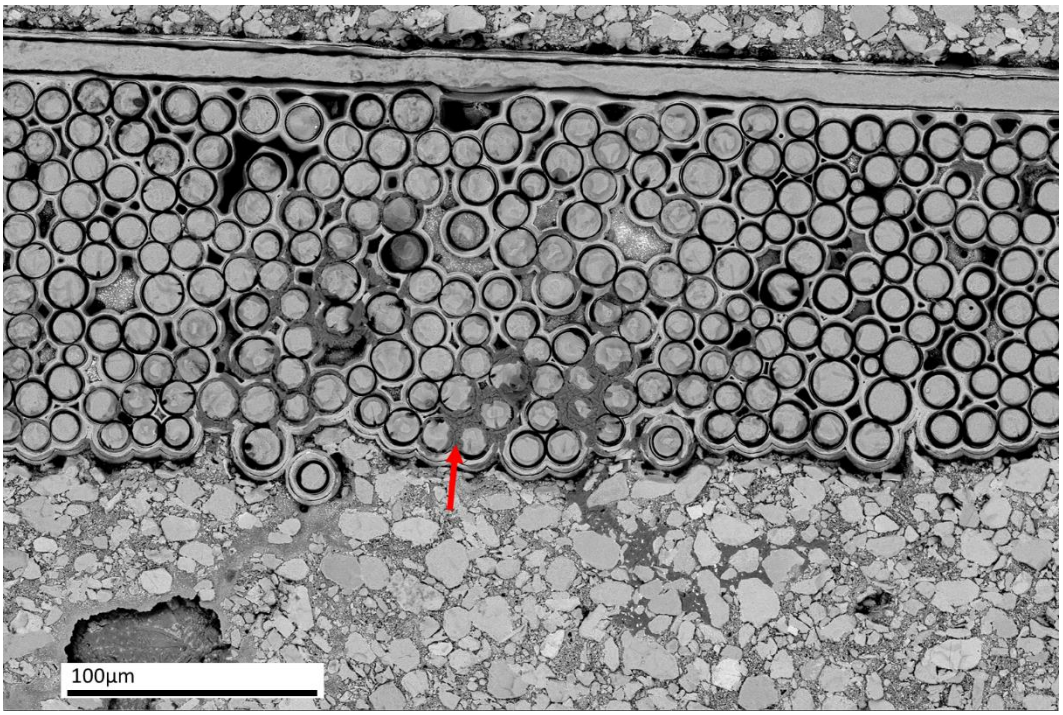

Figure 115. SEM image of an oxidized CMC (wet O_2, 1300°C, 100h) after digestion in an HF/H_2O solution showing Si-depletion in the matrix and a deposit on the BN interphase (arrow).

These results led to trials of alternative digestion processes for CMCs, as outlined in the following sections.

E.3.2. Digestion Procedure #2

The BN and Si phases that reacted with the HF/H_2O solutions in *Digestions Procedure #1* were primarily exposed along the cut face of the coupon half (Figure 113). Whole CMC coupons

(rather than halves) were digested to limit the exposure of the BN and Si phases to the HF/H_2O solution. In addition, several digestion steps for one CMC coupon were conducted to determine the minimum time required for the oxide product to be digested (while leaving the underlying substrate unreacted). Table 41 outlines the digestion steps used and the resulting Si and B concentrations detected by ICP-OES.

Table 42. Digestion procedure #2 steps and resulting Si and B concentrations (from ICP-OES) for a CMC oxidized in wet O_2, 1200°C, 50h

Digestion Step	Digestion Solution	Time in Solution (h)	Total Time Digested (h)	Si Concentration (ppm)	B Concentration (ppm)
1	4mL H_2O	15	15	0	0
2	4mL H_2O	19	34	0	0
3	4mL H_2O	24	58	0.009	1.025
4	4mL H_2O	23	81	0	0
5	1mL HF + 3mL H_2O	16.5	16.5	12	262

At the end of each digestion step, the liquid was decanted and saved for ICP-OES analysis, the CMC coupon was dried, and the CMC surface was characterized by SEM. The same area of the coupon was imaged after each digestion step, allowing for a visual comparison (Figure 116).

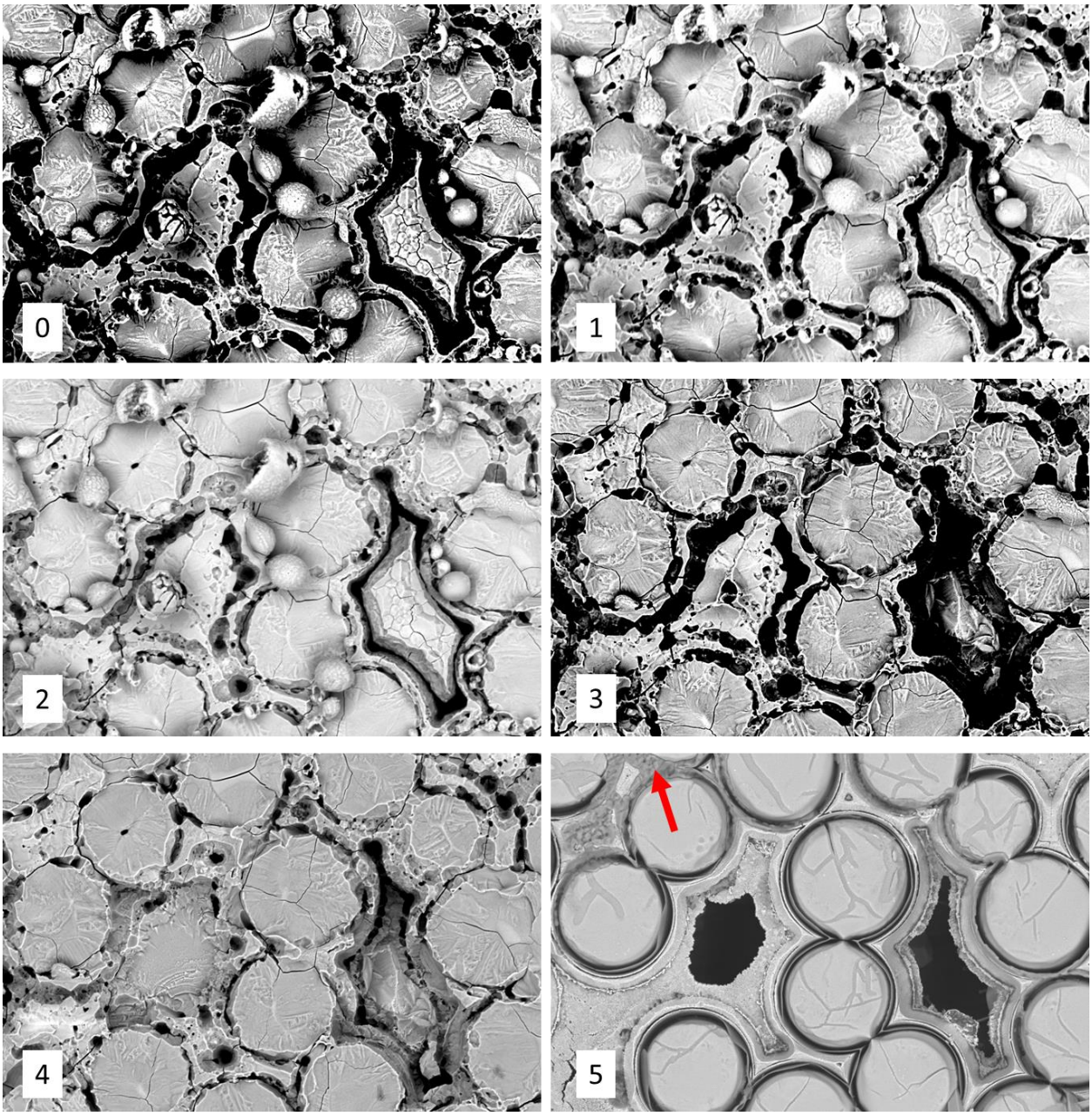

Figure 116. SEM images of a CMC (oxidized in wet O_2, 1200°C, 50h) after each digestion step (1-5, Table 42). The image marked "0" is after oxidation, before any digestion. The arrow shows the B-N-F deposit on the interphase.

Minimal visual differences were observed after digestion steps 1-2 (Figure 116, top right and middle left), which was consistent with no Si or B detected with ICP-OES for these steps (Table 42). After digestion step 3, the oxide droplets were gone, indicating that they were digested (Figure 116, middle right). Analysis from ICP-OES also showed Si and B signals, although the

Si concentration detected was below the minimum calibration of 0.1 ppm (Table 42). There was minimal visual change between digestion steps 3-4. Digestion step 5 was the first digestion solution that contained HF (25 vol% HF), 16.5h. There was a dramatic change observed with SEM after this step—all of the oxide was removed, leaving the fibers, matrix, and interphase visible (Figure 116, bottom right). In addition to removal of the oxide from the CMC surface, Si was depleted from the matrix and a B-N-F deposit was again observed on some BN interphase areas (arrow in Figure 116, bottom right). Although the available surface area for the Si depletion and B-N-F deposits was significantly decreased, the Si and B concentrations determined with ICP-OES (Table 42) should not be used to calculate mol% B_2O_3 in the surface oxide as significant attack of the substrate was observed.

E.3.3. Digestion Procedure #3

Because Si depletion and B-N-F deposits were observed on the CMC after 16.5h in the HF/H_2O solution during Digestion Procedure #2, a shorter digestion time was used for the final HF/H_2O step in Digestion Procedure #3. In this procedure, several digestion steps were again used, although the shortest H_2O digestion step was 48h (Table 43). It should be noted that the CMC oxidation conditions were different compared to the CMC used in Digestion Procedure #2.

Table 43. Digestion procedure #3 steps and resulting Si and B concentrations (from ICP-OES) for a CMC oxidized in dry O_2, 800°C, 1h

Digestion Step	Digestion Solution	Time in Solution (h)	Total Time Digested (h)	Si Concentration (ppm)	B Concentration (ppm)
1	4mL H_2O	48	48	0.9	0.06
2	4mL H_2O	8	56	0.2	0
3	1mL HF + 3mL H_2O	1	1	1.8	10

The exposed CMC face was again imaged after each digestion step (Figure 117).

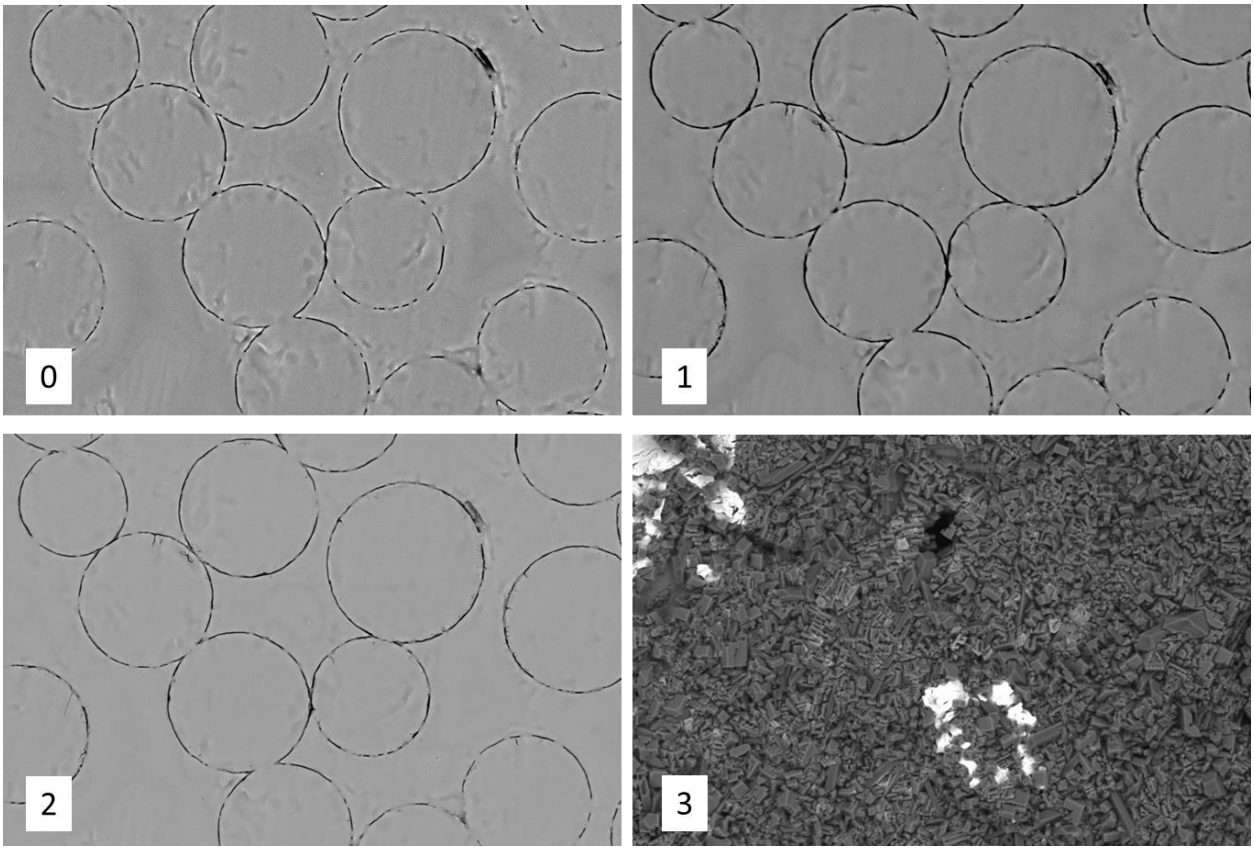

Figure 117. SEM images of a CMC (oxidized in dry O_2, 800°C, 1h) after each digestion step (1-3, Table 43).

There was no visible change in the surface oxide with SEM after digestion steps 1 and 2 (Figure 117, top right and bottom left)—small bits of oxide (gray) were observed to cross the BN interphase (black) in both cases. There were Si and B signals detected after digestion step 1, and Si after digestion step 2 (Table 43), but again these were close to the lower concentration calibration limit of 0.1 ppm.

A dramatic difference was observed with SEM after digestion step 3 (25 vol% HF, 1h). The entire fiber area was covered with a B-N-F deposit (Figure 117, bottom right). This was observed across the whole exposed CMC surface, not just locally on that fiber tow (Figure 118).

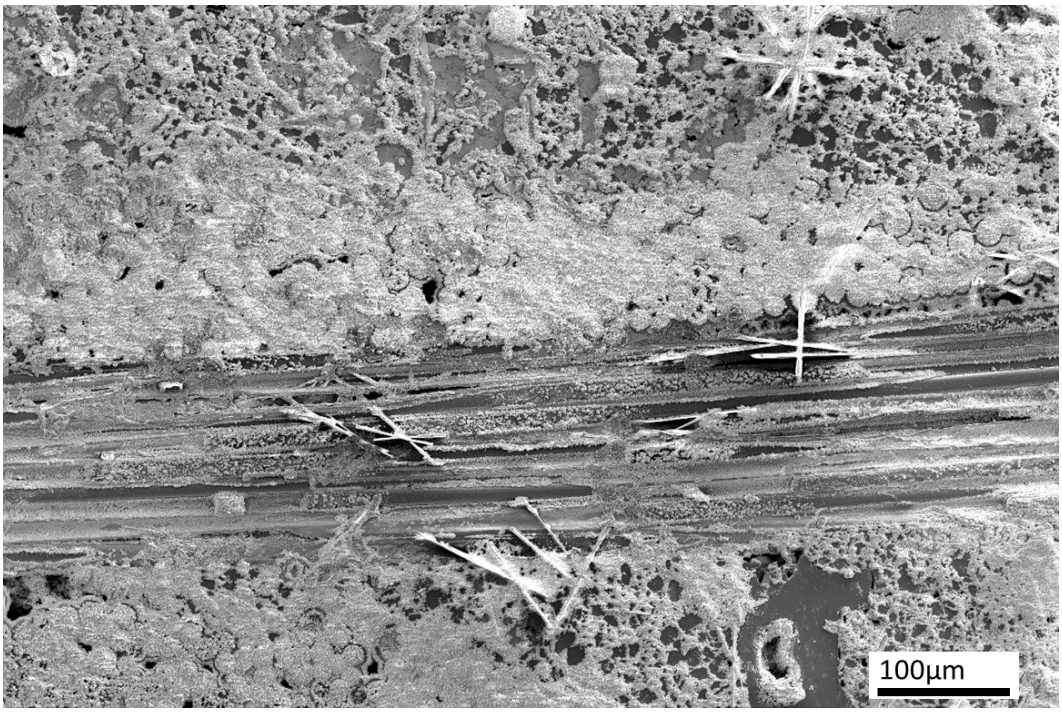

Figure 118. B-N-F deposit across the surface of a CMC (oxidized in dry O_2, 800C, 1h) after 1h of 25 vol% HF/ 75 vol% H_2O digestion (digestion step 3, Table 43).

Because of the significant coverage of the surface by the B-N-F deposit, the Si and B concentrations after digestion step 3 (Table 43) cannot be used to calculate mol% B_2O_3 in the surface oxide.

To determine the effect of the deposit on the CMC, the coupon was digested in 4mL DI H_2O for 53 hours (digestion step 4). The B-N-F deposit was found to be water soluble, so the Si and B concentrations were determined by ICP-OES (Table 44).

Table 44. Digestion procedure #3 step 4 and resulting Si and B concentrations (from ICP-OES) for a CMC oxidized in dry O_2, 800°C, 1h

Digestion Step	Digestion Solution	Time in Solution (h)	Total Time Digested (h)	Si Concentration (ppm)	B Concentration (ppm)
4	4mL H_2O	53	53	21	10

The deposit contained both Si and B, indicating that there was not only a reaction with B-containing phases (BN and B_2O_3), but also with Si-containing phases (SiC, Si, or SiO_2). The CMC was characterized with SEM after digestion step 4, to determine which Si-containing

phase(s) reacted to form the deposit. There was significant Si-depletion in the matrix, while the SiC fibers and CVI SiC coating were unaffected (Figure 119).

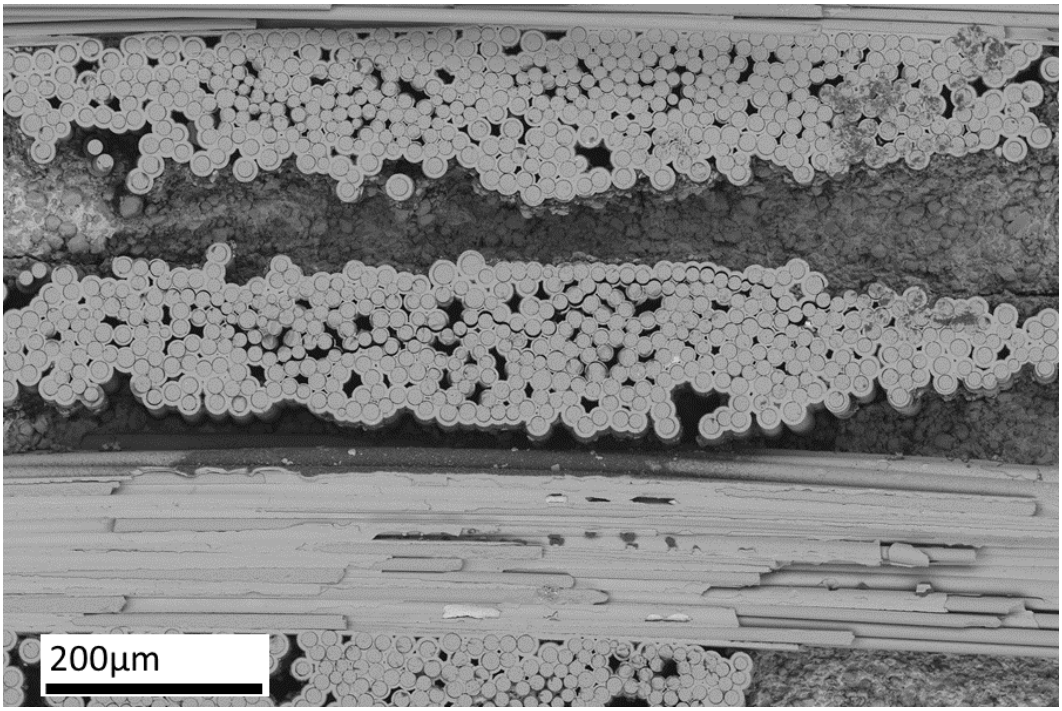

Figure 119. BSE-SEM image of a CMC (oxidized in dry O_2, 800°C, 1h) after H_2O digestion (step 4, Table 44) to remove B-N-F deposit, showing Si-depletion in the matrix.

The SiC particulates in the matrix were also depleted, which was assumed to be due to fall-out when the surrounding Si continuous phase depleted.

E.4. Discussion

From prior work in this laboratory,[104; 105; 106; 107] as well as the work of others,[110; 111; 112] it was expected that the Si, SiC, and BN phases in the CMC would not react with HF digestion solutions. However, it was found that the BN interphase and Si in the matrix of CMCs used in this study did react with the HF digestion solutions, in addition to the expected digestion of the oxide. Spierings discussed the HF-SiO_2 etching mechanism and stated that the Si-O-Si (siloxane) bonds react with HF.[112] Si wafers used for etching experiments[110; 111; 112] were most likely free of siloxane bonds, so the Si substrate did not react. It could hypothesized, therefore, that the Si in

the CMC matrix contained some siloxane bonds, allowing it react with the HF digestion solution in this work. However, no oxygen was in the Si-continuous phase of the matrix, as detected by EDS. It is also known that the Hi-Nicalon fibers in the CMCs also contain excess oxygen,[27] which could also form siloxane bonds, but the fibers did not react with the HF digestion solution. It is therefore unlikely that siloxane bonds in the matrix caused the reaction with HF.

ICP-OES analysis of a similar CMC material with a SMI Si-SiC matrix containing B-rich particulates by Hagan did not show Si depletion in the matrix after digestion in 5mL HF (no H_2O).[107] It could be hypothesized, therefore, that the SMI matrix in this work contained additional species—either due to the MI formulation or to impurities introduced during processing. However, little detail is known about the SMI process due to intellectual property restrictions from Rolls-Royce HTC and no impurities were detected by EDS in the matrix phase of the CMCs. It is possible that small concentrations of other species below EDS detectability limit (1-2 at%) are in solution with the Si phase, and that these impurities are causing the reaction with HF.

E.5. Conclusions

The depletion of Si and BN phases from the CMC during HF/H_2O digestion made ICP-OES an inadequate technique for determining the boria content in the thermally grown borosilicate glasses on the CMC coupons. Therefore, changes in the boria:silica ratio with changes in time, temperature, or environment could not be determined.

E.6. Complications for Future Work

It is recommended that an alternative technique is developed for determination of boria and silica concentrations in the thermally grown borosilicate glasses. ICP-OES was used for the high sensitivity of the technique for boron, however an appropriate etchant or digestion

procedure must be identified that dissolves the oxide, but not the substrate, if this technique is to be used. Additionally, boron is challenging to quantify using traditional techniques such as EDS due to its low atomic number. B_2O_3 volatility during characterization also presents a challenge for B-quantification.

Appendix F. CMC EELS Spectra

Several EELS spectra from a CMC oxidized at 800ºC in wet O_2 for 100h are given below. For all spectra in this appendix, five possible elements were detected with the following edge energies: Si-$L_{2,3}$ (99 eV), B-K (188 eV), C-K (284 eV), N-K (401 eV), and O-K (532 eV) These spectra correspond to the points and lines drawn in Figure 72 and the numerical data given in Table 20. Figure 120 shows a spectrum from a point (black x in Figure 72) in the oxide droplet.

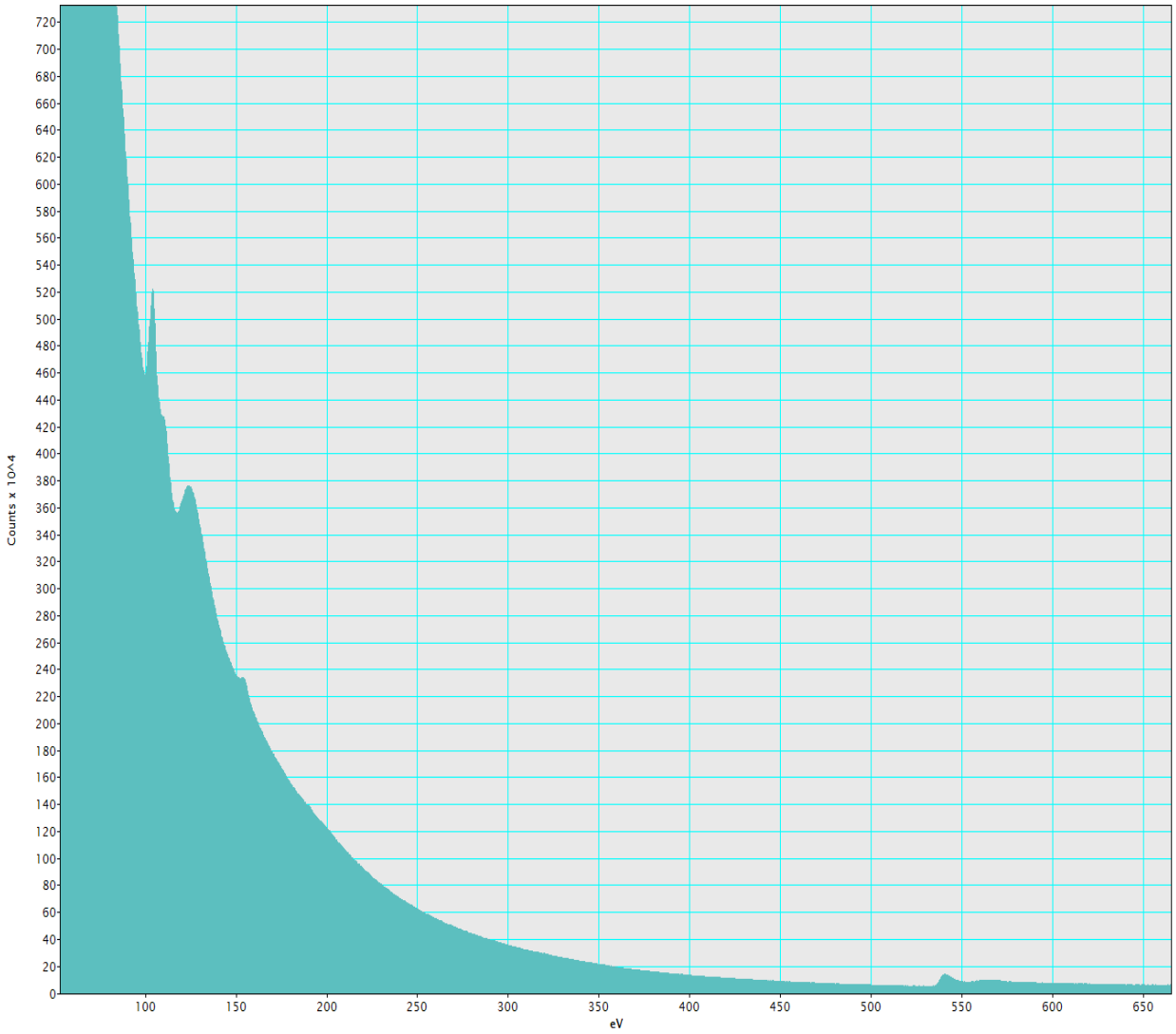

Figure 120. The EELS spectrum corresponding to a point in the oxide droplet after CMC oxidation at 800ºC in wet O_2 for 100h.

Figure 121 shows a spectrum from a point (red x in Figure 72) in the dark spot in the top right of the droplet.

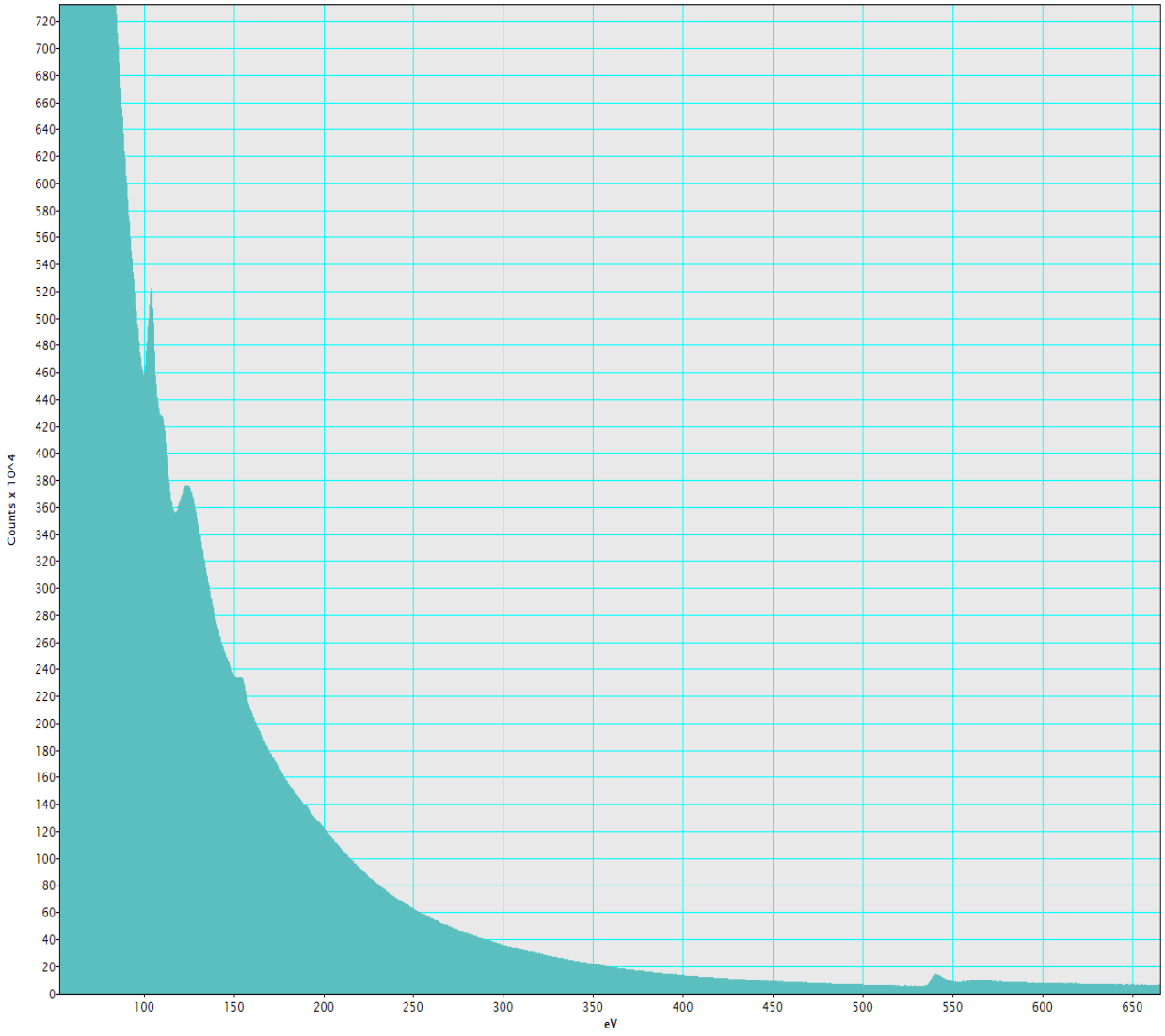

Figure 121. The EELS spectrum corresponding to a point in the dark "spot" in the oxide droplet after CMC oxidation at 800ºC in wet $O_2$for 100h.

Figure 122 shows a series of 78 spectra corresponding to the 78 points in the EELS line scan (black line in Figure 72). These data were analyzed by taking the square root of the intensity and off-setting the spectra by factors of 100. These steps were taken to ensure the visibility of all relevant EELS edges.

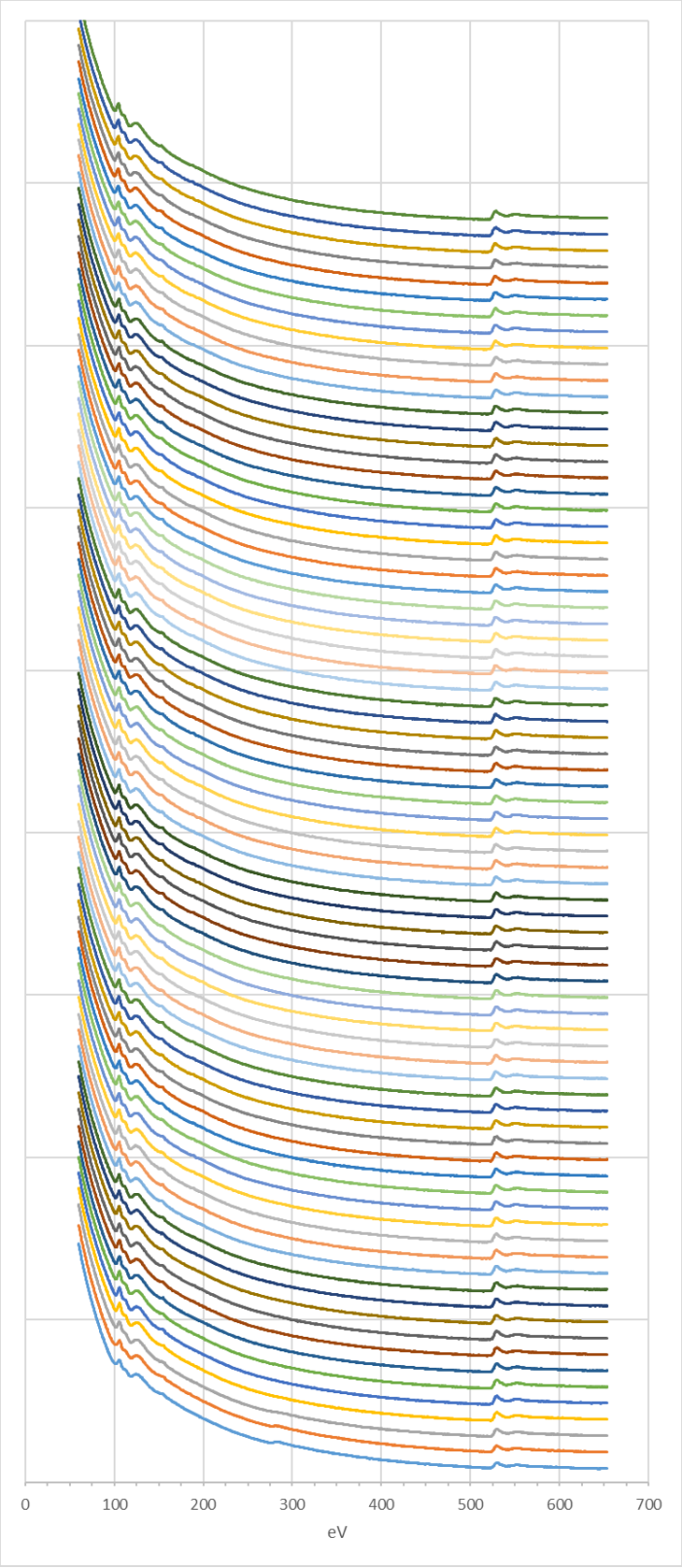

Figure 122. EELS spectra from 78 points in a line in the oxide after CMC oxidation at 800ºC in wet O_2 for 100h.

Figure 123 shows a series of 18 spectra corresponding to the 18 points in the EELS line scan (red line in Figure 72). These data were also analyzed by taking the square root of the intensity and off-setting the spectra by factors of 100 to make the edges visible.

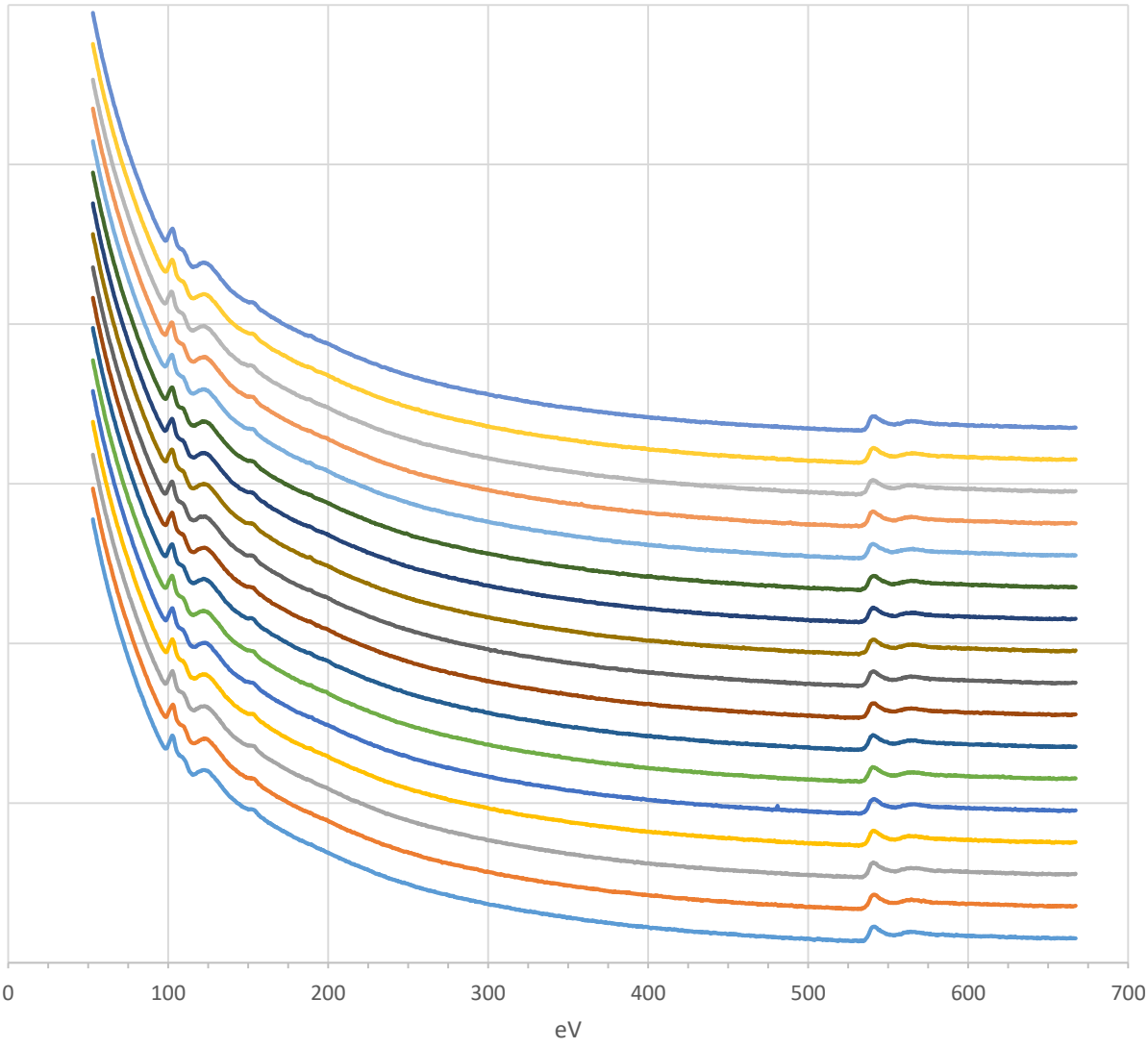

Figure 123. EELS spectra from 18 points in a line in the oxide after CMC oxidation at 800ºC in wet O_2 for 100h.

Several EELS spectra from a CMC oxidized at 1300ºC in wet O_2 for 100h are given below. These spectra correspond to the points (marked by black and red x's) in Figure 74. Figure 124 shows a spectrum corresponding to the black x in the B-rich region of the droplet.

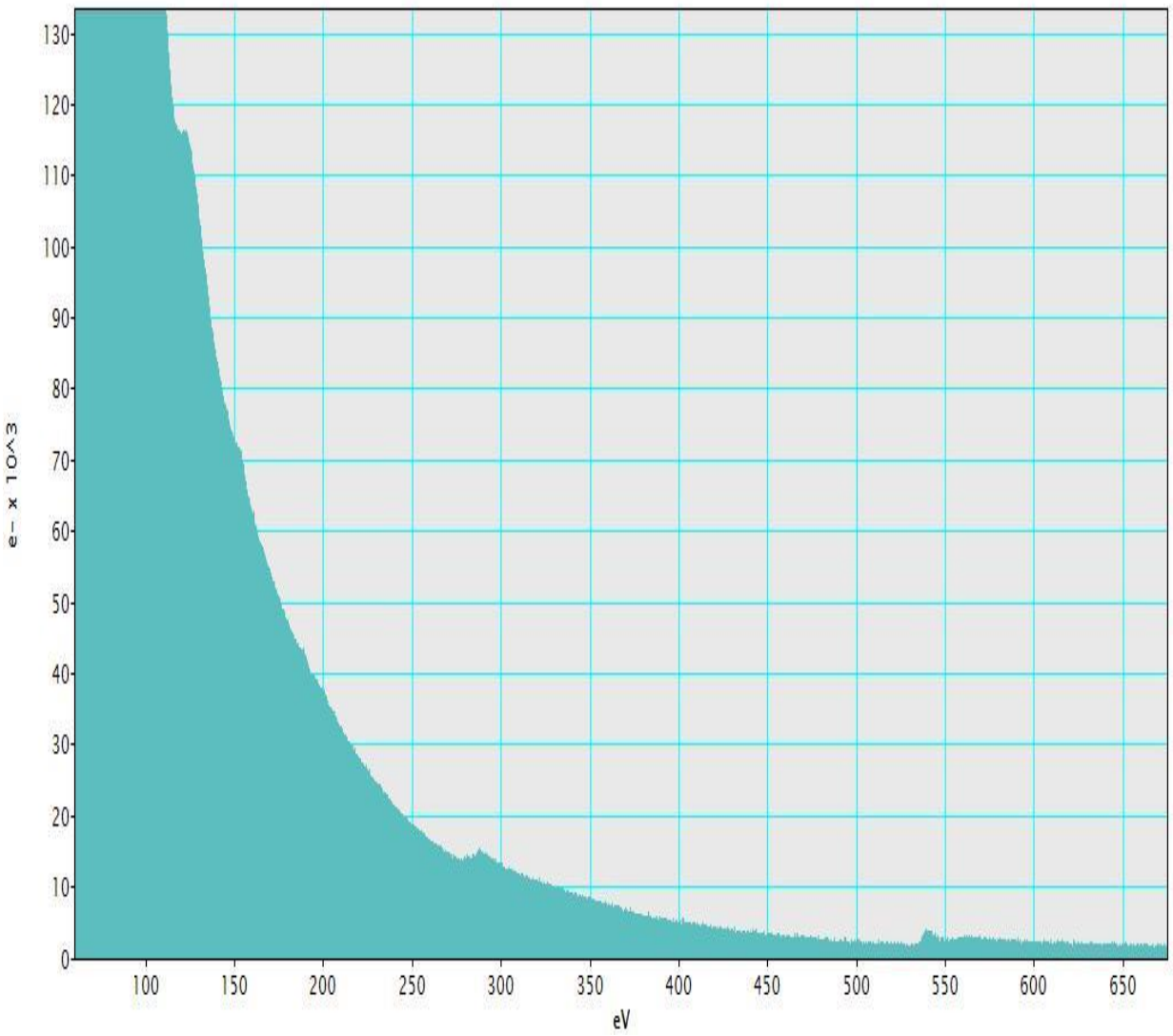

Figure 124. The EELS spectrum corresponding to a point in the B-rich region in the droplet after CMC oxidation at 1300ºC in wet O_2 for 100h.

Figure 125 shows a spectrum corresponding to the red x in the Si-rich region of the oxide droplet.

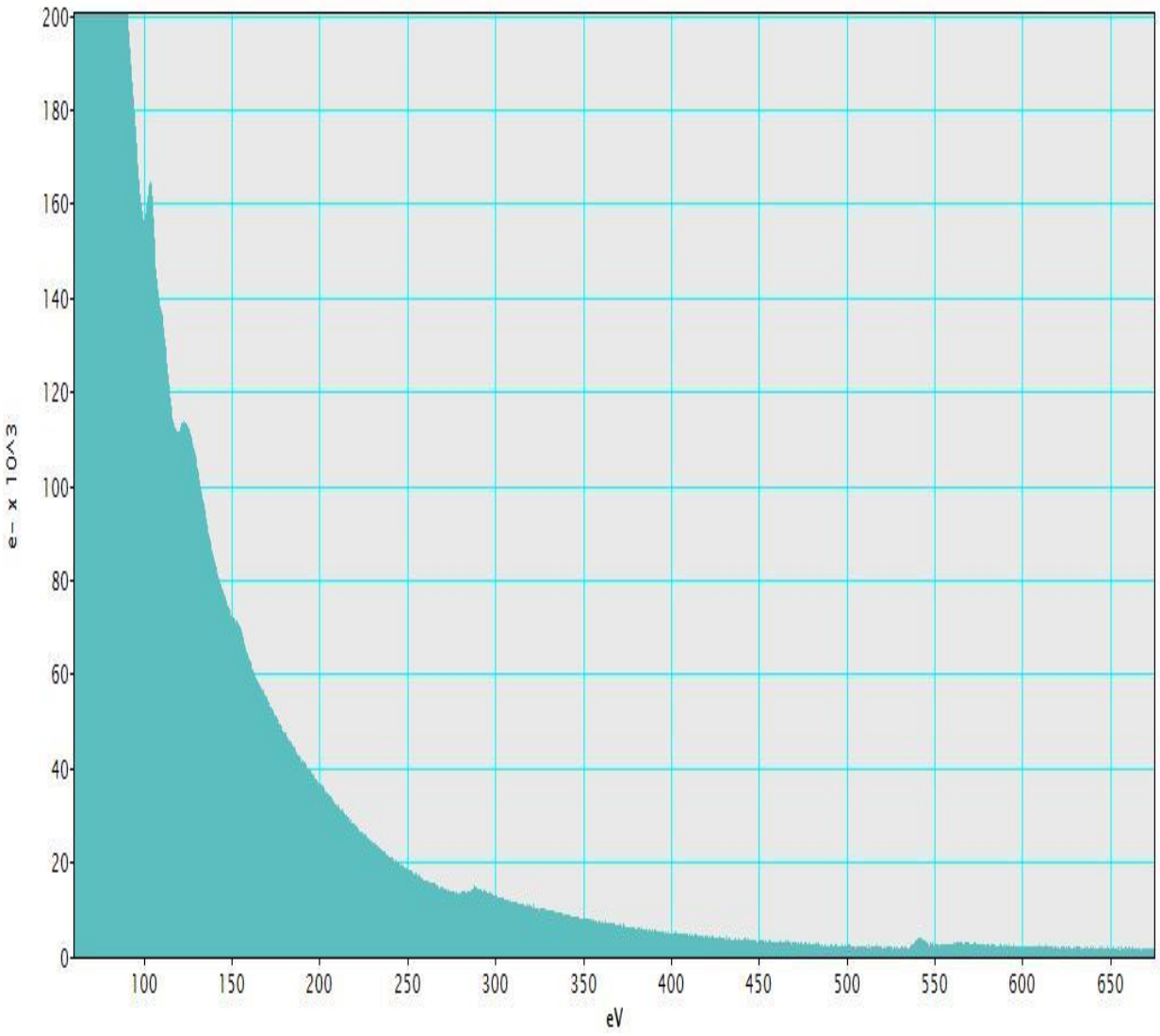

Figure 125. The EELS spectrum corresponding to a point in the Si-rich region in the droplet after CMC oxidation at 1300ºC in wet O_2 for 100h.

Several EELS spectra from a CMC oxidized at 1300ºC in wet O_2 for 100h are given below. These spectra correspond to the points (marked by black x's and squares) in Figure 77. The squares were used to gather data over a larger area. These results are shown in Figure 126 and Figure 127.

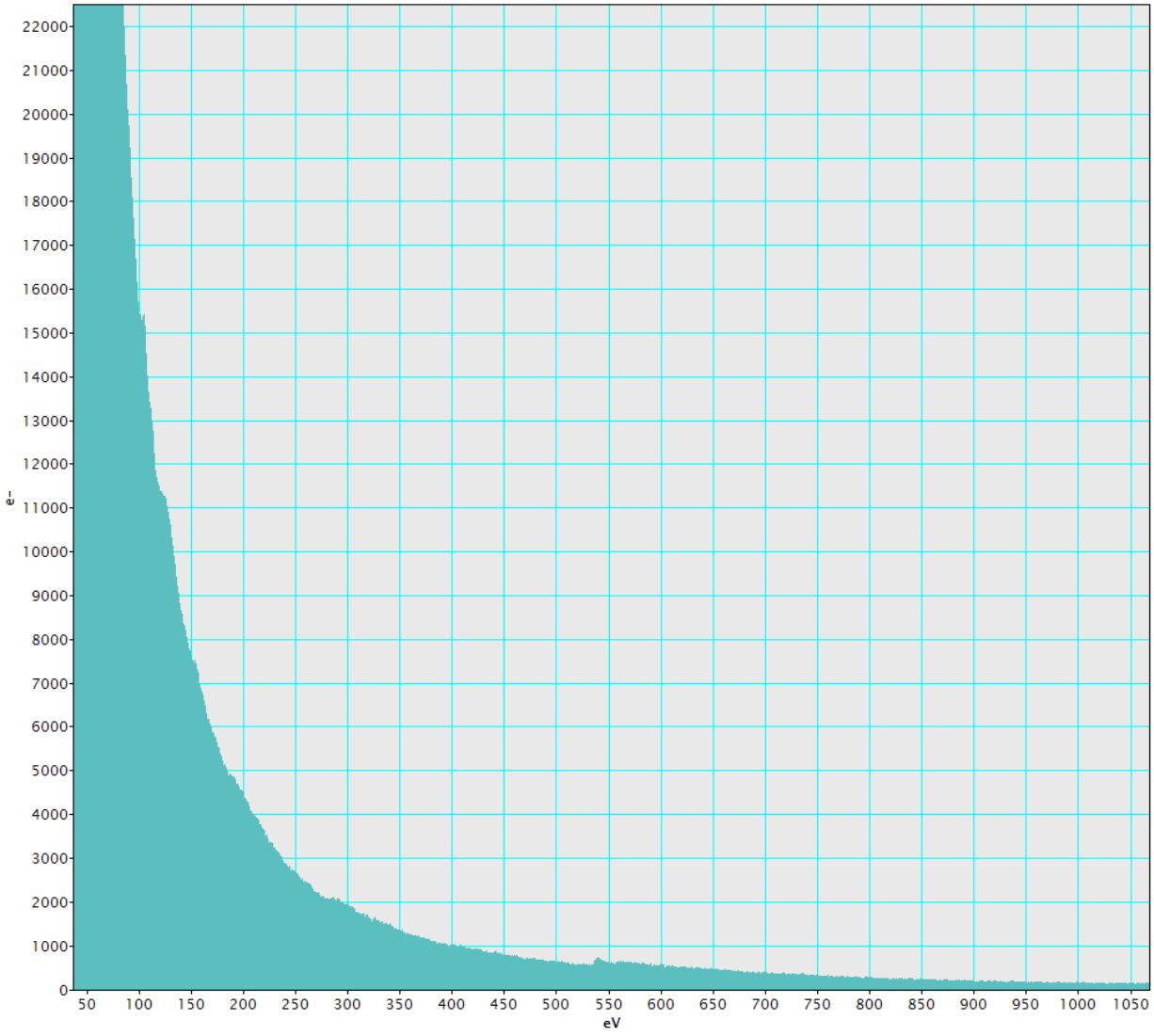

Figure 126. EELS spectrum from an area in a black square above the BN interphase in the oxide in a CMC after oxidation at 1300ºC in wet O_2 for 100h.

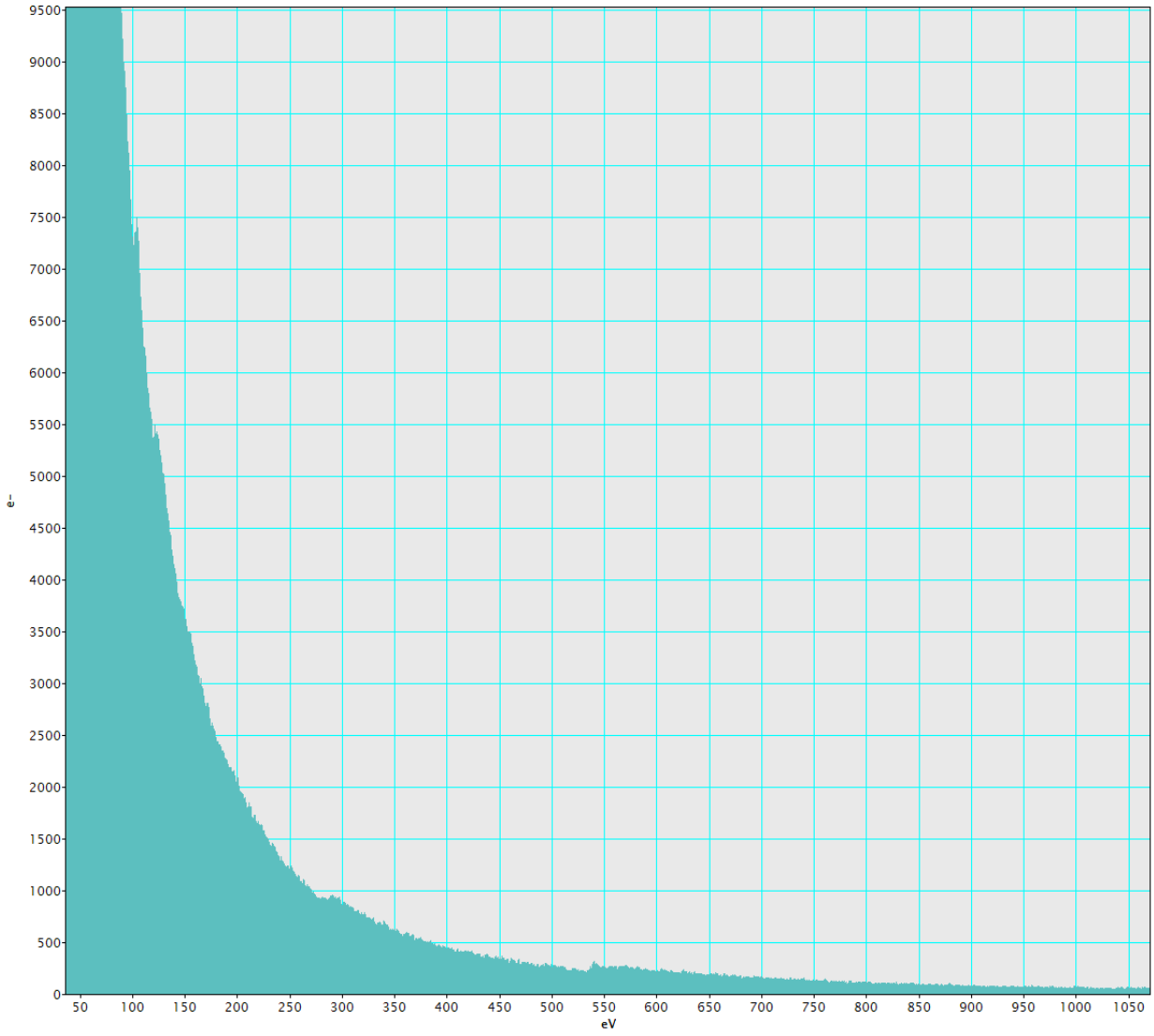

Figure 127. EELS spectrum from an area in a black square below the BN interphase in the oxide in a CMC after oxidation at 1300ºC in wet O_2 for 100h.

Figure 128 through Figure 131 show the spectrum for the four point analyses (points marked x_1 through x_4) corresponding to single points in the oxide.

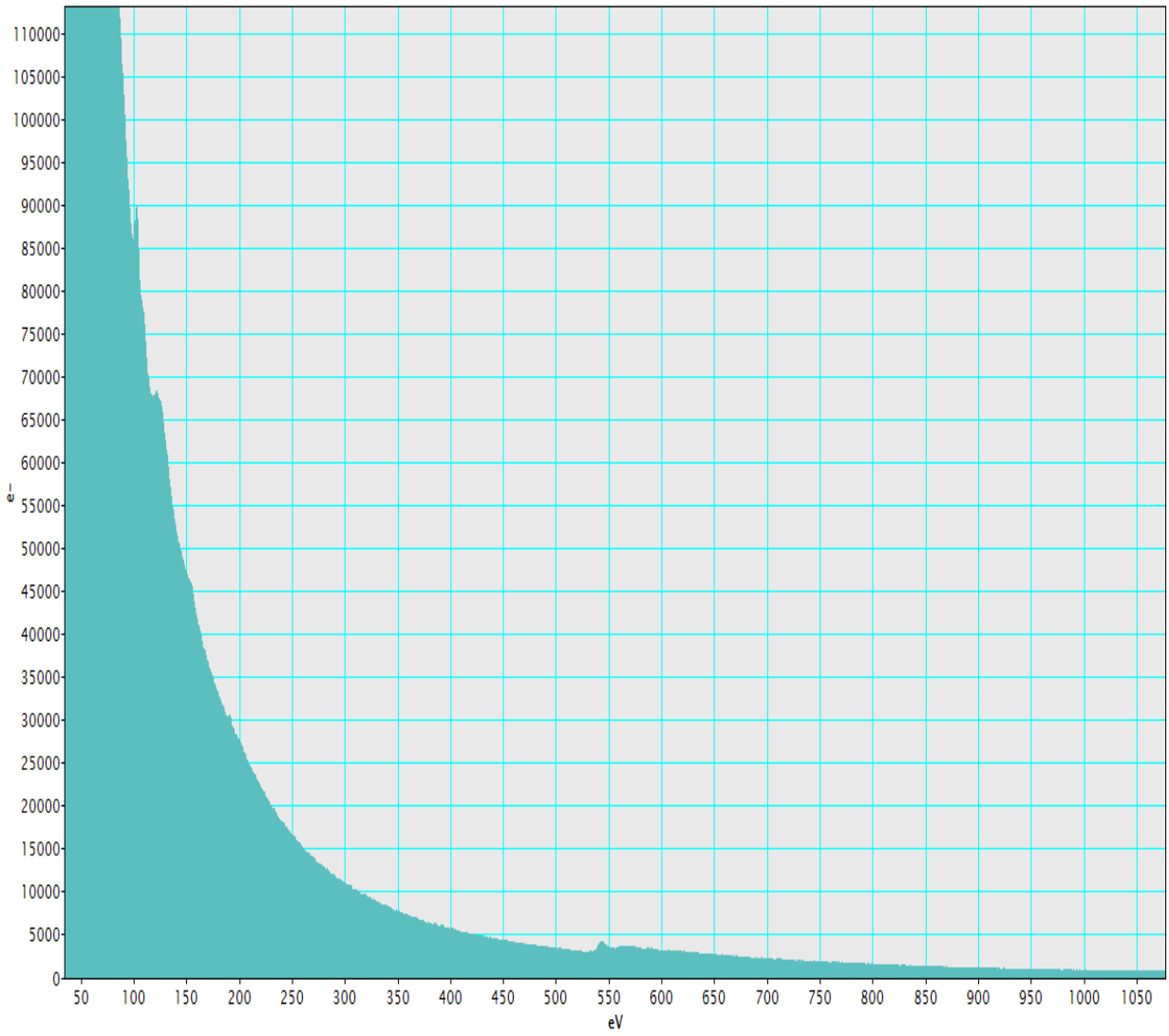

Figure 128. EELS spectrum corresponding to point x_1 in the oxide after CMC oxidation at 1300ºC in wet O_2 for 100h.

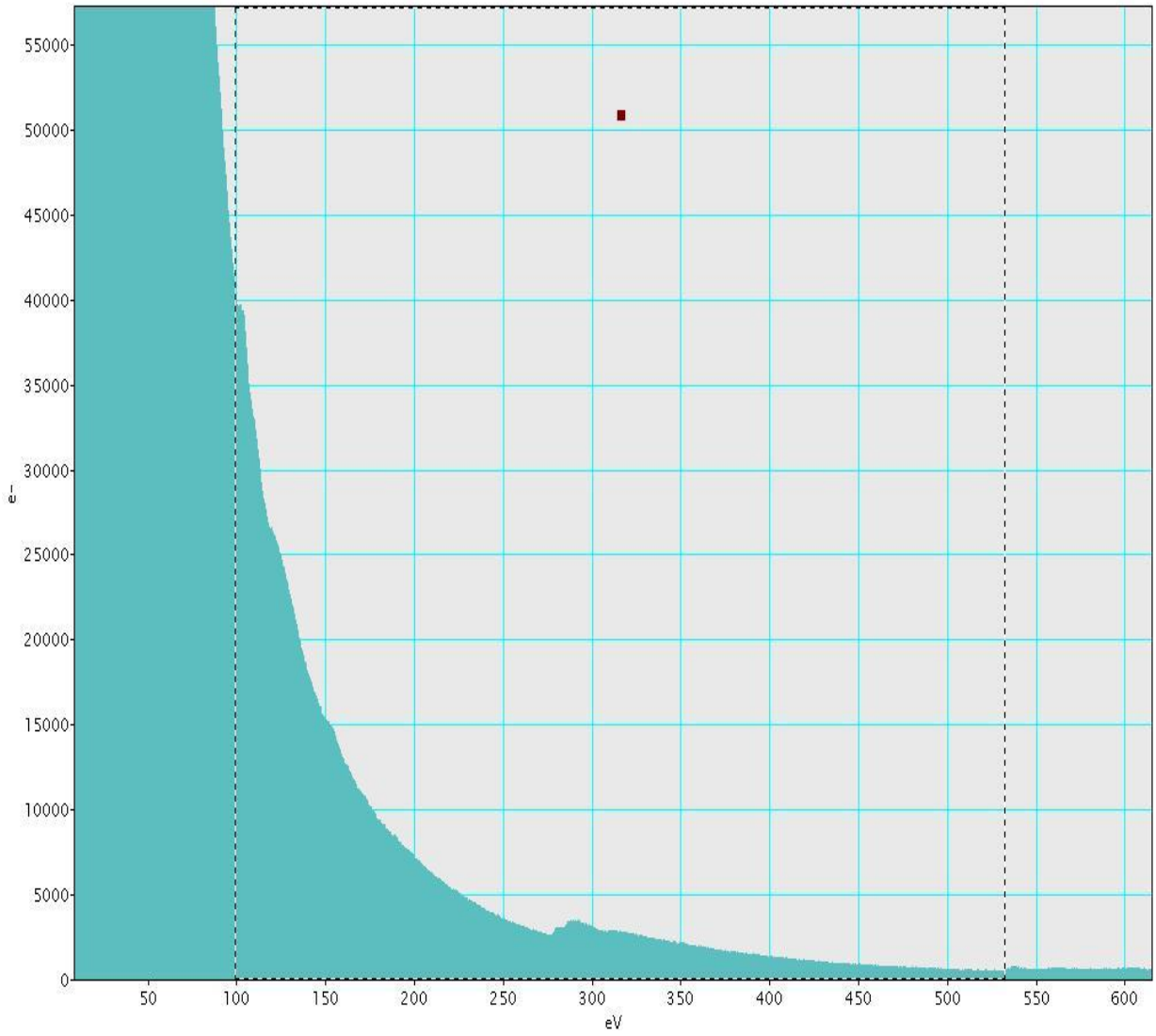

Figure 129. EELS spectrum corresponding to point x_2 in the oxide after CMC oxidation at 1300ºC in wet O_2 for 100h.

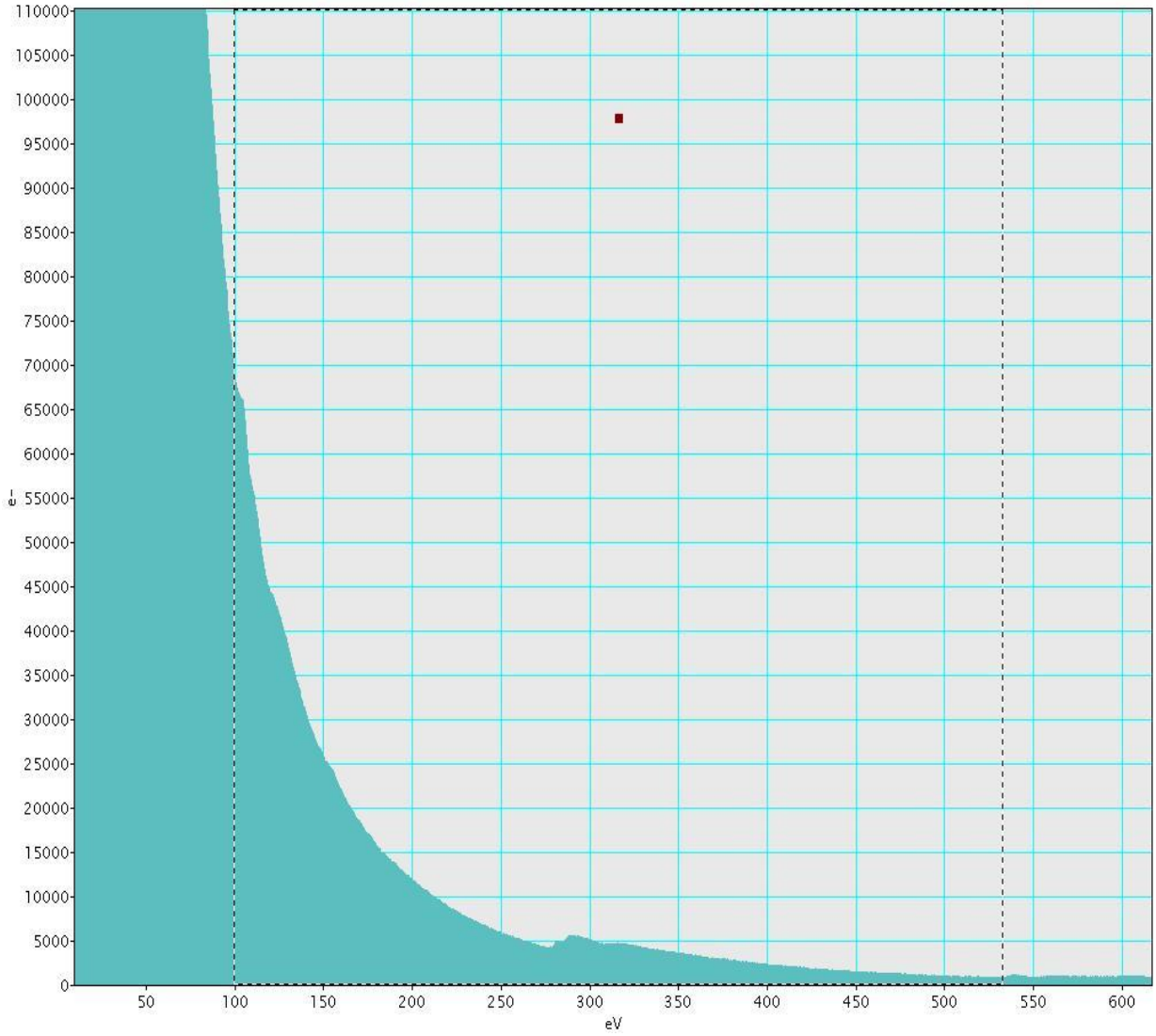

Figure 130. EELS spectrum corresponding to the point x_3 in the oxide after CMC oxidation at 1300ºC in wet O_2 for 100h.

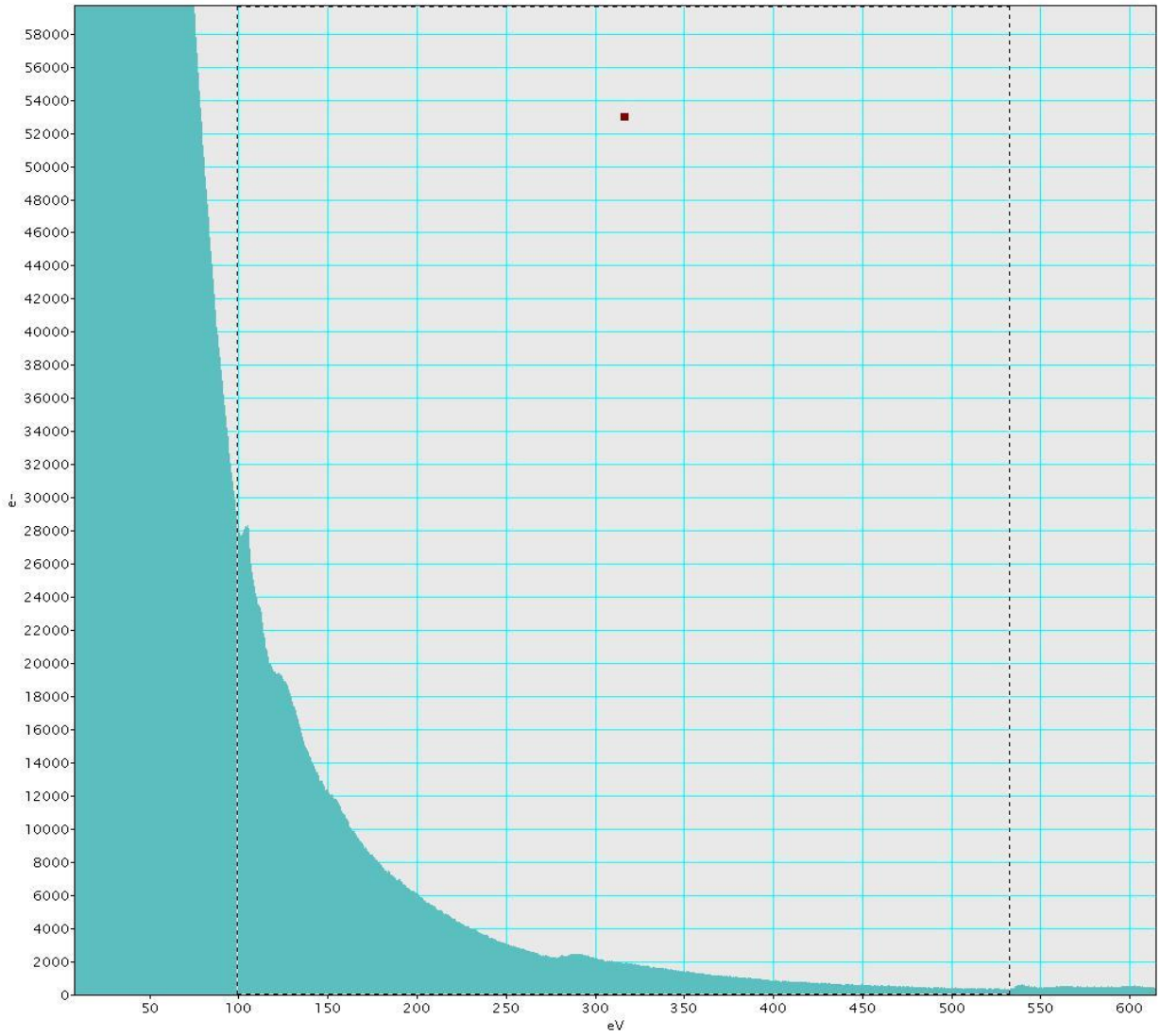

Figure 131. EELS spectrum corresponding to the point x_4 in the oxide after CMC oxidation at 1300ºC in wet O_2 for 100h.

Several EELS spectra from a CMC oxidized at 800ºC in dry O_2 for 100h are given below. These spectra correspond to the points (marked by black x's) in Figure 85.

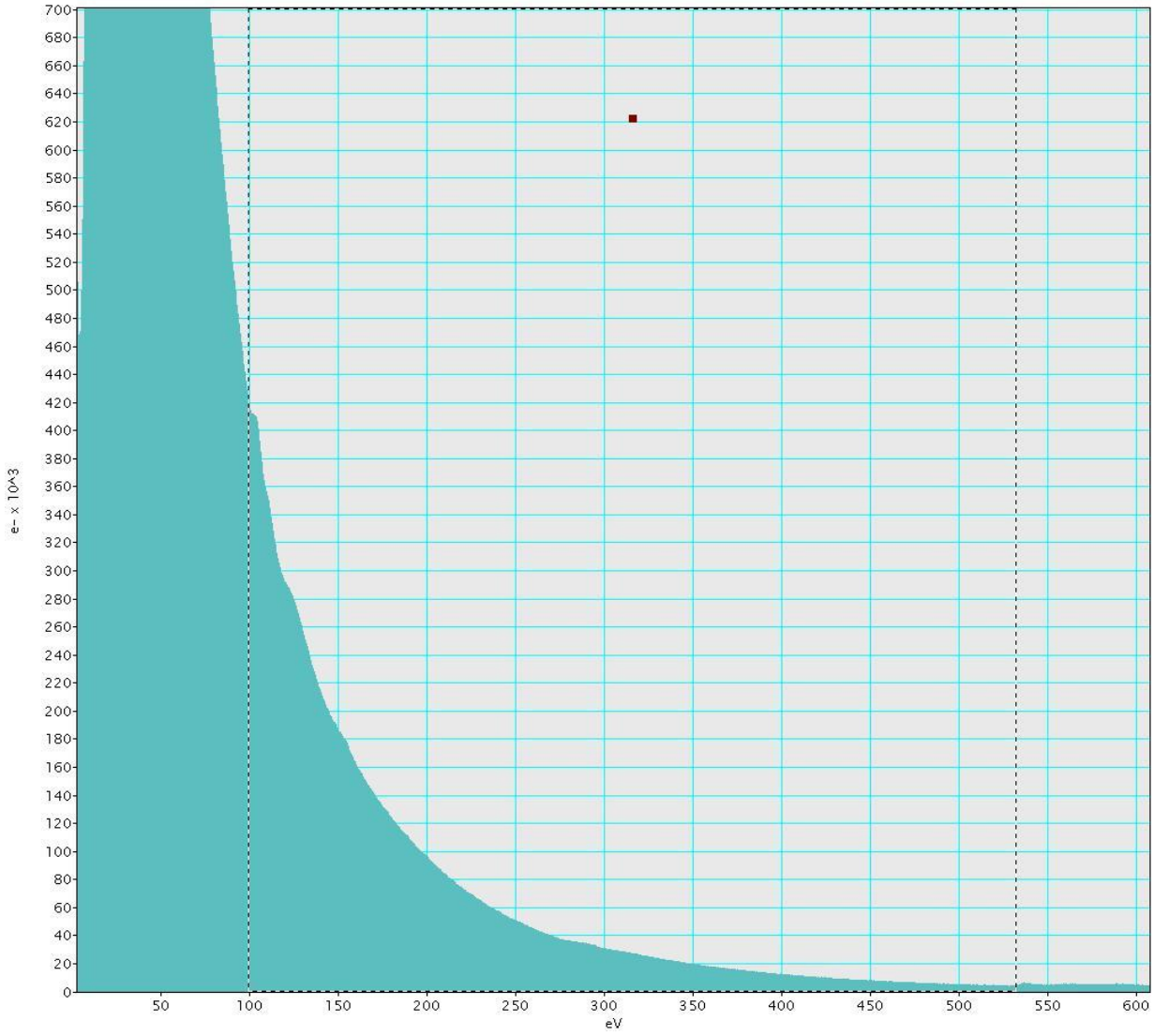

Figure 132. EELS spectrum corresponding to point x_1 in the oxide after CMC oxidation at 800ºC in dry O_2 for 100h.

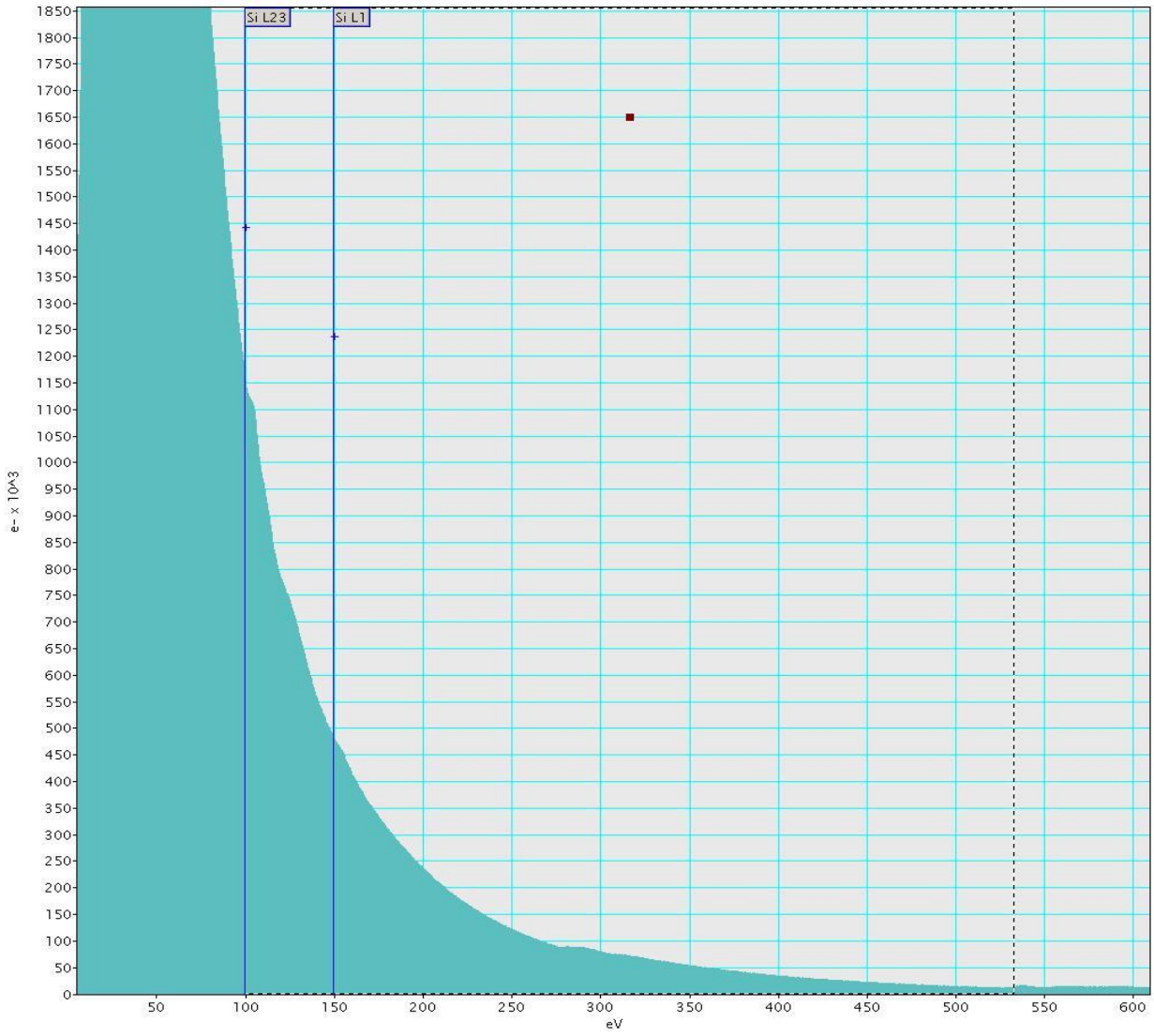

Figure 133. EELS spectrum corresponding to point x_2 in the oxide after CMC oxidation at 800ºC in dry O2 for 100h.

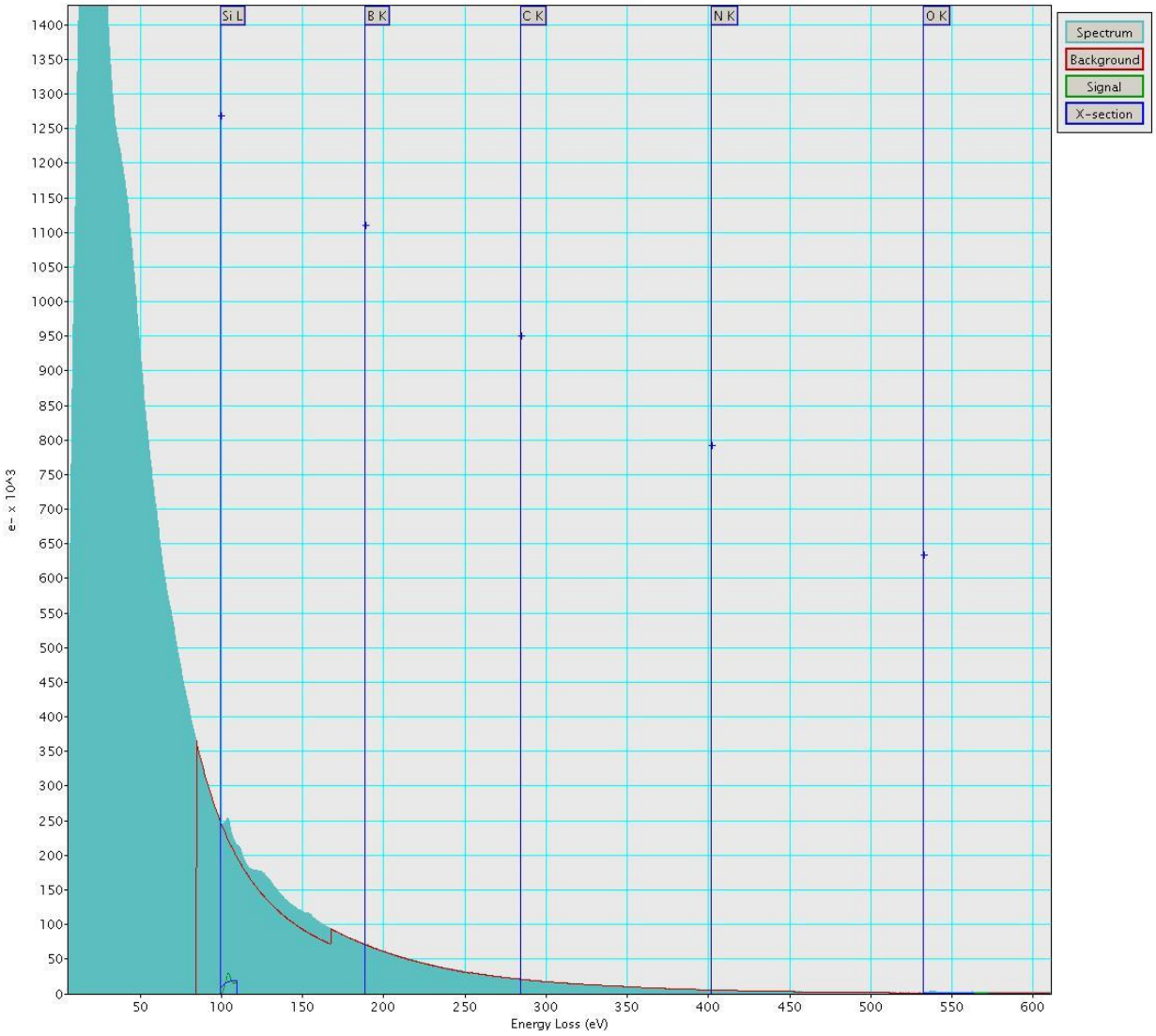

Figure 134. EELS spectrum corresponding to point x_3 in the oxide after CMC oxidation at 800ºC in dry O2 for 100h.

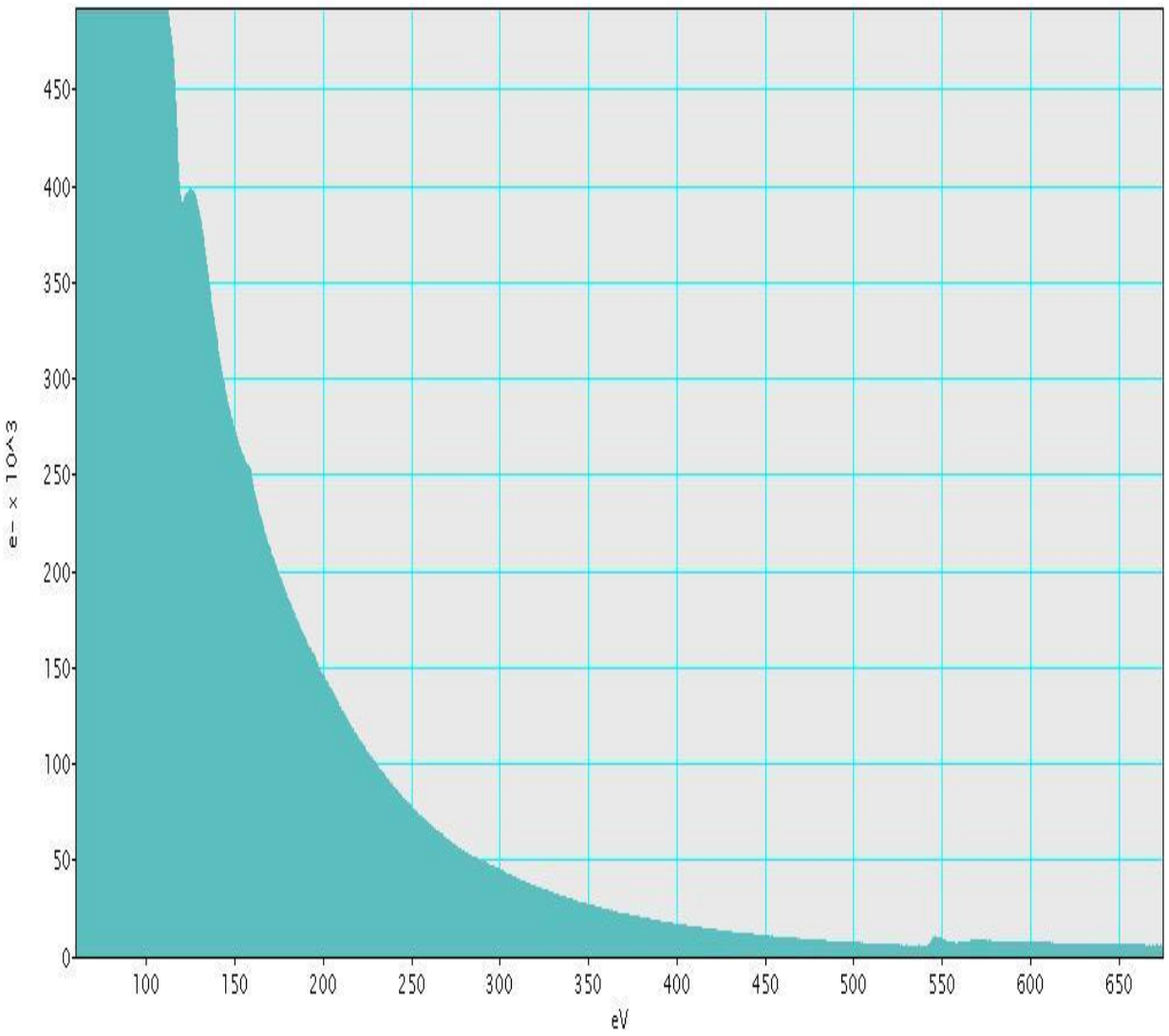

Figure 135. EELS spectrum corresponding to point x_4 in the oxide after CMC oxidation at 800ºC in dry O2 for 100h.

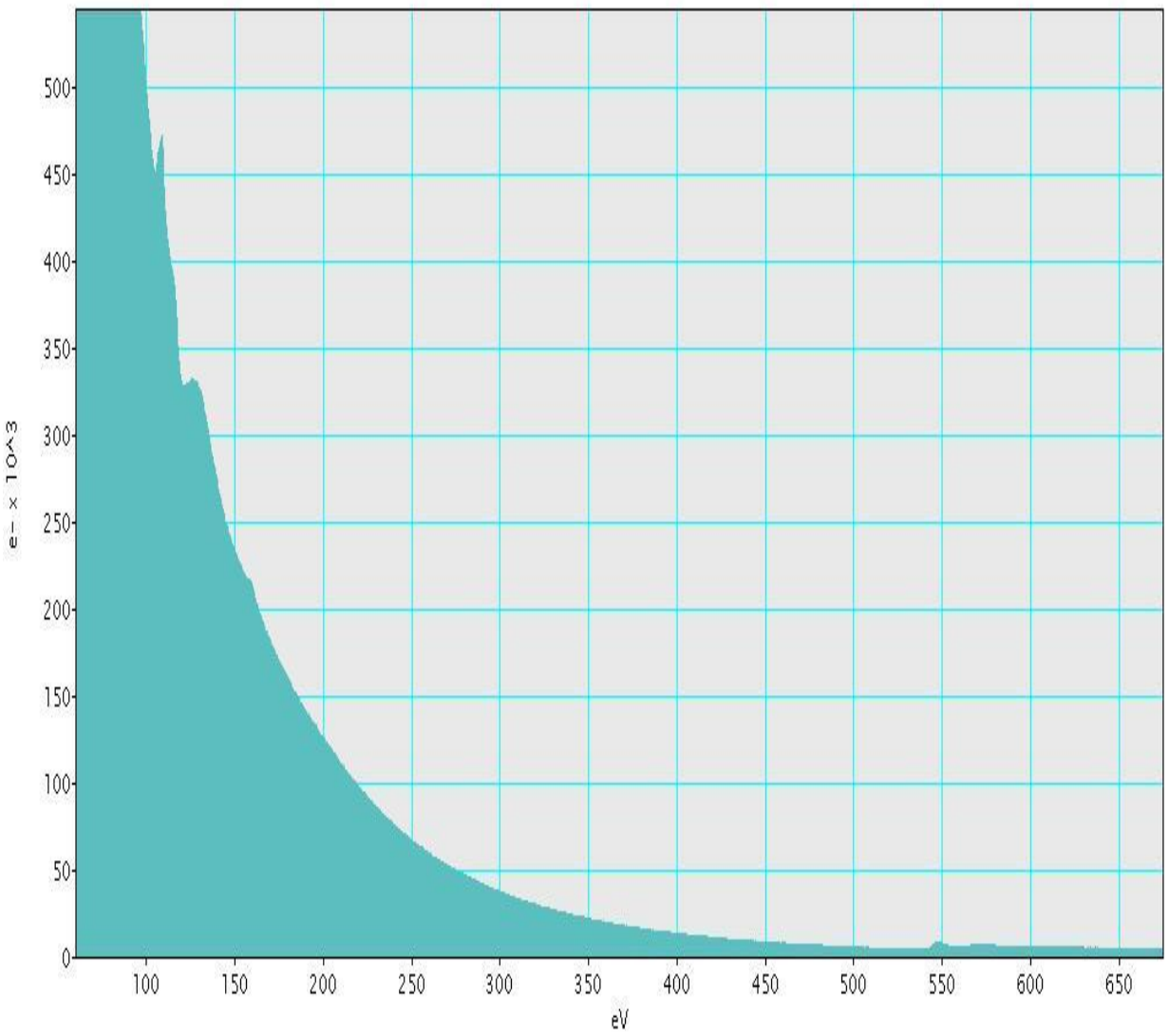

Figure 136. EELS spectrum corresponding to point x_5 in the oxide after CMC oxidation at 800ºC in dry O2 for 100h.

Appendix G. Stressed Permeability Experiments Conducted at Southern Research

Written by James Hawbaker, Southern Research

G.1. Stressed Permeability Experimental Procedure

Permeability is a measure of a material's inherent resistance to gas flow. This was measured in a facility shown schematically in Figure 137. The apparatus consists of a pressure vessel, means of measuring gas-flow through the specimen, means of measuring the pressure drop across the specimen, and means of varying the in-plane tensile load applied to the specimen.

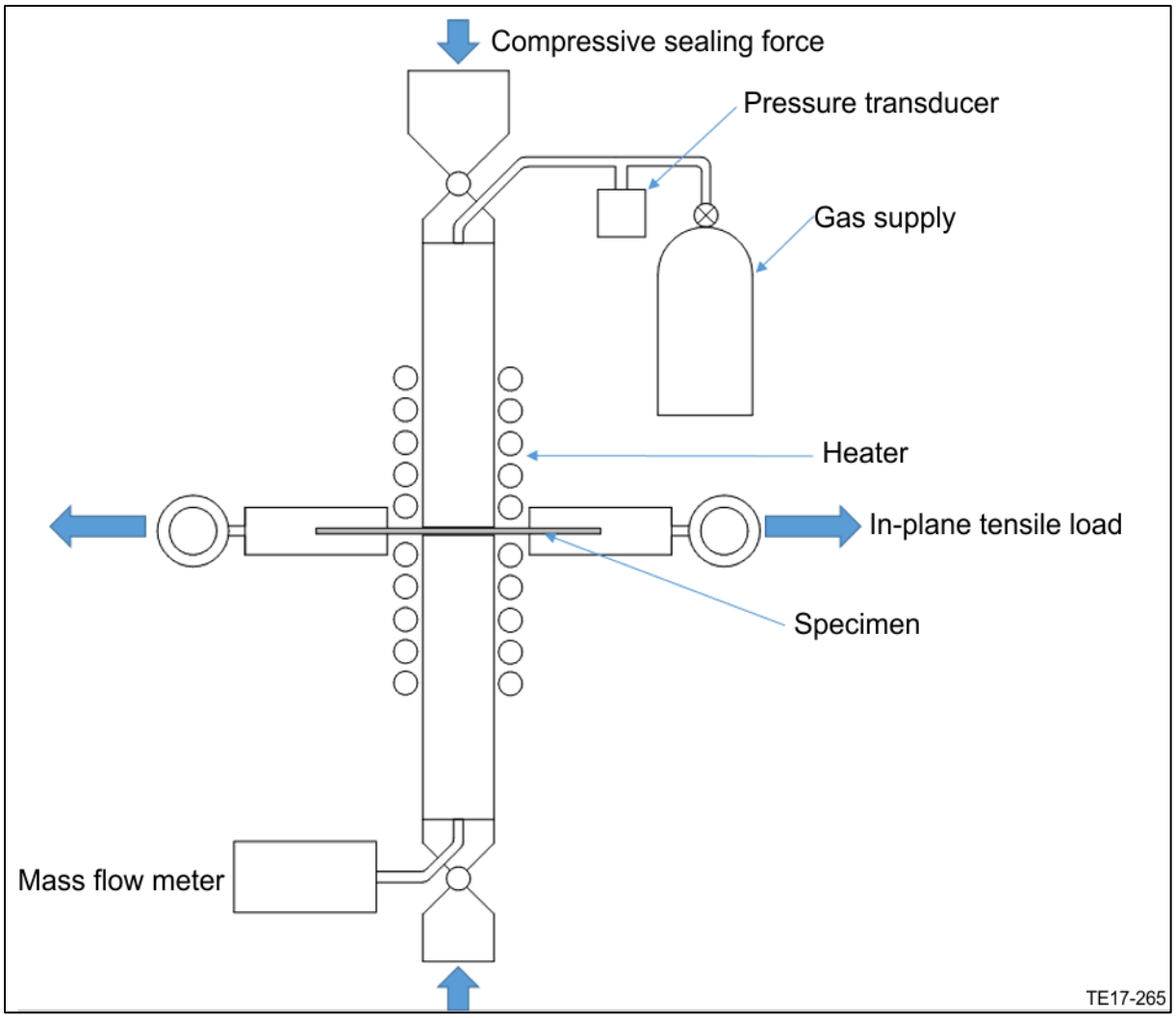

Figure 137. Schematic of Permeability Facility at Southern Research

To perform a test, the specimen is sealed between the two chambers of the pressure vessel. A compressive force is applied to ensure the sealing at the top and bottom of the pressure vessel and at the specimen. The downstream chamber is evacuated with a vacuum pump to the desired test pressure. Typically, the gas flow through the specimen is determined with a flowmeter and the absolute and differential pressures are monitored with pressure transducers. The gas supply is varied to obtain a range of applicable pressures and mass flow rates.

A new specimen configuration was designed for this effort that allowed for in-situ permeability measurements as a function of temperature and load (Figure 89). Pressurized gas was applied to the two slots machined in the center of the coupon. The test gas then flowed in the in-plane direction and exited the specimen through the one slot on the reverse side.

The reported result is a calculation of the Darcy's constant, calculated as follows. A semi-empirical relationship between the pressure gradient across the specimen and the type of flow through the specimen is:

$$-\frac{dP}{dx} = \frac{\mu}{B_o}\nu + A_o\rho\nu^2 \qquad \text{[G1]}$$

where:

$\frac{dP}{dx}$ = pressure gradient (Pa/cm)

μ = viscosity (Pa-s)

B_o = Darcy's Constant (cm²)

A_o = inertial flow coefficient (1/cm)

ρ = gas density (g/cm³)

ν = the superficial velocity (cm/s)

where:

$$\nu = \frac{Q}{A} \qquad \text{[G2]}$$

and:

Q = volumetric flow rate (cm^3/s)

A = cross-sectional area (cm^2)

G.2. Viscous Flow

For this material, the gas flow was low enough that the inertial flow term can be neglected. Thereby the first equation reduces to a form of Darcy's law:

$$v = \frac{-B_o}{\mu} \cdot \frac{dP}{dx} \qquad \text{[G3]}$$

This equation applies to incompressible fluids. In the case of gases, the rate of flow changes from point to point as the pressure decreases, but the mass flow rate per unit area, G, is ($g/(s\text{-}cm^2)$) constant.

Therefore:

$$G = \rho v = \frac{-B_o \rho}{\mu} \frac{dP}{dx} \qquad \text{[G4]}$$

and

$$\rho = \frac{PM}{RT} \qquad \text{[G5]}$$

Where*:*

P = Pressure of the gas (Pa)

M = Molecular weight of the gas (g/mol)

R = Ideal gas constant ((cm^3-Pa)/(mol-K))

T = Gas temperature (K)

So, for isothermal flow:

$$G = \frac{-B_o PM}{RT\mu} \frac{dP}{dx} \qquad \text{[G6]}$$

Integrating the equation above over the length of the sample, L (cm), and assuming that μ is constant at each test temperature, then:

$$\int_{o}^{L} G\,dx = \frac{-B_o M}{\mu RT}\int_{P_1}^{P_2} P\,dp \qquad [G7]$$

$$G\,x\Big|_{o}^{L} = \frac{-B_o M}{\mu RT}\,\frac{P^2}{2}\Big|_{P_1}^{P_2} \qquad [G8]$$

$$GL = \frac{-B_o M}{\mu RT}\left(\frac{P_2^2 - P_1^2}{2}\right) \qquad [G9]$$

or:

$$G = \frac{B_o M}{\mu LRT}\left(\frac{P_1^2 - P_2^2}{2}\right) \qquad [G10]$$

Since:

$$G = \frac{\rho Q}{A} \qquad [G11]$$

Therefore:

$$B_o = \frac{2Q\mu LRT\rho}{AM(P_1^2 - P_2^2)} \qquad [G12]$$

At each test temperature, the final equation permits Darcy's constant to be calculated from the known gas properties, upstream and downstream pressures, specimen geometry, and flow rate.

G.3. Testing Procedure

Each CMC coupon was cycled through seven steps of varying stress and temperature as outlined in Table 45. Due to the time it takes to make a tortuosity/diffusivity measurement, those tests were only performed at 4 of the steps as shown in Table 46. In step, 2 specimens were either preloaded to a Normalized Pre-Stress (NPS) of 1 or 0.8. Following exposure, the

specimens were shipped to UVa for sectioning and microscopy to determine the level of oxidation.

*Table 45. Combination stressed oxidation/permeability test steps, *Specimens were exposed for 1, 8, 20, or 100h*

Permeability measurements			
Step	**Temperature (°C)**	**NPS**	**Time (h)**
1	25	0	0
2	25	1/0.8	0
3	800	0	0
4	800	0.8	0
5	800	0.8	Full exposure*
6	800	0	Full exposure*
7	0	0	Full exposure*

*Table 46. Combination stressed oxidation/tortuosity test steps, *Specimens were exposed for 1, 8, 20, or 100h*

Diffusivity measurements			
Step	**Temperature (°C)**	**NPS**	**Time (h)**
1	25	0	0
2	25	1/0.8	0
3	-	-	-
4	-	-	-
5	800	0.8	Full exposure*
6	-	-	-
7	0	0	Full exposure*

Appendix H. Diffusivity Calculations for Oxidant Ingress along the SiC/BN Interfaces

To determine how oxidation progresses down the fiber/BN interface, the lengths of interphase-interface oxide were measured from the surface. Only 3 lengths were measurable from the SEM images. These lengths were used to calculated parabolic rate constants and estimate diffusivity values (Table 47). For diffusivity calculations, the H_2O solubility (C*) and N values were taken from Deal and Grove.[8]

Table 47. Interphase oxygen ingress lengths and estimated parabolic rate constants and diffusivity values

Environment	Temperature (°C)	Time (h)	Oxygen Ingress Length (μm)	k_p ($\mu m^2/h$)	Diffusivity (cm^2/s)
Wet O_2	800	100	9.7	9.4×10^{-1}	2.0×10^{-9}
Wet O_2	1300	1	5.47	29	6.2×10^{-8}
Wet O_2	1300	100	18.45	3.4	7.1×10^{-9}

A limited number of measurements were made, so these diffusivities should be considered first approximations, rather than definitive values. The interphase-interface oxide shown in Figure 88 was observed approximately 30 μm below the surface after 100h and the oxide in Figure 86 was observed approximately 135 μm below the surface after 100h. These lengths were also used to estimate parabolic rate constants and diffusivity values (Table 48).

Table 48. Approximate oxygen ingress lengths of constrained oxides and estimated parabolic rate constants and diffusivity values

Image	Environment	Temperature (°C)	Time (h)	Oxygen Ingress Length (μm)	k_p ($\mu m^2/h$)	Diffusivity (cm^2/s)
Figure 86	Dry O_2	1200	100	135	180	3.8×10^{-7}
Figure 88	Wet O_2	800	100	30	9	1.9×10^{-8}

These parabolic rate constants are larger than would be expected for SiC oxidation at those conditions, but the estimated diffusivity values are compared to oxidant permeabilities in SiO_2, oxygen diffusion in liquid oxides, and gas phase diffusion coefficients in the gas phase, and are a similar order of magnitude to transport through SiO_2 (Table 49) or a liquid slag.

Table 49. Reference diffusivity values for O_2 and H_2O (g)

Temperature (°C)	Diffusing Species	Material	Diffusivity (cm^2/s)	Reference
1078	O_2	SiO_2	1.2×10^{-8}	Norton[37]
1200	H_2O	SiO_2	1.9×10^{-9}	Moulson & Roberts[113]
1400	O^{2-}	Liquid Oxide-Slags	10^{-7}	Geiger & Poirier[114]
RT-1000	Gas	Gas	0.1-10	Geiger & Poirier[114]

It can therefore be concluded that diffusion along the SiC/BN interface is consistent with a condensed phase transport process: oxidant permeation through SiO_2 or a SiO_2-rich borosilicate, rather than gas phase transport in a gap between the fiber and BN interphase.

Appendix I. Oxidation Depths in CMCs from TEM

Oxidation depths from CMC TEM cross-sections were measured according to lengths A, B, and C as shown in Figure 79. From 11 CMCs, 129 measurements were taken using the ImageJ software (63 for length A, 50 for length A+B, and 16 for length A+B+C). The average measurements for each length along with the standard deviation are given in Table 50. Some conditions did not exist in some CMCs and are marked as N/A in the table. Numbers without standard deviations came from a single measurement.

Table 50. Average oxidation depths in CMCs from TEM measurements

Environment	Temperature (°C)	Exposure Time (h)	A Length (μm)	A+B Length (μm)	A+B+C Length (μm)
Dry O_2	800	1	0.7 ± 0.7	1.4 ± 0.8	1.5 ± 1.5
		100	1.8 ± 0.5	0.7 ± 0.5	2.08 ± 0.02
	1200	50	3 ± 2	3 ± 2	2.1
		100	1.3 ± 0.5	6 ± 2	n/a
	1300	1	0.84 ± 0.02	0.6 ± 0.1	n/a
		100	5 ± 2	5 ± 3	4.8 ± 0.5
Wet O_2	800	1	3.8	2 ± 1	n/a
		100	4.0 ± 0.8	5.1 ± 0.4	n/a
	1200	100	10 ± 3	3.5 ± 0.8	n/a
	1300	1	0.8 ± 0.2	0.8 ± 0.2	1.5 ± 0.2
		100	8 ± 4	7 ± 4	14 ± 3

List of Acronyms

at%: atom percent

atm: atmosphere pressure

B-containing: Boron-containing

BN: Boron Nitride

BSO: Borosilicate

CMC: Ceramic Matrix Composite

CVD: Chemical Vapor Deposited

CVI: Chemical Vapor Infiltrated

D&G: Deal & Grove

DSC: Differential Scanning Calorimetry

EDS: Energy Dispersive Spectroscopy

EELS: Electron Energy Loss Spectroscopy

EF-TEM: Energy Filtered TEM

FIB: Focused Ion Beam

HF: Hydrofluoric Acid

HS: Half Sphere

HSM: Hot Stage Microscope

HTC: High Temperature Composites (Rolls-Royce)

ICP: Inductively Coupled Plasma-Optical Emission Spectrometry

IP: Intellectual Property

MI: Melt Infiltrated

mol%: mole percent

NES: Normalized Exposure Stress

NP: Normalized Permeability

NPS: Normalized Pre-Stress

PET: Polyethylene Terephthalate

PIP: Polymer Infiltration and Pyrolysis

ppm: Parts Per Million

RF: Radio Frequency

RR: Rolls-Royce

RT: Room Temperature

sccm: Standard Cubic Centimeter per Minute

SEM: Scanning Electron Microscopy

SiC: Silicon Carbide

SMI: Silicon-Melt Infiltrated

TEM: Transmission Electron Microscopy

TGA: ThermoGravimetric Analysis

UVa: University of Virginia

wt%: weight percent

XRD: X-Ray Diffraction

References

1. Boyce, M. P. (2011). *Gas turbine engineering handbook* Elsevier.

2. Zok, F. W. (2016). Ceramic-matrix composites enable revolutionary gains in turbine engine efficiency. *Am Ceram Soc Bull, 95*, 22-28.

3. Padture, N. P. (2016). Advanced structural ceramics in aerospace propulsion. *Nature Materials, 15*(8), 804-809.

4. Johnson, D., Evans, A., Goettler, R., Harmer, M., Lipowitz, J., Luthra, K., Wilson, D. (1998). Ceramic fibers and coatings: Advanced materials for the twenty-first century. *Publication NMAB-494*, 20-36.

5. Poerschke, D. L., Rossol, M. N., & Zok, F. W. (2016). Intermediate temperature internal oxidation of a SiC/SiCN composite with a Polymer-Derived matrix. *Journal of the American Ceramic Society, 99*(9), 3120-3128.

6. Lee, K. N. (2000). Current status of environmental barrier coatings for si-based ceramics. *Surface and Coatings Technology, 133*, 1-7.

7. Rolls-Royce PLC. (2018). *TYPE-CERTIFICATE DATA SHEET for trent XWB series engines.* (No. EASA E.111, Issue 06).European Aviation Safety Agency.

8. Deal, B. E., & Grove, A. (1965). General relationship for the thermal oxidation of silicon. *Journal of Applied Physics, 36*(12), 3770-3778.

9. Presser, V., & Nickel, K. G. (2008). Silica on silicon carbide. *Critical Reviews in Solid State and Materials Sciences, 33*(1), 1-99.

10. Ogbuji, L. U., & Opila, E. J. (1995). A comparison of the oxidation kinetics of SiC and Si3 N 4. *Journal of the Electrochemical Society, 142*(3), 925-930.

11. Irene, E., & Ghez, R. (1977). Silicon oxidation studies: The role of H 2 O. *Journal of the Electrochemical Society, 124*(11), 1757-1761.

12. Singhal, S. (1976). Effect of water vapor on the oxidation of Hot-Pressed silicon nitride and silicon carbide. *Journal of the American Ceramic Society, 59*(1-2), 81-82.

13. Opila, E. J. (1994). Oxidation kinetics of chemically Vapor-Deposited silicon carbide in wet oxygen. *Journal of the American Ceramic Society, 77*(3), 730-736.

14. Opila, E. (1995). Influence of alumina reaction tube impurities on the oxidation of Chemically-Vapor-Deposited silicon carbide. *Journal of the American Ceramic Society, 78*(4), 1107-1110.

15. Opila, E. J. (1999). Variation of the oxidation rate of silicon carbide with water-vapor pressure. *Journal of the American Ceramic Society, 82*(3), 625-636.

16. Lie, L. N., Razouk, R. R., & Deal, B. E. (1982). High pressure oxidation of silicon in dry oxygen. *Journal of the Electrochemical Society, 129*(12), 2828-2834.

17. Costello, J. A., & Tressler, R. E. (1986). Oxidation kinetics of silicon carbide crystals and ceramics: I, in dry oxygen. *Journal of the American Ceramic Society, 69*(9), 674-681.

18. Opila, E. J. (2003). Oxidation and volatilization of silica formers in water vapor. *Journal of the American Ceramic Society, 86*(8), 1238-1248.

19. Tedmon, C. (1966). The effect of oxide volatilization on the oxidation kinetics of cr and Fe-Cr alloys. *Journal of the Electrochemical Society, 113*(8), 766-768.

20. Opila, E. J., & Hann, R. E. (1997). Paralinear oxidation of CVD SiC in water vapor. *Journal of the American Ceramic Society, 80*(1), 197-205.

21. Robinson, R. C., & Smialek, J. L. (1999). SiC recession caused by SiO2 scale volatility under combustion conditions: I, experimental results and empirical model. *Journal of the American Ceramic Society, 82*(7), 1817-1825.

22. Kingery, W. D., Bowen, H. K., & Uhlmann, D. R. (1960). *Introduction to ceramics* John Wiley & Sons.

23. Stull, D., & Prophet, H. (1985). JANAF thermochemical tables. US dept. *Commerce, Washington,*

24. Lamkin, M., Riley, F., & Fordham, R. (1992). Oxygen mobility in silicon dioxide and silicate glasses: A review. *Journal of the European Ceramic Society, 10*(5), 347-367.

25. PEACOR, D. B. (1973). High-temperature single-crystal study of the cristobalite inversion. *Zeitschrift Für Kristallographie-Crystalline Materials, 138*(1-6), 274-298.

26. Garofalini, S. H., & Miller, A. (1986). Kinetics of tridymite formation. *Journal of Crystal Growth, 78*(1), 85-96.

27. Flores, O., Bordia, R. K., Nestler, D., Krenkel, W., & Motz, G. (2014). Ceramic fibers based on SiC and SiCN systems: Current research, development, and commercial status. *Advanced Engineering Materials,*

28. Wilson, M., & Opila, E. (2016). A review of SiC fiber oxidation with a new study of Hi-Nicalon SiC fiber oxidation. *Advanced Engineering Materials, 18*(10), 1698-1709.

29. Hay, R., Fair, G., Bouffioux, R., Urban, E., Morrow, J., Hart, A., & Wilson, M. (2011). Hi-Nicalon^{TM}-S SiC fiber oxidation and scale crystallization kinetics. *Journal of the American Ceramic Society, 94*(11), 3983-3991.

30. Hay, R., Fair, G., Hart, A., Potticary, S., & Bouffioux, R. (2012). Kinetics of passive oxidation of Hi-Nicalon-S SiC fibers in wet air: Relationships between SiO2 scale thickness, crystallization, and fiber strength. *Mechanical Properties and Performance of Engineering Ceramics and Composites VII: Ceramic Engineering and Science Proceedings, Volume 33*, (2), 253.

31. Naslain, R. R., Pailler, R. J., & Lamon, J. L. (2010). Single-and multilayered interphases in SiC/SiC composites exposed to severe environmental conditions: An overview. *International Journal of Applied Ceramic Technology, 7*(3), 263-275.

32. Jacobson, N., Farmer, S., Moore, A., & Sayir, H. (1999). High-Temperature oxidation of boron nitride: I, monolithic boron nitride. *Journal of the American Ceramic Society, 82*(2), 393-398.

33. Jacobson, N. S., Morscher, G. N., Bryant, D. R., & Tressler, R. E. (1999). High-Temperature oxidation of boron nitride: II, boron nitride layers in composites. *Journal of the American Ceramic Society, 82*(6), 1473-1482.

34. Sheldon, B. W., Sun, E. Y., Nutt, S. R., & Brennan, J. J. (1996). Oxidation of BN-Coated SiC fibers in ceramic matrix composites. *Journal of the American Ceramic Society, 79*(2), 539-543.

35. Bale, C. W., Pelton, A. D., Thompson, W. T., Eriksson, G., Hack, K., Chartrand, P., Decterov, S., Jung, I., Melancon, J., & Petersen, S. Thermfact and GTT-Technologies 1976-2017.

36. Brown, R., & Doremus, R. (1976). Growth and dissolution of gas bubbles in molten boric oxide. *Journal of the American Ceramic Society, 59*(11-12), 510-514.

37. Norton, F. J. (1961). Permeation of gaseous oxygen through vitreous silica.

38. Schlichting, J. (1984). Oxygen transport through glass layers formed by a gel process. *Journal of Non-Crystalline Solids, 63*(1), 173-181.

39. Yan, M. F., MacChesney, J. B., Nagel, S. R., & Rhodes, W. (1980). Sintering of optical wave-guide glasses. *Journal of Materials Science, 15*(6), 1371-1378.

40. Bruckner, R., & Navarro, J. (1966). Physical and chemical investigation in the preparation of high silica glasses. *Glastechnolo.Bull, 39*, 283-283.

41. Dietzel, A., & Brückner, R. (1955). Aufbau eines absolutviskosimeters für hohe temperaturen und messung der zähigkeit geschmolzener borsäure für eichzwecke. *Glastech.Ber, 28*(12), 455-467.

42. Scholze, H. (1962). Influence of viscosity and surface tension on hot-stage microscopy measurements on glasses. *Ver.Dtsch.Keram.Ges, 391*(1), 63-68.

43. Pascual, M., & Pascual, L. (2001). Determination of the viscosity–temperature curve for glasses on the basis of fixed viscosity points determined by hot stage microscopy. *Physics and Chemistry of Glasses, 42*(1), 61-66.

44. Pascual, M., Durán, A., & Prado, M. (2005). A new method for determining fixed viscosity points of glasses. *Physics and Chemistry of Glasses, 46*(5), 512-520.

45. ASTM. (1985). D1857-68: Standard test method for fusibility of coal and coke ash. *Annual Book of Standards, 5*

46. Morscher, G. N., Yun, H. M., DiCarlo, J. A., & Thomas-Ogbuji, L. (2004). Effect of a boron nitride interphase that debonds between the interphase and the matrix in SiC/SiC composites. *Journal of the American Ceramic Society, 87*(1), 104-112.

47. EerNisse, E. (1979). Stress in thermal SiO2 during growth. *Applied Physics Letters, 35*(1), 8-10.

48. EerNisse, E. (1977). Viscous flow of thermal SiO2. *Applied Physics Letters, 30*(6), 290-293.

49. Xu, W., Zok, F. W., & McMeeking, R. M. (2014). Model of Oxidation-Induced fiber fracture in SiC/SiC composites. *Journal of the American Ceramic Society, 97*(11), 3676-3683.

50. Opila, E. J., Robinson, R. C., & Verrilli, M. J. (2015). Borosilicate Glass-Induced fiber degradation of SiC/BN/SiC composites exposed in combustion environments. *International Journal of Applied Ceramic Technology,*

51. Ogbuji, L. U. (1998). A pervasive mode of oxidative degradation in a SiC-SiC composite. *Journal of the American Ceramic Society, 81*(11), 2777-2784.

52. Morscher, G. N., Bryant, D., & Tressler, R. (1997). Environmental durability of BN-Based interphases (for SiCf/SiCm composites) in H2O containing atmospheres at intermediate temperatures. Paper presented at the *Proceedings of the 21st Annual Conference on Composites, Advanced Ceramics, Materials, and Structures: A: Ceramic Engineering and Science Proceedings, Volume 18, Issue 3,* 525-534.

53. Pérez-Rigueiro, J., Celemín, J. A., LLorca, J., & Herrero, P. (1999). Oxidation of BN/nicalon fiber interfaces in Ceramic-Matrix composites and its effect on fiber strength. *Journal of the American Ceramic Society, 82*(12), 3494-3500.

54. Opila, E. J., & Boyd, M. K. (2011). Oxidation of SiC fiber-reinforced SiC matrix composites with a BN interphase. Paper presented at the *Materials Science Forum, , 696* 342-347.

55. Liu, Y., Cheng, L., Zhang, L., Wu, S., Li, D., & Xu, Y. (2007). Oxidation protection of multilayer CVD SiC/B/SiC coatings for 3D C/SiC composite. *Materials Science and Engineering: A, 466*(1), 172-177.

56. Moore, A., Sayir, H., Fanner, S., & Morscher, G. (1995). Improved interface coatings for SiC fibers in ceramic composites. Paper presented at the *Proceedings of the 19th Annual Conference on Composites, Advanced Ceramics, Materials, and Structures-A: Ceramic Engineering and Science Proceedings, Volume 16, Issue 4,* 409-416.

57. Naslain, R., Guette, A., Rebillat, F., Le Gallet, S., Lamouroux, F., Filipuzzi, L., & Louchet, C. (2004). Oxidation mechanisms and kinetics of SiC-matrix composites and their constituents. *Journal of Materials Science, 39*(24), 7303-7316.

58. Naslain, R., Guette, A., Rebillat, F., Pailler, R., Langlais, F., & Bourrat, X. (2004). Boron-bearing species in ceramic matrix composites for long-term aerospace applications. *Journal of Solid State Chemistry, 177*(2), 449-456.

59. Bertrand, S., Boisron, O., Pailler, R., Lamon, J., & Naslain, R. R. (1999). (PyC/SiC) n and (BN/SiC) n nanoscale-multilayered interphases by pressure pulsed-CVI. Paper presented at the *Key Engineering Materials, , 164* 357-360.

60. Morscher, G. N., Hurst, J., & Brewer, D. (2000). Intermediate-Temperature stress rupture of a woven Hi-Nicalon, BN-Interphase, SiC-Matrix composite in air. *Journal of the American Ceramic Society, 83*(6), 1441-1449.

61. Halbig, M. C., Brewer, D. N., & Eckel, A. J. (2000). Degradation of continuous fiber ceramic matrix composites under constant load conditions. *Mechanical, thermal and environmental testing and performance of ceramic composites and components* () ASTM International.

62. Pailler, F., & Lamon, J. (2005). Micromechanics based model of fatigue/oxidation for ceramic matrix composites. *Composites Science and Technology, 65*(3), 369-374.

63. Sullivan, R. M. (2016). Time-dependent stress rupture strength of hi-nicalon fiber-reinforced silicon carbide composites at intermediate temperatures. *Journal of the European Ceramic Society, 36*(8), 1885-1892.

64. Lin, H., & Becher, P. F. (1997). Effect of fiber coating on lifetime of nicalon fiber-silicon carbide composites in air. *Materials Science and Engineering: A, 231*(1), 143-150.

65. Filipuzzi, L., & Naslain, R. (1994). Oxidation mechanisms and kinetics of 1D-SiC/C/SiC composite materials: II, modeling. *Journal of the American Ceramic Society, 77*(2), 467-480.

66. Przybyla, C., Cinibulk, M. K., Parthasarathy, T. A., Cox, B., & Sudre, O. (2017). Modeling environmental degradation of SiC/BN/SiC CMCs (preprint). *Interim Report, Air Force Research Laboratory,*

67. Parthasarathy, T. A., Przybyla, C. P., Hay, R. S., & Cinibulk, M. K. (2016). Modeling environmental degradation of SiC-Based fibers. *Journal of the American Ceramic Society, 99*(5), 1725-1734.

68. National Research Council. (1998). *Ceramic fibers and coatings: Advanced materials for the twenty-first century* National Academies Press.

69. Presser, V., Loges, A., Hemberger, Y., & Nickel, K. G. (2009). Microstructural evolution of silica on Single-Crystal silicon carbide. part I: Devitrification and oxidation rates. *Journal of the American Ceramic Society, 92*(3), 724-731.

70. Presser, V., Loges, A., Wirth, R., & Nickel, K. G. (2009). Microstructural evolution of silica on single crystal silicon carbide. part II: Influence of impurities and defects. *Journal of the American Ceramic Society, 92*(8), 1796-1805.

71. Ramberg, C. E., Cruciani, G., Spear, K. E., Tressler, R. E., & Ramberg, C. F. (1996). Passive-Oxidation kinetics of High-Purity silicon carbide from 800° to 1100° C. *Journal of the American Ceramic Society, 79*(11), 2897-2911.

72. Shimoo, T., Toyoda, F., & Okamura, K. (2000). Oxidation kinetics of low-oxygen silicon carbide fiber. *Journal of Materials Science, 35*(13), 3301-3306.

73. Chollon, G., Pailler, R., Naslain, R., Laanani, F., Monthioux, M., & Olry, P. (1997). Thermal stability of a PCS-derived SiC fibre with a low oxygen content (hi-nicalon). *Journal of Materials Science, 32*(2), 327-347.

74. Dulcey, C. S., Georger, J. H.,Jr, Krauthamer, V., Stenger, D. A., Fare, T. L., & Calvert, J. M. (1991). Deep UV photochemistry of chemisorbed monolayers: Patterned coplanar molecular assemblies. *Science (New York, N.Y.), 252*(5005), 551-554.

75. Hay, R. S., & Chater, R. J. (2017). Oxidation kinetics strength of Hi-NicalonTM-S SiC fiber after oxidation in dry and wet air. *Journal of the American Ceramic Society, 100*(9), 4110-4130.

76. Hay, R., Corns, R., Ross, A., Larson, B., & Kazmierski, P. (2017). Fiber strength of hi-nicalon(TM)-S after oxidation and scale crystallization in si(OH)4 saturated steam. *Mechanical Properties and Performance of Engineering Ceramics and Composites XI: Ceramic Engineering and Science Proceedings Volume 37,* (2), 109.

77. Moon, J., & Sahajwalla, V. (2001). Derivation of shrinking core model for finite cylinder. *ISIJ International, 41*(1), 1-9.

78. Levenspiel, O. (1999). Chemical reaction engineering. *Industrial & Engineering Chemistry Research, 38*(11), 4140-4143.

79. Opila, E. J. (2001). Oxidation oft-300 carbon fibers in water vapor environments. Paper presented at the *High Temperature Corrosion and Materials Chemistry III: Proceedings of the International Symposium, , 2001* 159.

80. Hsueh, C., & Evans, A. G. (1983). Oxidation induced stresses and some effects on the behavior of oxide films. *Journal of Applied Physics, 54*(11), 6672-6686.

81. Hay, R. (2012). Growth stress in SiO2 during oxidation of SiC fibers. *Journal of Applied Physics, 111*(6), 063527.

82. Manning, M. (1981). Geometrical effects on oxide scale integrity. *Corrosion Science, 21*(4), 301-316.

83. Wiederhorn, S. M., Freiman, S. W., Fuller, E. R., & Simmons, C. (1982). Effects of water and other dielectrics on crack growth. *Journal of Materials Science, 17*(12), 3460-3478.

84. Gy, R. (2003). Stress corrosion of silicate glass: A review. *Journal of Non-Crystalline Solids, 316*(1), 1-11.

85. Ciccotti, M. (2009). Stress-corrosion mechanisms in silicate glasses. *Journal of Physics D: Applied Physics, 42*(21), 214006.

86. Griffith, A. (1920). The phenomena of flow and rupture in solids: Phil. *Trans.Roy.Soc.Lond.Ser.A, 221*, 163-198.

87. Hay, R., Fair, G., Bouffioux, R., Urban, E., Morrow, J., Hart, A., & Wilson, M. (2011). Relationships between fiber strength, passive oxidation and scale crystallization kinetics of Hi-Nicalon™-S SiC fibers. *Mechanical Properties and Performance of Engineering Ceramics and Composites VI: Ceramic Engineering and Science Proceedings, Volume 32, ,* 37-51.

88. Schaeffer, H. A. (1984). Diffusion-controlled processes in glass forming melts. *Journal of Non-Crystalline Solids, 67*(1-3), 19-33.

89. More, K. L., Tortorelli, P. F., Ferber, M. K., & Keiser, J. R. (2000). Observations of accelerated silicon carbide recession by oxidation at high Water-Vapor pressures. *Journal of the American Ceramic Society, 83*(1), 211-213.

90. Wilson, M., & Opila, E. (2016). A review of SiC fiber oxidation with a new study of Hi-Nicalon SiC fiber oxidation. *Advanced Engineering Materials,*

91. Fultz, B., & Howe, J. M. (2012). *Transmission electron microscopy and diffractometry of materials* Springer Science & Business Media.

92. Kaplan, W. D., Chatain, D., Wynblatt, P., & Carter, W. C. (2013). A review of wetting versus adsorption, complexions, and related phenomena: The rosetta stone of wetting. *Journal of Materials Science, 48*(17), 5681-5717.

93. Shartsis, L., Spinner, S., & Smock, A. W. (1948). SURFACE TENSION OF COMPOSITIONS IN THE SYSTEMS PbO-B2O3 AND PbO-SiO2. *Journal of the American Ceramic Society, 31*(1), 23-27.

94. Uhlmann, D., Hays, J., & Turnbull, D. (1967). The effect of high pressure on B2O3: Crystallisation, densification, and the crystallisation anomaly. *Phys.Chem.Glasses, 8*(1), 1-1.

95. Vogel, W. (2012). *Glass chemistry* Springer Science & Business Media.

96. McFarland, B. (2017). *Boria effects on the high temperature oxidation of silicon carbide.* (Doctor of Philosophy, University of Virginia).

97. SCHOTT Glass.Borosilicate glass properties.

98. Petersen, K. E., & Guarnieri, C. (1979). Young's modulus measurements of thin films using micromechanics. *Journal of Applied Physics, 50*(11), 6761-6766.

99. Doremus, R. H. (2002). Viscosity of silica. *Journal of Applied Physics, 92*(12), 7619-7629.

100. Brown, D., Hu, S., & Morrissey, J. (1982). Flaws in sidewall oxides grown on polysilicon gate. *Journal of the Electrochemical Society, 129*(5), 1084-1089.

101. Jaccodine, R., & Schlegel, W. (1966). Measurement of strains at Si-SiO2 interface. *Journal of Applied Physics, 37*(6), 2429-2434.

102. COI Ceramics, I. (2006). Hi-nicalon^{TM} ceramic fiber data sheet.

103. Janssen, D., De Palma, R., Verlaak, S., Heremans, P., & Dehaen, W. (2006). Static solvent contact angle measurements, surface free energy and wettability determination of various self-assembled monolayers on silicon dioxide. *Thin Solid Films, 515*(4), 1433-1438.

104. Hagan, J. M., & Opila, E. J. (2017). High-temperature Na2SO4 deposit-assisted corrosion of silicon carbide–II: Effects of B, C, and si. *Journal of the American Ceramic Society, 100*(2), 761-773.

105. Hagan, J. M., & Opila, E. J. (2015). High-Temperature Na2SO4 Deposit-Assisted corrosion of silicon Carbide–I: Temperature and time dependence. *Journal of the American Ceramic Society, 98*(4), 1275-1284.

106. McFarland, B., & Opila, E. J. (2016). Sol–gel derived borosilicate glasses and thin film coatings on SiC substrates: Boron loss and carbon retention due to processing and heat treatment. *Journal of Non-Crystalline Solids, 449*, 59-69.

107. Hagan, J. (2015). *High temperature salt deposit-assisted corrosion of silicon carbide-based ceramic matrix composites: Effects of composite chemistry and architecture*. (Doctoral dissertation PHD Materials Science and Engineering, University of Virginia). (Published)

108. Jacobson, N. S., & Smialek, J. L. (1985). Hot corrosion of sintered α-Sic at 1000° C. *Journal of the American Ceramic Society, 68*(8), 432-439.

109. Shugart, K. (2014). *Oxidation behavior of zirconium diboride silicon carbide based materials at ultra-high temperatures.* (Doctor of Philosphy, University of Virginia). (Public)

110. Kern, W., & Heim, R. (1970). Chemical vapor deposition of silicate glasses for use with silicon devices II. film properties. *Journal of the Electrochemical Society, 117*(4), 568-573.

111. Knotter, D. M. (2000). Etching mechanism of vitreous silicon dioxide in HF-based solutions. *Journal of the American Chemical Society, 122*(18), 4345-4351.

112. Spierings, G. (1993). Wet chemical etching of silicate glasses in hydrofluoric acid based solutions. *Journal of Materials Science, 28*(23), 6261-6273.

113. Moulson, A., & Roberts, J. (1961). Water in silica glass. *Transactions of the Faraday Society, 57*, 1208-1216.

114. Geiger, G. H., & Poirier, D. R. (1973). Transport phenomena in metallurgy. *Addison-Wesley Publishing Co., Reading, Mass.1973, 616 P.*

ADVANCED ENGINEERING MATERIALS

DOI: 10.1002/adem.201600166

A Review of SiC Fiber Oxidation with a New Study of Hi-Nicalon SiC Fiber Oxidation**

By *Megan Wilson** and *Elizabeth Opila*

The linear and parabolic oxidation rate constants and activation energies for SiC fibers available in the literature are reviewed for the first time. Oxidation experiments are also conducted with Hi-Nicalon SiC fibers over 700–1 300 °C in dry O_2 with thermogravimetric analysis. Linear oxidation kinetics are observed from 700 to 800 °C and parabolic kinetics are observed from 900 to 1 300 °C. The linear and parabolic oxidation rate constant activation energies are determined to be 83 and 108 kJ mol^{-1}, respectively. These kinetic results are compared with the literature values. Differences in oxidation behavior are assessed as a function of fiber composition.

1. Introduction

Silicon carbide (SiC) fibers are used as reinforcements in ceramic matrix composites (CMCs) for high-temperature applications. It is important to understand the oxidation mechanisms of the SiC fibers to aid in determining the thermochemical life of the CMCs. This work provides a summary of SiC fiber oxidation data, as well as new results for Hi-Nicalon fibers.

SiC fiber oxidation results will be interpreted in terms of the oxidation mechanisms for bulk Si and SiC, which are now reviewed. Deal and Grove developed a linear–parabolic kinetic model for growth of the silicon oxidation product silica (SiO_2).[1] Linear oxidation kinetics occur when the rate-limiting step is the surface reaction of oxygen (O_2) gas with Si. This rate law applies when there is a thin oxide scale or at short times. Parabolic oxidation kinetics occur when the rate-limiting step is the transport of oxygen through the silica scale. This rate law applies at long times or when a thick oxide scale is present. Linear–parabolic oxidation kinetics occur when both mechanisms have similar rates and are observed at intermediate times and temperatures.[2] The Deal–Grove linear–parabolic kinetic model is given in simplified form by the following:

$$x^2 + Ax = Bt \tag{1}$$

where x is the oxide thickness, t is the oxidation time assuming no native oxide, B is equivalent to the parabolic rate constant, k_p in $\mu m^2 h^{-1}$, and B/A is equivalent to the linear rate constant, k_l in $\mu m\, h^{-1}$. At short times and for thin oxide scales, Equation 1 reduces to the following:

$$x = k_l t \tag{2}$$

At long times and for thick oxides, Equation 1 reduces to the following:

$$x^2 = k_p t \tag{3}$$

These equations can also be utilized for SiC and can be reformulated in terms of the overall mass increase attributed to the uptake of oxygen and loss of carbon, given by the following:

$$SiC + 3/2\, O_2(g) = SiO_2 + CO(g) \tag{4}$$

The conversion between oxide thickness and mass change for SiC is given by the following:

[*] *M. Wilson, Dr. E. Opila*
Department of Materials Science and Engineering, University of Virginia, Charlottesville, Virginia 22904, USA
E-mail: mew5rw@virginia.edu

[**] *The authors would like to thank the Rolls-Royce Corporation and the Air Force Research Laboratory (AFRL contract award FA8650-13-C-5211) for supporting this work.*

Megan Wilson received her Bachelor of Science in Chemical Engineering from Bucknell University, USA in 2013. In 2013, she joined the PhD program in the Materials Science and Engineering department at the University of Virginia, USA working with high-temperature ceramic materials.

Elizabeth Opila is associate professor of Materials Science and Engineering at the University of Virginia. She received her BS in Ceramic Engineering from the University of Illinois, Urbana-Champaign, her MS in Materials Science from the University of California, Berkeley, and her PhD in Materials Science from the Massachusetts Institute of Technology. She worked as a research scientist at the NASA Glenn Research Center in Cleveland, Ohio for 19 years. In 2010, she joined the University of Virginia as associate professor of Materials Science and Engineering. Elizabeth Opila holds six patents and is author or coauthor of more than 100 publications. She is a fellow of the Electrochemical Society and the American Ceramic Society.

$$\text{Oxide thickness (cm)} = \frac{\text{mass change (g)} \times \frac{MW\ SiO_2(\text{g mol}^{-1})}{MW\ \text{gain per mol}\ SiO_2\ \text{formed (g mol}^{-1})}}{SiO_2\ \text{density (g cm}^{-3}) \times \text{Surface area (cm}^2)} \quad (5)$$

The temperature dependence of each rate constant follows an Arrhenius dependence given by the following:

$$k = k_o \exp\left(\frac{-E_a}{RT}\right) \quad (6)$$

where k_o is the pre-exponential coefficient, E_a is the activation energy in J mol^{-1}, R is the universal gas constant, and T is the temperature in K.[1]

Linear rate constants reflect the surface reaction given by Equation 4. Deal and Grove attributed the activation energy for the Si oxidation linear reaction rate to the breaking of Si–Si bonds.[1] Schubert states that the energy required to break a Si–Si bond is greater than the energy to break a Si–C bond.[3] The activation energy for linear oxidation kinetics of SiC should therefore be smaller than that of Si oxidation based on bond breaking considerations. The temperature dependence of the parabolic rate constant reflects the enthalpy for the transport of oxidant through the growing SiO_2 scale and is expected to be the same for silicon and silicon carbide.[4]

Two important studies on bulk chemical vapor deposition (CVD) SiC are highlighted here. In the first, Ramberg provides a self-consistent set of linear and parabolic rate constants.[2] In the other by Ogbuji and Opila, oxidation rates were determined from carefully controlled environmental conditions during oxidation.[5] While bulk SiC oxidation is extensively reviewed,[6–8] an equivalent review on SiC fiber oxidation studies is needed. This study does not intend to contribute to the bulk SiC oxidation literature.

Therefore, the objectives of this paper are threefold. First, SiC fiber oxidation data are reviewed for the first time. The oxidation rate constants, activation energies, and experimental procedures are compared for both parabolic and linear oxidation kinetics of SiC fibers. Inconsistencies and gaps in the available data are identified. Second, new experimental results for Hi-Nicalon SiC fiber oxidation in dry O_2 in a well-controlled environment are reported. These results are compared to the oxidation rate constant and activation energy data available in the literature. Third, the effect of fiber composition on parabolic oxidation is examined. Ultimately, the oxidation results could be used in life prediction models of CMCs containing these fibers.

2. SiC Fiber Oxidation Literature Review

Several different SiC fibers have been developed and produced for use in CMCs. Polycarbosilane-derived fibers from Nippon Carbon include Nicalon, Hi-Nicalon, and Hi-Nicalon (S).[9] Nicalon was the first fiber developed by Nippon Carbon and has a Si–C–O composition.[10] These fibers contain a crystalline β-SiC phase, an amorphous Si–C–O phase, and excess free carbon.[9] Hi-Nicalon was developed to remove oxygen and contains SiC and excess carbon. Hi-Nicalon (S) was developed to be a nearly stoichiometric and highly crystalline SiC fiber.[10] Other SiC fibers include Sylramic (COI Ceramics) which is also a stoichiometric, polycrystalline SiC fiber, and a Si–C–N–O fiber derived from polysilazane and polycarbosilazane.[9,11] Several studies on the mechanical properties of SiC are available[12–18] including a review by Yun and DiCarlo.[19] SiC fiber oxidation has been studied to a lesser extent, of which less than half reported kinetic data for fiber oxidation.[10,13,20–28]

One goal of this paper was to compile all of the oxidation kinetics results that exist to our knowledge in the literature to use as a resource for future SiC fiber oxidation testing and CMC oxidation modeling. The data collected and compared include oxidation rate constants, activation energies, and experimental procedures. Table 1 gives a brief overview of studies on SiC fiber oxidation that include kinetic parameters.[11,29–34] The table outlines the fiber type, test temperature(s), atmosphere, and time used in each study, as well as the two studies of bulk SiC oxidation previously mentioned for comparison.[2,5]

Each study reviewed in Table 1, with the exception of Lipowitz et al.,[11] stated that an alumina tube furnace and/or an alumina crucible were used. These seven SiC fiber studies listed parabolic rate constants for the temperatures studied. Figure 1 is a plot of the log of these parabolic rate constants as

DOI: 10.1002/adem.201600166

Table 1. SiC fiber oxidation studies.

	Exposure temperature(s) [°C]										Exposure times		
Fibers studied	700	800	900	1 000	1 100	1 200	1 300	1 400	1 500	Oxidation atmospheres	≤20 h	100 h	References
Nicalon		x	x	x	x	x	x	x	x	O_2, air	x		[29]
Nicalon				x	x	x	x	x		2 vol% H_2O/dry air	x		[15]
Hi-Nicalon				x	x	x	x	x	x	O_2	x		[31]
Hi-Nicalon	x	x								O_2	x		[30]
Hi-Nicalon				x	x	x	x	x		2 vol% H_2O/dry air	x		[15]
Hi-Nicalon (S)	x	x	x	x	x	x	x	x		air		x	[32]
Hi-Nicalon (S)	x	x	x	x	x	x	x			1 vol% H_2O/dry air		x	[33]
Hi-Nicalon (S)				x	x	x	x	x		2 vol% H_2O/dry air	x		[15]
Sylramic						x				Dry air		x	[11]
Si–C–N–O				x	x	x	x	x		O_2	x	x	[34]
Bulk CVD-SiC		x	x	x	x					O_2		x	[2]
Bulk CVD-SiC					x	x	x	x	x	O_2		x	[5]
Hi-Nicalon	x	x	x	x	x	x	x			O_2		x	This study

a function of inverse temperature. Parabolic rate constants were extracted from figures in other studies and added to Figure 1.[22,29] Rate constants were also compared to two studies for bulk SiC,[2,5] as well as the results from this study. The data of Hay et al.[32–33] for Hi-Nicalon (S) were shown as lines since the rate constant expression (Eq. 6), rather than individual data points, were reported.

The plot in Figure 1 shows the variation in reported parabolic rate constants for SiC fibers. Factors that may affect the oxidation rate constants include the fiber composition, oxidation atmosphere, and the furnace or crucible materials. It is likely that a fiber containing SiOC or excess carbon would react with O_2 at a different rate than stoichiometric SiC, as will be considered in the discussion section. The oxygen partial pressure will also affect the rate so that reaction rates in air ($P_{O_2} = 0.21$ atm) were expected to be ~1/5 lower than those in pure oxygen. In addition, water vapor atmospheres will also increase parabolic oxidation rates due to the higher solubility of H_2O than O_2 in SiO_2.[1] Deal and Grove have shown that the parabolic rate constant, k_p is proportional to the P_{O_2} or P_{H_2O} for Si oxidation.[1] Furnace tubes or crucibles made of alumina were known to result in contamination of the SiO_2 scale at high temperatures, which could also increase the oxidation rate.[35,36]

The activation energy represents the energy required to overcome the kinetic barrier for any mechanism and the effect of fiber composition, oxidizing gases, and environment on oxidation. Table 2 lists the reported activation energies for parabolic oxidation of SiC fibers available in the literature.

The activation energies listed in Table 2 range from 69 to 249 kJ mol^{-1}. This large range shows the inconsistencies associated with SiC fiber oxidation results.

Rate constants and activation energies were also reported for linear oxidation kinetics of the SiC fibers in two studies.[32,33] Figure 2 shows the linear rate constants on a plot of the log of the rate constant versus inverse temperature. Again, the data of Hay et al.[32,33] were shown as lines. Results were compared to those obtained for bulk high-purity SiC,[2] SiC whiskers,[38] and the results of this study.

This plot shows consistent data between the Hay et al. studies in air and 3 mol% steam. However, no other data were found for the linear oxidation rate constants of SiC fibers. Hay et al.[32,33] also gave activation energies for the linear oxidation process. The two reported values for the activation energy are listed in Table 3 compared with values from this study, bulk SiC,[2] SiC whiskers,[38] and single-crystal Si.[1]

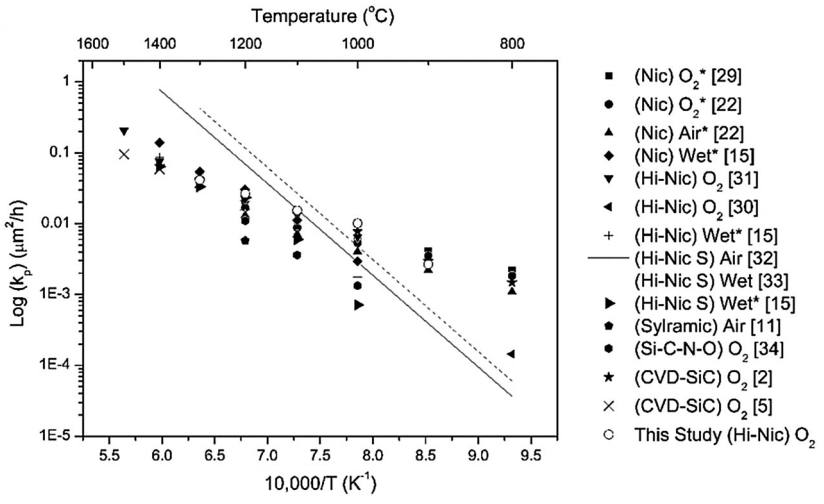

Fig. 1. Parabolic rate constants for SiC fiber oxidation plotted as log(k_p) versus inverse temperature. (indicates data extracted from a plot).*

Table 2. SiC fiber oxidation studies that reported activation energies for parabolic oxidation kinetics.

Fibers studied	Oxidation atmospheres	E_a [kJ mol^{-1}]	References
Nicalon	O_2	69	[29]
Nicalon	Air	77	[29]
Nicalon	Air	80	[24]
Nicalon	O_2	70	[22]
Hi-Nicalon	O_2	144	[22]
Hi-Nicalon	O_2	107	[31]
Hi-Nicalon	O_2	109	[17]
Hi-Nicalon	CO_2	151	[37]
Hi-Nicalon	10 vol% H_2O/20% O_2/N_2	86	[22]
Hi-Nicalon	20 vol% H_2O/20% O_2/N_2	60	[22]
Hi-Nicalon (S)	Dry air	248	[32]
Hi-Nicalon (S)	1 vol% H_2O/Dry air	249	[33]
Si–C–N–O	O_2	170	[34]
Bulk CVD-SiC	O_2	94	[2]
Bulk CVD-SiC	O_2	118	[5]
Hi-Nicalon	O_2	108 ± 15	This study

Table 3. SiC fiber oxidation studies that reported activation energies for linear oxidation kinetics.

Fibers studied	Oxidation atmospheres	E_a [kJ mol^{-1}]	References
Hi-Nicalon (S)	Air	138	[32]
Hi-Nicalon (S)	1 vol% H_2O/Air	141	[33]
Bulk CVD-SiC	O_2	170	[2]
SiC Whiskers	Air	72	[38]
Single Crystal Si	O_2	192	[1]
Hi-Nicalon	O_2	83 ± 150	This study

The available data for SiC fiber oxidation show large variations in the parabolic oxidation rate constants. Few results for linear oxidation rate constants are available. In addition, much of the data were obtained in equipment containing Al_2O_3 which is known to affect parabolic oxidation results.[35,36] In this work, oxidation of Hi-Nicalon SiC fibers was conducted in a clean environment (99.995% high-purity fused quartz furnace tubes) over a wide temperature range for comparison to the literature, as described in the following sections.

3. Experimental Section

Hi-Nicalon fiber tows (each tow comprised of 500 individual fibers) were cut in 10 cm lengths and twisted into a "lanyard" shape (Figure 3).

The as-received Hi-Nicalon fibers had a polyvinyl alcohol (PVA) sizing which was removed by placing lanyards in a boiling MilliQ deionized water bath at 100 °C for 1 h following the procedure of Hay et al.[32] The lanyards were removed from the water bath and dried while suspended in a convection oven for 20 min at 120 °C. The lanyards were reintroduced in the boiling water bath for another hour and the drying procedure was repeated. The desized lanyard was weighed on a bench-top balance (MS105D4, Mettler Toledo, Columbus, OH). The lanyard was suspended from a SetSys Setaram microbalance (Setaram Instruments, KEP Technologies, France) using an alumina hanger (99.5% pure, CoorsTek, Inc., Golden, CO) inside a 22 mm ID fused quartz tube (99.995% pure, Quartz Scientific, Inc., Fairport Harbor, OH) in the furnace for thermogravimetric analysis (TGA), similar to the setup used by Opila.[39] The TGA furnace was brought to temperature prior to the placing of the lanyard in the hot zone of the furnace. The test was initiated and mass change was recorded as a function of time. In addition to the mass change recorded by the TGA, the initial and final mass of each lanyard was recorded on the bench-top balance.

The benefits of this TGA setup include minimization of sample contamination from the alumina hanger, laminar gas flow over the sample, a clean environment provided by the fused quartz tube, and a 5 cm uniform furnace hot zone ($T \pm 5$ °C), enabling large specimen size for increased sensitivity of small mass changes monitored by the microbalance.

All oxidation experiments were conducted in dry O_2 gas flowing at 100 sccm (room temperature) sequentially through a desiccant (anhydrous $CaSO_4$) and then through the furnace tubes. Experiments were conducted between 700 and 1 300 °C in 100 °C intervals. The experiment times were 100 h for all exposures. Additional experiments at times less than 100 h were conducted at 900 °C to evaluate fit to a linear–parabolic rate law expected at this temperature, as explained further in the results section. During each oxidation experiment, mass, time, and temperature were acquired and recorded digitally. After an oxidation experiment was complete, the lanyard was removed from the furnace and weighed on

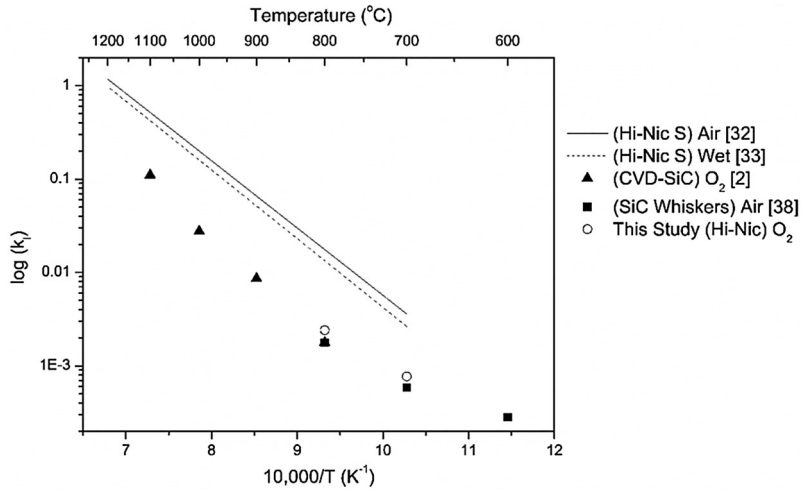

Fig. 2. Linear rate constants for SiC fiber oxidation plotted as log(k_l) versus inverse temperature.

DOI: 10.1002/adem.201600166

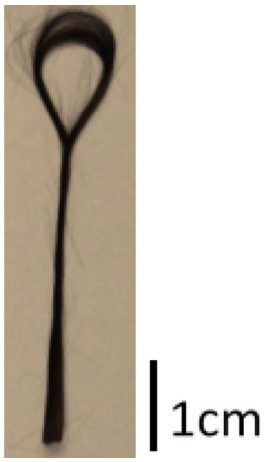

Fig. 3. Hi-Nicalon fiber lanyard.

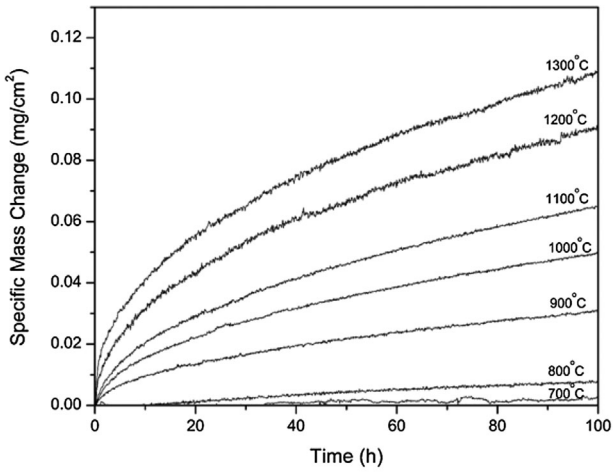

Fig. 4. Specific mass change versus time data for Hi-Nicalon fibers dry O_2 exposures.

the bench-top balance to determine the mass change after oxidation.

The morphology of the thermally grown oxide was characterized by scanning electron microscopy (SEM) (FEI Quanta 650, Hillsboro, Oregon). The fiber lanyards were cut or broken 9 mm from the straight end and adhered to a 90° aluminum stub with carbon tape and paint for SEM characterization. The oxide thicknesses on individual fibers were measured using the direct measurement tool in the SEM software. The measurement tool was found to agree with the National Institute of Standards and Technology (NIST) calibration standard (861/280822-11). Oxide thickness values were obtained from 1–6 locations on each fiber for 9–18 fibers from each oxidation experiment. At least three oxidation experiments were conducted at each test condition except 700 °C, and a statistical average and standard deviation were calculated from the measured oxide thicknesses.

4. Results

4.1. Parabolic Oxidation Kinetics

Figure 4 shows selected mass change versus time data for 100 h experiments conducted at 700–1 300 °C. Mass gains were normalized by the geometric surface area of the lanyards calculated as a product of the surface area of 500 cylindrical fibers (500 fibers in a tow), each 10 cm in length, and 1.4×10^{-3} cm in diameter. This calculation of surface area does not account for change in surface area due to fibers breaking when forming the lanyard shape or surface area reduction during oxidation.

As seen in Figure 4, the shapes of the mass gain versus time data demonstrate which oxidation mechanism was relevant at each temperature. At high temperatures ($T \geq 1\,000$ °C), a parabolic mass gain was observed over the 100 h experiment, indicating parabolic kinetics. At low temperatures ($T \leq 800$ °C), a linear mass gain was observed, indicating linear kinetics over the 100 h experiment. It is expected that at longer times, when the oxide is sufficiently thick, the linear oxidation kinetics would gradually change to parabolic oxidation kinetics.[1] At an intermediate temperature ($T = 900$ °C), a parabolic mass gain was observed; however, further experiments were conducted at this temperature to determine whether some contribution of both linear reaction and/or parabolic oxidation mechanisms limited the overall oxidation rate. Linear–parabolic kinetics were expected for intermediate temperatures where both linear and parabolic mechanisms were competing.[2]

Experiments were conducted at 900 °C for times less than 100 h to accumulate oxide thickness versus time data to characterize any transition between linear (800 °C) and parabolic (1 000 °C) kinetics. Experimental times of 6.25, 25, 56.25, and 100 h were selected such that they would be evenly distributed on an oxide thickness versus root time plot. The oxide thicknesses after each experiment were characterized with SEM and the averages are displayed in Table 4 along with the statistical information used to determine each reported value.

The oxide thickness versus root time data obtained at 900 °C are plotted in Figure 5. There is variability in the data at both short times (6.25 h) and long times (100 h). Contamination and temperature gradients were considered as possible sources of variability. All fiber lanyards were desized using

Table 4. Average measured oxide thicknesses for Hi-Nicalon fibers dry O_2 experiments conducted at 900 °C for each exposure time.

Time [h]	Oxide thickness [μm]	# Experiments, # measurements, # fibers
4	0.11 ± 0.02	3, 105, 35
6.25	0.13 ± 0.08	3, 135, 39
25	0.27 ± 0.03	3, 118, 42
56.25	0.44 ± 0.04	3, 132, 39
100	0.53 ± 0.07	3, 135, 35

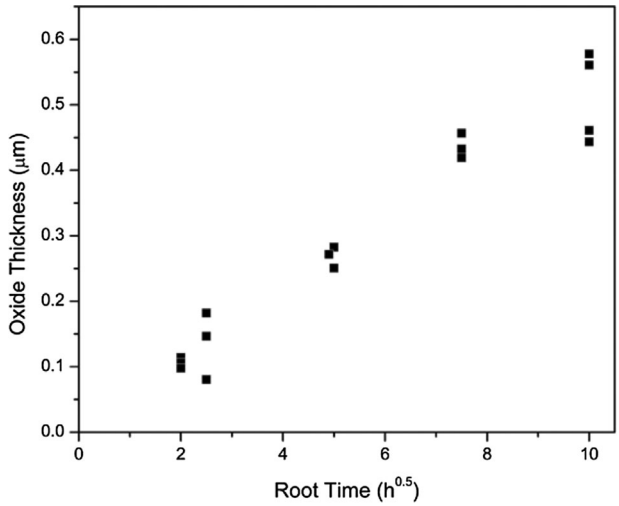

Fig. 5. Oxide thickness versus root time for all Hi-Nicalon dry O_2 exposures conducted at 900 °C.

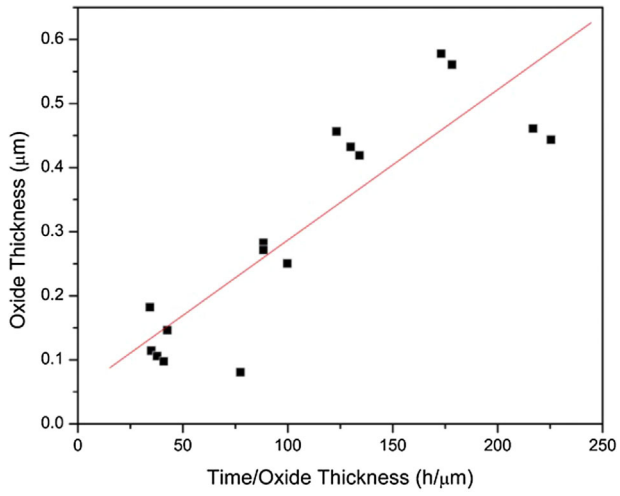

Fig. 6. Oxide thickness versus time/oxide thickness for all Hi-Nicalon dry O_2 exposures conducted at 900 °C.

the same method and should result in the same removal of PVA coating. Moreover, two of the lanyards oxidized at 900 °C for 100 h were desized at the same time but formed different oxide thicknesses (0.44 and 0.56 μm). This was also true at the shorter times. All of the lanyards used for the 6.25 h experiments were desized at the same time. The desizing method was therefore not the source of the variability. Under optical inspection, the fiber lanyards oxidized at 900 °C (and below) showed interference colors, indicating thin oxides on the fibers.[40] All of the fiber lanyards oxidized at 900 °C were uniform in color along the length of the lanyard. It was concluded, therefore, that the entire lanyard was oxidized in the hot zone of the furnace and that there was no temperature gradient present during the oxidation process. Variation in temperature is not the source of variability in the oxide thickness data. The source of this variability remains unknown.

For linear–parabolic oxidation kinetics, Deal and Grove suggest determining both the linear and parabolic rate constants from the best fit line on a plot of the oxide thickness versus time/oxide thickness.[1] When the data are plotted in this manner, the slope of the line is equivalent to the parameter B (of Eq. 1) and the intercept of the line is equivalent to $-A$ (of Eq. 1). Figure 6 shows the data in this form. The variability seen in Figure 5 is amplified in this plot.

A parabolic rate constant of $2.3 \times 10^{-3} \pm 0.7 \times 10^{-3}\ \mu m^2\,h^{-1}$ was calculated from the slope of the best-fit line shown in Figure 6. The intercept of the best-fit line in Figure 6 yielded a negative value of A, which is nonphysical for a linear rate constant. When a linear regression was performed on to the data in Figure 5 (typical analysis for purely parabolic oxidation kinetics), a parabolic rate constant of $2.7 \times 10^{-3}\ \mu m^2\,h^{-1}$ was obtained from the square of the slope. This was in good agreement with the value from the slope in Figure 6, considering the variability in the data. The raw mass change versus root time data from the TGA, plotted in Figure 7, result in a linear plot, also consistent with parabolic oxidation and a parabolic rate constant of $3.1 \times 10^{-3}\ \mu m^2\,h^{-1}$, in good agreement with values obtained in Figure 5 and 6.

It was therefore concluded that purely parabolic oxidation occurred at 900 °C (and above) for Hi-Nicalon SiC fibers and linear oxidation for these fibers occurred at 800 °C and below. It was unnecessary to use the full linear–parabolic rate law at any conditions studied. Naslain et al.[22] also found oxidation of Hi-Nicalon to be parabolic over the range of 900–1 400 °C.

For all temperatures studied (700–1 300 °C), the total mass gains (from the bench-top and the TGA) were used to predict the oxide thickness grown on each individual fiber using Equation 5. Table 5 shows typical results from these calculations for a single experiment at each temperature studied.

The oxide thickness predicted from the TGA mass gain was greater than the oxide thickness predicted from the bench-top

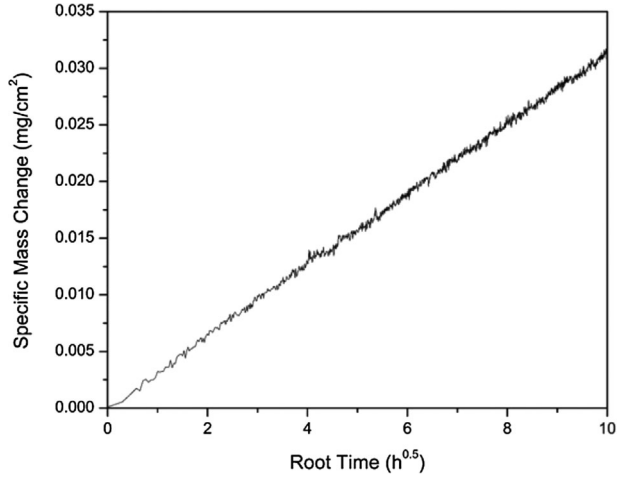

Fig. 7. Specific mass change versus root time data from a TGA experiment for Hi-Nicalon exposed in dry O_2 at 900 °C for 100 h.

DOI: 10.1002/adem.201600166

Table 5. Oxide thicknesses predicted from mass gain for Hi-Nicalon fibers oxidized in dry O_2 as a function of temperature.

Temp. [°C]	Predicted oxide thickness from bench-top mass gain [μm]	Predicted oxide thickness from TGA mass gain [μm]
700	0.04	0.03
800	0.09	0.12
900	0.28	0.36
1 000	0.52	0.68
1 100	0.82	0.90
1 200	1.02	1.16
1 300	1.23	1.42

Table 6. Average measured oxide thicknesses for Hi-Nicalon fibers after exposure in dry O_2 for 100 h at each temperature studied.

Temp. [°C]	Oxide thickness [μm]	# Experiments, # measurements, # fibers
700	0.077 ± 0.011	1, 57, 17
800	0.24 ± 0.08	3, 81, 33
900	0.53 ± 0.07	3, 135, 35
1 000	1.01 ± 0.09	3, 128, 39
1 100	1.24 ± 0.11	3, 141, 41
1 200	1.63 ± 0.07	5, 110, 33
1 300	2.10 ± 0.14	2, 108, 27

balance (except at 700 °C where the oxide is predicted to be small) and is attributed to drift in the TGA voltage signal associated with the mass change.

After each experiment, the oxide thicknesses were measured with the SEM measurement tool. Figure 8 shows selected examples of oxide thicknesses and fiber cross-sections for all seven temperatures studied. Measurements were made only on fibers that were aligned perpendicular to the SEM detector. Arrows in Figure 8f show an example of the oxide thickness measured.

An average oxide thickness and standard deviation were calculated for each experimental temperature. Table 6 shows the average oxide thicknesses observed with SEM for lanyards exposed for 100 h at temperatures 700–1 300 °C.

If the oxidation mechanism is known, a rate constant can be calculated from the oxide thickness. For linear oxidation kinetics (700–800 °C), Equation 7 was used to calculate the linear rate constant, k_l, in μm per hour.

$$k_l\left(\frac{\mu m}{h}\right) = \frac{\text{Average observed oxide thickness } (\mu m)}{\text{Total oxidation time (h)}} \quad (7)$$

For parabolic oxidation kinetics (900–1 300 °C), Equation 8 was used to calculate the parabolic rate constant, k_p, in μm^2 per hour.

$$k_p\left(\frac{\mu m^2}{h}\right) = \frac{\left(\text{Average observed oxide thickness } (\mu m)\right)^2}{\text{Total oxidation time (h)}} \quad (8)$$

The linear rate constants for experiments conducted at 700–800 °C and parabolic rate constants for 900–1 300 °C calculated from the average observed oxide thicknesses are listed in Table 7.

Rate constants can also be calculated from the total mass gain, or the mass gain as a function of time in units of mg cm^{-2} h (Eq. 7) or $mg^2\,cm^{-4}$ h (Eq. 8). Both of these calculations require normalizing the mass change by the surface area of SiC fibers exposed for oxidation. This surface area is not constant, however, due to fibers joining together during oxidation (as seen in Figure 8f), causing an underestimation of the rate constants. The rate constants derived from the oxide thicknesses are therefore considered the most accurate.

Rate constants, both linear and parabolic, are exponentially dependent on temperature as given by Equation 6. The activation energy (E_a) is different for linear and parabolic oxidation since this value provides information about the energetics of the rate-limiting mechanism. The activation energy can be determined by plotting the log of the rate constant versus inverse temperature. The slope of the line is used to determine the activation energy. Figure 9 shows the log of the parabolic rate constants versus inverse temperature

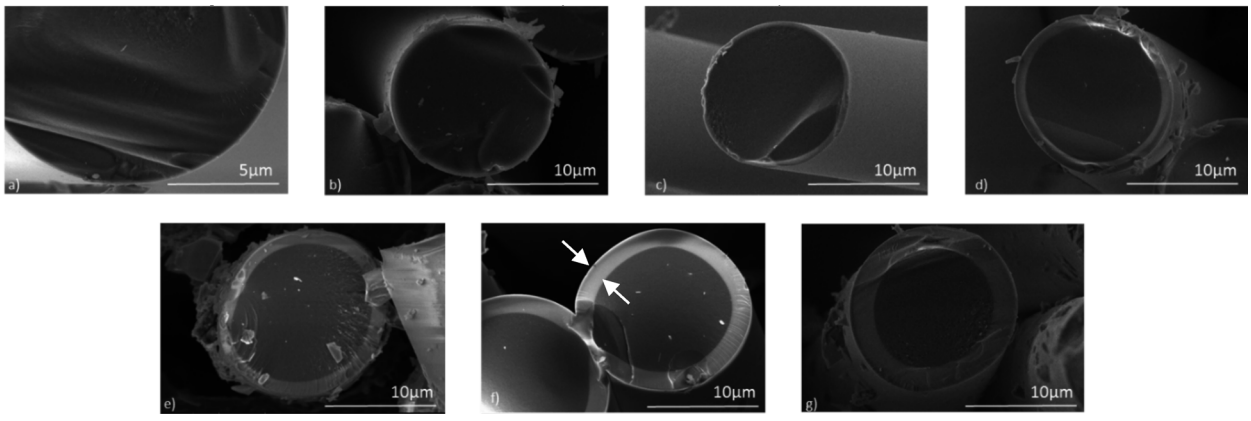

Fig. 8. Typical observed oxide thicknesses after 100 h exposures of Hi-Nicalon fibers in dry O_2 at (a) 700, (b) 800, (c) 900, (d) 1 000, (e) 1 100, (f) 1 200, and (g) 1 300 °C. Arrows in (f) show an example of the measured oxide thickness.

Table 7. Linear and parabolic rate constants calculated from the average measured oxide thicknesses for Hi-Nicalon fibers dry O_2 exposures conducted at 700–1 300 °C.

Temp. [°C]	k_l from observed thickness [μm h^{-1}]	k_p from observed thickness [$\mu m^2 h^{-1}$]
700	7.70×10^{-4}	
800	2.41×10^{-3}	
900		2.35×10^{-3}
1 000		1.01×10^{-2}
1 100		1.54×10^{-2}
1 200		2.65×10^{-2}
1 300		4.44×10^{-2}

for temperatures ranging from 900 to 1 300 °C. Oxide crystallization was observed in two of four experiments conducted at 1 300 °C. The oxide thicknesses reported and used for k_p calculations were all for amorphous SiO_2.

Using the slope of the best-fit line from Figure 9, the activation energy for parabolic oxidation kinetics was calculated to be 108 ± 15 kJ mol^{-1} with a pre-exponential coefficient of 198 ± 33 $\mu m^2 h^{-1}$ with 95% confidence. This value will be compared with the literature values in the discussion section.

4.2. Linear Oxidation Kinetics

The temperature dependence for linear rate constants is also included in Figure 9. Using the slope and Equation 6, the activation energy for linear oxidation kinetics was calculated to be 83 ± 150 kJ mol^{-1} with a pre-exponential coefficient of $22 \pm 2\,500$ μm h^{-1} with 95% confidence. Only two experimental temperatures exhibited linear behavior, so the error associated with this small amount of data is larger than the error for parabolic oxidation. The linear oxidation activation energy value will also be compared with the literature values in the discussion section.

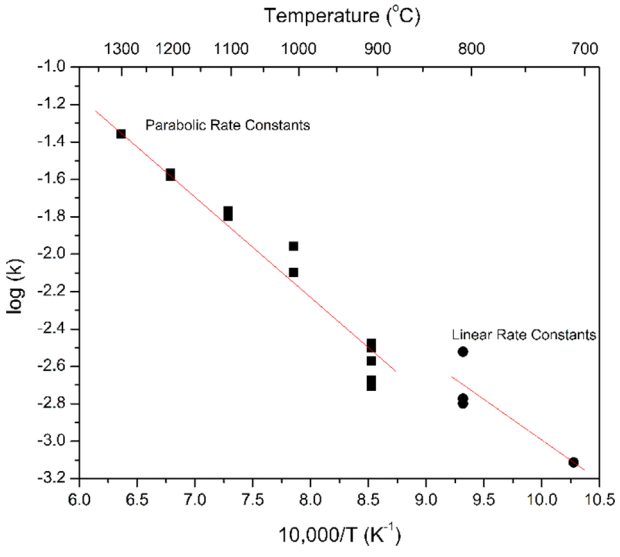

Fig. 9. Plot of log(k) versus inverse temperature for Hi-Nicalon fibers exposed in dry O_2 used to calculate the activation energy for parabolic oxidation kinetics (900–1 300 °C) and linear oxidation kinetics (700–800 °C).

5. Discussion

5.1. Parabolic Oxidation Kinetics

The parabolic rate constants determined in this study are compared with the rate constants reviewed earlier (Figure 1). The rate constants from this study at 900–1 100 °C were in good agreement with the constants from bulk SiC given by Ramberg et al.[2] while the rate constant at 1 200 and 1 300 °C were closest in agreement with Hi-Nicalon fiber oxidation studies conducted by Chollon et al.[31] and CVD-SiC oxidation studies conducted by Ogbuji and Opila.[5] When comparing the rate constant data from the literature (Figure 1), it is noticeable that the rate data for Hi-Nicalon (S) fibers reported by Hay et al.[32–33] have a steeper slope and higher activation energy relative to the data reported from any other study (including this one). There is an overlap at 1 100 °C in the Hi-Nicalon (S) data from Hay et al.[32] and the Hi-Nicalon data from this study. Takeda and Urano[15] report rate constants for Nicalon, Hi-Nicalon, and Hi-Nicalon (S) obtained in 2 vol% H_2O in air that are similar to values reported for other Hi-Nicalon studies at temperatures of 1 100–1 300 °C. It is therefore unclear whether the steep slopes for Hi-Nicalon (S) reported by Hay et al. in Figure 1 are a result of the test environment or of the fiber type. The effect of fiber composition on parabolic oxidation will be discussed below.

It can also be noted in the parabolic kinetic data by Hay et al., that the activation energies are nearly identical for two different gas environments: air and wet air.[32,33] Deal and Grove state that the activation energy for a wet environment is lower than for a dry environment and that the parabolic rate constants are higher for wet oxidation than for dry oxidation.[1] Deal and Grove used 95 °C water to saturate an oxygen stream, giving a saturation of 84 vol% H_2O in the gas stream.[1] Hay used 3 mol% H_2O (≈1 vol%) in air,[33] which is significantly less water content than Deal and Grove used in their study. Opila reported that for water-vapor partial pressure to have a significant effect on the oxidation, P_{H_2O} must be greater than 2.5 vol% at 1 200 °C or 4.8 vol% at 1 400 °C.[41] The small vol% of H_2O used by Hay et al.[33] may account for the similarities in parabolic rate constants and the activation energy observed in the wet and dry experiments.

The activation energies calculated in this study are also compared with those in the literature. The two studies that oxidized Hi-Nicalon fibers in O_2 gas reported activation energies of 109 and 107 kJ mol^{-1}, respectively,[17,31] for parabolic oxidation kinetics. The activation energy of 108 ± 15 kJ mol^{-1} from this study is not statistically different from the aforementioned activation energies. Studies of CVD-SiC oxidation reported an activation energy of 94 and 118 kJ

ADVANCED ENGINEERING MATERIALS 2016,
DOI: 10.1002/adem.201600166

mol^{-1}.[2,5] Deal and Grove reported an activation energy of 119 kJ mol^{-1} for Si oxidation in dry oxygen,[1] and this value was attributed to oxidation limited by permeation of molecular oxygen through silica.[42] Therefore, there is good agreement of the activation energies determined in this study with values reported in the literature for Hi-Nicalon fiber, CVD-SiC, and Si parabolic oxidation kinetics.

The large range of parabolic activation energies in Table 2 (69–249 kJ mol^{-1}) can be categorized by fiber type. The parabolic activation energies reported for Nicalon fibers range from 69 to 80 kJ mol^{-1}, Hi-Nicalon from 107 to 151 kJ mol^{-1}, Hi-Nicalon (S) from 248 to 249 kJ mol^{-1}, and CVD-SiC from 94 to 118 kJ mol^{-1}. This observation suggests that the fiber composition affects the temperature dependence for parabolic oxidation kinetics which is inconsistent with oxidation limited by transport of O_2 through SiO_2, regardless of fiber composition.

5.2. Linear Oxidation Kinetics

The linear rate constants determined in this study are compared with the rate constants from the literature in Figure 2. The linear rate constants from this study are in good agreement with those for CVD-SiC and SiC whiskers, but not with those for Hi-Nicalon (S).[2,32,33,38] Ramberg suggests that linear oxidation is important up to 1100 °C, but this study found that linear oxidation of Hi-Nicalon fibers only occurred at and below 800 °C.[2] The differences of an order of magnitude between the data from Hay et al.[32,33] and this study could be attributed to a variety of factors including fiber composition, or oxidizing atmosphere/environment. Further studies need to be conducted to determine the cause of the difference.

There are fewer activation energies for linear oxidation kinetics reported in the literature than for parabolic oxidation kinetics. The range in the reported values of activation energies for linear oxidation kinetics is 72–170 kJ mol^{-1}, compared to Deal and Grove's value of 192 kJ mol^{-1} for linear oxidation of single-crystal Si (Table 3). As mentioned above, Schubert stated that the energy released when a Si–Si bond is broken is greater the energy released when breaking a Si–C bond.[3] Grunenberg also reported a higher Si–Si bond energy than Si–C bond energy.[43] These arguments agree with the trend seen in Table 3. The linear oxidation activation energy reported in this study for Hi-Nicalon SiC fibers, although it has a large uncertainty, is even lower than the bulk CVD-SiC (Table 3). It is hypothesized that this is due to the excess free carbon in the fiber; C–C bonds have an even lower bond energy than Si–C bonds.[43] It follows that a SiC fiber further from stoichiometry would require less energy to break Si–C bonds, lowering the temperature dependence for oxidation at short times and low temperatures. This is also consistent with the activation energy reported for SiC whisker oxidation by Wang et al.[38] The whiskers have an excess of free carbon as seen by X-ray photoelectron spectroscopy (XPS) and therefore it is reasonable that the activation energy for SiC whisker oxidation is lower than bulk CVD-SiC or Hi-Nicalon (S) fibers.[38]

5.3. Fiber Composition Effects on Parabolic Oxidation

In this section, the effect of the fiber composition on the oxidation rate in the parabolic regime is explored. While parabolic oxidation rates are limited by the diffusion of O_2 gas through the oxide layer, the overall mass change, oxide thickness, and fiber recession will be affected by the amount of available Si in the form of SiC to oxidize. Thus, it is expected that the temperature dependence will be the same for all fibers, but the magnitude of the rates will differ with composition. In a high-oxygen (Nicalon) or non-stoichiometric (Hi-Nicalon) SiC fiber, there is a lower mol% of Si available to oxidize than in a pure, stoichiometric fiber (Hi-Nicalon (S)). The mass% compositions of various SiC fibers from Flores et al.[9] are converted to mol% compositions (Table 8).

To explore differences in expected mass change, oxide growth, and fiber recession, two models were considered. The two models examine fibers with either constant phase areas or constant phase thicknesses, respectively. First, a number of simplifying assumptions were made for both models. While these assumptions may not be rigorously correct, they provide a means of exploring differences in oxidation behavior attributed to compositional differences. In both models, every oxygen atom in the fiber was considered as bonded to a silicon atom (as SiO_2). All remaining Si was assumed to be SiC. All remaining C was assumed to be free graphitic carbon. It was assumed that any initial SiO_2 in the fiber does not react through an oxidation process. The remaining phases, SiC and free C, were subject to oxidation. A SiC density of 3.1 g cm^{-3},[44] a C density of 2.26 g cm^{-3},[45] and a SiO_2 density of 2.65 g cm^{-3}[46] were assumed. In the first model, the molecular weights and densities were used to convert the moles of SiC and free C to volumes (assuming 1 mole total). The vol% of each phase is shown in Table 9, along with the mol%, in each fiber based on these assumptions.

The following oxidation rates were assumed in both models. The rate at which SiC oxidizes to SiO_2 was assumed to be that reported by Ogbuji and Opila for CVD-SiC at 1 200 °C (1.8×10^{-2} μm h^{-1}).[5] Free C will oxidize and leave the system faster than SiC will oxidize, so it is not considered as the rate determining step. However, it was assumed for the models that the rate at which free C leaves the system as CO/CO_2 is proportional to the rate at which SiC oxidizes by the mol ratio

Table 8. Mole percent compositions of three SiC fibers converted from Flores et al.[9]

Fibers	Mol% Si	Mol% C	Mol% O
Nicalon	36.9	49.3	13.9
Hi-Nicalon	41.5	57.9	0.6
Hi-Nicalon (S)	48.6	51.1	0.2

Table 9. Assumed mole and volume percent of phases in SiC fibers.

Fibers	Mol% SiC	Vol % SiC	Mol% C	Vol % C	Mol% SiO_2	Vol % SiO_2
Nicalon	51.5	58.1	35.7	16.6	12.8	25.3
Hi-Nicalon	69.3	83.8	30.2	15.0	0.5	1.2
Hi-Nicalon (s)	94.4	97.3	5.4	2.3	0.2	0.4

of C:SiC, assuming additional free carbon is exposed to oxygen as the SiC is consumed. In the first model, SiC recession was examined for a fiber with constant phase areas and in the second model, mass change due to oxidation was examined for a fiber with constant phase thicknesses.

In Model 1: SiC recession for equal phase area exposed, the physical form of the fiber was simplified to three volumes (one for each phase). Each phase was assumed to be 1 cm^2 times a depth relative to the assumed volume fraction of each phase. Oxidation was measured by SiC recession in this model since fiber recession determines the lifetime of the fiber. The calculations from Model 1 indicate that SiC was completely consumed after 88 h for Nicalon, 184 h for Hi-Nicalon, and 248 h for Hi-Nicalon (S). The dimensional change equivalent to the consumption of SiC and C, and the growth of SiO_2 in all fibers was normalized to that of Hi-Nicalon (S) after 248 h (Figure 10). The dimensional increase occurs because the density of SiO_2 is less than that of SiC.

This model showed that the fiber composition affected both the oxidation time for complete fiber consumption as well as the dimensional change of the fibers with time. Hi-Nicalon (S) exhibited greatest dimensional change and longest oxidation time for complete consumption of the fiber.

In Model 2: mass change at constant phase thickness, the same initial volume percents as shown in Table 9 were assumed, but the volumes had constant depths of 1 μm and surface areas proportional to volume fraction. This model examined the mass change as a function of available surface area. Using this model, SiC was consumed in 250 h for all fiber types. However, there was more SiC originally in Hi-Nicalon (S) than the other fibers, resulting in a higher amount of SiO_2 and greater overall mass gain. Figure 11 shows the mass changes for each fiber normalized to that of Hi-Nicalon (S) after 250 h. This model showed that the fiber composition affected the mass change of the fibers with time as well as the total mass change of the fiber.

The fiber composition should therefore be considered a key parameter for CMC applications and comparison of oxidation behavior by weight change is only valid for fibers of the same composition. Although the parabolic rate constant was assumed to be the same for all three fibers, the starting amount of SiC available for oxidation as well as the final amount of SiO_2 after complete oxidation increased with increasing purity and stoichiometry of the fiber in both models. It is expected from these results that the amount of SiO_2 formed at any time would be greatest for Hi-Nicalon (S), followed by Hi-Nicalon and Nicalon. Thus, it is predicted that Hi-Nicalon (S) would have a higher parabolic rate constant at any given temperature than Hi-Nicalon and Nicalon. This is in qualitative agreement with the results at $T > 1\,200\,^{\circ}C$ as in Figure 1.

The observed differences in activation energies are not addressed by the simple models presented here. Ogbuji and Bryan found that oxidation of Si_3N_4 resulted in an in situ substitution of O for N to form a silicon oxynitride, changing the activation energy for oxidation.[47] It could be speculated that a similar silicon oxycarbide could form at the SiC/SiO_2 interface during oxidation of Hi-Nicalon (S). A thin interfacial oxycarbide layer was observed by Guinel and Norton in polycrystalline SiC;[48] however, this phase has not yet been observed for SiC fibers. The mechanism for changes in transport rate of oxygen in SiO_2 formed on the Hi-Nicalon (S) remains to be identified. Nevertheless, the activation energy

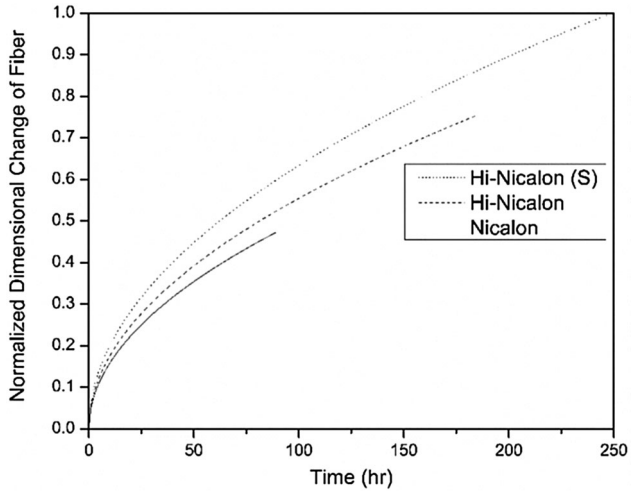

Fig. 10. Normalized dimensional change of each SiC fiber as calculated in model 1.

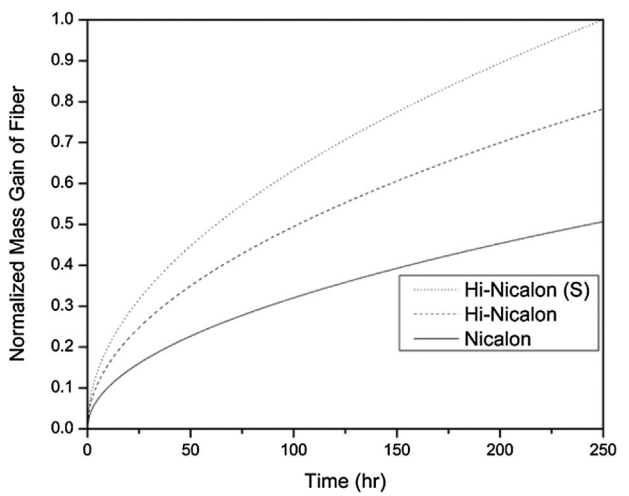

Fig. 11. Normalized mass changes of each SiC fiber as calculated in model 2.

DOI: 10.1002/adem.201600166

differences and the results of the models give evidence that the composition of the fiber does affect the oxidation process and that the fiber types should be considered in any CMC oxidation model.

5.4. Recommendations for Future Work

After reviewing the literature and the results of this study, there remain critical unanswered questions that should be considered for the development of accurate fiber oxidation and CMC life prediction models. First, only three studies (this study and two by Hay et al.[32,33]), provided kinetic data for linear oxidation kinetics at short times and low temperatures. This study is the first to report linear oxidation kinetic data for Hi-Nicalon fibers; Hay's studies were conducted with Hi-Nicalon (S).[32,33] A study of linear oxidation is critical when considering the intermediate temperatures, near 800 °C, of significant interest for use of SiC CMC materials.

Secondly, other than Takeda et al.[15] and Hay et al.,[33] there are no studies that report oxidation kinetic data obtained in H_2O(g) containing environments, linear or parabolic. As mentioned above, both Takeda and Hay used 1–2 vol% H_2O, which shows negligible effects of water vapor on Hi-Nicalon (S) oxidation. Oxidation with high water-vapor partial pressures provides a more realistic simulation of a combustion environment than dry O_2 and should be studied to provide more relevant kinetic data. The current study provided oxidation kinetics of Hi-Nicalon fibers in dry oxygen to supplement the available literature and will also be used as a baseline for future SiC fiber oxidation studies in wet oxygen (50 vol% H_2O, 50 vol% O_2).

As shown by the simple models above, the composition of the SiC fiber affects the oxidation kinetics. A study to quantitatively prove this point would be to repeat oxidation studies of the three different fibers in identical environments (time, temperature, furnace, and laboratory) to eliminate the uncertainty associated with various experimental setups and experimenters. In addition, an explanation for the variation in parabolic oxidation activation energies is still lacking.

A final issue that has not been addressed is the usefulness of these fiber oxidation data without consideration of the composite matrix/fiber interphase. A typical interphase material used in CMCs is Boron Nitride (BN) which will oxidize to form boria (B_2O_3).[49,50] The SiO_2 and B_2O_3 products react to form a borosilicate glass, which will dramatically affect the oxidant transport rate in the glass and therefore the parabolic rate constant.[51,52] The presence of the BN interphase is likely to dominate the SiC fiber oxidation kinetics and an understanding of boria effects is critical to development of accurate CMC degradation models or thermochemical lifetime predictions.

6. Conclusions

The data available in the literature for the oxidation of SiC fibers were reviewed. Linear and parabolic rate constants and associated activation energies were reported and compared to results found in this laboratory. The reported parabolic oxidation rate activation energies in the literature ranged from 69 to 249 kJ mol^{-1} but it was noted that the activation energies varied for each fiber type (Nicalon, Hi-Nicalon, and Hi-Nicalon (S)). This implies that compositional differences between the SiC fibers affect the oxidation behavior.

Hi-Nicalon SiC fibers were oxidized in dry oxygen over the temperature range 700–1 300 °C. It was found that linear oxidation kinetics were followed from 700 to 800 °C and parabolic oxidation kinetics were followed from 900 to 1 300 °C. The parabolic activation energy reported for this study was in agreement with other Hi-Nicalon oxidation studies as well as bulk CVD-SiC oxidation studies.

Two simple models were developed in this review to demonstrate the effect of fiber composition on oxidation; the starting amount of SiC available for oxidation as well as the final amount of SiO_2 after complete oxidation increased with increasing purity and stoichiometry of the fiber.

Article first published online: xxxx
Manuscript Revised: May 24, 2016
Manuscript Received: March 29, 2016

[1] B. E. Deal, A. Grove, *J. Appl. Phys*. **1965**, *36*, 3770.
[2] C. E. Ramberg, G. Cruciani, K. E. Spear, R. E. Tressler, C. F. Ramberg, *J. Am. Ceram. Soc*. **1996**, *79*, 2897.
[3] U. Schubert, *Angew. Chem. Int. Edit*. **1994**, *33*, 419.
[4] M. Lamkin, F. Riley, R. Fordham, *J. Eur. Ceram. Soc*. **1992**, *10*, 347.
[5] L. U. Ogbuji, E. J. Opila, *J. Electrochem. Soc*. **1995**, *142*, 925.
[6] V. Presser, K. G. Nickel, *Cr. Rev. Sol. State. Mater. Sci*. **2008**, *33*, 1.
[7] N. S. Jacobson, *J. Am. Ceram. Soc*. **1993**, *76*, 3.
[8] T. Narushima, T. Goto, T. Hirai, Y. Iguchi, *Mater. Trans*. **1997**, *38*, 821.
[9] O. Flores, R. K. Bordia, D. Nestler, W. Krenkel, G. Motz, *Adv. Eng. Mater*. **2014**, *16*, 621.
[10] K. Okamura, T. Shimoo, K. Suzuya, K. Suzuki, *J. Ceram. Soc. Jpn*. **2006**, *114*, 445.
[11] J. Lipowitz, J. Rabe, A. Zangvil, Y. Xu, *Ceram. Eng. Sci. Proc*. **1997**, *51* 147.
[12] R. Tressler, J. DiCarlo, *Ceram. Trans*. **1995**, *57*, 141.
[13] T. Shimoo, F. Toyoda, K. Okamura, *K, J. Am. Ceram. Soc*. **2000**, *83*, 1450.
[14] H. Kim, A. J. Moorhead, *J. Am. Ceram. Soc*. **1991**, *74*, 666.
[15] M. Takeda, A. Urano, J. Sakamoto, Y. Imai, *J. Am. Ceram. Soc*. **2000**, *83*, 1171.
[16] R. Yao, Z. Feng, L. Chen, Y. Zhang, B. Zhang, *Corros. Sci*. **2012**, *57*, 182.
[17] T. Shimoo, F. Toyoda, K. Okamura, *J. Mater. Sci*. **2000**, *35*, 3301.
[18] P. Le Coustumer, M. Monthioux, A. Oberlin, *J. Eur. Ceram. Soc*. **1993**, *11*, 95.
[19] H. M. Yun, J. A. DiCarlo, *Proc. 23rd Ann. Conf. Compos. Mater. Struct*. **1999**, *20*, 259.

[20] T. Shimoo, K. Okamura, Y. Morisada, *J. Mater. Sci*. **2002**, *37*, 1793.
[21] Y. T. Zhu, S. T. Taylor, M. G. Stout, D. P. Butt, T. C. Lowe, *J. Am. Ceram. Soc*. **1998**, *81*, 655.
[22] R. Naslain, A. Guette, F. Rebillat, S. Le Gallet, F. Lamouroux, L. Filipuzzi, C. Louchet, *J. Mater. Sci*. **2004**, *39*, 7303.
[23] T. Zima, N. Baklanova, A. Titov, *J. Eur. Ceram. Soc*. **2005**, *25*, 1943.
[24] M. Huger, S. Souchard, C. Gault, *J. Mater. Sci. Lett*. **1993**, *12*, 414.
[25] C. Vix-Guterl, P. Ehrburger, *J. Mater. Sci*. **1996**, *31*, 5363.
[26] S. Wu, L. Cheng, L. Zhang, Y. Xu, J. Zhang, H. Mei, *Appl. Surf. Sci*. **2006**, *253*, 1447.
[27] S. Wu, L. Cheng, L. Zhang, Y. Xu, Q. Zhang, *Mater. Lett*. **2007**, *30*, 215.
[28] D. Gosset, C. Colin, A. Jankowiak, T. Vandenberghe, N. Lochet, *J. Am. Ceram. Soc*. **2013**, *96*, 1622.
[29] L. Filipuzzi, R. Naslain, *Proc. 7th CIMTEC* **1991**, 35.
[30] W. Gauthier, F. Pailler, J. Lamon, R. Pailler, *J. Am. Ceram. Soc*. **2009**, *92*, 2067.
[31] G. Chollon, R. Pailler, R. Naslain, F. Laanani, M. Monthioux, P. Olry, *J. Mater. Sci*. **1997**, *32*, 327.
[32] R. Hay, G. Fair, R. Bouffioux, E. Urban, J. Morrow, A. Hart, M. Wilson, *J. Am. Ceram. Soc*. **2011**, *94*, 3983.
[33] R. Hay, G. Fair, A. Hart, S. Potticary, R. Bouffioux, *Ceram. Eng. Sci. Proc*. **2012**, *33*, 253.
[34] D. Mocaer, R. Pailler, R. Naslain, G. Chollon, L. Filipuzzi, *J. Mater. Sci*. **1993**, *28*, 3059.
[35] E. Opila, *J. Am. Ceram. Soc*. **1995**, *78*, 1107.
[36] C. E. Ramberg, W. L. Worrell, *J. Am. Ceram. Soc*. **2001**, *84*, 2607.
[37] T. Shimoo, T. Morita, K. Okamura, *J. Am. Ceram. Soc*. **2001**, *84*, 2975.
[38] P. S. Wang, S. M. Hsu, T. N. Wittberg, *J. Mater. Sci*. **1991**, *26*, 1665.
[39] E. J. Opila, *J. Am. Ceram. Soc*. **1994**, *77*, 730.
[40] J. Henrie, S. Kellis, S. Schultz, A. Hawkins, *Opt. Express* **2004**, *12*, 1464.
[41] E. J. Opila, *J. Am. Ceram. Soc*. **1999**, *82*, 625.
[42] F. J. Norton, *Nature* **1961**, *4783*, 701.
[43] J. Grunenberg, *Angew. Chem. Int. Edit*. **2001**, *40*, 4027.
[44] E. Kern, D. Hamill, H. Deem, H. Sheets, *Mater. Res. Bull*. **1969**, *4*, S25.
[45] R. G. Sheppard, D. M. Mathes, D. J. Bray, *Properties and Characteristics of Graphite For Industrial Applications*, Poco Graphite, Inc., Decatur, Texas, USA **2001**.
[46] S. Maj, *Phys. Chem. Miner*. **1984**, *10*, 133.
[47] L. U. Ogbuji, S. R. Bryan, *J. Am. Ceram. Soc*. **1995**, *78*, 1272.
[48] M. Guinel, F. J. Norton, M. Grant, M. G. Norton, *J. Mater. Res*. **2006**, *21*, 2550.
[49] G. Corman, K. Luthra, *Handbook of Ceramic Composites*, Springer, Berlin, Germany **2005**, 99.
[50] E. J. Opila, M. K. Boyd, *Mater. Sci. Forum* **2011**, *696*, 342.
[51] E. J. Opila, R. C. Robinson, M. J. Verrilli, *Int. J. Appl. Ceram. Technol*. **2015**, *13*, 434.
[52] J. Schlichting, *J. Non-Cryst. Solids* **1984**, *63*, 173.

ADVANCED ENGINEERING MATERIALS **2016**,
DOI: 10.1002/adem.201600166